DETERMINACIÓN DE Δm_d Y CALIBRACIÓN ABSOLUTA DEL ETIQUETADO DE SABOR PARA LA MEDIDA DE Δm_s, EN DESINTEGRACIONES RECONSTRUIDAS COMPLETAMENTE EN EL EXPERIMENTO CDF

DETERMINATION OF Δm_d AND ABSOLUTE CALIBRATION OF FLAVOR TAGGERS FOR THE Δm_s ANALYSIS, IN FULLY RECONSTRUCTED DECAYS AT THE CDF EXPERIMENT

Instituto de Física de Cantabria
(CSIC-Universidad de Cantabria)
y
Departamento de Física Moderna
(Universidad de Cantabria)

Memoria presentada por:
Jónatan Piedra Gómez
para optar al grado de Doctor
en Ciencias Físicas

D. Alberto Ruiz Jimeno, Catedrático de Universidad del área de Física Atómica, Molecular y Nuclear de la Facultad de Ciencias de la Universidad de Cantabria, y **D. Iván Vila Álvarez**, contratado Ramón y Cajal adscrito al Instituto de Física de Cantabria (CSIC-Universidad de Cantabria),

Certifican:

Que la presente memoria: **"Determinación de Δm_d y calibración absoluta del etiquetado de sabor para la medida de Δm_s, en desintegraciones reconstruidas completamente en el experimento CDF"**, ha sido realizada bajo nuestra dirección en el Departamento de Física Moderna de la Facultad de Ciencias de la Universidad de Cantabria por *Jónatan Piedra Gómez*, para optar al grado de Doctor en Ciencias Físicas.

Y para que así conste, en cumplimiento de la legislación vigente, presentamos ante la Universidad de Cantabria esta memoria, firmando el presente certificado:

Santander, a 21 de Abril de 2005

Contents

Notation

$\boldsymbol{S}$ – signal;

$\boldsymbol{B}$ – combinatorial background;

$\boldsymbol{ct'}$ – true proper decay-length;

$\boldsymbol{ct}$ – reconstructed proper decay-length;

$\boldsymbol{\tau}$ – lifetime of the B meson;

$\boldsymbol{\xi(ct)}$ – decay-length efficiency curve;

$\boldsymbol{\epsilon}$ – flavor tagging efficiency;

$\boldsymbol{\mathcal{D}}$ – flavor tagging average dilution;

$\boldsymbol{D}$ – flavor tagging event-by-event dilution;

$\boldsymbol{\langle m \rangle}$ – mass of the B meson;

$\boldsymbol{\sigma_{\langle m \rangle}}$ – width of the B meson mass peak;

$\boldsymbol{\mathcal{M}_{\mathbf{min}}}$, $\boldsymbol{\mathcal{M}_{\mathbf{max}}}$ – binned fits mass limits;

$\mathbf{M_{min}}$, $\mathbf{M_{max}}$ – unbinned fits mass limits.

Chapter 1

Introduction

Nature is wonderful, from a little flower to a vast forest; from a magnificent lion to a humble hummingbird. Different approaches can be made to Nature, the most common respect and enjoy it. Some people do not stop there and aim for the understanding of what lies beneath. These people can look at the stars, study the human body or comprehend the behavior of dolphins, among the thousand ways human research can take.

In particle physics we try to understand the nature of the fundamental particles and their interactions. Our current knowledge reduces any matter to be formed by what we call *quarks* and *leptons*; these are half integer spin particles, i.e., *fermions*. They are arranged in three *generations*, each of them containing two quarks and two leptons. We do not know yet why there are three generations, but different experiments and theories find difficult the existence of a fourth one.

The *Standard Model* (SM) of particle physics has been able to accurately describe the immense majority of data provided by experiments along the years. In this model, the interactions among the fundamental particles are described by integer spin particles, i.e., *bosons*: the electroweak interaction is mediated by the $W^{\pm}$, Z^0 and the photon γ, and eight gluons are responsible for the strong interaction.

The success of the SM can be seen as a proof that it is an effective low energy description of Nature. Yet, there are many unanswered questions to believe that the SM has to be extended, among them: baryogenesis, gauge coupling unifications, hierarchy problem, neutrino masses, gravity, ...; therefore, we are interested in probing a *more fundamental theory*. One way to go is to search for new particles that can be produced in yet unreached energies; the way of the new LHC Era. Another way to follow is to search for indirect effects of heavy unknown particles. Flavor physics, and B physics in particular, is an excellent place for probing such indirect signals of physics beyond the Standard Model.

In general, flavor bounds provide strong constraints on new physics models. This fact is called *the new physics flavor problem*, the mismatch between the new physics scale that is required to solve the hierarchy problem, and the one that is needed for satisfying the experimental bounds from flavor physics.

The success of the asymmetric B factories at the Υ resonance has shifted the goals of the of B physics community, the aim is now overconstrain the Unitarity Triangle geometry by measuring observables dominated by box and loop diagrams susceptible of new physics contributions; in words of Lincoln Wolfenstein: *"The next step is NOT the precise determination of γ in addition to β, or equivalently, my parameters ρ and η. No one cares what the exact values are. The goal is to find quantitative checks of the Cabibbo-Kobayashi-Maskawa (CKM) model or, hopefully, signals of new physics."*

The combined measurement of neutral B mesons mixing frequencies, Δm_d and Δm_s, is one of those tests that L. Wolfenstein is referring to; it will provide an important constraint, theoretically precise, to the Unitarity Triangle.

Currently, B_s^0 mesons are only produced at the Tevatron collider; and for the first time in a hadron collider, in the Collider Detector at Fermilab (CDF), a new trigger processor allows one to select the heavy flavor enriched displaced tracks; cutting on the impact parameter of the tracks suppresses the huge background of prompt tracks coming from light flavor production and decays. The addition of this new trigger processor has dramatically increased (by several orders of magnitude) the collecting efficiency of fully hadronic decays of long lived hadrons, like the beauty and charm hadrons. It is fair to say that, in this new data taking period, CDF can be considered an almost completely new detector from the point of view of heavy flavor physics.

The goals of the analysis, here summarized, are motivated by the final measurement of the Δm_s mixing frequency of the B_s^0 meson. More precisely, we are aiming to do a determination of Δm_d and the absolute calibration of the opposite side tagger algorithms required by the Δm_s measurement. In achieving our goals, as a byproduct, likelihood definition and procedure have been fully developed and validated for its, slightly modified, use in measuring Δm_s.

In this thesis report, we have carefully described the key aspects of a mixing measurement with special detail on determining the absolute scale of the flavor taggers dilution. This analysis is just another step forward to constrain Δm_s; new steps will follow soon, as the integrated luminosity and detector understanding improve. Whether we will be able to reach our goals at Tevatron or whether we will have to wait for the next LHC Era, it will mostly depend on the kindness of this *wonderful Nature.*

Chapter 2

Neutral B Mesons Mixing Phenomenology

The main goal of this thesis is the definition of a strategy for the optimal measurement of the mixing oscillations of neutral B mesons, collected by the Collider Detector at Fermilab (CDF II) at the Tevatron Collider. In this chapter I will introduce the theoretical formal context of the neutral B mesons dynamics, how their b-flavor content can mix, and what is the knowledge we can get from measuring those oscillations, in particular in the Standard Model layout. I will also show the present status of the mixing measurements, and their implications in the Cabibbo-Kobayashi-Maskawa (CKM) unitarity matrix elements.

The neutral $B_d^0 = \bar{b}d$, $B_s^0 = \bar{b}s$ mesons, and their charge-conjugates $\bar{B}_d^0 = b\bar{d}$, $\bar{B}_s^0 = b\bar{s}$, contain a heavy antiquark $\bar{b}$ (quark b), and a light quark d, s (antiquark $\bar{d}, \bar{s}$). They are pseudoscalar mesons, which I will denote in the following by $|P^0\rangle$ and $|\bar{P}^0\rangle$. Both are "flavor" eigenstates of the strong interaction hamiltonian, H_s.

Nevertheless, they are not eigenstates of the weak hamiltonian H_w and, consequently, they are not "mass" eigenstates of the total hamiltonian $H = H_s + H_w$. So, their temporal evolution does not correspond to the stationary states, and at each time t the vector state which has evolved from a state initially formed as $|P^0\rangle$ or $|\bar{P}^0\rangle$, is a mixed state of both. During the temporal evolution, H_w defines the content of $|P^0\rangle$ and $|\bar{P}^0\rangle$ (indicated by $|P^0(t)\rangle$ and $|\bar{P}^0(t)\rangle$), via the following expression:

$$i\,\frac{d}{dt}\begin{pmatrix}|P^0(t)\rangle \\ |\bar{P}^0(t)\rangle\end{pmatrix} = \left(M - i\,\frac{\Gamma}{2}\right)\begin{pmatrix}|P^0(t)\rangle \\ |\bar{P}^0(t)\rangle\end{pmatrix}, \tag{2.1}$$

where the *mass matrix* M and the *decay matrix* Γ are t-independent, Hermitian 2×2 matrices. The CPT invariance implies that

$$M_{11} = M_{22}\,, \qquad\qquad \Gamma_{11} = \Gamma_{22}\,. \tag{2.2}$$

Moreover, the non-diagonal terms $H_{12} = H_{21}^*$ can induce transitions between charge-conjugate states. The mass eigenstates of $M - i\,\Gamma/2$ can be expressed in terms of the flavor eigenstates as

$$\begin{aligned} |P^0_L\rangle &= p\,|P^0\rangle + q\,|\bar{P}^0\rangle\,, \\ |P^0_H\rangle &= p\,|P^0\rangle - q\,|\bar{P}^0\rangle\,, \end{aligned} \tag{2.3}$$

with $|p|^2 + |q|^2 = 1$. In (2.3), L and H refer to the *heavy* and *light* mass eigenstates. The temporal evolution of the mass eigenstates is given by

$$|P^0_{H,L}(t)\rangle = e^{-\left(iM_{H,L} + \frac{\Gamma_{H,L}}{2}\right)t}\,|P^0_{H,L}\rangle\,, \tag{2.4}$$

where

$$M_{L,H} \equiv M_{11} \pm Re(H_{12}H_{21})^{1/2}\,, \qquad \Gamma_{L,H} \equiv \Gamma_{11} \mp 2Im(H_{12}H_{21})^{1/2}\,. \tag{2.5}$$

In the following, I will define the average mass m and width Γ, and the mass and width differences Δm and $\Delta\Gamma$, of the mass eigenstates, as:

$$\begin{aligned} m &\equiv \frac{M_H + M_L}{2} = M_{11}\,, & \Gamma &\equiv \frac{\Gamma_L + \Gamma_H}{2} = \Gamma_{11}\,, \\ \Delta m &\equiv M_H - M_L\,, & \Delta\Gamma &\equiv \Gamma_L - \Gamma_H\,. \end{aligned} \tag{2.6}$$

Inverting (2.3) to express the flavor eigenstates $|P^0\rangle$ and $|\bar{P}^0\rangle$ in terms of the mass eigenstates, and using (2.4), we have the time evolution of the flavor eigenstates produced, at time $t = 0$, in the strong interaction:

$$\begin{aligned} |P^0(t)\rangle &= \frac{1}{2p}\left[e^{-\left(iM_L+\frac{\Gamma_L}{2}\right)t}\,|P^0_L\rangle \,+\, e^{-\left(iM_H+\frac{\Gamma_H}{2}\right)t}\,|P^0_H\rangle\right], \\ |\bar{P}^0(t)\rangle &= \frac{1}{2q}\left[e^{-\left(iM_H+\frac{\Gamma_H}{2}\right)t}\,|P^0_H\rangle \,-\, e^{-\left(iM_L+\frac{\Gamma_L}{2}\right)t}\,|P^0_L\rangle\right]. \end{aligned} \tag{2.7}$$

Finally, using (2.3) we get a useful expression for mixing analysis:

$$\begin{aligned} |P^0(t)\rangle &= g_+(t)\,|P^0\rangle - \frac{q}{p}\,g_-(t)\,|\bar{P}^0\rangle\,, \\ |\bar{P}^0(t)\rangle &= -\frac{p}{q}\,g_-(t)\,|P^0\rangle + g_+(t)\,|\bar{P}^0\rangle\,, \end{aligned} \tag{2.8}$$

where

$$\begin{aligned} g_+(t) &\equiv \frac{1}{2}\left[e^{-\left(iM_L+\frac{\Gamma_L}{2}\right)t} + e^{-\left(iM_H+\frac{\Gamma_H}{2}\right)t}\right], \\ g_-(t) &\equiv \frac{1}{2}\left[e^{-\left(iM_L+\frac{\Gamma_L}{2}\right)t} - e^{-\left(iM_H+\frac{\Gamma_H}{2}\right)t}\right]. \end{aligned} \tag{2.9}$$

Now the probabilities of no mixing and mixing can be formulated by:

$$\begin{aligned}
Prob\left[|\bar{P}^0(t)\rangle = |\bar{P}^0\rangle\right] &= \frac{1}{2}\left[\Gamma - \frac{(\Delta\Gamma)^2}{4\Gamma}\right] e^{-\Gamma t}\left[\cosh\left(\frac{\Delta\Gamma}{2}t\right) + \cos\left(\Delta m\, t\right)\right], \quad (2.10)\\
Prob\left[|P^0(t)\rangle = |P^0\rangle\right] &= Prob\left[|\bar{P}^0(t)\rangle = |\bar{P}^0\rangle\right],\\
Prob\left[|\bar{P}^0(t)\rangle = |P^0\rangle\right] &= \frac{1}{2}\left[\Gamma - \frac{(\Delta\Gamma)^2}{4\Gamma}\right]\left|\frac{p}{q}\right|^2 e^{-\Gamma t}\left[\cosh\left(\frac{\Delta\Gamma}{2}t\right) - \cos(\Delta m\, t)\right],\\
Prob\left[|P^0(t)\rangle = |\bar{P}^0\rangle\right] &= \frac{1}{2}\left[\Gamma - \frac{(\Delta\Gamma)^2}{4\Gamma}\right]\left|\frac{q}{p}\right|^2 e^{-\Gamma t}\left[\cosh\left(\frac{\Delta\Gamma}{2}t\right) - \cos(\Delta m\, t)\right].
\end{aligned}$$

Integrating over time, we get:

$$\int_0^\infty g_\pm(t)\,dt = \frac{1}{2\Gamma}\left(\frac{1}{1-y^2} \pm \frac{1}{1+x^2}\right), \quad (2.11)$$

where

$$\begin{aligned}
y &\equiv \frac{\Delta\Gamma}{2\Gamma},\\
x &\equiv \frac{\Delta m}{\Gamma}, \quad (2.12)
\end{aligned}$$

and the ratio of the total probabilities of mixing (no mixing):

$$\begin{aligned}
r &\equiv \frac{Prob[|P^0(t)\rangle = |\bar{P}^0\rangle]}{Prob[|P^0(t)\rangle = |P^0\rangle]} = \left|\frac{q}{p}\right|^2 \frac{x^2+y^2}{2+x^2-y^2},\\
\bar{r} &\equiv \frac{Prob[|\bar{P}^0(t)\rangle = |P^0\rangle]}{Prob[|\bar{P}^0(t)\rangle = |\bar{P}^0\rangle]} = \left|\frac{p}{q}\right|^2 \frac{x^2+y^2}{2+x^2-y^2}.
\end{aligned} \quad (2.13)$$

2.1 *B* Mixing in the Standard Model

In the Standard Model, $B^0 - \bar{B}^0$ mixing refers to transitions between the two flavor eigenstates $|B^0\rangle$ and $|\bar{B}^0\rangle$, which are caused by the fourth order flavor-changing weak interaction described by the box diagrams in Fig. 2.1 (in the figure, the $B^0_d - \bar{B}^0_d$ mixing box diagrams are shown; similar diagrams correspond to $B^0_s - \bar{B}^0_s$ mixing).

As it has been shown previously, the key ingredients to describe the mixing are the off-diagonal elements M_{12} and Γ_{12} entering (2.1) in the effective Hamiltonian of the

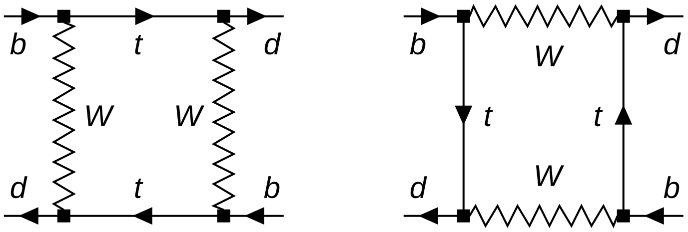

Figure 2.1: Standard Model box diagrams inducing $B_d^0 - \bar{B}_d^0$ mixing.

Schrödinger equation. By solving for the eigenvalues and eigenvectors of the matrix $M - i\,\Gamma/2$, one finds

$$\begin{aligned}
(\Delta m)^2 - \frac{1}{4}(\Delta\Gamma)^2 &= 4\,|M_{12}|^2 - |\Gamma_{12}|^2\,, && (2.14)\\
\Delta m\,\Delta\Gamma &= -4\,\mathrm{Re}\,(M_{12}\Gamma_{12}^*)\,, && (2.15)\\
\frac{q}{p} &= -\frac{\Delta m + i\,\Delta\Gamma/2}{2M_{12} - i\,\Gamma_{12}} = -\frac{2M_{12}^* - i\,\Gamma_{12}^*}{\Delta m + i\,\Delta\Gamma/2}\,, && (2.16)
\end{aligned}$$

from which it is possible to solve (2.14) for Δm , q/p and $\Delta\Gamma$ in terms of $|M_{12}|$ and $|\Gamma_{12}|$. In fact M_{12} holds for the virtual transition between B^0 and $\bar{B}^0$, and Γ_{12} for real transitions to common decay modes. Those common decay modes are very rare and experimentally known to have a branching ratio less than 10^{-3}. So $|\Gamma_{12}| \ll |M_{12}|$ and, consequently, both B_d^0 and B_s^0 have $\Delta\Gamma \ll \Delta m$, because Δm_d has been measured to be about 0.5 ps^{-1}, and Δm_s much larger. In a good approximation, the following inequalities hold for both B_d^0 and B_s^0 systems:

$$\begin{aligned}
|\Gamma_{12}| &\ll |M_{12}|\,,\\
\left|\frac{q}{p}\right| &= 1\,,\\
\Delta\Gamma &\ll \Delta m\,.
\end{aligned} \qquad (2.17)$$

Now, from (2.12-2.13), the ratio of total probabilities to mix and no mix are:

$$r \approx \bar{r} \approx \frac{x^2}{2+x^2}\,. \qquad (2.18)$$

As it was said previously, in the Standard Model, the lowest order contribution to B mixing is given by the box diagrams in Fig. 2.1. Using an effective field theory, the Standard Model prediction is readily obtained to be:

$$\Delta m_q \simeq 2|M_{12}^q| = \frac{G_F^2}{6\pi^2}\,\eta_B\, m_{B_q}\,\widehat{B}_{B_q} f_{B_q}^2 M_W^2\, S\!\left(\frac{m_t^2}{M_W^2}\right)|V_{tb}V_{tq}|^2\,, \qquad (2.19)$$

with $q = s$ or d, and where f_{B_q} and $\widehat{B}_{B_q}$ are constants related to the hadronic matrix element of the box operators, η_B is a QCD correction factor, $S(m_t^2/M_W^2)$ is a function

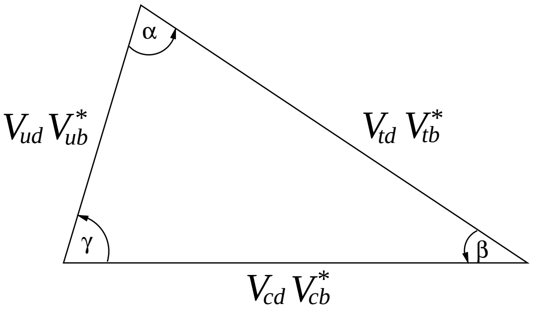

Figure 2.2: The unitarity triangle defined in (2.21).

coming from the box diagram calculation, and $V_{q_1q_2}$ are the matrix elements of the unitary CKM matrix V,

$$V = \begin{pmatrix} V_{ud} & V_{us} & V_{ub} \\ V_{cd} & V_{cs} & V_{cb} \\ V_{td} & V_{ts} & V_{tb} \end{pmatrix} . \tag{2.20}$$

Because V is unitary, one has

$$V_{ud}V_{ub}^* + V_{cd}V_{cb}^* + V_{td}V_{tb}^* = 0 , \tag{2.21}$$

and similarly for all other rows and columns. The equation (2.21) says that the three terms in the sum trace out a triangle on the complex plane, shown in Fig. 2.2. The lengths of the sides are simply $|V_{ud}V_{ub}^*|$, etc, and the angles are

$$\alpha = \arg\left[-\frac{V_{td}V_{tb}^*}{V_{ud}V_{ub}^*}\right], \qquad \beta = \arg\left[-\frac{V_{cd}V_{cb}^*}{V_{td}V_{tb}^*}\right], \qquad \gamma = \arg\left[-\frac{V_{ud}V_{ub}^*}{V_{cd}V_{cb}^*}\right]. \tag{2.22}$$

Separate measurements of lengths through decay and mixing rates, and angles through *CP* asymmetries, should fit together in the unitarity triangle(s). If there are non-CKM contributions to flavor or *CP* violation, however, the interpretation of rates and asymmetries as measurements of the sides and angles no longer holds; the triangle built from experimentally defined sides and angles will not fit with the CKM picture, giving hints of new physics beyond the Standard Model.

A convenient parameterization of the CKM matrix is due to Wolfenstein [1]. It is based on the observation that the measured matrix obeys a hierarchy, with diagonal elements close to 1, and progressively smaller elements away from the diagonal. Phenomenologically, it is possible to expand V in terms of λ, A, ρ and η parameters, where $\lambda \approx 0.22$, $A \approx 0.8$, and $\sqrt{\rho^2 + \eta^2} \approx 0.4$, so:

$$V = \begin{pmatrix} 1 - \frac{1}{2}\lambda^2 & \lambda & A\lambda^3(\rho - i\eta) \\ -\lambda & 1 - \frac{1}{2}\lambda^2 & A\lambda^2 \\ A\lambda^3(1 - \rho - i\eta) & -A\lambda^2 & 1 \end{pmatrix} + \mathcal{O}(\lambda^4) . \tag{2.23}$$

It is customary to rescale Eq. (2.21) by the common factor $A\lambda^3$, to focus on the less well-determined parameters (ρ, η). We choose to divide all three terms in Eq. (2.21) by

$V_{cd}V_{cb}^*$ and define

$$\bar{\rho} + i\bar{\eta} \equiv -\frac{V_{ud}V_{ub}^*}{V_{cd}V_{cb}^*} \,. \tag{2.24}$$

Then the rescaled triangle has its apex in the complex plane at $(\bar{\rho}, \bar{\eta})$. The angles of the triangle are easily expressed:

$$\alpha = \tan^{-1}\left(\frac{\bar{\eta}}{\bar{\eta}^2 + \bar{\rho}(\bar{\rho}-1)}\right) , \quad \beta = \tan^{-1}\left(\frac{\bar{\eta}}{1-\bar{\rho}}\right) , \quad \gamma = \tan^{-1}\left(\frac{\bar{\eta}}{\bar{\rho}}\right) . \tag{2.25}$$

Since $\bar{\eta}$, $\bar{\rho}$ and $1-\bar{\rho}$ could easily be of comparable size, the angles and, thus, the corresponding *CP* asymmetries, could be large.

The elements of the third row of the CKM matrix can be measured from the B_d^0, B_s^0 oscillation frequencies Δm_d and Δm_s. Using the expected values obtained from theoretical calculations and lattice QCD calculations into (2.19) [2]:

- the QCD factor $\eta_B = 0.55$, from NLL perturbative QCD [3];
- the $\overline{\mathrm{MS}}$ value of $m_t = 167$ GeV/c^2, numerically smaller than the pole mass measured at the Tevatron by roughly 7 GeV/c^2;
- the lattice calculations of $f_{B_d}\sqrt{\widehat{B}_{B_d}} = 214 \pm 38$ MeV [4];
- the Inami-Lin function calculated at $m_t = 167$ GeV/c^2, $S\left(\frac{m_t^2}{M_W^2}\right) = 2.40 \pm 0.1$,

and solving for $|V_{td}|$, one finds $|V_{td}| = (8.5 \pm 1.0) \times 10^{-3}$, and the input parameters dependence:

$$|V_{td}| = 0.0083\sqrt{\frac{\Delta m_d}{0.50\,\mathrm{ps}^{-1}}}\,\frac{214\,\mathrm{MeV}}{f_{B_d}\sqrt{\widehat{B}_{B_d}}}\,\sqrt{\frac{0.55}{\eta_B}}\,\sqrt{\frac{2.4}{S(m_t^2/M_W^2)}} \,. \tag{2.26}$$

The relation of $|V_{td}|$ to the improved Wolfenstein parameters is

$$|V_{td}| = A\lambda^3 R_t\left(1 + \mathcal{O}(\lambda^4)\right) \;=\; |V_{cb}|\,\lambda\,R_t\left(1 + \mathcal{O}(\lambda^4)\right) , \tag{2.27}$$

with

$$R_t = \sqrt{(1-\overline{\rho})^2 + \overline{\eta}^2} \tag{2.28}$$

the length of the right side of the rescaled unitarity triangle. Hence the measurement of Δm_d defines a circle in the $(\overline{\rho}, \overline{\eta})$ plane centered around $(1,0)$. Yet the hadronic uncertainties associated with $f_{B_d}\sqrt{\widehat{B}_{B_d}}$ obscure a clean extraction of $|V_{td}|$ and R_t from the well-measured Δm_d.

The other CKM parameter which can be analysed by mixing measurements is $|V_{ts}|$, where we can use the Δm_s limits got from B_s^0 mixing analyses to obtain a lower bound, once $f_{B_s}\sqrt{\widehat{B}_{B_s}}$ is known. The last parameter has been calculated by lattice QCD to be $255 \pm 13 \pm 14 \pm 13$ MeV, with the first error statistical and the other two theoretical [5]. In fact, other analyses show higher values, so the current lattice precision is about 17%.

The ratio $\Delta m_d/\Delta m_s$ is used to constrain R_t, using the ratio

$$\xi = \frac{f_{B_s}\sqrt{\widehat{B}_{B_s}}}{f_{B_d}\sqrt{\widehat{B}_{B_d}}}\,, \tag{2.29}$$

which equals 1 in the limit of exact $SU(3)_F$ symmetry. The current value from lattice calculations is [6]

$$\xi = 1.20 \pm 0.10. \tag{2.30}$$

Finally, we get:

$$R_t = 0.90\sqrt{\frac{\Delta m_d}{0.50\,\mathrm{ps}^{-1}}}\sqrt{\frac{17.3\,\mathrm{ps}^{-1}}{\Delta m_s}}\,\frac{0.22}{\lambda}\,\frac{\xi}{1.20}\,, \tag{2.31}$$

where $\Delta m_s = 17.3^{+1.5}_{-0.7}$ is the best fit from CKM unitarity fits.

2.2 Present Status of *B* Oscillations Measurements

The present results on B_d^0, B_s^0 oscillations have been compiled by the "Heavy Flavour Averaging Group" [7], which uses them to make world combined fits. A summary of the last results prepared for PDG2005 is shown in this section.

The B_d^0 oscillation frequency $\Delta m_d = 0.505 \pm 0.005$ ps^{-1} has been measured at high energy colliders and asymmetric B factories from time-dependent measurements. In Fig. 2.3 the individual measurements are listed as well as the averages taking into account the known correlations.

The world combined B_s^0 amplitude is displayed in Fig. 2.4 as a function of Δm_s. The world average bound is $\Delta m_s > 14.4$ ps^{-1}. It yields

$$\frac{|V_{td}|}{|V_{ts}|} > 0.22\,. \tag{2.32}$$

The allowed ranges of the CKM Wolfenstein parameters obtained from a global fit of the data are shown in Fig. 2.5.

All individual measurements of the B_s^0 oscillation amplitude at $\Delta m_s = 15$ ps^{-1} are listed in Fig. 2.6. The sensitivity quoted for each experiment is obtained from the positive amplitude uncertainty. The sensitivities are defined as the value of Δm_s at which the positive uncertainty on the measured amplitude is equal to 1/1.645; they correspond to sensitivities for 95% Confidence Level exclusion limits.

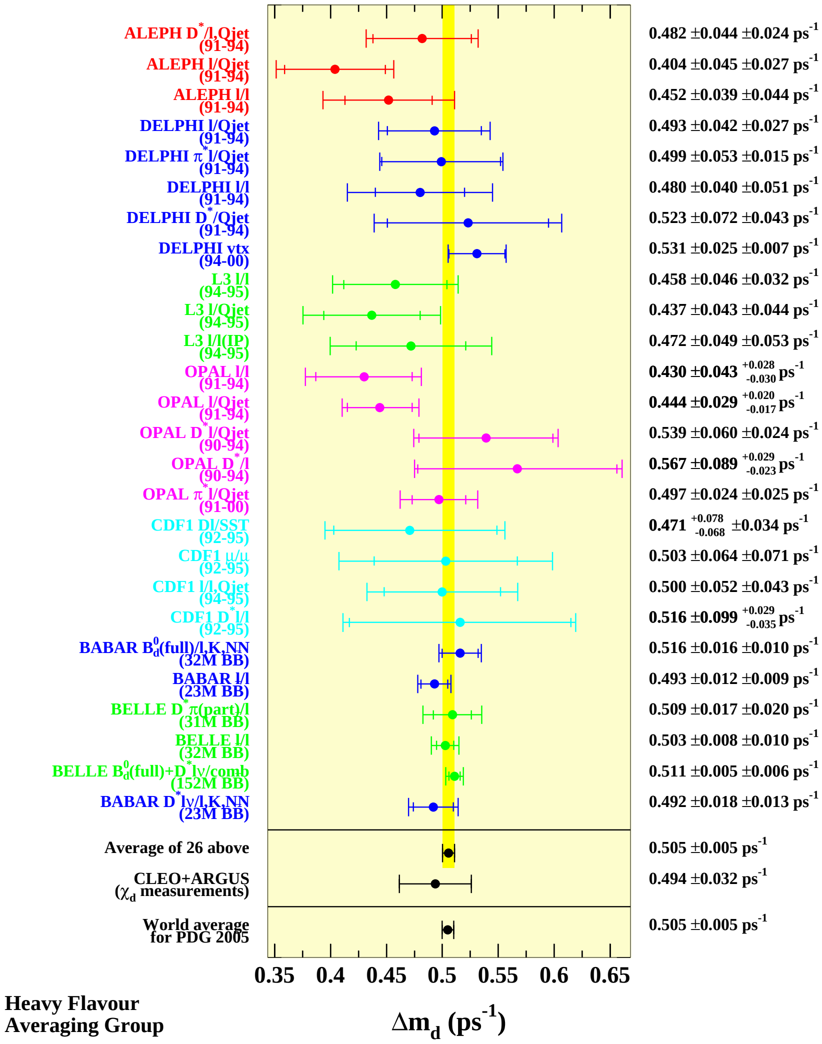

Figure 2.3: Experimental measurements of Δm_d and world average.

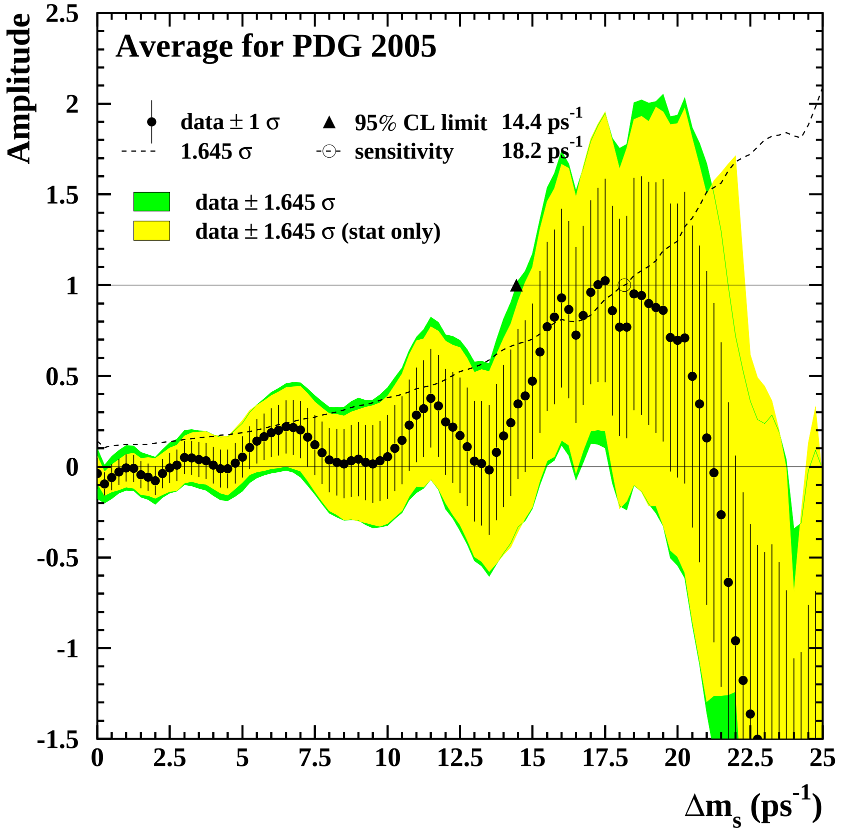

Figure 2.4: World combined results on B_s^0 oscillations.

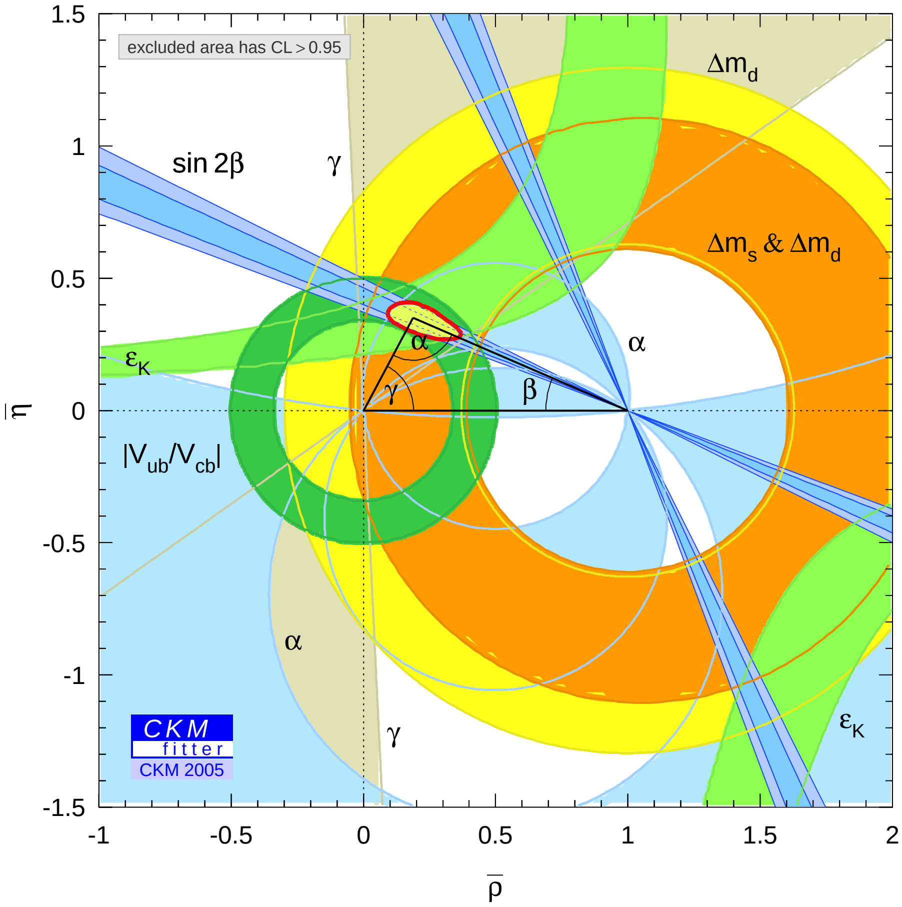

Figure 2.5: Global fit of the Wolfenstein parameters. The rescaled $(\bar{\rho}, \bar{\eta})$ limits given by Δm_d and Δm_s mixing evaluations are shown.

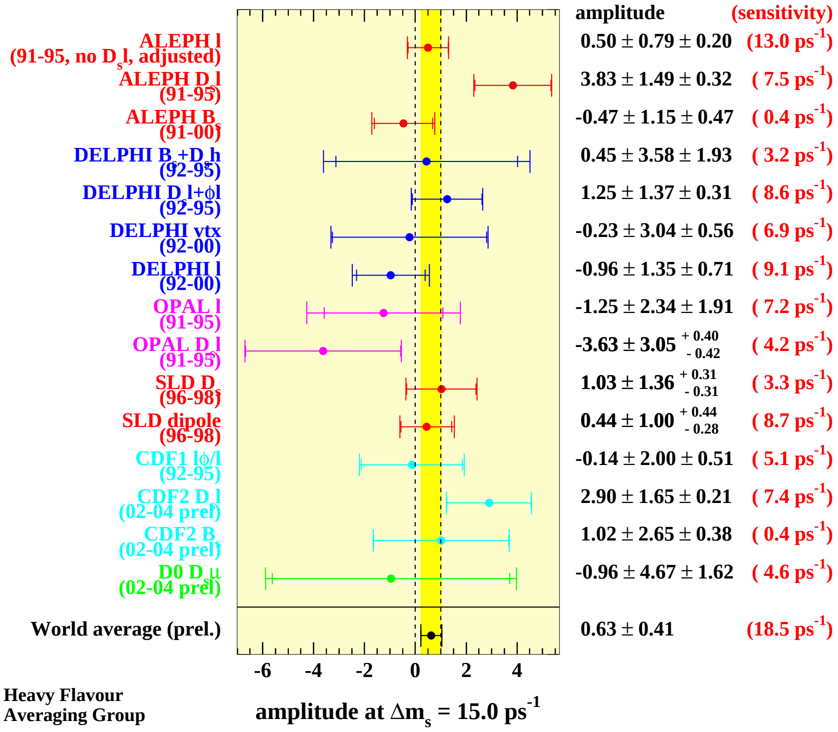

Figure 2.6: Experimental amplitudes and sensitivities at $\Delta m_s = 15$ ps^{-1}.

Chapter 3

Experimental Framework

Fermilab's Tevatron Collider represents the high energy frontier in particle physics. It is currently the source of the highest energy proton-antiproton ($p\bar{p}$) collisions. The collisions occur at two points on an underground ring, which has a radius of about 1 km. At these collision points there are two detectors: the Collider Detector at Fermilab (CDF II) and DØ . This analysis uses data collected by the CDF II Detector.

Between 1997 and 2001, both the accelerator complex and the collider detectors underwent major upgrades, mainly aimed at increasing the luminosity of the accelerator, and gathering data samples of 2 fb^{-1} or more. The upgraded machine accelerates 36 bunches of protons and antiprotons, whereas the previous version of the accelerator operated with only 6. Consequently, the time between bunch crossings has been decreased from 3.5 μs for the previous version to 396 ns for the current collider.

The new configuration required detector upgrades at CDF II to ensure a maximum response time shorter than the time between beam crossings. In the following pages, we describe how the proton and antiproton beams are produced, accelerated to their final center of mass energy of 1.96 TeV, and collided. We then describe the components used to identify and measure properties of the particles produced in the collision.

3.1 The Tevatron Collider

To create the world's most powerful particle beams, Fermilab uses a series of accelerators. The diagram in Fig. 3.1 shows the paths taken by protons and antiprotons from initial acceleration to collision in the Tevatron.

The Cockcroft-Walton [8] pre-accelerator provides the first stage of acceleration. Inside this device, hydrogen gas is ionized to create H^- ions, which are accelerated to 750 keV of kinetic energy. Next, the H^- ions enter a linear accelerator (Linac) [9], approximately 500 feet long, where they are accelerated to 400 MeV. The acceleration in the Linac is done by a series of "kicks" from Radio Frequency (RF) cavities. The oscillating electric field of the RF cavities groups the ions into bunches.

The 400 MeV H^- ions are then injected into the Booster, a circular synchrotron [9] 74.5 m in diameter. A carbon foil strips the electrons from the H^- ions at injection,

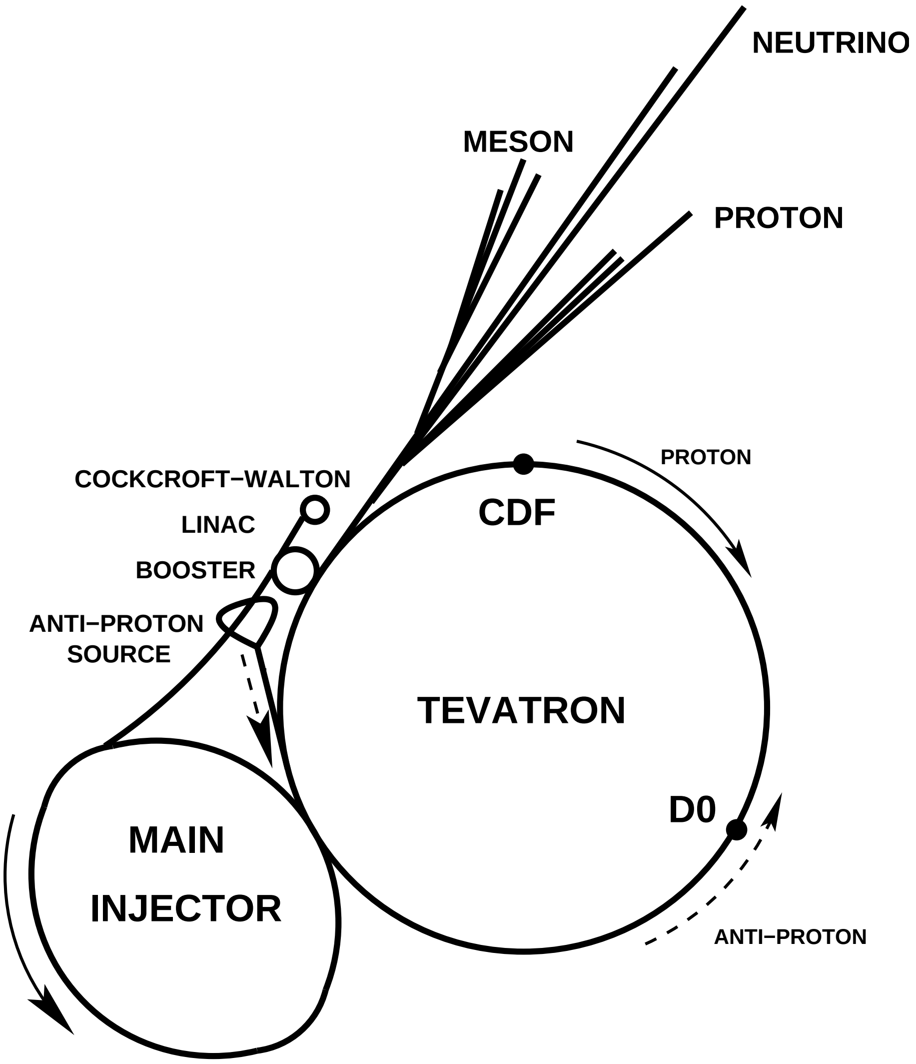

Figure 3.1: Layout of the Fermilab accelerator complex.

leaving bare protons. The intensity of the proton beam is increased by injecting new protons into the same orbit as the circulating ones. The protons are accelerated from 400 MeV to 8 GeV by a series of “kicks” applied by RF cavities. Each turn around the Booster, the protons accrue about 500 keV of kinetic energy.

Protons are extracted from the Booster into the Main Injector [10], which operates at 53 MHz. It has four functions. It accelerates protons from 8 GeV to 150 GeV before injection into the Tevatron, it produces 120 GeV protons which are used for antiproton production, it receives antiprotons from the Antiproton Source and accelerates them to 150 GeV for injection into the Tevatron, and finally, it injects protons and antiprotons into the Tevatron.

The Main Injector replaced the Main Ring accelerator which was situated in the Tevatron tunnel. The Injector is capable of containing larger proton currents than its predecessor, which results in a higher rate of antiproton production. The Main Injector tunnel also houses the Antiproton Recycler. Not all antiprotons in a given store are used up by the collisions. Recycling the unused antiprotons and reusing them in the next store significantly reduces the stacking time. The task of the Antiproton Recycler is to receive antiprotons from a Tevatron store, cool them and re-integrate them into the stack, so that they can be used in the next store.

To produce antiprotons, 120 GeV protons from the Main Injector are directed into a nickel target. In the collisions, about 20 antiprotons are produced per one million protons, with a mean kinetic energy of 8 GeV. The antiprotons are focused by a lithium lens and separated from other particle species by a pulsed magnet.

Before the antiprotons can be used in the narrow beams needed in the collider, the differences in kinetic energy between the different particles need to be reduced. Since this process reduces the spread of the kinetic energy spectrum of the beam, it is referred to as “cooling” the beam. New batches of antiprotons are initially cooled in the Debuncher synchrotron, collected and further cooled using stochastic cooling [11] in the 8 GeV Accumulator synchrotron. The principle of stochastic cooling is to sample a particles motion with a pickup sensor and correct its trajectory later with a kicker magnet. In reality, the pickup sensor samples the average motion of particles in the beam and corrects for the average. Integrated over a long period of time, this manifests itself as a damping force applied onto individual particles which evens out their kinetic energies. It takes between 10 and 20 hours to build up a “stack” of antiprotons which is then used in collisions in the Tevatron. Antiproton availability is the most limiting factor for attaining high luminosities, assuming there are no technical problems with the accelerator (assuming, for example, perfect transfer efficiencies between accelerator subsystems) [9, 10].

Roughly once a day, the stacked antiprotons (36 bunches of about 3×10^{10} antiprotons per bunch) are injected back into the Main Injector. They are accelerated to 150 GeV together with 36 bunches of roughly 3×10^{11} protons. Both the protons and antiprotons are transferred to the Tevatron.

The Tevatron is the last stage of Fermilab’s accelerator chain. It receives 150 GeV protons and antiprotons from the Main Injector and accelerates them to 980 GeV. The protons and antiprotons circle the Tevatron in opposite directions. The beams are brought

parameter	Run I	Run II
number of bunches (N_B)	6	36
bunch rms [m]	0.6	0.37
bunch spacing [ns]	3500	396
protons/bunch (N_p)	2.3×10^{11}	2.7×10^{11}
antiprotons/bunch ($N_{\bar{p}}$)	5.5×10^{10}	3.0×10^{10}
total antiprotons	3.3×10^{11}	1.1×10^{12}
β^* [cm]	35	35
interactions/crossing	2.5	2.3
integrated luminosity [pb^{-1}]	112	450
peak luminosity [$\mathrm{cm}^{-2}\mathrm{s}^{-1}$]	2×10^{31}	1.2×10^{32}

Table 3.1: Accelerator parameters for Run I and Run II configurations.

to collision at two “collision points”, B0 and D0. The two collider detectors, the Collider Detector at Fermilab (CDF II) and DØ, are built around the respective collision points.

The luminosity of collisions can be expressed as:

$$\mathcal{L} = \frac{f N_B N_p N_{\bar{p}}}{2\pi(\sigma_p^2 + \sigma_{\bar{p}}^2)} F\left(\frac{\sigma_l}{\beta^*}\right), \tag{3.1}$$

where f is the revolution frequency, N_B is the number of bunches, $N_{p(\bar{p})}$ is the number of protons(antiprotons) per bunch, and $\sigma_{p(\bar{p})}$ is the protons(antiprotons) rms beam size at the interaction point. F is a form factor which corrects for the bunch shape and depends on the ratio of σ_l, the bunch length to β^*, the beta function, at the interaction point. The beta function is a measure of the beam width, and it is proportional to the beam's x and y extent in phase space.

Table 3.1 shows a comparison of Run I and design Run II [10] accelerator parameters.

3.2 The CDF II Detector

The CDF II Detector [12] is a substantial upgrade of the original CDF Detector [13]. It is located at the B0 collision point of the Tevatron Collider. The detector is designed to detect and measure properties of particles emanating from $p\bar{p}$ collisions. The design is not geared toward one particular physics measurement, but rather optimized toward extracting a number of different properties about all particle species created in the $p\bar{p}$ collision. Such particle detectors are often called multi-purpose detectors.

A diagram of the CDF II Detector is shown in Fig. 3.2. A quadrant of the detector is cut out to expose the different subdetectors. The detector subsystems can be grouped as follows. The innermost system is the integrated tracking system. The tracking system is barrel-shaped and consists of cylindrical subsystems which are concentric with the beam. It is designed to detect charged particles, measure their momenta and displacements from

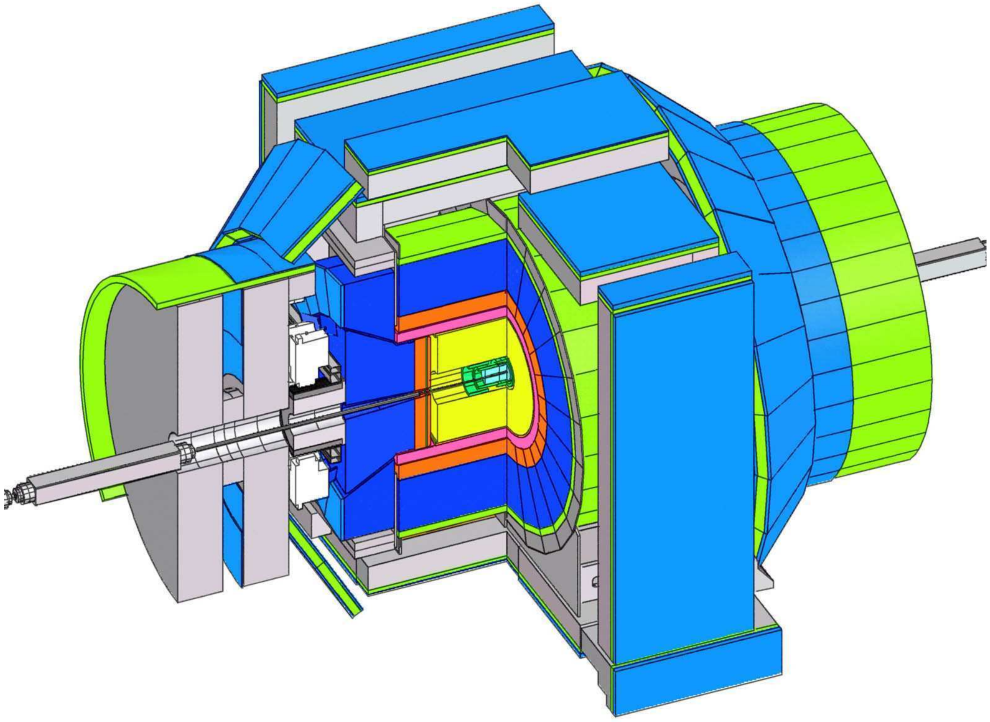

Figure 3.2: The CDF II Detector with quadrant cut to expose the different subdetectors.

the point of collision (primary interaction vertex). The tracking system is surrounded by the Time of Flight system, designed to provide particle identification for low-momentum charged particles. Both the tracking and Time of Flight systems are placed inside a superconducting coil, which generates a 1.4 T solenoidal magnetic field. The coil is surrounded by calorimetry systems, which measure the energy of particles that shower when interacting with matter. The calorimetry systems are surrounded by muon detector systems. When interacting with matter, muons act as "minimally ionizing particles" - they only deposit small amounts of ionization energy in the material. Therefore, they are able to penetrate both the tracking and calorimeter systems. The integrated material of the tracking system, TOF, solenoid and calorimetry systems serves as a particle filter. Particles which penetrate through all that material are mostly muons, and they are detected by leaving tracks in the muon detection system, located outside of the calorimeter.

The most important parts of the detector for this analysis are the tracking system and the trigger, and these will be described in detail in the following sections. The description of the remaining systems will be brief. More detailed information on these systems can be found in the Technical Design Reports of the CDF II Detector [12, 13].

3.3 Standard Definitions in CDF

Because of its barrel-like detector shape, the CDF II Detector uses a cylindrical coordinate system (r, ϕ, z) with the origin at the center of the detector and the z-axis along the nominal direction of the proton beam. The y-axis points upwards. Since the coordinate system is right-handed, this also defines the direction of the x-axis. Particles moving through a homogeneous solenoidal magnetic field follow helical trajectories. Reconstructed charged particle trajectories are referred to as "tracks". The plane perpendicular to the beam is referred to as the "transverse plane", and the transverse momentum of the track is referred to as p_T. As opposed to e^+e^- collisions, in $p\bar{p}$ collisions not all of the center of mass energy of the $p\bar{p}$ system is absorbed in the collision. The colliding partons inside the proton carry only a fraction of the kinetic energy of the proton. As a result, the center of mass system of the parton collisions is boosted along the beam direction (the "longitudinal" direction) by an unknown amount, but quantities defined in the transverse plane are conserved in the collisions. For instance, the sum of all transverse momenta of particles in a collision is zero, $\sum \vec{p_T} = 0$.

To uniquely parameterize a helix in three dimensions, five parameters are needed. The CDF II coordinate system chooses three of these parameters to describe a position, and two more to describe the momentum vector at that position. The three parameters which describe a position describe the point of closest approach of the helix to the beam line. These parameters are d_0, ϕ_0, and z_0, which are the ρ, ϕ and z cylindrical coordinates of the point of closest approach of the helix to the beam. The momentum vector is described by the track curvature (c) and the angle of the momentum in the $r-z$ plane ($\cot\theta$). From the track curvature we can calculate the transverse momentum. The curvature is signed so that the charge of the particle matches the charge of the curvature. From $\cot\theta$, we can calculate $p_z = p_T \cdot \cot\theta$. At any given point of the helix, the track momentum is a tangent to the helix. This basically means that the angle ϕ_0 implicitly defines the direction of the transverse momentum vector at the point of closest approach, $\vec{p_T}$.

The impact parameter (d_0) of a track is another signed variable; its absolute value corresponds to the distance of closest approach of the track to the beamline. The sign of d_0 is taken to be that of $\hat{p} \times \hat{d} \cdot \hat{z}$, where $\hat{p}$, $\hat{d}$ and $\hat{z}$ are unit vectors in the directions of $\vec{p}$, $\vec{d_0}$ and $\vec{z}$, respectively. An alternate variable that describes the angle between the z-axis and the momentum of the particle is the pseudorapidity η, which is defined as:

$$\eta \equiv -\ln\tan\left(\frac{\theta}{2}\right). \tag{3.2}$$

For decaying particles, we often define the displacement L_{xy},

$$L_{xy} = \vec{d} \cdot \hat{p_T}\,, \tag{3.3}$$

where $\vec{d}$ is the displacement of the decay vertex in the transverse plane, and $\hat{p_T}$ is the unit vector in the direction of $\vec{p_T}$.

3.4 Tracking Systems

The detector has a cylindrical tracking system immersed in a 1.4 T solenoidal magnetic field for the measurement of charged-particles momenta. We will describe this system starting from the devices closest to the beam and moving outwards. The innermost tracking device is a silicon strip vertex detector, which consists of three subdetectors. A layer of silicon sensors, called Layer 00 (L00) [14], is installed directly onto the beryllium vacuum beam pipe, with the sensors at radii 1.35 and 1.62 cm from the beam. The beam pipe is made of beryllium because this metal has the best mechanical qualities, yet lowest nuclear interaction cross section of all materials.

The layer of silicon on the beam pipe is followed by five concentric layers of silicon sensors (SVX-II) [15] located at radii between 2.45 and 10.6 cm. The Intermediate Silicon Layers (ISL) [16] are the outermost silicon subdetector systems, consisting of one layer at a radius of 22 cm in the central region and two layers at radii 20 and 28 cm in the forward regions. Surrounding the silicon detector is the Central Outer Tracker (COT) [17], a 3.1 m-long cylindrical open-cell drift chamber covering radii from 43.4 to 132.3 cm.

3.4.1 Silicon Tracking Detectors

Silicon tracking detectors are used to obtain precise position measurements of the path of a charged particle. A silicon tracking detector is fundamentally a reverse-biased p-n junction. When a charged particle passes through the detector material, it causes ionization. In the case of a semiconductor material, this means that electron-hole pairs will be produced. Electrons drift towards the anode, and holes drift toward the cathode,

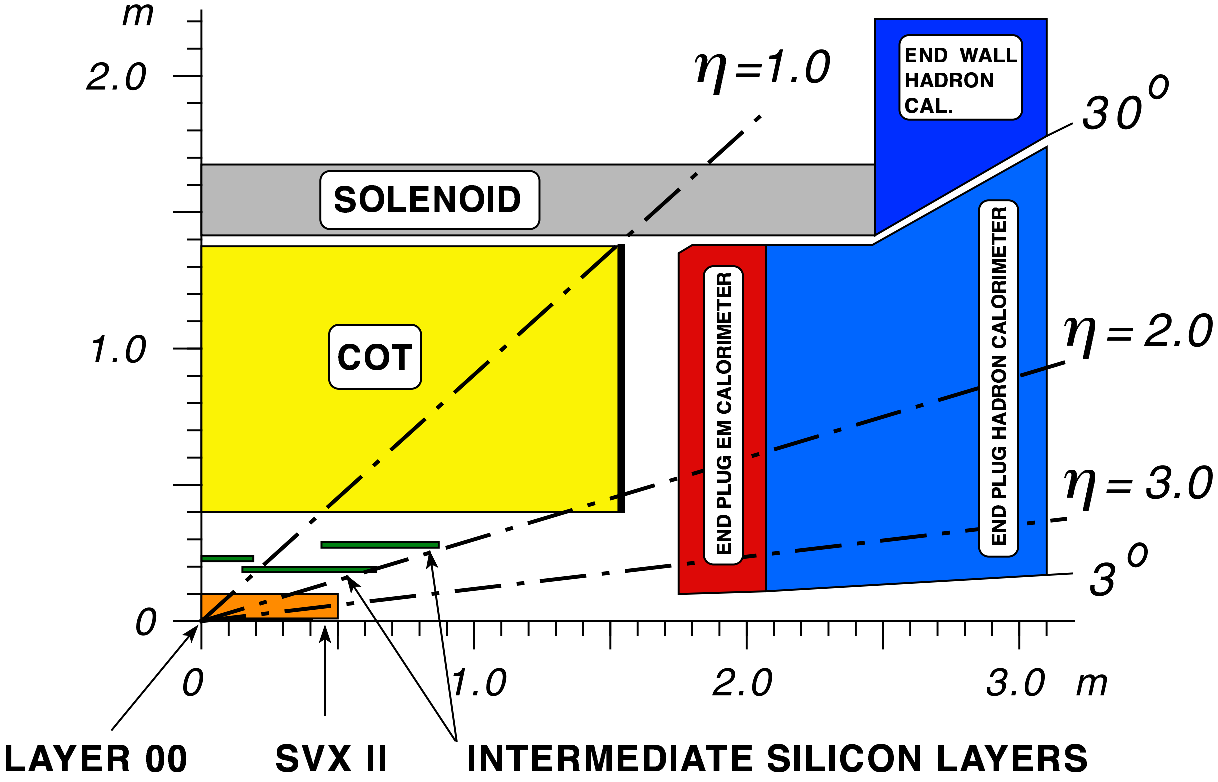

Figure 3.3: The CDF II tracker layout showing the different subdetector systems.

property	Layer 0	Layer 1	Layer 2	Layer 3	Layer 4
number of ϕ strips	256	384	640	768	869
number of z strips	256	576	640	512	869
stereo angle	90°	90°	+1.2°	90°	-1.2°
ϕ strip pitch [μm]	60	62	60	60	65
z strip pitch [μm]	141	125.5	60	141	65
active width [mm]	15.30	23.75	38.34	46.02	58.18
active length [mm]	72.43	72.43	72.38	72.43	72.43

Table 3.2: Relevant parameters for the layout of the sensors of the SVX-II layers.

where the charge is gathered. The amount of charge is, to first order, proportional to the path length traversed in the detector material by the charged particle.

By segmenting the p or n side of the junction into "strips" and reading out the charge deposition separately on every strip, we obtain sensitivity to the position of the charged particle. All the CDF II silicon tracking detectors are implemented as microstrip detectors. The typical distance between two strips is about 60 μm. Charge deposition from a single particle passing through the silicon sensor will be read out on one or more strips. This charge deposition is called a "cluster". There are two types of microstrip detectors: single and double-sided. In single-sided detectors only one (p) side of the junction is segmented into strips. Double-sided detectors have both sides of the junction segmented into strips. The benefit of double-sided detectors is that while one (p) side has strips parallel to the z direction, providing $r-\phi$ position measurements, the other (n) side can have strips at an angle (stereo angle) with respect to the z direction, which will give z position information.

The innermost layer, L00, is made of single-sided silicon sensors which only provide $r-\phi$ measurements. The SVX-II and ISL are made of double-sided silicon sensors. As shown in Table 3.2, the SVX-II layers have different stereo angles. Two layers have a 1.2° stereo angle and three have a 90° stereo angle. The ISL detector provides small angle (1.2°) stereo information.

Four silicon sensors are stacked length-wise into a "ladder" structure which is 29 cm long. The readout electronics are mounted onto the ends of the ladders. The ladders are organized in an approximately cylindrical configuration, creating "barrels". A SVX-II barrel is segmented into 12 wedges, each covering approximately 30° in ϕ with a small overlap at the edges, allowing for several silicon hits per track. There are three SVX-II barrels, adjacent to each other along the z-axis, covering the nominal interaction point in the center of the CDF II Detector. The coverage of the silicon detector subsystems is shown in Fig. 3.4. The silicon tracking system is used in stand-alone mode to provide an extension of tracking down to 2.8 in pseudorapidity.

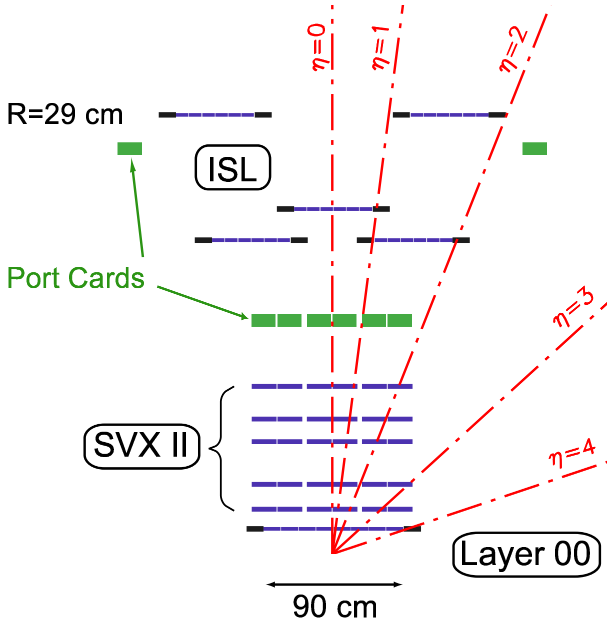

Figure 3.4: Coverage of the different silicon subdetectors projected into the $r-z$ plane. The r and z axes have different scales.

3.4.2 Central Outer Tracker

The COT drift chamber provides accurate information in the $r-\phi$ plane for the measurement of transverse momentum, and substantially less accurate information in the $r-z$ plane for the measurement of the z component of the momentum, p_z. The COT contains 96 sense wire layers, which are radially grouped into eight "superlayers", as inferred from the end plate section shown in Fig. 3.5. Each superlayer is divided in ϕ into "supercells", and each supercell has 12 sense wires and a maximum drift distance that is approximately the same for all superlayers. Therefore, the number of supercells in a given superlayer scales approximately with the radius of the superlayer. The entire COT contains 30,240 sense wires. Approximately half the wires run along the z direction ("axial"). The other half are strung at a small angle (2°) with respect to the z direction ("stereo").

The active volume of the COT begins at a radius of 43.4 cm from the nominal beamline and extends out to a radius of 132.3 cm. The chamber is 310 cm long. Particles originating from the interaction point which have $|\eta| < 1$ pass through all 8 superlayers of the COT. Particles which have $|\eta| < 1.3$ pass through 4 or more superlayers.

The supercell layout, shown in Fig. 3.6 for superlayer 2, consists of a wire plane containing sense and potential (for field shaping) wires and a field (or cathode) sheet on either side. Both the sense and potential wires are 40 μm diameter gold plated Tungsten. The field sheet is 6.35 μm thick Mylar with vapor-deposited gold on both sides. Each field sheet is shared with the neighboring supercell.

The COT is filled with an Argon-Ethane gas mixture and Isopropyl alcohol

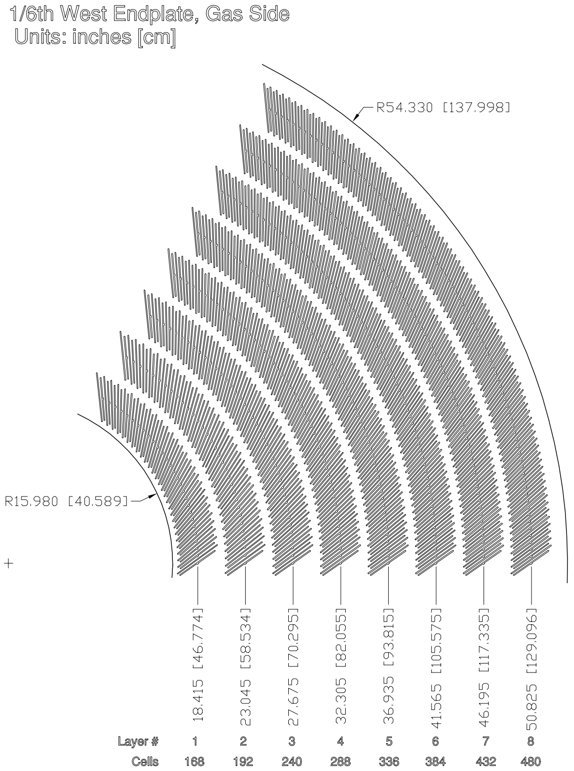

Figure 3.5: Layout of wire planes on a COT endplate.

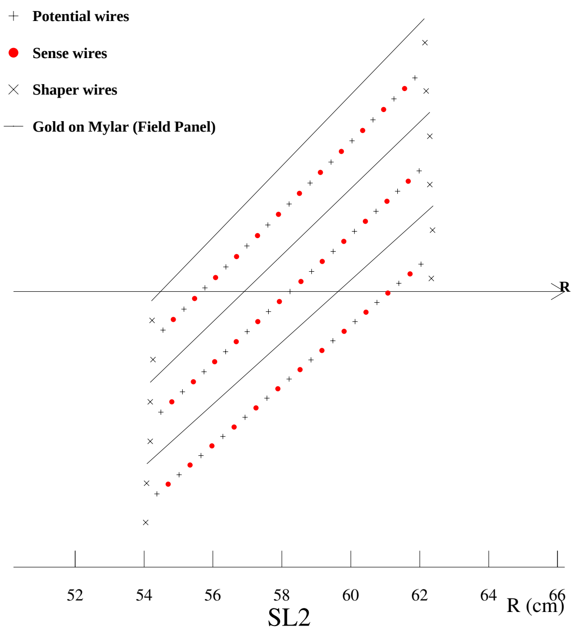

Figure 3.6: Layout of wires in a COT supercell.

(49.5:49.5:1). The mixture is chosen to have a constant drift velocity across the cell width. When a charged particle passes through, the gas is ionized. Electrons drift towards the sense wires. The electric field in a cylindrical system grows exponentially with decreasing radius. As a result, the electric field very close to the sense wire is large, resulting in an avalanche discharge when the charge drifts close to the wire surface. This effect provides a gain of $\sim 10^4$. The maximum electron drift time is approximately 100 ns. Due to the magnetic field that the COT is immersed in, electrons drift at a Lorentz angle of $\sim 35°$. The supercell is tilted by 35° with respect to the radial direction to compensate for this effect.

Signals on the sense wires are processed by the ASDQ (Amplifier, Shaper, Discriminator with charge encoding) chip, which provides input protection, amplification, pulse shaping, baseline restoration, discrimination and charge measurement [18]. The charge measurement is encoded in the width of the discriminator output pulse, and is used for particle identification by measuring the ionization along the trail of the charged particle (dE/dx). The pulse is sent through ~ 11 m of micro-coaxial cable, via repeater cards to Time to Digital Converter (TDC) boards in the collision hall. Hit times are later processed by pattern recognition (tracking) software to form helical tracks. The hit resolution of the COT is about 140 μm. The transverse momentum resolution has been measured using cosmic ray events to be

$$\frac{\sigma_{p_T}}{p_T^2} = 0.0017\ [\mathrm{GeV/c}]^{-1}. \tag{3.4}$$

3.4.3 Pattern Recognition Algorithms

As explained in the previous sections, charged particles leave small charge depositions as they pass through the tracking system. By following, or "tracking", these depositions, pattern recognition algorithms can reconstruct the charged particle track.

There are several pattern recognition algorithms used to reconstruct tracks in the CDF II tracking system. Most of the tracks are reconstructed using "Outside-In" algorithms which we will describe here. The name of this group of algorithms suggests that the track is followed from the outside of the tracking system inwards.

The track is first reconstructed using only COT information. The COT electronics report hit time and integrated charge for every wire in an event. The hit time corresponds to the time that an avalanche occurred at a sense wire. The hit time can be interpreted as the drift time of the charge in the gas, but first it has to be corrected for time of flight. The hit timing resolution is of the order of a few ns; this roughly corresponds to the average spread in collision times. It is assumed that the collision times always happen at the same time in a cycle during a store. An average of collision times is done for many previous events and this is used as the event collision time. Hit times corrected for the collision time are interpreted as drift times and used in pattern recognition. To perform the final track fit, an additional time of flight correction is performed assuming massless particles.

The helical track, when projected into the two dimensional $r-\phi$ plane, is a circle. This simplifies pattern recognition, so the first step of pattern recognition in the COT looks for circular paths in radial superlayers of the COT. Supercells in the radial superlayers are searched for sets of 4 or more hits that can be fit to a straight line. These sets are called "segments". The straight-line fit for a segment gives sufficient information to extrapolate rough measurements of curvature and ϕ_0. Once segments are found, there are two approaches to track finding. One approach is to link together segments for which the measurements of curvature and ϕ_0 are consistent. The other approach is to improve the curvature and ϕ_0 measurement of a segment reconstructed in superlayer 8 by constraining its circular fit to the beamline, and then adding hits which are consistent with this path. Once a circular path is found in the $r-\phi$ plane, segments and hits in the stereo superlayers are added by their proximity to the circular fit. This results in a three-dimensional track fit. Typically, if one algorithm fails to reconstruct a track, the other algorithm will not. This results in a high track reconstruction efficiency ($\sim 95\%$) in the COT for tracks which pass through all 8 superlayers ($p_T \geq 400$ MeV/c). The track reconstruction efficiency mostly depends on how many tracks there are to be reconstructed in the event. If there are many tracks present close to each other, hits from one track can shadow hits from the other track, resulting in efficiency loss.

Once a track is reconstructed in the COT, it is extrapolated into the SVX-II. Based on the estimated errors on the track parameters, a three-dimensional "road" is formed around the extrapolated track. Starting from the outermost layer, and working inwards, silicon clusters found inside the road are added to the track. As a cluster gets added, the road gets narrowed according to the knowledge of the updated track parameters.

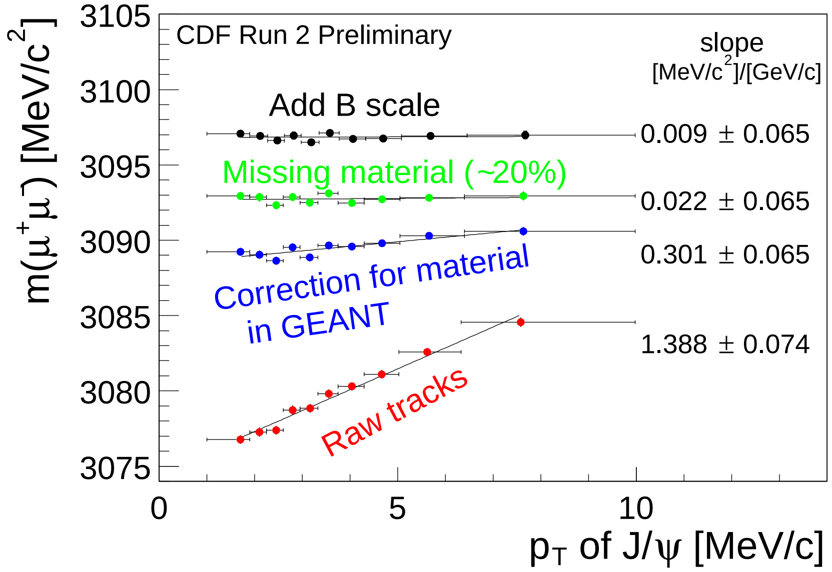

Figure 3.7: Dependence of the reconstructed invariant mass of $J/\psi \to \mu^+\mu^-$ decays on the p_T of the J/ψ.

Reducing the width of the road reduces the chance of adding a wrong hit to the track, and also reduces computation time. In the first pass of this algorithm, $r{-}\phi$ clusters are added. In the second pass, clusters with stereo information are added to the track.

3.4.4 Momentum Scale

As the charged particle traverses through the tracker material, it loses energy. For a track that passes through the entire SVX-II volume, the amount of energy loss is roughly 9 MeV. The value is practically independent of the momentum of the particle. In the reconstructed distribution of invariant mass of $J/\psi \to \mu^+\mu^-$ decays, this effect will be more noticeable for low-momentum J/ψ decays than for high-momentum decays. Fig. 3.7 illustrates this effect. We use the momentum-dependence of the $\mu^+\mu^-$ invariant mass to calibrate the momentum scale of our detector. The J/ψ mass has to be invariant of transverse momentum and match with the world average [19] value if the momentum scale is correctly calibrated. Our calibration procedure follows two steps. First, the momentum dependence of the J/ψ mass is removed by correctly accounting for the energy loss in the tracker material, and then the overall shift of the J/ψ mass is removed by correcting the value of the magnetic field used in the conversion of curvature into transverse momentum.

There are two types of material in the SVX-II tracker. The silicon sensors are read out and therefore called active material. Everything else in the silicon tracker (readout chips, cards, cables, cooling pipes) is passive material. The energy loss in the active material of the tracking system is taken into account by mapping out the material in the

GEANT [20] description of our detector. The passive material in the detector description is not complete, so some energy loss is unaccounted for by this method. An additional layer of material is added to the detector description, to correct for the missing material on average. By tuning the amount of missing material, the momentum dependence of the J/ψ mass is removed. The remaining discrepancy with respect to the PDG average is corrected for by scaling the magnetic field. Because of the implementation of this procedure, we can not use it to measure the J/ψ mass, but the results of the calibration process (the amount of missing material and the corresponding magnetic field) can be used to correct the momentum scale in any other measurement. A more detailed description can be found in [21].

3.5 Time of Flight

Outside the tracking system, still inside the superconducting magnetic coil, CDF II has a Time of Flight (TOF) [22] system. The TOF system is designed to distinguish low momentum pions, kaons and protons by measuring the time it takes these particles to travel from the primary vertex of the $p\bar{p}$ collision to the TOF system. The system consists of 216 bars of scintillating material, roughly 300 cm in length and with a cross section of 4×4 cm. The bars are arranged into a barrel around the COT cylinder. They are surrounded by the superconducting solenoid on the outside. Particles passing through the scintillating material of the bars deposit energy causing small flashes of visible light. This light is detected by photomultiplier (PMT) tubes which are attached at both ends of each bar. The signal from the photomultiplier tube is processed by a pre-amplifier circuit mounted directly onto the tube. The amplified signal is sent via a twisted pair to the readout electronics in the collision hall. The readout electronics perform both time and amplitude digitization of the signal. The TDC information is a digitization of the time when the signal pulse reaches a fixed discriminator threshold. This time depends on the amplitude of the pulse, since a large pulse crosses the threshold earlier (time walk). The digitization of the pulse amplitude is needed to correct for this effect. After correcting for time walk effects, the timing resolution of the TOF system is currently about 110 ps for particles crossing the bar exactly in front of one of the photomultiplier tubes. The timing resolution varies with displacement from the photomultiplier tube. Large pulses give better timing resolution, and light attenuates while travelling through the scintillator material. Therefore, particles passing through the bar near the photomultiplier tube have better timing resolution than those which are farther away.

3.6 Calorimeters

The main effort of the Run II upgrade of the CDF II calorimeter system dealt with upgrading the electronics to handle the faster bunch crossings. The active detector parts were taken over from Run I without modification. Since this analysis does not use calorimetry

system	η coverage	energy resolution (%)	thickness
CEM	$\|\eta\| < 1.1$	$13.5/\sqrt{E_T} \oplus 3$	$18X_0$
PEM	$1.1 < \|\eta\| < 2.4$	$28/\sqrt{E_T} \oplus 2$	$18 - 21X_0$
FEM	$2.2 < \|\eta\| < 4.2$	$25/\sqrt{E_T} \oplus 2$	$25X_0$
CHA	$\|\eta\| < 0.9$	$50/\sqrt{E_T} \oplus 3$	$4.5\lambda_0$
WHA	$0.7 < \|\eta\| < 1.3$	$75/\sqrt{E_T} \oplus 4$	$4.5\lambda_0$
PHA	$1.3 < \|\eta\| < 2.4$	$90/\sqrt{E_T} \oplus 4$	$5.7\lambda_0$
FHA	$2.4 < \|\eta\| < 4.2$	$130/\sqrt{E_T} \oplus 4$	$7.7\lambda_0$

Table 3.3: Pseudorapidity coverage, energy resolution and thickness for the different calorimeter subdetectors of the CDF II Detector. The $\oplus$ symbol means that the constant term is added in quadrature to the resolution. λ_0 signifies interaction lengths and X_0 radiation lengths.

information, this system will be described briefly. A detailed description can be found in the CDF II Technical Design Report [13].

The CDF II calorimeter has a "projective tower" geometry. This means that it is segmented in η and ϕ "towers" that point to the interaction region. The coverage of the calorimetry system is 2π in ϕ and $|\eta| < 4.2$ in pseudorapidity. The calorimeter system is divided into three regions: central, plug and forward. Corresponding to these regions, the subsystems will have one of the letters C, P and F in their acronym. Each calorimeter tower consists of an electromagnetic shower counter followed by a hadron calorimeter. This allows for comparison of the electromagnetic and hadronic energies deposited in each tower, and therefore separation of electrons and photons from hadrons.

There are three subdetectors for the electromagnetic calorimeter: CEM, PEM and FEM. These correspond to the central, plug and forward regions of $|\eta|$, respectively. The CEM uses lead sheets interspersed with scintillator as the active detector medium. The PEM and FEM use proportional chambers. The hadron calorimeters in the central region are the central (CHA) and the endwall (WHA). The plug and forward regions are covered by the PHA and FHA calorimeters, respectively. The CHA and WHA are composed of alternating layers of iron and scintillator. The PHA and FHA subdetectors are made of alternating layers of iron and gas proportional chambers. The pseudorapidity coverage, resolutions and thickness for the different electromagnetic and hadron calorimeters are given in Table 3.3.

3.7 Muon Systems

Muons are particles which interact with matter only by ionization. For energies relevant to this experiment, they do not cause showers in the electromagnetic or hadronic calorimeters. As a result, if a muon is created in the collision and has enough momentum, it will pass through the calorimeter with minimal interaction with the material inside.

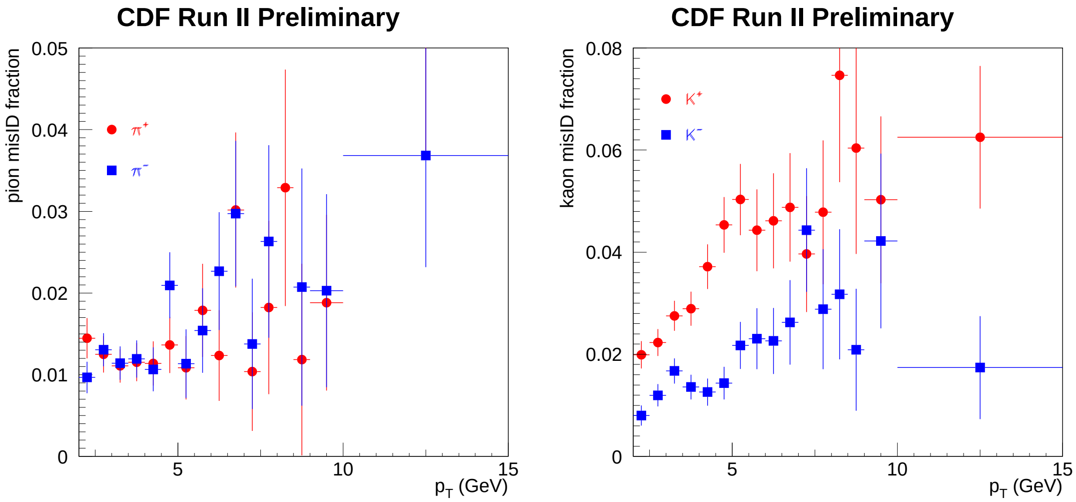

Figure 3.8: Rate of kaon and pion tracks faking muon signals in the CDF II Detector. Roughly 1% of all pions (left) and $2-4\%$ of all kaons (right) will fake a muon signal.

Therefore, the calorimeter can be considered as a filter which retains particles that shower when interacting with matter and muons, which do not. Muon detection systems are therefore placed radially outside the calorimeters.

The CDF II Detector has four muon systems: the Central Muon Detector (CMU), the Central Muon Upgrade Detector (CMP), the Central Muon Extension Detector (CMX), and the Intermediate Muon Detector (IMU) [23]. The CMU and CMP detectors are made of drift cells, and the CMX detector is made of drift cells and scintillation counters, which are used to reject background based on timing information. Using the timing information from the drift cells of the muon systems, short tracks (called "stubs") are reconstructed. Tracks reconstructed in the COT are extrapolated to the muon systems. Based on the projected track trajectory in the muon system, the estimated errors on the tracking parameters and the position of the muon stub, a χ^2 value of the track-stub match is computed. To ensure good quality of muons, an upper limit is placed on the value of χ^2_ϕ, the χ^2 of the track-stub match in the ϕ coordinate.

Most of the particles that pass through the calorimeter without showering are muons, but it is also possible for pions or kaons to survive the passage. These particles can then fake muon signals in the muon chambers. Typically, these fake rates are at the percent level, as seen in Fig. 3.8 for the CMU and CMP detectors combined. The Fig. 3.8 shows the rate at which charged pions and kaons fake muon signals in the muon systems. The difference between K^+ and K^- rates comes from the different cross section for interaction of these two mesons with the calorimeter material. The different interaction cross section for these two mesons comes from their quark content. In the K^+, the strange quark is the antiquark.

3.8 Trigger

Triggering systems are necessary because it is not physically possible to store information about every single $p\bar{p}$ collision. Collisions happen roughly at a rate of 2.5 MHz, and the readout of the full detector produces an event roughly the size of 250 kB. There is no medium available which is capable of recording data this quickly, nor would it be practical to analyze all this data later on. The trigger system is a pre-filter, which reduces data rates and volumes to manageable levels, according to all possible or foreseen physics prescriptions.

The CDF II triggering system is designed based on three conditions. The first condition is that the trigger has to be deadtimeless. This means that the trigger system has to be quick enough to make a decision for every single event, before the next event occurs. The second condition is imposed by the Tevatron upgrade for Run II, and it is the time between collisions, 396 ns. The last condition is that the data logging system can write about 30-50 events per second to tape, because of limited resources. In short, the trigger has to be fast enough to analyze every collision, and it has to figure out which 50 of 2.5 million events it should save in a given second. This is achieved by staging trigger decisions in three levels, as shown in Fig. 3.9.

Each level of the trigger is given a certain amount of time to reach a decision about accepting or rejecting an event. By increasing the time allowed for triggering at different levels of the trigger, the complexity of reconstruction tasks can be increased at every level. At the first level of the trigger, only very rough and quick pattern recognition and filtering algorithms are used. In order to do this in time, the Level 1 and Level 2 triggering mechanisms are implemented with custom electronics. The third level of the trigger is implemented with a PC farm with about 300 CPUs. Using each CPU as an event buffer allows for nearly one second to be allocated for the trigger decision. As a result, nearly offline quality of event reconstruction is available at the third level of triggering. The Level 3 rejection rate is about 10, resulting in 30 events/sec being accepted by the Level 3 trigger and written to tape.

The delay necessary to make a trigger decision is achieved by storing detector readout information in a storage pipeline. At Level 1, for every Tevatron clock cycle, the event is moved up one slot in the pipeline. By the time it reaches the end of the pipeline, the trigger will have reached a decision whether to accept or reject this event. If the event is accepted, its information will be sent to the higher level of the trigger. Otherwise, the event is simply ignored. Since the Level 1 buffer has 42 slots, the time allocated for making a trigger decision is about 5 μs. The rejection factor after Level 1 is about 150, so the Level 1 accept rate is below 40 kHz. At Level 2 there are 4 event buffers available. This allows for 20 μs for the trigger decision. The Level 2 rejection factor is again around 150, and the accept rate is around 300 Hz.

A set of requirements that an event has to fulfill at Level 1, Level 2 and Level 3 constitutes a trigger path. Requiring that an event be accepted through a well defined trigger path eliminates volunteer events. A volunteer event is an event which passed a higher level (L2, L3) trigger requirement but did not pass the preceding lower level (L1,

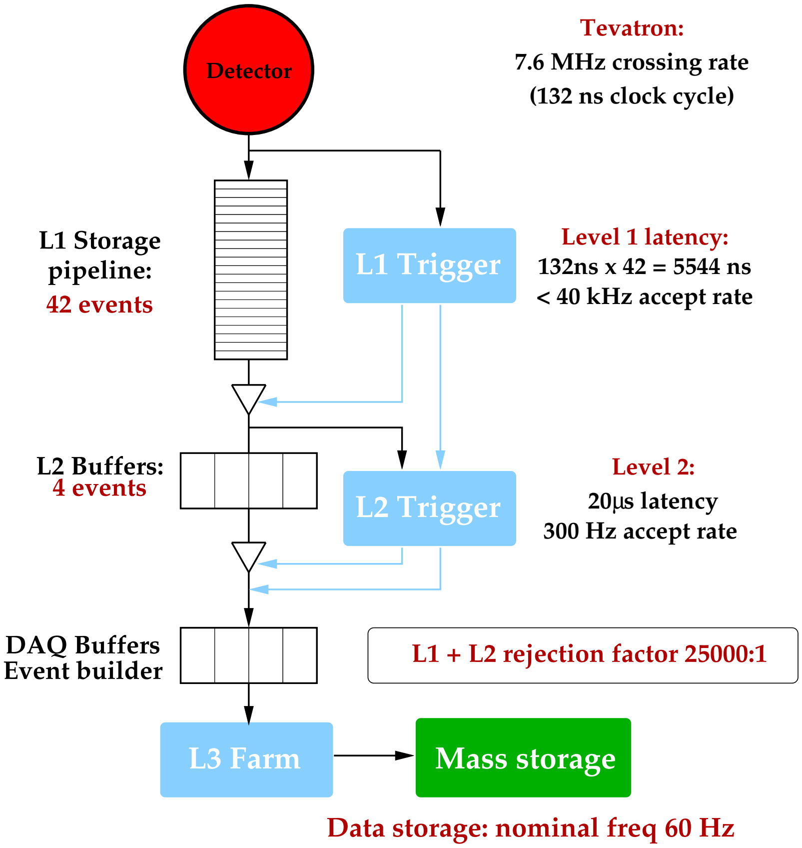

Figure 3.9: Diagram of the CDF II Detector trigger system.

L1/L2) trigger requirement. The CDF II trigger system implements about 100 trigger paths. An event will be accepted if it passes the requirements of any one of these paths.

3.8.1 Di-Muon Trigger

In this thesis two trigger paths have been used, and both will be described in detail. The first one is oriented to collect a sample rich in J/ψ mesons. It is defined by specific trigger requirements at Level 1 and Level 3. In this data sample, any event which passes the Level 1 J/ψ trigger is automatically accepted by Level 2. To be considered a J/ψ candidate at Level 1, there must be either two muon stubs in the CMU, or one muon stub in the CMU and one in the CMX. The muon stubs must be matched to an XFT (eXtremely Fast Tracker) track [24]. The XTRP [25] extrapolates the XFT tracks into the muon chambers. Taking into account multiple scattering and alignment corrections, a maximum $\delta\phi$ between the track and muon stub is determined. In the CMU, the XFT tracks are required to have $p_T > 1.5$ GeV/c. Stubs in the CMX must match an XFT track with $p_T > 2.0$ GeV/c.

At Level 3, muon pairs are required to have opposite charge. Muon matching requirements are again enforced. The requirement is $\Delta x(\text{track, stub}) < 30$ cm for CMU muons and $\Delta x(\text{track, stub}) < 50$ cm for CMX muons. The two muon tracks are required to have $\Delta z < 5$ cm at the point of closest approach to the origin. Finally, for an event to be part of the J/ψ dataset, it is required that $2.7 < M_{\mu\mu} < 4$ GeV/c^2, where $M_{\mu\mu}$ is the invariant mass of the di-muon pair.

3.8.2 Hadronic Trigger

The other trigger path used in this thesis is the “two-track” trigger path. It is optimized for finding charm and bottom hadrons that decay in hadronic final states. The strategy of the trigger path is as follows. At Level 1, fast measurements of track momenta are available. By cutting on track momenta and angles, most of the inelastic background will be rejected. At Level 2, the additional time available for reconstruction allows to use SVX-II information and obtain better impact parameter measurements of the tracks. Requiring non-zero impact parameters of tracks will imply that they come from decays of long-lived particles: charmed and bottom hadrons.

Hadronic Level 1 Trigger

The Level 1 trigger decision is based on the information from the eXtremely Fast Tracker. This device examines the hit information of the COT in wedges of 15°. It reports the measurement of the track p_T and ϕ_6, the angle of the transverse momentum at the sixth superlayer of the COT, which is located 106 cm radially from the beamline. Based on pre-loaded patterns of COT hits, it is capable of recognizing track segments for tracks with $p_T > 1.5$ GeV/c in 15° wedges of the COT. Two tracks are reported from a given 15° wedge, the two tracks which are closest to the left and right boundaries of

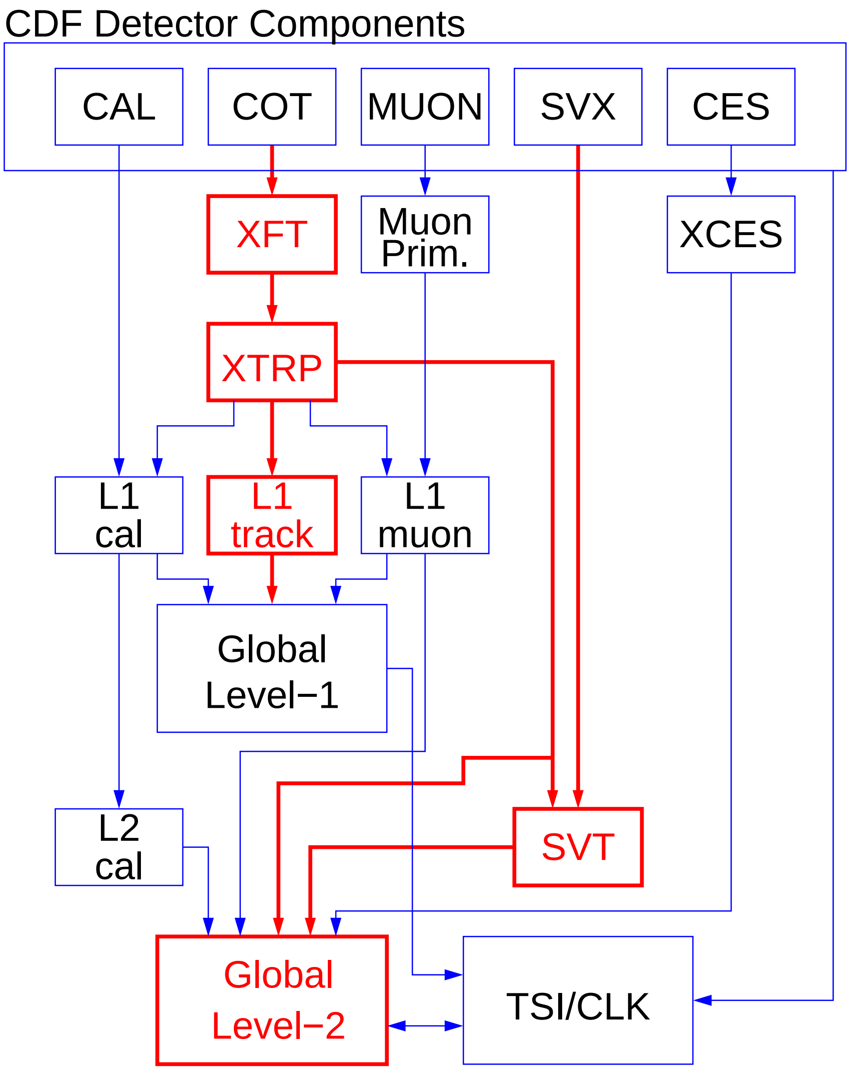

Figure 3.10: Diagram of the different trigger paths at Level 1 and Level 2. The data flow for the track trigger paths is outlined in red.

a given wedge. As mentioned in Sec. 3.4.3, based on the hit information from a single COT cell, assuming that the track comes from the beamline, a rough measurement of the track p_T and ϕ_6 is obtained. This is the information that the XFT device determines per track. An event is accepted at Level 1 if two tracks are found in the event such that they have opposite charge, both tracks have $p_T > 2$ GeV/c, the scalar sum of transverse momenta $p_{T1} + p_{T2} > 5.5$ GeV/c and the ϕ separation between the tracks at superlayer 6 is $|\Delta\phi_6| < 135°$.

Hadronic Level 2 Trigger

At Level 2 tracking information from the XFT is combined with SVX-II cluster information by the Silicon Vertex Tracker (SVT) [26]. The goal of the second level of the trigger is to obtain a precise measurement of the track d_0, and improved measurements of p_T and ϕ_0.

As mentioned in Sec. 3.4.1, the SVX-II is segmented into 12 wedges in ϕ and three mechanical barrels in z. The SVT makes use of this symmetry and does tracking separately for each wedge and barrel. Tracks which cross wedge and barrel boundaries are only reconstructed under certain circumstances. A SVT track starts with a two dimensional XFT "seed". The XFT measurement is extrapolated into the SVX-II forming a "road". Clusters of charge on the inner four $r-\phi$ layers of the given wedge have to be found inside this road. The silicon cluster information and the XFT segment information are fed into a linearized fitter which returns the measurements of p_T, ϕ_0 and d_0 for the track.

As shown in Fig. 3.11, the impact parameter resolution is about 35 μm for tracks with $p_T > 2$ GeV/c. The width of the Gaussian fit for the distribution of track impact parameters in Fig. 3.11 is 47 μm. This width is a combination of the intrinsic impact parameter resolution of the SVT measurement, and the transverse intensity profile of the interaction region. The region profile is roughly circular in the transverse plane and can be approximated by a Gaussian distribution with $\sigma \sim 35$ μm. The intrinsic SVT resolution is obtained by subtracting the beamline width from the width of the d_0 distribution in quadrature. The Level 1 trigger conditions are confirmed with the improved measurements of p_T and ϕ_0. An event passes Level 2 selection if there is a track pair reconstructed in the SVT such that the tracks have opposite charge, each track has $p_T > 2$ GeV/c and 120 μm $< |d_0| < 1$ mm. The vertex of the track pair has to have $L_{xy} > 200$ μm with respect to the beamline.

3.8.3 Level 3 Trigger

The third level of the trigger system is implemented as a PC farm. Every CPU in the farm provides a processing slot for one event. With roughly 300 CPUs, and an input rate of ~ 300 Hz, this allocates approximately 1 second to do event reconstruction and reach a trigger decision.

Fig. 3.12 shows the implementation of the Level 3 farm. The detector readout from the Level 2 buffers is received via an Asynchronous Transfer Mode (ATM) switch and

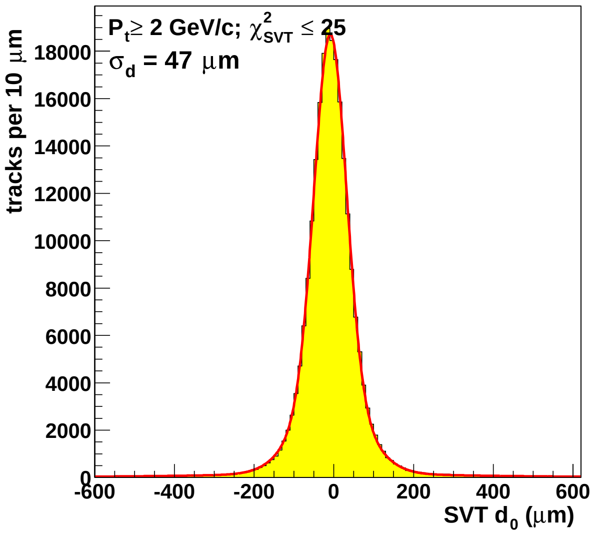

Figure 3.11: SVT impact parameter resolution.

distributed to 16 "converter" node PCs , shown in Fig. 3.12 in light blue. The main task of these nodes is to assemble all the pieces of the same event as they are delivered from different subdetector systems through the ATM switch. The event is then passed via an Ethernet connection to a "processor" node, which there are about 150 in the farm and are shown in Fig. 3.12. Each processor node is a separate dual-processor PC. Each of the two CPUs on the node process a single event at a time. The Level 3 decision is based on near-final quality reconstruction performed by a "filter" executable. If the executable decides to accept an event, it is then passed to the "output" nodes of the farm. These nodes send the event onward to the Consumer Server / Data Logger (CSL) system for storage first on disk, and later on tape.

For most of the data used in this thesis, full COT tracking has been used to reconstruct tracks. The measurements of p_T, z_0, ϕ_0 and $\cot\theta$ from the COT are combined with the d_0 measurement from the SVT to create a further improved track. The Level 1 and Level 2 trigger conditions (including the requirement on the two-track vertex L_{xy}) are repeated at Level 3 using improved track measurements. For later data full SVX-II tracking is available, and the trigger conditions are repeated using a combined COT/SVX-II fit of the track helices.

3.9 Luminosity Measurement

At hadron collider experiments the beam luminosity can be measured using the process of inelastic $p\bar{p}$ scattering. It has a large cross section, $\sigma_{in} \sim 60$ mb. The rate of inelastic $p\bar{p}$ interactions is given by:

$$\mu \cdot f_{bc} = \sigma_{in} \cdot L \,, \tag{3.5}$$

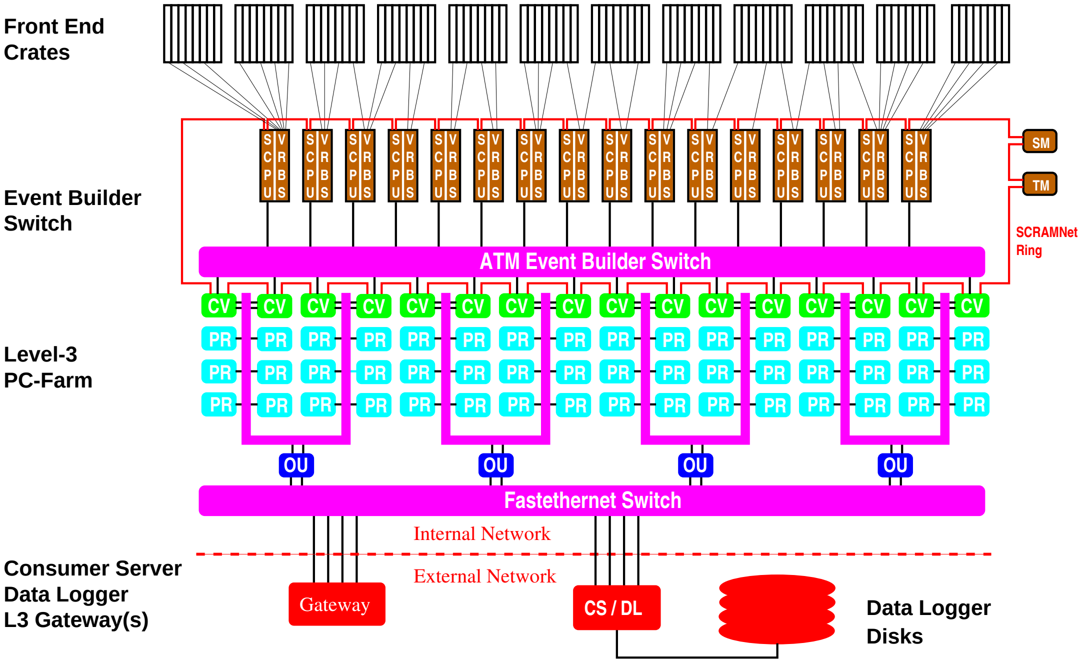

Figure 3.12: Principle of Event Building and Level 3 Filtering. Data from the front end crates is prepared by Scanner CPUs (SCPU) and fed into the ATM switch. On the other side of the switch, converter nodes (CV) assemble events and pass them to processor nodes (PR). Accepted events are passed to output nodes (OU) which send them to the Consumer Server and Data Logging systems (CS/DL).

where L is the instantaneous luminosity, f_{bc} is the rate of bunch crossings in the Tevatron and μ is the average number of $p\bar{p}$ interactions per bunch crossing.

To detect inelastic $p\bar{p}$ events efficiently a dedicated detector at small angles, operating at high rate and occupancy, is required. The Cherenkov Luminosity Counters (CLC) are being used by CDF to measure the Tevatron luminosity. The CLC is designed to measure μ accurately (within a few percent) all the way up to the high luminosity regime $L \sim 2 \times 10^{32}$ cm^{-2}s^{-1}. The CLC modules and the luminosity measurement method are described in detail in [27].

There are two CLC modules in the CDF detector, installed at small angles in the proton (East) and antiproton (West) directions with pseudorapidity coverage between 3.75 and 4.75. Each module consists of 48 thin, long, gas-filled, Cherenkov counters. The counters are arranged around the beam pipe in three concentric layers, with 16 counters each, and pointing to the center of the interaction region. The cones in the two outer layers are about 180 cm long and the inner layer counters (closer to the beam pipe) have a length of 110 cm. The Cherenkov light is detected with fast, 2.5 cm diameter, photomultiplier tubes. The tubes have a concave-convex, 1 mm thick, quartz window for efficient collection of the ultraviolet part of Cherenkov spectra and operate at a gain of 2×10^5.

The counters are mounted inside a thin pressure vessel made of aluminum and filled with isobutane. The Cherenkov angle is 3.1° and the momentum threshold for light emission is 9.3 MeV/c for electrons and 2.6 GeV/c for pions.

The number of $p\bar{p}$ interactions in a bunch crossing follows Poisson statistics with mean μ, where the probability of empty crossings is given by $P_0(\mu) = e^{-\mu}$. An empty crossing is observed when there are fewer than two tubes with signals above threshold in either module of the CLC. The measured fraction of empty bunch crossings is corrected for the CLC acceptance and the value of μ is calculated. The measured value of μ is combined with the inelastic $p\bar{p}$ cross section to determine the instantaneous luminosity using (3.5).

The CLC is one of the upgrades of the CDF II Detector. It provides an improved measurement of the luminosity with respect to the Run I device. The luminosity measured by the CLC is used to monitor the Tevatron's performance.

Chapter 4

Sample Selection

The data sample used in this thesis has been taken by the CDF detector between March 2002 and August 2004, and it corresponds to an integrated luminosity of about 450 pb^{-1}. We apply the B Physics Group at CDF Good Runs Selection (appendix A) on such data sample, defining an effective luminosity of $\sim$ 355 pb^{-1}. Two charged and two neutral B meson fully reconstructed decays have been analyzed,

- $B^+ \to J/\psi K^+$, $J/\psi \to \mu^+\mu^-$;
- $B^+ \to \bar{D}^0\pi^+$, $\bar{D}^0 \to K^+\pi^-$;
- $B^0_d \to J/\psi K^{*0}$, $J/\psi \to \mu^+\mu^-$, $K^{*0} \to K^+\pi^-$;
- $B^0_d \to D^-\pi^+$, $D^- \to K^+\pi^-\pi^-$.

Throughout this thesis, references to a specific charge state imply the charge-conjugate state as well. Such decays come from the *di-muon* and the *two-track* trigger paths, described in 3.8 and reviewed here. Illustrations of the four decay topologies can be seen in Figs. 4.1 and 4.2. Besides the requirements that an event has to pass to be accepted by any of those trigger paths, further selection cuts are mandatory for enriching the signal content of our sample.

4.1 Trigger Paths

The trigger paths that have been used in this analysis are the di-muon trigger and the two-track trigger. Both are triggers based on the requirement of some conditions on tracks. Those tracks that fulfill the trigger requirements are called *trigger tracks*.

4.1.1 Di-Muon Trigger

This is the trigger path used for selecting decay channels with J/ψ mesons in the final state. Muons are particles with clean identification, and the requirement of two opposite

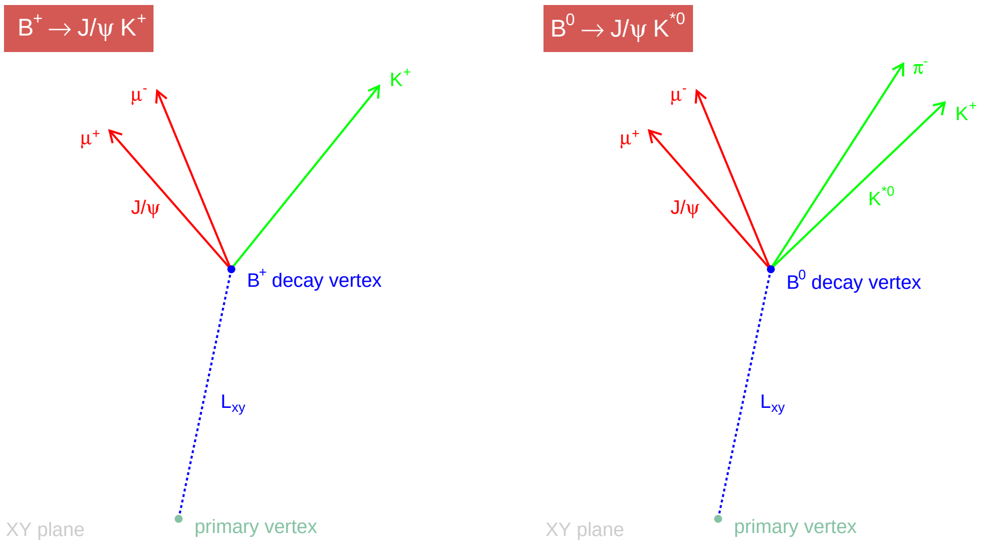

Figure 4.1: Topologies of closed-charm mediated decays, projected on the CDF transverse plane. Left is $B^+ \to J/\psi K^+$ and right is $B^0_d \to J/\psi K^{*0}$.

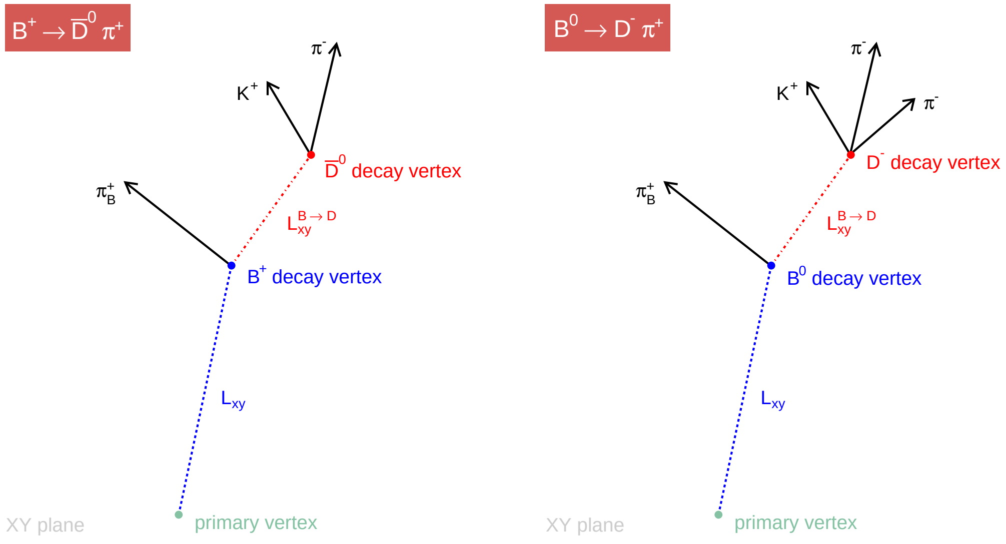

Figure 4.2: Topologies of open-charm mediated decays, projected on the CDF transverse plane. Left is $B^+ \to \bar{D}^0\pi^+$ and right is $B^0_d \to D^-\pi^+$.

charge muons with an invariant mass close to the J/ψ mass already provides a visible J/ψ resonance or peak. The di-muon trigger is a combination of the CMU-CMU and the CMU-CMX triggers, where CMU-CMU/CMX indicates that one muon is from the CMU and the other one is from the CMU/CMX muons sytems:

1. Level 1
    - two XFT tracks with opposite charge;
    - each track is matched with two muon stubs;
    - each CMU (CMX) muon has $p_T^{XFT} > 1.5\,(2.2)$ GeV/c;
    - $\Delta\phi_6(\mathrm{CMU}, \mathrm{CMU}) < 135°$;
    - no cut in $\Delta\phi_6(\mathrm{CMU}, \mathrm{CMX})$.
2. Level 2
    - no requirements.
3. Level 3
    - confirmation of Level 1 cuts on the fully reconstructed tracks;
    - $2.7 < M_{\mu\mu} < 4$ GeV/c^2,

where $M_{\mu\mu}$ is the di-muon pair invariant mass. In addition, we require at least 3 $r-\phi$ hits in the silicon detector for both muons.

4.1.2 Two-Track Trigger

For the first time in a hadron detector, a novel Silicon Vertex Trigger (SVT) is being used at CDF. This new Level 2 trigger processor allows to select the long-lived heavy flavor particles by cutting on the track impact parameter with a precision similar to that achieved by the full event offline reconstruction:

1. Level 1
    - two XFT tracks with opposite charge;
    - each track has at least 4 XFT layers with hits;
    - each track has $p_T^{XFT} > 2.04$ GeV/c;
    - $\sum p_T^{XFT} > 5.5$ GeV/c;
    - $0° < \Delta\phi_6 < 135°$.
2. Level 2
    - each track is required to be matched by the SVT;

  - for each track 100 μm $\leq |d_0^{SVT}| \leq 1$ mm;
  - each track has $p_T^{SVT} > 2$ GeV/c;
  - $\sum p_T^{SVT} > 5.5$ GeV/c;
  - $2° < \Delta\phi_0 < 90°$.

3. Level 3
  - $|\Delta z_0| < 5$ cm;
  - two-track vertex $L_{xy} > 200$ μm,

where p_T^{XFT} is the transverse momentum as measured in the XFT and $\Delta\phi_6$ is the opening angle at superlayer 6 of the COT, d_0^{SVT} is the impact parameter as measured in the SVT, Δz_0 is the distance between the two tracks along the beam axis and L_{xy} is the distance in the transverse plane of the two-track vertex with respect to the primary vertex.

Trigger Efficiencies

Detector and reconstruction efficiencies for finding different B mesons are not exactly the same. To better understand the *total* efficiency ϵ_{tot} for finding a given B decay, we break it up into two factors, the *trigger* efficiency ϵ_{trig} and the *reconstruction* efficiency ϵ_{reco}, $\epsilon_{tot} = \epsilon_{trig}\,\epsilon_{reco}$. The trigger efficiency is the efficiency with which the trigger path accepts a given B meson decay. Using Monte Carlo simulation, it is calculated as:

$$\epsilon_{trig} = \frac{N_{trig}}{N_{gen}}\,, \tag{4.1}$$

where N_{gen} is the number of generated events and N_{trig} is the number of events that pass the trigger selection. The number of generated events N_{gen} depends on the parameters (minimum p_T, maximum $|\eta|$) of the generation. Our choice of these parameters ($p_T > 0$ GeV/c, $|\eta| < 6$) is loose enough for the entire B meson production cross section to be included in the denominator. The reconstruction efficiency is the efficiency of our analysis selection on the B meson decays that have passed the trigger requirements, and it is calculated as well using Monte Carlo simulation:

$$\epsilon_{reco} = \frac{N_{reco}}{N_{trig}}\,, \tag{4.2}$$

where N_{reco} is the number of events in which the B meson decay has been reconstructed by the analysis. Luminosity averaged efficiencies taken from [35] are listed in Table 4.1.

4.2 Offline Candidates Selection

For the candidates reconstruction we do not use any particle identification information, relying only on tracking information. Candidates for each particle decay tree are

ϵ	$B^+ \to \bar{D}^0\pi^+$	$B_d^0 \to D^-\pi^+$
ϵ_{trig} (%)	0.3083 ± 0.0018	0.2895 ± 0.0017
ϵ_{reco}	0.3917 ± 0.0028	0.2960 ± 0.0027
ϵ_{tot} (%)	0.1209 ± 0.0011	0.0858 ± 0.0009

Table 4.1: Luminosity averaged efficiencies from Monte Carlo [35].

constructed from the bottom up. This means for example in the case of $B^+ \to \bar{D}^0\pi^+$, $\bar{D}^0 \to K^+\pi^-$, we start with a $\bar{D}^0 \to K^+\pi^-$ decay, which is in the next step used to make candidates for a $B^+ \to \bar{D}^0\pi^+$ decay. To make up higher level candidates like B, J/ψ, K^{*0} or D, tracks are fitted to a secondary vertex applying mass and pointing constraints and are forced to comply with the proper vertex topology. From this secondary vertex fit, mass, transverse decay-length L_{xy} and impact parameter d_0 of the higher level candidates are extracted. Fig. 4.2 depicts the topologies of $B^+ \to \bar{D}^0\pi^+$ and $B_d^0 \to D^-\pi^+$ decays. The B meson has a finite lifetime, so its vertex is displaced from the primary vertex. Furthermore, the D meson has a finite lifetime as well, and its decay vertex is displaced from the B decay vertex. The resulting topology has a two-prong ($\bar{D}^0 \to K^+\pi^-$) or three-prong ($D^- \to K^+\pi^-\pi^-$) vertex and a single displaced track, the B meson daughter pion, π_B. The following quantities are available to select such decays: the $\chi^2_{r-\phi}$ of both D and B meson vertex fits, the transverse momenta p_T of both D and B mesons, the significance of the transverse decay-length $L_{xy}/\sigma_{L_{xy}}$ of the D and the B mesons with respect to the primary interaction vertex, the displacement in the transverse plane $L_{xy}^{B\to D}$ of the D meson vertex with respect to the B meson vertex, the transverse momentum of the B meson daughter pion $p_T(\pi_B)$, the $\Delta R(D,\pi_B) \equiv \sqrt{\Delta\phi(D,\pi_B)^2 + \Delta\eta(D,\pi_B)^2}$ between the D meson and the B daughter pion, and the B meson impact parameter with respect to the primary vertex, $d_0(B)$.

4.2.1 Signal and Background Description

To estimate the sample composition we perform binned likelihood fits on the reconstructed invariant mass distribution of the B meson candidates. Signal decays are expected to distribute with a Gaussian function centered at the nominal B meson mass with a width that depends on the detector characteristics. At CDF mass resolutions of B mesons are $\sigma_m = 10 - 20$ MeV/c^2. The B^+ and B_d^0 nominal masses are $\mathrm{M_{B^+}} = 5279.0 \pm 0.5$ MeV/c^2 and $\mathrm{M_{B_d^0}} = 5279.4 \pm 0.7$ MeV/c^2 (PDG world average). Usually the signal region is defined as the mass window that lies in $\pm 3\sigma_m$ within the nominal B meson mass. The problem arises when beneath the signal peak also background candidates are found:

1. The main background source at CDF comes from B meson candidates formed with at least one track that is not a real B meson daughter track, but due to its kinematic properties it faked a B meson daughter track. This background spans along a wide region and therefore it has candidates in the signal region.

2. In smaller amount there are background sources coming from partially reconstructed b-hadrons. The decay chains of these b-hadrons can have neutral particles that are not reconstructed by the tracking system, but the invariant mass of the remaining b-hadron daughter tracks happens to be close enough to our signal region. The same effect can happen when a charged daughter of such b-hadrons has been missed by the tracking system. These partially reconstructed backgrounds lie on the left of the signal mass region, because at least one daughter track has not been used in the invariant mass reconstruction of the B meson candidate.

3. The last background source corresponds to misreconstructed B meson decays where a particle has been wrongly identified, i.e., a kaon has been identified as a pion. Due to the relative small mass difference among the possible b-hadron daughter tracks (pions, kaons and protons) when compared with the momentum of such particles, this background source tends to be in the signal region.

Along this thesis we will refer to the first background as combinatorial background, and the last two sources will be called physics backgrounds because they are real b-hadrons.

$J/\psi K$ Modes Mass Description

The reconstructed invariant mass distributions of $B^+ \to J/\psi K^+$ and $B_d^0 \to J/\psi K^{*0}$ candidates are fit in the mass range [5.17 – 5.39 GeV/c^2] with the binned likelihood method. The signal component is described by a Gaussian function, and the combinatorial background is parameterized with a linear function. The mass range has been chosen that short to avoid partially reconstructed decays, as can be inferred from Fig. 4.3 [34]. For the making of Fig. 4.3, every closed-charm mediated b-hadron has been generated in Monte Carlo, with $J/\psi \to \mu^+\mu^-$. In Table 4.2 the majority of the decays that survive our selection cuts are summarized.

Two physics backgrounds enter the narrow mass region in a non-negligible amount. In the $B_d^0 \to J/\psi K^{*0}$, $K^{*0} \to K^+\pi^-$ decay, the self-reflection background lies exactly beneath the signal peak. This self-reflection happens when the K^+ and the π^- daughters of the K^{*0} particle have the mass assignments swapped, and still their reconstructed invariant mass is in a 50 MeV/c^2 mass window with respect to the K^{*0} nominal mass, $M_{K^{*0}} = 896.10 \pm 0.27$ MeV/c^2 (this mass window is part of the $B_d^0 \to J/\psi K^{*0}$ selection cuts). From the same Monte Carlo study it has been found that 12% of the signal fraction corresponds to this self-reflection, with a Gaussian shape that shares the mean value with the signal but it has a larger width, 25 MeV/c^2. In the $B^+ \to J/\psi K^+$ decay, the Cabibbo-suppressed $B^+ \to J/\psi \pi^+$ mode accounts for 2.5% of the signal fraction. This background happens when the π^+ is assigned a kaon mass, and its mass template is determined with the same Monte Carlo as before, described in (5.15).

$D\pi$ Modes Mass Description

The mass spectrum of the $B \to D\pi$ decays has a complicated shape since it contains contributions from signal, combinatorial background and partially or misreconstructed

decays reconstructed as $B^+ \to J/\psi K^+$	
$B^+ \to J/\psi\pi^+$	π^+ assigned M_K
$B_d^0 \to J/\psi K^+\pi^-$	π^- missed
$B_d^0 \to J/\psi K_s^0$, $K_s^0 \to \pi^+\pi^-$	π^- missed and π^+ assigned M_K
$\Lambda_b^0 \to J/\psi\Lambda^0$, $\Lambda^0 \to p^+\pi^-$	π^- missed and p^+ assigned M_K
decays reconstructed as $B_d^0 \to J/\psi K^{*0}$, $K^{*0} \to K^+\pi^-$	
$B_d^0 \to J/\psi K^{*0}$, $K^{*0} \to K^+\pi^-$	$K^+(\pi^-)$ assigned $M_{\pi(K)}$
$B^+ \to J/\psi K^{*+}$, $K^{*+} \to K^+\pi^-\pi^+$	π^+ missed
$B_s^0 \to J/\psi\phi$, $\phi \to K^+K^-$	K^- assigned M_π
$B^+ \to J/\psi K^+\pi^-\pi^+$	π^+ missed and potential $K\pi$ swap
$B_d^0 \to J/\psi K^+\pi^-$	non-resonant and potential $K\pi$ swap

Table 4.2: Physics background decays reconstructed as $B^+ \to J/\psi K^+$ and $B_d^0 \to J/\psi K^{*0}$, $K^{*0} \to K^+\pi^-$ signals. The kaon mass is referred to as $M_K = 493.677 \pm 0.016$ MeV/c^2, and the pion mass is $M_\pi = 139.57018 \pm 0.00035$ MeV/c^2 (PDG world average).

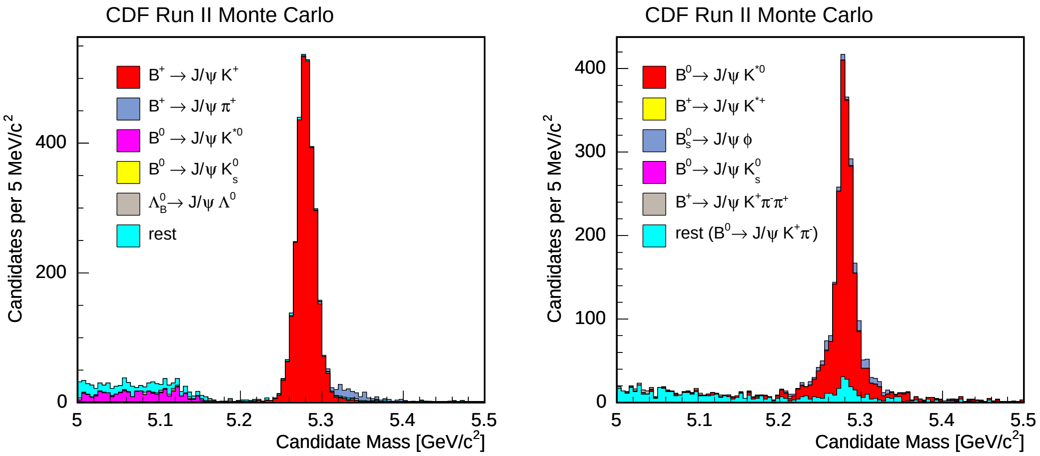

Figure 4.3: b-hadron $\to J/\psi X$, $J/\psi \to \mu^+\mu^-$ mass distributions from Monte Carlo. Modes reconstructed as $B^+ \to J/\psi K^+$ (left) and $B_d^0 \to J/\psi K^{*0}$, $K^{*0} \to K^+\pi^-$ (right) are shown.

b-hadron decays. For the signal yields extraction, the reconstructed invariant mass distributions of the B meson candidates have been fitted with the binned likelihood method. The fitting model for $B_d^0 \to D^-\pi^+$ and $B^+ \to \bar{D}^0\pi^+$ closely follows that used in [35]:

- a single/double (B^+/B_d^0) Gaussian for the signal decay mode;
- a single Gaussian for the corresponding Cabibbo-suppressed decay $B \to DK$;
- a template for the partially and misreconstructed $B \to DX$ decays;
- an exponential for the combinatorial background,

where a double Gaussian is needed to parameterize the signal in the $B_d^0 \to D^-\pi^+$ mode because with a single Gaussian the shape of the signal peak is not well described. The Cabibbo-suppressed $B \to DK$ decays reconstructed as $B \to D\pi$ produce a small contamination under the signal peak. For this contribution we use a Gaussian with its central position and width taken from simulation. The normalization is fixed, relative to that of the signal peak, based on the PDG [19] values of branching fractions for these modes. The functional form of the physics backgrounds coming from the partially and incorrectly reconstructed $B \to DX$ decays derives from simulation and it is taken from [35]. Mass spectra have been generated for $B \to \bar{D}^0 X$, $\bar{D}^0 \to K^+\pi^-$ and $B \to D^- Y$, $D^- \to K^+\pi^-\pi^-$ decays, and are shown in Fig. 4.4.

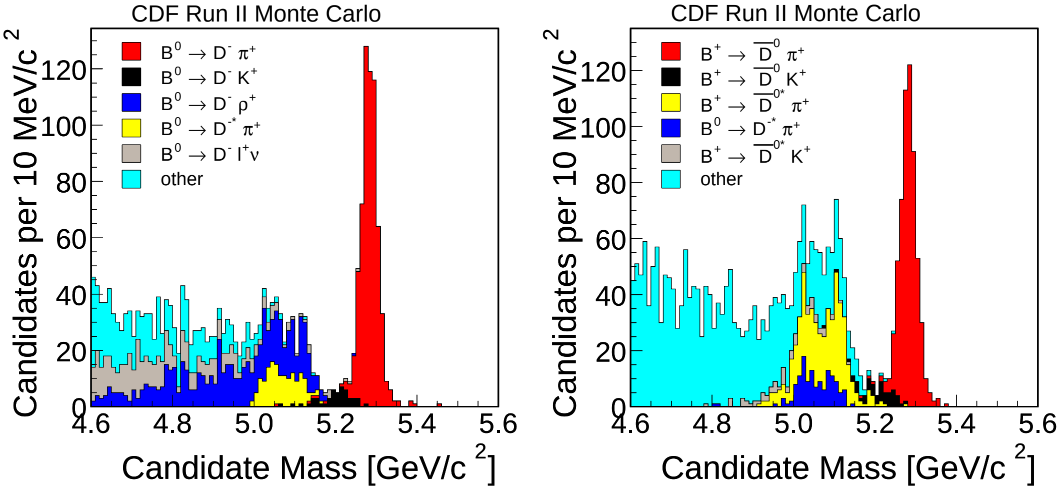

Figure 4.4: $B \to DX$ mass distributions from Monte Carlo. Modes reconstructed as $B_d^0 \to D^-\pi^+$, $D^- \to K^+\pi^-\pi^-$ (left) and $B^+ \to \bar{D}^0\pi^+$, $\bar{D}^0 \to K^+\pi^-$ (right) are shown.

The double horn structure on the mass distribution for both B^+ and B_d^0 comes from the highly polarized nature of $B^+ \to D^{*0}\pi^+$ and $B_d^0 \to D^{*-}\pi^+$ decays. In these modes, the angle between the D direction in the D^* frame and the D^* direction follows $p(\theta) \approx cos^2\theta$. Which is to say, most of the time the D is either in the same direction or exactly opposite to the D^* boost direction. So, the high mass reflection occurs when the D gets all the Q and the low mass reflection is due to those decays where the π gets all the Q.

4.2.2 Offline Tracks Preparation

Because our analysis is track based, we take special care to ensure that the tracks used for reconstructing candidates are of best available quality. We therefore apply track quality requirements on the trigger tracks and do additional preparation of all the tracks of the event, so that the track parameters and their error estimates are more realistic.

Due to misalignments in the tracking systems and hits caused by noise in the tracking systems, fake and mismeasured tracks appear in the events. A very simple way to reduce the number of these tracks is to require a minimum number of hits in the drift chamber and silicon detector. We select trigger tracks which have at least three SVX-II $r-\phi$ hits. Standalone silicon tracks which have been successfully extended by the inside-out tracking by adding COT hits are as well included into the sample. We also require the track to have an error matrix which can be inverted and a helix fit attached to it.

The following detailed procedure is applied to the tracks: all tracks are refitted dropping silicon hits from the Intermediate Silicon Layer. This silicon component has not yet been sufficiently well studied to base an analysis on. The refitting procedure is performed using the TrackRefitter [28] interface and is done separately for pion, kaon and muon hypotheses. Monte Carlo studies, as well as studies in data, have demonstrated that the error matrix of the COT fit of tracks underestimates the measurement errors. In order to correct for this problem the TrackRefitter interface performs a scaling of the COT covariance matrix with the following scale factors (with p_T in GeV/c):

$$\begin{aligned}
s(\lambda) &= \sqrt{1+p_\lambda(1+\lambda^2)^{1.5}/p_T^2} && \text{with } p_\lambda = 0.580;\\
s(c) &= \sqrt{1+p_c/p_T^2} && \text{with } p_c = 5.33;\\
s(z_0) &= \sqrt{1+p_{z_0}(1+\lambda^2)^{1.5}/p_T^2} && \text{with } p_{z_0} = 0.653;\\
s(d_0) &= \sqrt{1+p_{d_0}/p_T^2} && \text{with } p_{d_0} = 3.01;\\
s(\phi_0) &= \sqrt{1+p_{\phi_0}/p_T^2} && \text{with } p_{\phi_0} = 3.7,
\end{aligned}$$

where $\lambda = \cot\theta$, with θ the polar angle of the track. The signed *curvature* of the track is referred to as c, with magnitude equal to 1/*diameter* of the track. The position of closest approach to the Z-axis of the CDF global coordinate system is z_0. With d_0 we refer to the signed distance of closest approach to the Z-axis. It is given a sign opposite to that of L_z, the z component of the track's angular momentum about the origin. Finally, ϕ_0 is the direction of the track at point of closest approach to the Z-axis.

The factors are applied to the covariance matrix as $c_{ij}^{\text{new}} = s_i s_j c_{ij}^{\text{old}}$, where the indices i and j represent the various parameters. Finally an alignment table is used to properly position the already identified silicon hits. The relocation of silicon hits is necessary since in the early data older versions of the alignment have been used. The model for the material description is based on [29].

4.2.3 Selection Optimization

Optimization Criterion

The goal of any optimization procedure is maximizing or minimizing a certain variable, depending on the analysis being performed. We aim for the measurement of the B_s^0 meson oscillation frequency Δm_s. More precisely, with current yields, flavor taggers and proper decay-length resolution, CDF is still unable to measure Δm_s and therefore our goal is the improvement of the world average lower limit on Δm_s. The potential for observing the time dependence of an oscillation asymmetry is inferred from the estimation of the corresponding sensitivity, in other words, the largest value of the oscillation frequency for which the measurement has a certain significance level. Expressions for the expected significance of an oscillating signal have been derived in [49], and here we reproduce their significance $\mathcal{S}$ estimate,

$$\mathcal{S}(\Delta m_s) = \frac{S}{\sqrt{S+B}}\sqrt{\frac{\epsilon\mathcal{D}^2}{2}}e^{-\frac{1}{2}\sigma_{ct}^2\Delta m_s^2}\,, \tag{4.3}$$

where S is the number of signal candidates, B is the number of background candidates, ϵ and $\mathcal{D}$ are the flavor tagging efficiency and dilution, and σ_{ct} is the proper decay-length resolution. A logical optimization procedure would maximize $\mathcal{S}$. Although such thing is technically duable, for the time being we have maximized the three factors on which $\mathcal{S}$ depends individually: large and pure signal yields ($S/\sqrt{S+B}$), flavor tagging ($\sqrt{\epsilon\mathcal{D}^2/2}$) and good proper decay-length resolution ($e^{-\frac{1}{2}\sigma_{ct}^2\Delta m_s^2}$). The optimization procedure described here maximizes $S/\sqrt{S+B}$.

To estimate the amount of background candidates in the signal region, only the combinatorial background is used among the different background sources. In the $B \to D\pi$ decays we fit the mass distribution from 5.2 to 6.0 GeV/c^2 with an exponential, dropping from the fit a $\pm 3\sigma_m$ signal window, where Monte Carlo has been used to estimate the signal width and mean. An illustration of the fitting region can be seen in Fig. 4.5. The number of signal events is determined from the same Monte Carlo, which is rescaled to the number of events seen in the mass peak in the data before cut optimization. A description on how the selection optimization has been done in the $B \to J/\psi K$ decays can be found in [34].

Optimization Procedure

In any selection, a variable on which a cut is applied should have non-trivial separation power between signal S and background B. Therefore, the first step to be followed is a comparison between combinatorial background events from data and signal events from Monte Carlo. A cut should not only provide separation power between signal and background events, but also be as uncorrelated as possible with other cuts. Once the most powerful variables are found, the final values of the cuts are chosen through an optimization procedure, described below:

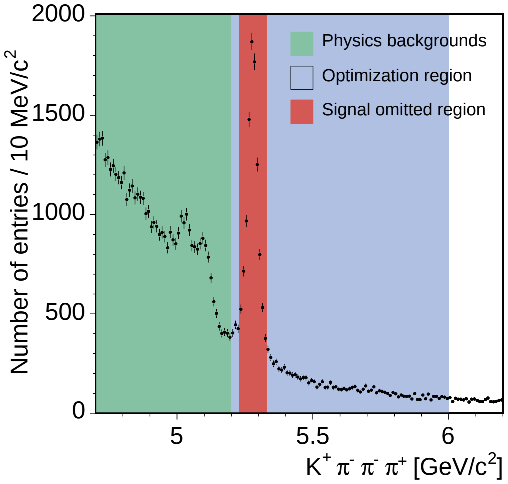

Figure 4.5: Fit region used for optimization procedure. Left sideband is avoided due to the presence of physics backgrounds, and signal region is omitted.

1. Get default cuts and variation windows.
2. Get the expected signal with default cuts.
3. Fit MC signal with default cuts.
4. Scale MC to signal provided by the user.
    (a) Change one cut while fixing the others at default values.
    (b) Fit scaled MC signal, get the width.
    (c) Choose blind region as $\pm 3\sigma_m$ of MC signal width.
    (d) Fit data for background, omitting the blind region.
    (e) Integrate background under $\pm 2.5\sigma_m$ signal region.
    (f) Integrate scaled MC signal in the same $\pm 2.5\sigma_m$ region.
    (g) Save the significance $\frac{S_{\mathrm{MC}}}{\sqrt{S_{\mathrm{MC}}+B_{\mathrm{Data}}}}$.
    (h) Go to the next cut value.
5. Change if needed default cuts and variation window, then go to 1.

When a set of points with similar significance is found, the point with the highest efficiency is chosen. In Fig. 4.6 an illustration of the trends on efficiency and significance for a given variable can be seen.

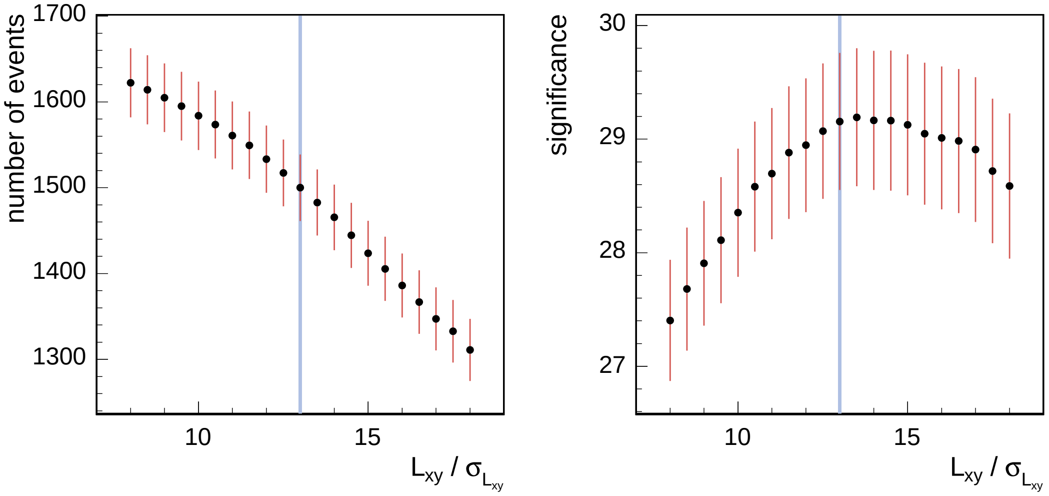

Figure 4.6: Cut optimization efficiency (left) and significance (right) trends for $L_{xy}/\sigma_{L_{xy}}$.

4.2.4 Final Selection and Event Yields

The reconstruction of the $B^+ \rightarrow J/\psi K^+$ and $B_d^0 \rightarrow J/\psi K^{*0}$ decay samples take cut values from [34]. The optimal selection cuts are summarized in Table 4.3, and the mass fits of all reconstructed events can be seen in Fig. 4.7. Table 4.4 lists the optimal selection criteria used for the reconstruction of the two-track trigger decay modes, $B^+ \rightarrow \bar{D}^0\pi^+$ and $B_d^0 \rightarrow D^-\pi^+$. The mass models are found to fit the data reasonably well, as shown in Fig. 4.8. The signal yields of each of the four modes are collected in Table 4.5.

$B^+ \rightarrow J/\psi K^+$	$B_d^0 \rightarrow J/\psi K^{*0}$
$p_T(\mu^\pm) > 1.5$ GeV/c	$p_T(\mu^\pm) > 1.5$ GeV/c
$N(\mu^\pm)_{COT\ axial\ hits} \geq 15$	$N(\mu^\pm)_{COT\ axial\ hits} \geq 15$
$\|m_{J/\psi} - 3096.88\| < 80$ MeV/c^2	$\|m_{J/\psi} - 3096.88\| < 80$ MeV/c^2
Prob$(\chi^2) > 10^{-3}$	Prob$(\chi^2) > 10^{-4}$
$p_T(B) > 5.5$ GeV/c	$p_T(B) > 6.0$ GeV/c
$p_T(K^+) > 1.6$ GeV/c	$p_T(K^{*0}) > 2.6$ GeV/c
–	$\|m_{K^{*0}} - 896\| < 50$ MeV/c^2

Table 4.3: $J/\psi K$ decays final selection cuts.

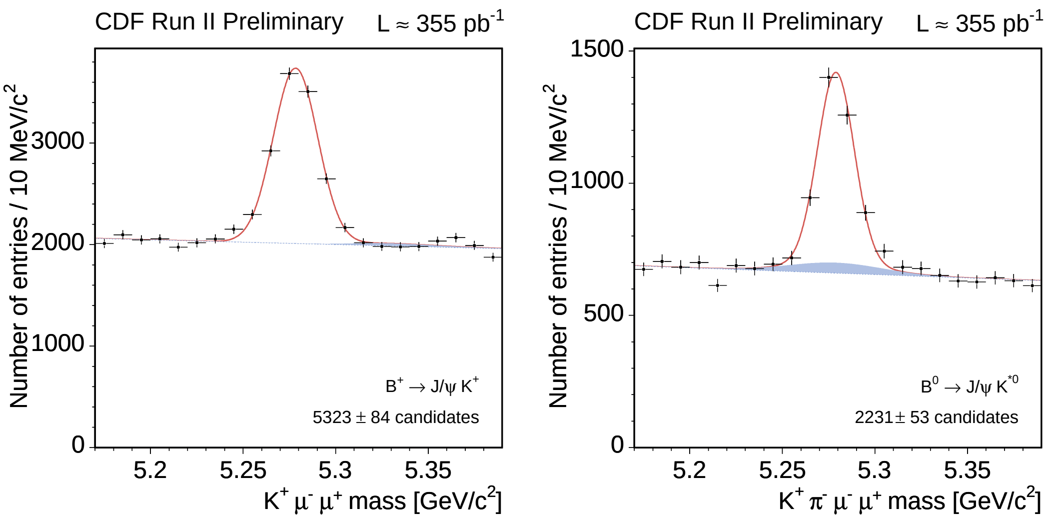

Figure 4.7: Mass distributions of the $B^+ \rightarrow J/\psi K^+$, $J/\psi \rightarrow \mu^+\mu^-$ (left) and $B_d^0 \rightarrow J/\psi K^{*0}$, $J/\psi \rightarrow \mu^+\mu^-$, $K^{*0} \rightarrow K^+\pi^-$ (right) candidates. The shaded areas represent misreconstructed backgrounds: $B^+ \rightarrow J/\psi\pi^+$ (left) and $B_d^0 \rightarrow J/\psi K^{*0}$, $K^{*0} \rightarrow K^+\pi^-$ where the mass asignments of the K^+ and the π^- have been swapped (right). The dotted blue line represents the combinatorial background.

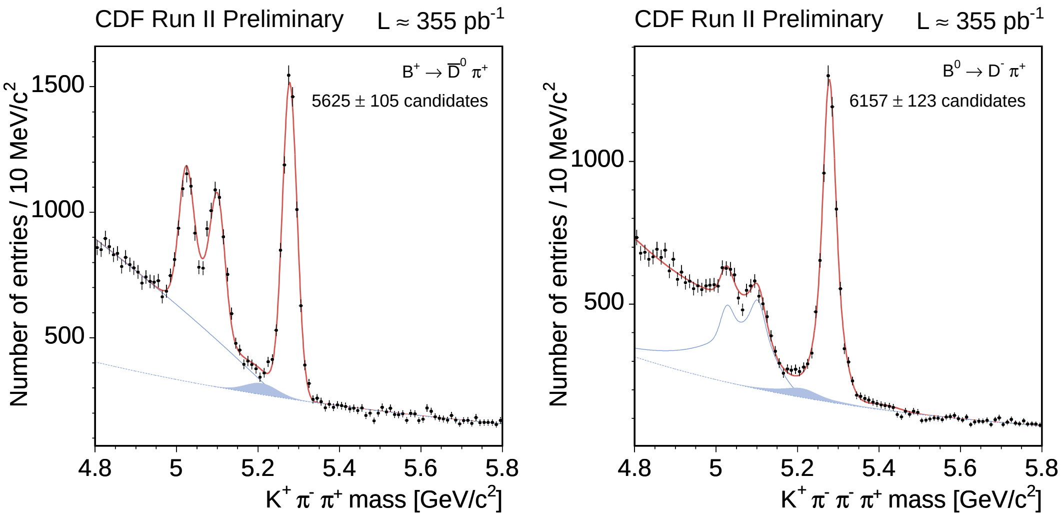

Figure 4.8: Mass distributions of the $B^+ \rightarrow \bar{D}^0\pi^+$, $\bar{D}^0 \rightarrow K^+\pi^-$ (left) and $B_d^0 \rightarrow D^-\pi^+$, $D^- \rightarrow K^+\pi^-\pi^-$ (right) candidates. The shaded areas represent the Cabibbo-suppressed $B \rightarrow DK$ decays, that lie on the fit of the combinatorial background (dotted blue line). The fit of $B \rightarrow DX$ decays (solid blue line) is shown in the B^+ case (left), and the fit of $B \rightarrow D^*\pi$ decays (solid blue line) is shown in the B_d^0 case (right).

$B^+ \to \bar{D}^0\pi^+$	$B_d^0 \to D^-\pi^+$
$\chi^2_{r-\phi}(D) < 15$	$\chi^2_{r-\phi}(D) < 15$
$\chi^2_{r-\phi}(B) < 15$	$\chi^2_{r-\phi}(B) < 15$
$L_{xy}^{B\to D} > -150\ \mu$m	$L_{xy}^{B\to D} > -300\ \mu$m
$L_{xy}/\sigma_{L_{xy}}(B) > 8$	$L_{xy}/\sigma_{L_{xy}}(B) > 11$
$\Delta R(D, \pi_B) < 2.0$	$\Delta R(D, \pi_B) < 1.5$
$p_T(\pi_B) > 1.0$ GeV/c	$p_T(\pi_B) > 1.2$ GeV/c
$\lvert d_0(B)\rvert < 80\ \mu$m	$\lvert d_0(B)\rvert < 110\ \mu$m

Table 4.4: $D\pi$ decays final selection cuts.

decay	N_B	M_B [MeV/c^2]	σ_B [MeV/c^2]
$B^+ \to J/\psi K^+$	5323 ± 84	5278.6 ± 0.2	12.2 ± 0.2
$B^+ \to \bar{D}^0\pi^+$	5625 ± 105	5277.9 ± 0.3	17.7 ± 0.3
$B_d^0 \to J/\psi K^{*0}$	2231 ± 53	5279.2 ± 0.3	10.5 ± 0.3
$B_d^0 \to D^-\pi^+$	6157 ± 123	5278.5 ± 0.4	13.4 ± 0.3

Table 4.5: Mass fits results.

4.3 Monte Carlo Samples

Monte Carlo samples are needed in several places along this thesis. For all of them the same realistic (as opposed to parametric) Monte Carlo simulation has been used. Before entering into a description on how the Monte Carlo samples were produced, the different purposes of such samples are summarized:

1. Signal yield determination in the selection optimization procedure.
2. Physics backgrounds reconstructed as signal invariant mass description.
3. Reconstructed invariant mass and proper decay-length modeling of misreconstructed b-hadrons accepted by trigger, selection cuts and invariant mass window.
4. Characterization of the two-track trigger and selection cuts effect on the proper decay-length distribution of the B meson candidates.

4.3.1 Generation and Decay of b-hadrons

For the b-hadrons generation we employ the `Bgenerator` [30] Monte Carlo tool. It is based on Next to Leading Order QCD calculations [31], using the NDE spectrum for single b quarks. The b quark mass is set to 4.75 GeV/c^2. `Bgenerator` uses the Peterson fragmentation function [32], with the Peterson fragmentation parameter set to $\epsilon_B = 0.006$. There is no minimum requirement in the b quark transverse momentum, and the maximum absolute pseudorapidity of the b quark is set to $|\eta| < 10$. This Monte Carlo generator only produces b-hadrons, therefore no fragmentation products or proton remnants are present. For simulating b-hadron decays we use the `EvtGen` package [33], extensively tuned by the experiments at the $\Upsilon(4S)$ resonance.

4.3.2 Realistic Simulation

The detector simulation is subdivided into trigger and reconstructed quantities. The detector geometry and the active components are simulated by the `GEANT` [20] simulation framework, that models the detector response at the hit level, i.e., the energy deposition in every active and passive component is simulated. Furthermore, the data acquisition systems response to the active detector components is also simulated, and the output of the simulation mimics the real data structure. Real data has time dependent inefficiencies, electronic noise and effects from malfunctioning subdetector parts. For instance, fractions of the silicon detector have been turned off temporarily or even for good. Such imperfections have been incorporated in the detector simulation, and the data taking period is divided in smaller periods were the detector performance is constant.

We also correct the shapes of the B meson p_T spectra that were used in the Monte Carlo generation. Each Monte Carlo event is reweighed in order to make the B p_T spectrum of Monte Carlo events match the one measured in the inclusive J/ψ analysis at CDF [48]. Four Monte Carlo samples have been produced in this thesis, with the generation of 61,683,263 events for each sample. The number of events that survive trigger and analysis selection cuts are quoted in Table 4.6.

decay	N_{trig}	N_{reco}
$B_d^0 \to D^-\pi^+$, $D^- \to K^+\pi^-\pi^-$	$397,835$	$117,048$
$B^+ \to \bar{D}^0\pi^+$, $\bar{D}^0 \to K^+\pi^-$	$399,061$	$79,021$
$B_s^0 \to D_s^-\pi^+$, $D_s^- \to K^+K^-\pi^-$	$461,261$	$81,537$
$\Lambda_b^0 \to \Lambda_c^+\pi^-$, $\Lambda_c^+ \to p^+K^-\pi^+$	$301,537$	$7,338$

Table 4.6: Accepted events by trigger and analysis cuts in the Monte Carlo samples. Both $B_s^0 \to D_s^-\pi^+$ and $\Lambda_b^0 \to \Lambda_c^+\pi^-$ decays are reconstructed and selected as $B_d^0 \to D^-\pi^+$.

Chapter 5

Lifetime Measurements

We have already introduced which are the ingredients for a mixing measurement: signal reconstruction, proper decay-length measurement and flavor tagging. This chapter is dedicated to the proper decay-length measurement. More precisely, our aim is evaluating the lifetime of B_d^0 and B^+ mesons in the four decay modes described in chapter 4, and build the pillars of the decay-length PDF terms that will appear in the final likelihood, to be introduced in chapter 7.

We have seen that two decay modes come from the di-muon trigger and the other two are provided by the two-track trigger. The first ones are unbiased in the sense that nor trigger neither selection cuts bias the lifetime of the B mesons, i.e., modify the shape of the proper decay-length distribution. Therefore, the $B \to J/\psi K$ decays are ideal for setting the basis of our likelihood model, but more important is that unbiased decays are needed for a correct understanding of the proper decay-length resolution. On the other hand, the two-track trigger decay modes have suffered cuts that strongly modify the proper decay-length distribution, i.e., Level 2 trigger cut in the impact parameter of the trigger tracks, Level 3 trigger cut in the transversal decay-length of the vertex formed by the two trigger tracks, and offline tighter cut on the same variable. The main challenge here is the correct Monte Carlo simulation sculpting of the decay-length PDF for signal candidates.

To perform a mixing measurement it is necessary that the final state products of a neutral B meson provide information on its b-flavor at decay time. That is not the case of the main B_s^0 closed-charm mediated decay, $B_s^0 \to J/\psi\phi$, with $J/\psi \to \mu^+\mu^-$ and $\phi \to K^+K^-$. That is a signature that makes it impossible to identify its b-flavor at decay time. It is thus needed to pursue the B_s^0 oscillation mixing frequency in trigger biased decays such as $B_s^0 \to D_s^-\pi^+$ and $B_s^0 \to D_s^- l^+ \nu_l X$, where the charge of the B meson daughters determines the b-flavor content at decay time.

We will start measuring the unbiased lifetimes and afterwards we will move to the more complicated trigger biased decays.

5.1 Lifetime Likelihood

To measure B meson lifetimes as well as other parameters of the model, we use the unbinned maximum likelihood fitting method. In this method the likelihood function $\mathcal{L}$ is constructed as the product of Probability Density Functions (PDFs) of all candidates in a given sample. The PDFs depend on the parameters of the model being fit. The most likely values of the parameters are determined by maximizing $\mathcal{L}$. Technically, the maximization procedure is performed using the `MINUIT` package [37]. For a lifetime measurement the following variables define a B meson candidate:

$\boldsymbol{m}$, $\boldsymbol{\sigma_m}$ – reconstructed invariant mass of the B meson candidate, and its uncertainty. They are calculated as a result of the B vertex fit, performed with the `CTVMFT` package [38];

$\boldsymbol{L_{xy}}$, $\boldsymbol{\sigma_{L_{xy}}}$ – transversal decay-length, and its uncertainty; where L_{xy} is the distance in the transverse plane between the primary interaction vertex and the B decay vertex. They are determined in the same B vertex fit as the reconstructed invariant mass;

$\boldsymbol{p_T}$ – transverse momentum of the B meson candidate. The momentum vector of a B meson candidate is defined as the vectorial sum of the momenta of the B daughter tracks.

The proper decay-length ct and its associated error σ_{ct} are related to the previous variables L_{xy}, $\sigma_{L_{xy}}$ and p_T by

$$ct \equiv \mathrm{M}_{\mathrm{B}}^{\mathrm{PDG}} \frac{L_{xy}}{p_T}, \tag{5.1}$$

$$\sigma_{ct} \equiv \mathrm{M}_{\mathrm{B}}^{\mathrm{PDG}} \frac{\sigma_{L_{xy}}}{p_T}, \tag{5.2}$$

where $\mathrm{M}_{\mathrm{B}}^{\mathrm{PDG}}$ is the PDG (nominal) B meson mass. The uncertainty in the transverse momentum of the B meson candidates has been neglected in the determination of σ_{ct} because $\sigma_{p_T}/p_T \ll \sigma_{L_{xy}}/L_{xy}$ in the four decay modes studied in this thesis, where the B meson is fully reconstructed.

To extract the B meson lifetimes we will have to deal with samples that contain both signal and background events. To separate them, the mass subspace is included in the PDF definition. It provides the best separation power between signal and background events. The latter can be divided in three groups, as it has been described in 4.2.1:

1. *combinatorial background*, with smooth behavior in the reconstructed invariant mass distribution. It is linear in the $B \to J/\psi K$ decay modes, and exponential in the $B \to D\pi$ ones;

2. *partially reconstructed b-hadron decays.* Due to the absence of one or more tracks among the b-hadron daughters, this background usually lies on the left side of the signal mass peak;

3. *misreconstructed b-hadron decays.* Background source due to wrong particle identification, e.g., a kaon is identified as a pion.

With the above described ingredients, a general expression for the likelihood is defined,

$$\mathcal{L}(\vec{x}) = \prod_i P_i(\vec{x}), \tag{5.3}$$

$$\begin{aligned} P_i(\vec{x}) = & (1 - f_B)\, L^S_M(m_i, \sigma_{m_i})\, L^S_{\sigma_m}(\sigma_{m_i})\, L^S_{ct}(ct_i, \sigma_{ct_i})\, L^S_{\sigma_{ct}}(\sigma_{ct_i}) \\ & + f_B\, L^B_M(m_i, \sigma_{m_i})\, L^B_{\sigma_m}(\sigma_{m_i})\, L^B_{ct}(ct_i, \sigma_{ct_i})\, L^B_{\sigma_{ct}}(\sigma_{ct_i}), \end{aligned}$$

where $\vec{x} \equiv (m_i, \sigma_{m_i}, ct_i, \sigma_{ct_i})$, and the index i runs over the B meson candidates sample. The terms L_M, L_{σ_m}, L_{ct} and $L_{\sigma_{ct}}$ are the PDF components in the reconstructed invariant mass, its uncertainty, proper decay-length and proper decay-length resolution subspaces, respectively. The signal is referred to as S and for the background we use B. The relative weights of signal and background candidates in the likelihood are determined by f_B, the background fraction. The analytical expressions of L_M, L_{σ_m}, L_{ct} and $L_{\sigma_{ct}}$ will in principle depend upon the B meson candidates sample for which the lifetime is measured, but there are some parameters that appear in every sample, briefly described here:

- τ – lifetime of the B meson candidates;
- f_B – fraction of background candidates;
- $\langle m \rangle$ – mean of the signal mass distribution;
- $\sigma_{\langle m \rangle}$ – width of the signal mass distribution;
- S_{ct} – ct resolution scale factor,

where S_{ct} is a parameter that accounts for the underestimation of the ct resolution, as measured by any secondary vertex fit with respect to the ct resolution measured in data. Therefore, in those places where the model depends on σ_{ct}, a multiplicative factor is introduced, $f(\sigma_{ct}) \rightarrow f(S_{ct}\sigma_{ct})$. It will be seen later that currently S_{ct} can only be measured in unbiased samples like $B \rightarrow J/\psi K$.

For the real fit to data, a simplified version of the likelihood defined in (5.3) has been used. The reconstructed invariant mass resolution distributions for signal and background B meson candidates are negligibly different, therefore we can drop such terms from the likelihood. Furthermore, the reconstructed invariant mass resolution σ_{m_i} of the B meson candidate i is not used in any of the fits to follow; we assume an average mass resolution $\sigma_{\langle m \rangle}$ for all candidates, parameter that will be determined in the fit to data. Under the assumption of $L^S_{\sigma_{ct}} \approx L^B_{\sigma_{ct}}$, such terms have been removed from the signal and background components of the PDF; this approximation introduces a systematic error due to the difference between the σ_{ct} distributions of signal and background B meson candidates. We reproduce here the general PDF for an event without the L_{σ_m} and $L_{\sigma_{ct}}$ terms, with $\vec{x} = (m, ct, \sigma_{ct})$ and the index i omitted,

$$P(\vec{x}) = (1 - f_B)\, L^S_M(m) L^S_{ct}(ct, \sigma_{ct}) + f_B\, L^B_M(m) L^B_{ct}(ct, \sigma_{ct}). \tag{5.4}$$

Proper Decay-Length Resolution Function

To parameterize the detector smearing a simple gaussian appears to be an adequate description of the resolution function. Studies on variations of the model have been done in [34]. If we define ct' as the real proper decay-length of a B meson candidate and ct as the reconstructed proper decay-length after detector smearing, the resolution function is

$$G(ct - ct', S_{ct}\sigma_{ct}) = \frac{1}{\sqrt{2\pi}S_{ct}\sigma_{ct}} e^{-\frac{1}{2}\left(\frac{ct-ct'}{S_{ct}\sigma_{ct}}\right)^2} \tag{5.5}$$

5.2 Unbiased Lifetime Fits

The di-muon trigger provides B meson decays without introducing any bias in their proper decay-length distribution. The purpose of measuring lifetimes in unbiased decays like $B_d^0 \to J/\psi K^{*0}$ or $B^+ \to J/\psi K^+$ is double: first, it allows us to set the basis of our likelihood with a fairly simple model; second and most important, a lifetime fit on the unbiased decays is needed if we want to measure the proper decay-length resolution scale factor. The general PDF for an event has been described in Section 5.1 and formulated in (5.4). Here we describe the common characteristics in mass and proper decay-length subspaces that apply to both $J/\psi K$ decays, adopting the model described in [34]. Specific properties of $B_d^0 \to J/\psi K^{*0}$ and $B^+ \to J/\psi K^+$ decays will follow.

5.2.1 Mass PDF

In Sec. 5.1 we have denoted the mass PDF for signal candidates as $L_M^S(m)$. It happens that both $B_d^0 \to J/\psi K^{*0}$ and $B^+ \to J/\psi K^+$ decays suffer from misreconstructed background candidates in the signal mass region. The general likelihood expression written in (5.3) is a sum of two terms, one for signal events and one for background events. We decide to keep the background term only for combinatorial background events, and thus include the physics backgrounds in the signal term, since the proper decay-length PDF is the same for signal and physics backgrounds, and the latter are actual misreconstructed signal events. To distinguish *real* signal candidates from the physics backgrounds in the signal likelihood definition, the mass PDF for real signal candidates will be referred to as $L_M^{J/\psi K}(m)$. It is modeled with a single gaussian distribution. The combinatorial background mass follows a linear shape,

$$L_M^{J/\psi K}(m) \;=\; \mathcal{G}(m; \langle m\rangle, \sigma_{\langle m\rangle}, \mathrm{M_{min}}, \mathrm{M_{max}}), \tag{5.6}$$

$$L_M^{B}(m) \;=\; a\,m + \frac{1}{\mathrm{M_{max}} - \mathrm{M_{min}}}\left[1 - \frac{a}{2}\left({\mathrm{M_{max}}}^2 - {\mathrm{M_{min}}}^2\right)\right], \tag{5.7}$$

$$\mathcal{G}(m; \langle m\rangle, \sigma_{\langle m\rangle}, \mathrm{M_{min}}, \mathrm{M_{max}}) \;\equiv\; \frac{\frac{1}{\sqrt{2\pi}\sigma_{\langle m\rangle}} e^{-\frac{1}{2}\left(\frac{m-\langle m\rangle}{\sigma_{\langle m\rangle}}\right)^2}}{\frac{1}{2}\left[\frac{2}{\sqrt{\pi}}\int_0^{\frac{\mathrm{M_{max}}-\langle m\rangle}{\sqrt{2}\sigma_{\langle m\rangle}}} e^{-x^2}\,dx \;+\; \frac{2}{\sqrt{\pi}}\int_0^{\frac{\langle m\rangle-\mathrm{M_{min}}}{\sqrt{2}\sigma_{\langle m\rangle}}} e^{-x^2}\,dx\right]},$$

with a the background slope. The function $\mathcal{G}$ is a gaussian function unit-normalized in the mass range $[\mathrm{M_{min}} - \mathrm{M_{max}}]$. The background PDF defined in (5.7) is as well unit-normalized between $\mathrm{M_{min}} = 5.17$ GeV/c^2 and $\mathrm{M_{max}} = 5.39$ GeV/c^2, the mass fitting window limits for $J/\psi K$ decays.

5.2.2 Proper Decay-Length PDF

Following the notation introduced for the signal mass PDF, we define the proper decay-length PDF for real signal candidates as $L_{ct}^{J/\psi K}(ct, \sigma_{ct})$. True B mesons have a positive exponential shape, that suffers the smearing introduced by the detector resolution. The prompt combinatorial background ct distribution is dominated by a peak centered at $ct \sim 0$; candidates in that peak are constructed with tracks coming from the primary vertex, in most of the cases a prompt J/ψ paired with one or more prompt tracks. The true lifetime of these candidates should be zero and therefore it is described by a Delta function, $\delta(ct')$, smeared with the detector resolution. Without this background peak, the measurement of the ct resolution scale factor S_{ct} could not be possible. The remainder of the background is described by three exponential tails, with the following physics motivation:

- a long-lived positive exponential tail – it accounts for background contributions from residual physics backgrounds that are not explicitly parameterized in the likelihood, true displaced J/ψ mesons paired with a random track, or two sequential muonic decays $b \to c\,\mu^- \bar{\nu}_\mu$, $c \to s\,\mu^+ \nu_\mu$, where the muon pair can fake a J/ψ meson;
- two short-lived negative and positive exponential tails – they include tracks that make use of erroneous hits, or tracks that in reality belong to different displaced vertices.

The proper decay-length PDFs of real signal events and the background sources described above are parameterized in the following empirical way:

$$L_{ct}^{J/\psi K}(ct, \sigma_{ct}) \;=\; \mathcal{E}(ct, S_{ct}\sigma_{ct}; c\tau)\,, \tag{5.8}$$

$$\begin{aligned}\mathcal{E}(ct, \sigma_{ct}; c\tau) \;&\equiv\; \frac{1}{c\tau}\, e^{-\frac{ct'}{c\tau}}\theta(ct') \otimes G(ct - ct', \sigma_{ct}) \\ &=\; \frac{1}{2c\tau}\, e^{-\frac{1}{c\tau}\left(ct - \frac{\sigma_{ct}^2}{2c\tau}\right)} Erfc\left(\frac{\sigma_{ct}^2 - ct\, c\tau}{\sqrt{2}\sigma_{ct}\, c\tau}\right)\,,\end{aligned} \tag{5.9}$$

$$\begin{aligned}L_{ct}^{B}(ct, \sigma_{ct}) \;=\; &(1 - f_- - f_+ - f_{++})\,\delta(ct') \otimes G(ct - ct', S_{ct}\sigma_{ct}) \\ &+\; f_-\, \mathcal{E}(-ct, S_{ct}\sigma_{ct}; \lambda_-) \\ &+\; f_+\, \mathcal{E}(ct, S_{ct}\sigma_{ct}; \lambda_+) \\ &+\; f_{++}\, \mathcal{E}(ct, S_{ct}\sigma_{ct}; \lambda_{++})\,,\end{aligned} \tag{5.10}$$

where $f_{-,+,++}$ are the fractions of the background exponential tails: short-lived negative tail, short-lived positive tail and long-lived positive tail, respectively. The corresponding decay constants are $\lambda_{-,+,++}$. In the previous expressions θ refers to the Heaviside function and by *Erfc* we refer to the complementary error function.

5.2.3 Physics Backgrounds

$K\pi$-swapped candidates in $B_d^0 \to J/\psi K^{*0}$ sample

In the case of $B_d^0 \to J/\psi K^{*0}$, $K^{*0} \to K^+\pi^-$ decays, it can happen that a K^{*0} candidate has been reconstructed with the wrong mass assignment, i.e., a real kaon has been assigned the pion mass and a real pion has been assigned the kaon mass. With our selection cuts, that include a mass window of 50 MeV/c^2 with respect to the K^{*0} PDG mass, this wrong mass assignment accounts for $\sim$ 12% of the signal candidates. Based on a Monte Carlo study [34] it has been found that the mass distribution of the $K\pi$-swapped candidates is a gaussian function with same mean value as the signal and a width of 25 MeV/c^2. The proper decay-length distribution is negligibly different to that of correctly reconstructed candidates,

$$L_M^S(m) \;=\; (1 - f_{\rm swap})\, L_M^{J/\psi K}(m) \;+\; f_{\rm swap}\, L_M^{\rm swap}(m)\,, \tag{5.11}$$

$$L_M^{\rm swap}(m) \;=\; \mathcal{G}(m; \langle m \rangle\,, \sigma_{\rm swap}, {\rm M_{min}}, {\rm M_{max}})\,, \tag{5.12}$$

$$L_{ct}^S(ct, \sigma_{ct}) \;=\; L_{ct}^{J/\psi K}(ct, \sigma_{ct})\,, \tag{5.13}$$

where "swap" refers to candidates with the wrong $K\pi$ mass assignment, $f_{\rm swap} = 0.12$ and $\sigma_{\rm swap} = 25$ MeV/c^2. Both $f_{\rm swap}$ and $\sigma_{\rm swap}$ are fixed values in any fit to follow.

$B^+ \to J/\psi\pi^+$ decays reconstructed as $B^+ \to J/\psi K^+$

The $B^+ \to J/\psi\pi^+$ decays reconstructed as $B^+ \to J/\psi K^+$ candidates are described with a quite complicated mass PDF, empirically determined to accurately describe the Monte Carlo reconstructed invariant mass distribution [34]. The proper decay-length distribution is described by an exponential very similar to the true signal,

$$\begin{aligned} L^S_M(m)L^S_{ct}(ct,\sigma_{ct}) &= (1-f_{J/\psi\pi})\, L^{J/\psi K}_M(m)L^{J/\psi K}_{ct}(ct,\sigma_{ct}) \\ &\quad + f_{J/\psi\pi}\, L^{J/\psi\pi}_M(m)L^{J/\psi\pi}_{ct}(ct,\sigma_{ct})\,, \end{aligned} \tag{5.14}$$

$$\begin{aligned} L^{J/\psi\pi}_M(m) &= \frac{1}{N_{J/\psi\pi}}\left(m-\widetilde{\delta}_{J/\psi\pi}\right)^6 e^{\frac{\widetilde{\delta}_{J/\psi\pi}-m}{b}}\,, \\ \widetilde{\delta}_{J/\psi\pi} &\equiv \langle m\rangle - \delta_{J/\psi\pi}\,, \\ N_{J/\psi\pi} &\equiv a_6 b^7 - e^{\frac{\widetilde{\delta}_{J/\psi\pi}-\mathrm{M_{max}}}{b}}\left[a_6 b^7 + \sum_{i=1}^{i=6} a_i b^i \left(\mathrm{M_{max}}-\widetilde{\delta}_{J/\psi\pi}\right)^{7-i}\right], \\ \vec{a} &\equiv (1,5,30,120,360,720)\,, \end{aligned} \tag{5.15}$$

$$L^{J/\psi\pi}_{ct}(ct,\sigma_{ct}) = \mathcal{E}(ct, S_{ct}\sigma_{ct}; h_{J/\psi\pi}c\tau)\,, \tag{5.16}$$

where $J/\psi\pi$ denotes the Cabibbo-suppressed decay. The fraction of such decays is $f_{J/\psi\pi}$, and the values of the different parameters obtained from Monte Carlo are quoted in Table 5.1.

parameter	value
$f_{J/\psi\pi}$	0.025
$\delta_{J/\psi\pi}$[GeV/c^2]	-0.003
b [GeV/c^2]	0.009
$h_{J/\psi\pi}$	1.01

Table 5.1: Parameter values of $B^+ \to J/\psi\pi^+$ Monte Carlo templates. They are fixed in any forthcoming fit.

5.2.4 Likelihood Consistency

The unbinned likelihood fitter procedure has been tested with toy Monte Carlo in order to see if any bias is introduced. The required input from data in our lifetime fit includes the following variables: m (mass), ct and σ_{ct}. Then we only need Monte Carlo events with such information, and this is the description of how they are generated:

1. Parameter values are taken from fits on data.
2. For the lifetime generation we assume $\sigma_{ct}^{MC} \equiv 30\ \mu$m.
3. Generate a random uniform number r between 0 and 1.
4. If $r < f_B$ it is a background event:
    (a) another random uniform number determines which background is to be generated;
    (b) mass and ct are generated in accordance with the previously described PDF functions.
5. If $r \geq f_B$ it is a signal event:
    (a) another random uniform number determines if the event is $J/\psi K$ or a physics background ($K\pi$-swapped or $J/\psi\pi$);
    (b) mass and ct are generated in accordance with the previously described PDF functions.

The previous steps define a toy Monte Carlo event. Once a given number of events has been generated and recorded, we have what we call an "experiment". An experiment is saved exactly in the same format as the real data, and we apply the fitter on such experiment. When several experiments are fitted we expect that the distribution of pulls for each parameter will resolve to a unit gaussian, with a mean value of zero and a width of one. As a test of the technical validity of the fitter, we perform 1,000 toy experiments comprised of 16,000 events each for the B_d^0 model. The parameter inputs of the toy Monte Carlo are set to values very similar to the fit results that later will be documented. All parameters are allowed to float and a full fit is performed. To determine the mean μ_{pull} and the width σ_{pull} of the pull distributions, they are fitted to a single gaussian.

Within the uncertainties, most of the values quoted in Table 5.2 are consistent with the unit gaussian. The few discrepancies are found for the short background tails. We can explain this small bias by noticing that the short tail components have fractional weight (f_-) of only a few percent, and there are thus insufficient events for them to be fully populated and to allow the fit to completely resolve the tails from the prompt background.

5.2.5 Results

The fit results for $B_d^0 \rightarrow J/\psi K^{*0}$ and $B^+ \rightarrow J/\psi K^+$ are shown in Table 5.3. The fit projections onto the mass and ct subspaces can be seen in Figs. 5.1 and 5.2.

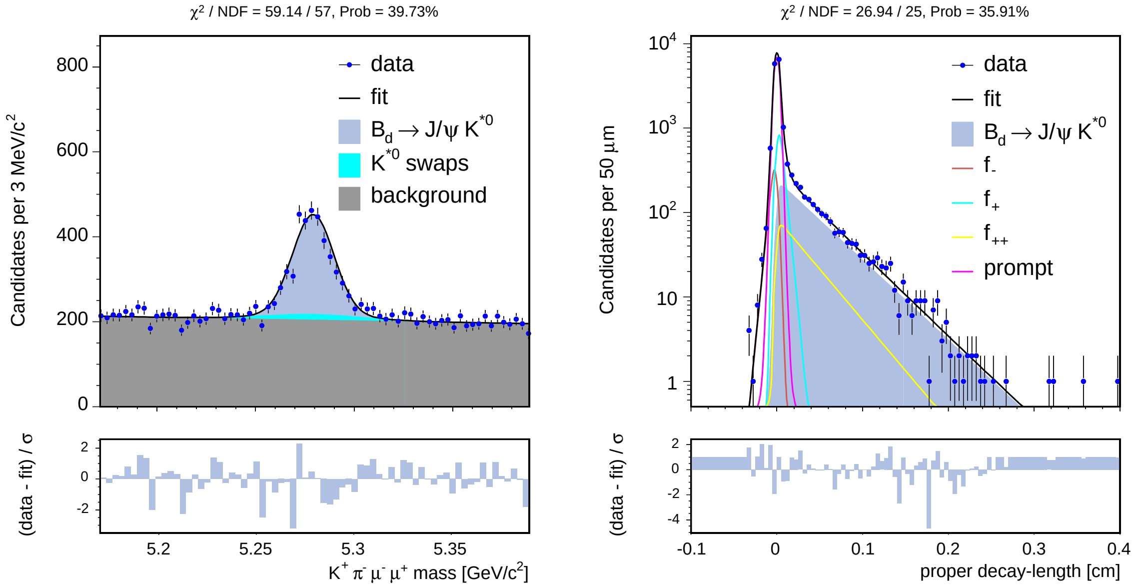

Figure 5.1: Mass and lifetime fit projections for $B_d^0 \to J/\psi K^{*0}$ decay.

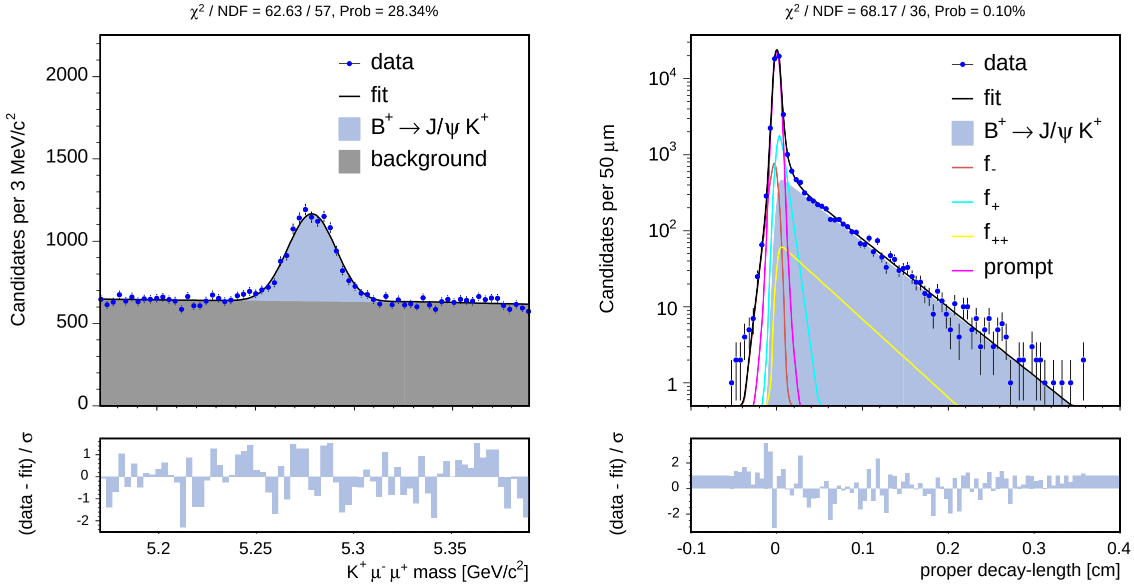

Figure 5.2: Mass and lifetime fit projections for $B^+ \to J/\psi K^+$ decay.

parameter	μ_{pull}	σ_{pull}	fit probability
$1 - f_B$	-0.005 ± 0.032	1.016 ± 0.023	0.708
$\langle m \rangle$	-0.017 ± 0.033	1.024 ± 0.023	0.079
a	-0.008 ± 0.031	0.979 ± 0.022	0.601
$c\tau$	-0.020 ± 0.032	1.020 ± 0.023	0.838
S_{ct}	-0.016 ± 0.032	0.994 ± 0.022	0.470
f_-	-0.089 ± 0.032	1.011 ± 0.023	0.000
f_+	-0.018 ± 0.033	1.025 ± 0.023	0.482
f_{++}	0.033 ± 0.033	1.034 ± 0.023	0.046
λ_-	-0.076 ± 0.031	0.974 ± 0.022	0.000
λ_+	-0.085 ± 0.033	1.033 ± 0.023	0.052
λ_{++}	-0.076 ± 0.033	1.030 ± 0.023	0.168

Table 5.2: Gaussian fit results on $B_d^0 \to J/\psi K^{*0}$ lifetime pull distributions. A total of 1,000 toy experiments with 16,000 events each were generated.

parameter	$B_d^0 \to J/\psi K^{*0}$	$B^+ \to J/\psi K^+$
$\langle m \rangle$ [MeV/c^2]	5279.2 ± 0.3	5278.6 ± 0.2
$\sigma_{\langle m \rangle}$ [MeV/c^2]	10.5 ± 0.3	12.2 ± 0.2
f_B	0.865 ± 0.003	0.893 ± 0.002
a	-1.79 ± 0.60	-1.07 ± 0.34
$c\tau$ [μm]	458.5 ± 10.9	489.2 ± 7.6
S_{ct}	1.084 ± 0.014	1.062 ± 0.007
f_-	0.047 ± 0.008	0.039 ± 0.004
f_+	0.121 ± 0.012	0.097 ± 0.005
f_{++}	0.043 ± 0.004	0.014 ± 0.002
λ_- [μm]	41.8 ± 3.7	45.2 ± 2.5
λ_+ [μm]	41.9 ± 4.9	53.5 ± 3.3
λ_{++} [μm]	360.9 ± 28.5	422.9 ± 38.4

Table 5.3: Mass and lifetime fit results for J/ψ modes.

5.3 Trigger Biased Lifetime Fits

As we have seen in the previous section, the di-muon trigger provides an excellent place for B mesons lifetime measurements, determination of a scale factor for the proper decay-length S_{ct}, and B_d^0 mixing studies; it supplies very clean samples without any cut in L_{xy} or impact parameter of the B meson candidates.

On the contrary, in the B_s^0 sector the mixing analysis with the closed-charm is disfavored; the signature of the dominant tree-level decay $B_s^0 \to J/\psi\phi$, with $J/\psi \to \mu^+\mu^-$ and $\phi \to K^+K^-$, does not tag the b-flavor at its decay. This is not the case for the open-charm signatures. The analysis challenge for these decay modes is the understanding of the decay-length bias introduced by trigger and offline selection cuts. Thanks to its similar topology, kinematics and relatively large yields, the $B_d^0 \to D^-\pi^+$ and $B^+ \to \bar{D}^0\pi^+$ decay modes are the natural candidates to establish the analysis procedure for a biased lifetime measurement.

5.3.1 Mass PDF

The reconstructed invariant mass distributions of $B_d^0 \to D^-\pi^+$ and $B^+ \to \bar{D}^0\pi^+$ candidates are complicated by partially reconstructed B decays that constitute most of the background in the lower mass sideband, as it can be seen in Fig. 5.3. To avoid such structures, a narrower mass range with $\mathrm{M}_{\min} = 5.2$ GeV/c^2 and $\mathrm{M}_{\max} = 5.6$ GeV/c^2 has been chosen when the simultaneous fit of mass and proper decay-length is performed. In this new range the contribution of partially reconstructed B decays is $< 2\%$ and it is thus neglected. The main contribution to the background in the reduced mass range is the combinatorial background, described by an exponential function,

$$L_M^B(m) = \frac{\lambda e^{-\lambda m}}{e^{-\lambda \mathrm{M}_{\min}} - e^{-\lambda \mathrm{M}_{\max}}}, \tag{5.17}$$

with the value of the parameter λ determined in a mass fit, performed in the mass range $[\mathcal{M}_{\min} = 4.8 - \mathcal{M}_{\max} = 5.8 \text{ GeV/c}^2]$. In this range the partially reconstructed backgrounds are considered in the fit, allowing for a better determination of λ. In Table 5.4 we summarize the values of λ for both $B \to D\pi$ decays. These values will be fixed in the simultaneous fits of mass and proper decay-length.

parameter	value	
	$B_d^0 \to D^-\pi^+$	$B^+ \to \bar{D}^0\pi^+$
λ	1.52 ± 0.10	0.95 ± 0.07

Table 5.4: Parameter values of the combinatorial background mass PDF. They are determined in a binned fit of the reconstructed invariant mass distribution, in the range $[\mathcal{M}_{\min} - \mathcal{M}_{\max}]$.

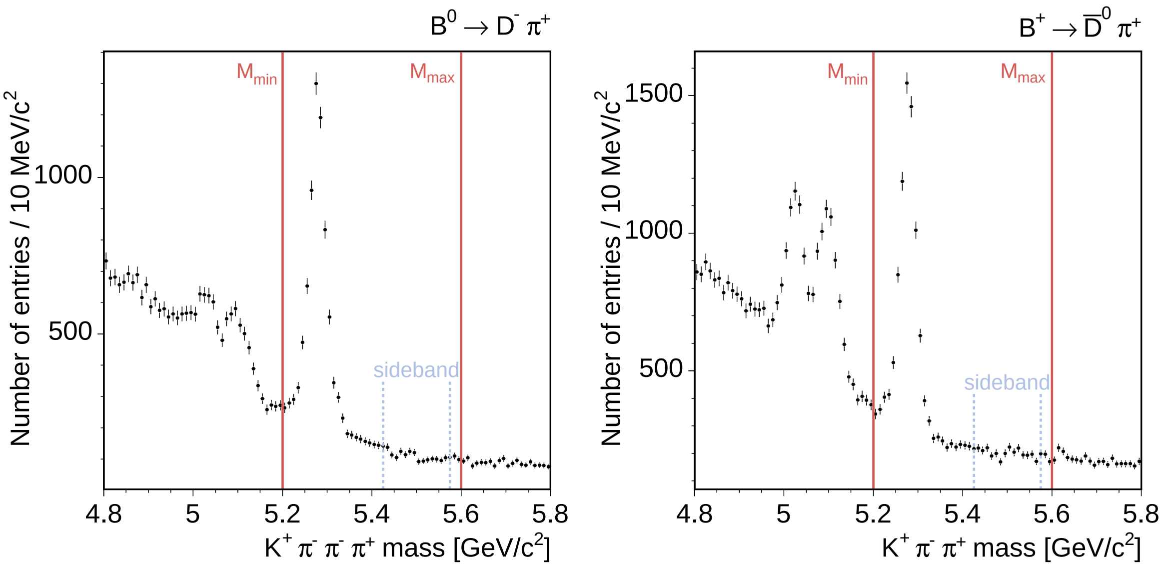

Figure 5.3: Invariant mass range used for $B_d^0 \to D^-\pi^+$ (left) and $B^+ \to \bar{D}^0\pi^+$ (right) lifetime measurements. The sideband region used for the determination of the combinatorial background proper decay-length template is also shown.

$B_d^0 \to D^-\pi^+$

In the general likelihood expression defined in (5.3), both signal and background mass terms had dependence on the reconstructed invariant mass resolution σ_m. In the real fits to data, instead of considering such variable, we empirically described the signal mass peak by a gaussian function, with a common resolution $\sigma_{\langle m\rangle}$ to all B meson candidates in a given sample. This model has been found to perfectly describe the unbiased samples and also the $B^+ \to \bar{D}^0\pi^+$ decay. In the $B_d^0 \to D^-\pi^+$ case, on the contrary, two resolutions were necessary. Therefore, this decay mode is parameterized with two gaussian functions, that share the mean value $\langle m\rangle$, and with the wider resolution defined as a factor r times the narrower one. The mass PDF for the signal component is then

$$\begin{aligned} L_M^{D\pi}(m) &= (1-f)\,\mathcal{G}(m;\langle m\rangle\,,\sigma_{\langle m\rangle},\mathrm{M}_{\min},\mathrm{M}_{\max}) \\ &\quad + f\,\mathcal{G}(m;\langle m\rangle\,,r\sigma_{\langle m\rangle},\mathrm{M}_{\min},\mathrm{M}_{\max})\,, \end{aligned} \tag{5.18}$$

with f and r determined in a binned fit of the reconstructed invariant mass distribution, in the mass range $[\mathcal{M}_{\min} - \mathcal{M}_{\max}]$. Both f and r are as well fixed in forthcoming fits, for fit stability reasons. We quote them in Table 5.5.

$B^+ \to \bar{D}^0\pi^+$

The reconstructed invariant mass distribution of $B^+ \to \bar{D}^0\pi^+$ signal candidates is simpler than in the $B_d^0 \to D^-\pi^+$ case, and a single gaussian function suffices to describe

parameter	value
f	0.547 ± 0.084
r	2.082 ± 0.133

Table 5.5: Some parameter values of the $B_d^0 \to D^-\pi^+$ signal mass PDF. They are determined in a binned fit of the reconstructed invariant mass distribution, in the range $[\mathcal{M}_{\min} - \mathcal{M}_{\max}]$.

it accurately,

$$L_M^{D\pi}(m) \;=\; \mathcal{G}(m; \langle m\rangle, \sigma_{\langle m\rangle}, \mathrm{M}_{\min}, \mathrm{M}_{\max})\,.$$

5.3.2 Proper Decay-Length PDF

Signal

Trigger and selection requirements on impact parameter and transversal decay-length modify the ct distribution of the B meson candidates. When performing an unbinned likelihood fit, it is mandatory that an appropriate description of the modified ct distribution is incorporated into the likelihood definition. The needed description is achieved in our model by including a multiplicative decay-length efficiency factor, $\xi(ct)$, obtained from Monte Carlo simulation, into the signal proper decay-length PDF. The PDF describing the proper decay-length for the signal part of the likelihood is therefore represented as follows,

$$L_{ct}^S(ct, \sigma_{ct}) \;=\; \frac{1}{N(\sigma_{ct})}\left[\frac{1}{c\tau}e^{-\frac{ct'}{c\tau}}\theta(ct') \otimes G(ct - ct', S_{ct}\sigma_{ct})\right]\xi(ct)\,, \tag{5.19}$$

$$N(\sigma_{ct}) \;\equiv\; \int_{-\infty}^{+\infty} \frac{1}{c\tau}e^{-\frac{ct'}{c\tau}}\theta(ct') \otimes G(ct - ct', S_{ct}\sigma_{ct})\,\xi(ct)\,d(ct)\,, \tag{5.20}$$

where the inclusion of a decay-length efficiency curve $\xi(ct)$ requires $L_{ct}^S(ct, \sigma_{ct})$ to be unit-normalized by analytical integration of $N(\sigma_{ct})$, for every event. The analytical expression of $N(\sigma_{ct})$ is given in (B.2). In the following we describe how the decay-length efficiency curve is defined and parameterized:

1. The decay-length efficiency curve $\xi(ct)$ is based on a Monte Carlo simulation of signal events, i.e., $B_d^0 \to D^-\pi^+$ with $D^- \to K^+\pi^-\pi^-$, or $B^+ \to \bar{D}^0\pi^+$ with $\bar{D}^0 \to K^+\pi^-$.
2. Both two-track trigger and selection cuts summarized in Table 4.4 are applied on the Monte Carlo signal events. The number of accepted events is denoted by N.
3. We define $\xi(ct)$ as the ratio of two ct histograms or distributions.
4. The numerator is the ct distribution of the N signal events that survived both two-track trigger and selection cuts.

5. For each accepted event i, the expected ct distribution without any bias is an exponential smeared by a decay-length resolution function, where the width is the ct error (σ_{ct_i}) of that event. The denominator is the sum of these N distributions,

$$\xi(ct) \equiv \frac{\text{reconstructed } ct \text{ after trigger} + \text{cuts}}{\sum_{i=1}^{N} \mathcal{E}(ct, S_{ct}^{MC}\sigma_{ct_i}; c\tau)}\,, \tag{5.21}$$

   where the factor S_{ct}^{MC} is the width of the pull distribution $(t^{\text{reconstructed}} - t^{\text{true}})/\sigma_t$ obtained from the Monte Carlo sample; its numerical value is $S_{ct}^{MC} = 1.107 \pm 0.004$.

6. We need only the shape of $\xi(ct)$, because $L_{ct}^{S}(ct, \sigma_{ct})$ is properly normalized by the term $N(\sigma_{ct})$, given in (5.20).

7. The shape of the decay-length efficiency curve is parameterized by the following template:

$$\xi(ct) \;=\; \sum_{j=1}^{3} \alpha_j \,(ct - \beta_j)^2 \, e^{-\frac{ct}{\gamma_j}} \, \theta(ct - \beta_j)\,. \tag{5.22}$$

The template used in (5.22) is motivated by the possibility of analytical normalization of the proper decay-length signal PDF. The effect of the two-track trigger and selection cuts on the proper decay-length distribution is illustrated in Fig. 5.4. The results of the fits for the parameters α_j, β_j and γ_j can be seen in Fig. 5.5.

Combinatorial Background

The main concern for describing the decay-length template of combinatorial background events comes from the fact that only upper mass sidebands can be used, since lower mass sidebands also contain contributions from partially reconstructed B decays, as seen in Fig. 5.3.

The observable defined in (5.1) for the lifetime fits, ct, is meaningless for combinatorial background events, i.e., the reconstructed invariant mass m of these events is in general different from $\mathrm{M_B^{PDG}}$. We therefore use ct_{rec} for combinatorial background events, defined as

$$ct_{rec} \;\equiv\; m\,\frac{L_{xy}}{p_T}\,. \tag{5.23}$$

Let $f(ct_{rec})$ be the ct_{rec} distribution of combinatorial background events in the mass range $[5.425 - 5.575\ \mathrm{GeV/c^2}]$. We refer to this mass range as sideband, shown in Fig. 5.3. The template needed to describe the combinatorial background decay-length ct distribution in the mass range $[\mathrm{M_{min}} - \mathrm{M_{max}}]$ is obtained by rescaling $f(ct_{rec})$ with a mass

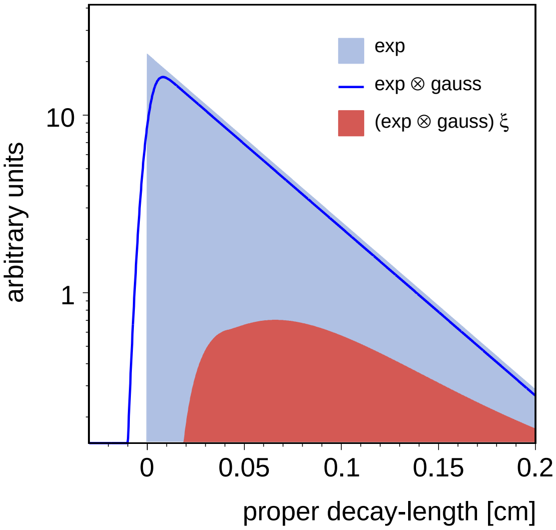

Figure 5.4: Illustration of the degradation of the B mesons ct distribution. With perfect decay-length resolution and no decay-length efficiency curve, we have a simple exponential distribution (solid blue). The effect of a finite decay-length resolution introduces a smearing in the exponential (blue line). The final addition of a decay-length efficiency curve, such as that of the two-track trigger on $B \to D\pi$ decays, returns a more complex shape (solid red). The distributions do not keep the relative normalizations in data.

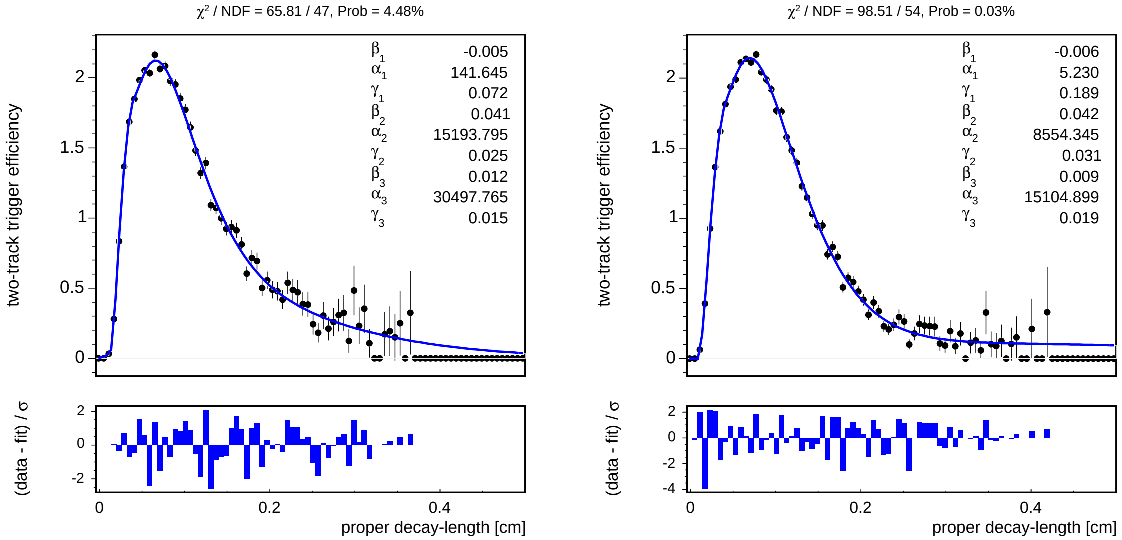

Figure 5.5: Monte Carlo trigger efficiency functional form for $B_d^0 \to D^-\pi^+$ (left) and $B^+ \to \bar{D}^0\pi^+$ (right) decays.

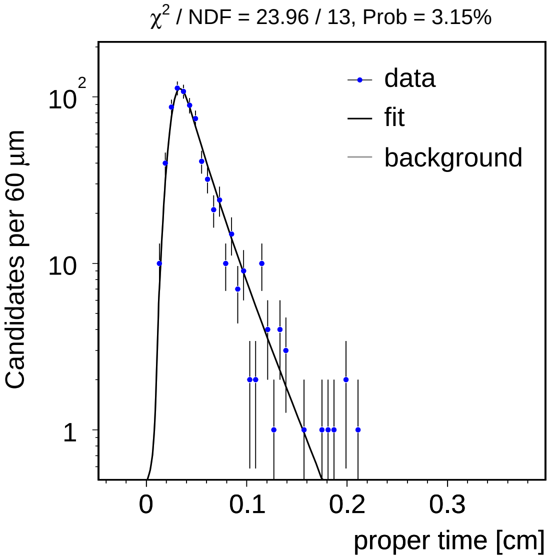

Figure 5.6: Lifetime fit projection onto the sideband region [5.45 − 5.6 GeV/c^2].

dependent factor, reweighing the rescaled function with the mass PDF of combinatorial background events $L_M^B(m)$, and integrating it in the whole mass range. The formal expression is the following:

$$L_{ct}^B(ct) \quad = \quad \int_{\mathrm{M_{min}}}^{\mathrm{M_{max}}} f\left(ct_{rec}\frac{\mathrm{M_B^{PDG}}}{u}\right) L_M^B(u)\,du\,. \tag{5.24}$$

Using the procedure defined in (5.24), the template which describes the ct distribution of combinatorial background events is prepared. It contains two exponential functions convoluted with two gaussians. The exponential functions have different decay constants, while the gaussians with which they are smeared have the same mean and width. The total number of parameters is five: λ_1, λ_2, μ, σ_B and f_2. The two exponentials share also the cut-off point μ, and f_2 is the fraction of candidates in the second exponential,

$$L_{ct}^B(ct) \quad = \quad \left(\frac{1-f_2}{\lambda_1}e^{-\frac{ct'}{\lambda_1}} + \frac{f_2}{\lambda_2}e^{-\frac{ct'}{\lambda_2}}\right)\theta(ct') \otimes G(ct-ct'-\mu,\sigma_B)\,. \tag{5.25}$$

A lifetime fit projection onto the sideband region [5.45 − 5.6 GeV/c^2] can be seen in Fig. 5.6. It shows the template accuracy describing the combinatorial background events lifetime.

5.3.3 Physics Backgrounds

Both $B_d^0 \to D^-\pi^+$ and $B^+ \to \bar{D}^0\pi^+$ samples suffer from Cabibbo-suppressed decays beneath the signal mass peak, thus modifying the signal mass PDF. So, we use:

$$L_M^S(m) = \frac{1}{1+r_{DK}} L_M^{D\pi}(m) + \frac{r_{DK}}{1+r_{DK}} L_M^{DK}(m)\,, \tag{5.26}$$

$$r_{DK} \equiv \frac{N(B \to DK \text{ rec. as } B \to D\pi)}{N(B \to D\pi)}\,, \tag{5.27}$$

$$L_M^{DK}(m) = \mathcal{G}(m; \langle m\rangle - \delta_{DK}, \sigma_{m_{DK}}, \mathrm{M}_{\min}, \mathrm{M}_{\max})\,. \tag{5.28}$$

The parameter values, obtained from Monte Carlo, are summarized in Table 5.6 and they are fixed in fits on data. The signal proper decay-length PDF is left unchanged.

parameter	value	
	$B_d^0 \to D^-K^+$	$B^+ \to \bar{D}^0K^+$
r_{DK}	0.067 ± 0.023	0.079 ± 0.013
δ_{DK} [GeV/c^2]	0.067 ± 0.006	0.069 ± 0.011
$\sigma_{m_{DK}}$[GeV/c^2]	0.032 ± 0.009	0.040 ± 0.009

Table 5.6: $B \to DK$ mass parameter values from MC.

B_s^0 and Λ_b^0 reconstructed as $B_d^0 \to D^-\pi^+$

Two physics backgrounds affect the $B_d^0 \to D^-\pi^+$ sample:

- $B_s^0 \to D_s^-\pi^+$, $D_s^- \to K^+K^-\pi^-$;
- $\Lambda_b^0 \to \Lambda_c^+\pi^-$, $\Lambda_c^+ \to p^+K^-\pi^+$.

These physics backgrounds increase the complexity of the likelihood expression, described now as

$$P(\vec{x}) = \frac{1-f_B}{1+r_{B_s^0}+r_{\Lambda_b^0}} \left(L_M^S L_{ct}^S + r_{B_s^0} L_M^{B_s^0} L_{ct}^{B_s^0} + r_{\Lambda_b^0} L_M^{\Lambda_b^0} L_{ct}^{\Lambda_b^0} \right) + f_B L_M^B L_{ct}^B\,, \tag{5.29}$$

where $\vec{x} = (m, ct, \sigma_{ct})$. The mass PDF which describes the B_s^0 background is obtained from Monte Carlo. It is accurately described with two gaussian functions, as it can be seen in Fig. 5.7 (right). The parameter values of the B_s^0 mass PDF defined in (5.30) are summarized in Table 5.8, and are fixed in any fit on data.

$$\begin{aligned} L_M^{B_s^0}(m) &= (1-f_{B_s^0})\,\mathcal{G}(m; \langle m\rangle_{B_s^0}, \sigma_{m_{B_s^0}}, \mathrm{M}_{\min}, \mathrm{M}_{\max}) \\ &+ f_{B_s^0}\,\mathcal{G}(m; \langle m\rangle_{B_s^0}, h_{B_s^0}\sigma_{m_{B_s^0}}, \mathrm{M}_{\min}, \mathrm{M}_{\max})\,. \end{aligned} \tag{5.30}$$

The contribution from B_s^0 decays to the background in the $B_d^0 \to D^- \pi^+$ channel is estimated using the expression that follows:

$$r_{B_s^0} \equiv \frac{N(B_s^0)}{N(B_d^0)} = \frac{f_s}{f_d} \cdot \frac{\mathrm{BR}(B_s^0 \to D_s^- \pi^+)}{\mathrm{BR}(B_d^0 \to D^- \pi^+)} \cdot \frac{\mathrm{BR}(D_s^- \to \phi \pi^-)\mathrm{BR}(\phi \to K^+ K^-)}{\mathrm{BR}(D^- \to K^+ \pi^- \pi^-)} \cdot \frac{\Gamma(D_s^- \to K^+ K^- \pi^-)}{\Gamma(D_s^- \to \phi(K^+ K^-)\pi^-)} \cdot \frac{\epsilon_{MC}(B_s^0 \text{ rec. as } B_d^0)}{\epsilon_{MC}(B_d^0)}, \quad (5.31)$$

with values taken from the PDG [19] and [46]. The efficiencies ϵ_{MC} are measured using our Monte Carlo samples of $B_s^0 \to D_s^- \pi^+$, $D_s^- \to K^+ K^- \pi^-$ and $B_d^0 \to D^- \pi^+$, $D^- \to K^+ \pi^- \pi^-$.

The decay chain $\Lambda_b^0 \to \Lambda_c^+ \pi^-$, $\Lambda_c^+ \to p^+ K^- \pi^+$ contributes to non-combinatorial background in the upper mass sideband, when the proton from the Λ_c^+ is misidentified as a pion. From a Monte Carlo sample we derive the mass PDF of Λ_b^0 candidates when they are reconstructed as B_d^0,

$$\begin{aligned} L_M^{\Lambda_b^0}(m) &= (1 - f_{\Lambda_b^0})\,\mathcal{A}(m; \kappa_{\Lambda_b^0}, \langle m \rangle_{\Lambda_b^0}, \sigma_{m_{\Lambda_b^0}}, N_{\Lambda_b^0}) \\ &\quad + f_{\Lambda_b^0}\,\mathcal{G}(m; \langle m \rangle_{\Lambda_b^0}, \sigma_{m_{\Lambda_b^0}}, \mathrm{M_{min}}, \mathrm{M_{max}}), \end{aligned} \quad (5.32)$$

$$\mathcal{A}(m; \kappa, \langle m \rangle, \sigma, N_{\Lambda_b^0}) \equiv \frac{1}{2\kappa N_{\Lambda_b^0}}\, Erfc\left(\frac{\sigma}{\sqrt{2}\kappa} - \frac{\langle m \rangle - m}{\sigma}\right) e^{\frac{\sigma^2}{2\kappa^2} - \frac{\langle m \rangle - m}{\kappa}},$$

with parameter values summarized in Table 5.8. In Fig. 5.7 (left) the agreement between the Monte Carlo candidates that passed the selection and the derived template can be seen. The number of Λ_b^0 candidates expected to pollute the $B_d^0 \to D^- \pi^+$ sample is:

$$r_{\Lambda_b^0} \equiv \frac{N(\Lambda_b^0)}{N(B_d^0)} = \frac{\sigma_{\Lambda_b^0}(p_T > 6.0 \text{ GeV/c})}{\sigma_{B_d^0}(p_T > 6.0 \text{ GeV/c})} \cdot \frac{\mathrm{BR}(\Lambda_b^0 \to \Lambda_c^+ \pi^-)}{\mathrm{BR}(B_d^0 \to D^- \pi^+)} \cdot \frac{\mathrm{BR}(\Lambda_c^+ \to p K^- \pi^+)}{\mathrm{BR}(D^- \to K^+ \pi^- \pi^-)} \cdot \frac{\epsilon_{MC}(\Lambda_b^0 \text{ rec. as } B_d^0)}{\epsilon_{MC}(B_d^0)}, \quad (5.33)$$

with numbers taken from the PDG [19] and [47]. The ratio of Monte Carlo reconstructed efficiencies is measured using $\Lambda_b^0 \to \Lambda_c^+ \pi^-$, $\Lambda_c^+ \to p^+ K^- \pi^+$ and the already mentioned signal Monte Carlo. In Table 5.7 the numbers used for the estimates of $r_{B_s^0}$ and $r_{\Lambda_b^0}$ ratios in our data sample are reported. These ratios are fixed as well in all fits on data. The proper decay-length PDFs of B_s^0 and Λ_b^0 backgrounds were obtained from the same Monte Carlo used for the mass PDFs determination. The parameter values of these physics backgrounds proper decay-length PDFs are summarized in Table 5.9.

$$L_{ct}^{\Lambda_b^0}(ct) = \mathcal{E}(ct - \delta_{\Lambda_b^0}; \sigma_{ct_{\Lambda_b^0}}, \lambda_{\Lambda_b^0}), \quad (5.34)$$

$$\begin{aligned} L_{ct}^{B_s^0}(ct) &= (1 - f_{B_s^0}^{++})\,\mathcal{E}(ct - \delta_{B_s^0}^{+}; \sigma_{ct_{B_s^0}}^{+}, \lambda_{B_s^0}^{+}) \\ &\quad + f_{B_s^0}^{++}\,\mathcal{E}(ct - \delta_{B_s^0}^{++}; \sigma_{ct_{B_s^0}}^{++}, \lambda_{B_s^0}^{++}). \end{aligned} \quad (5.35)$$

$\frac{f_s}{f_d}\frac{\mathrm{BR}(B_s^0 \to D_s^- \pi^+)}{\mathrm{BR}(B_d^0 \to D^- \pi^+)}$	$1.32 \pm 0.18 \pm 0.10$
$\mathrm{BR}(D_s^- \to \phi\pi^-)$	$3.6 \pm 0.9\%$
$\mathrm{BR}(\phi \to K^+K^-)$	$49.1 \pm 0.6\%$
$\mathrm{BR}(D^- \to K^+\pi^-\pi^-)$	$9.2 \pm 0.6\%$
$\frac{\Gamma(D_s^- \to \phi\pi^-)}{\Gamma(D_s^- \to K^+K^-\pi^-)}$	0.81 ± 0.08
$\epsilon_{MC}(B_s^0 \text{ rec. as } B_d^0)/\epsilon_{MC}(B_d^0)$	$11.6 \pm 0.1\%$
$r_{B_s^0}$	$2.01 \pm 0.38\%$
$\frac{\sigma_{\Lambda_b^0}(p_T > 6.0 \text{ GeV/c})}{\sigma_{B_d^0}(p_T > 6.0 \text{ GeV/c})}\frac{\mathrm{BR}(\Lambda_b^0 \to \Lambda_c^+ \pi^-)}{\mathrm{BR}(B_d^0 \to D^- \pi^+)}$	$0.81 \pm 0.08 \pm 0.11$
$\mathrm{BR}(\Lambda_c^+ \to pK^-\pi^+)$	$5.0 \pm 1.3\%$
$\epsilon_{MC}(\Lambda_b^0 \text{ rec. as } B_d^0)/\epsilon_{MC}(B_d^0)$	$9.3 \pm 0.1\%$
$r_{\Lambda_b^0}$	$4.11 \pm 0.74\%$

Table 5.7: Numerical values used to estimate B_s^0 and Λ_b^0 backgrounds.

parameter	value
$f_{\Lambda_b^0}$	0.001
$\langle m \rangle_{\Lambda_b^0}$ [GeV/c^2]	5.439
$\sigma_{m_{\Lambda_b^0}}$ [GeV/c^2]	0.036
$\kappa_{\Lambda_b^0}$ [GeV/c^2]	0.076
$f_{B_s^0}$	0.192
$\langle m \rangle_{B_s^0}$ [GeV/c^2]	5.315
$\sigma_{m_{B_s^0}}$ [GeV/c^2]	0.022
$h_{B_s^0}$	2.048

Table 5.8: B_s^0 and Λ_b^0 backgrounds mass parameter values from MC.

5.3.4 Likelihood Consistency

As a test of the fitter we perform 1,000 toy experiments with 7,000 events in each, similar size to that of the data sample. The pull distributions for all fit parameters are shown in Fig. 5.8, and the numerical results can be found in Table 5.10. We expect the pull distributions to have a gaussian behavior, with mean value at zero and width one. Within the uncertainties, all the values quoted in Table 5.10 are consistent with the unit gaussian. The B_d^0 lifetime is the only parameter that shows a consistently (4σ) non-zero bias. Nonetheless, the corresponding shift in the value of $c\tau$ is a measly 1.4 μm.

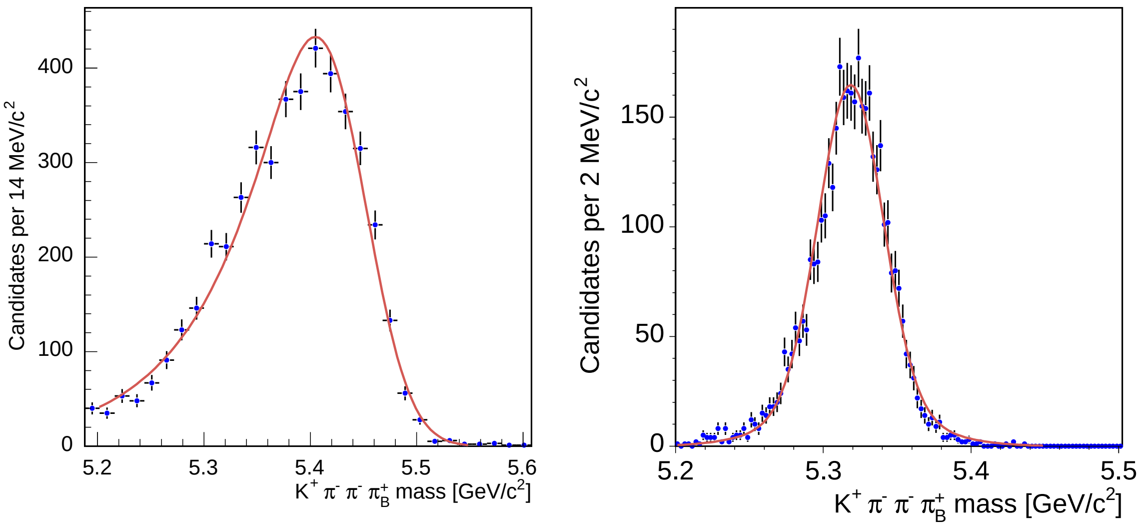

Figure 5.7: Monte Carlo reconstructed invariant mass distributions of $\Lambda_b^0 \to \Lambda_c^+\pi^-$, $\Lambda_c^+ \to p^+K^-\pi^+$ (left) and $B_s^0 \to D_s^-\pi^+$, $D_s^- \to K^+K^-\pi^-$ (right) events, in both cases reconstructed as $B_d^0 \to D^-\pi^+$, $D^- \to K^+\pi^-\pi^-$. Fitted mass templates are overlaid.

5.3.5 Results

As the prompt component of the background is suppressed by the two-track trigger, we have no handle on the scale factor for the error on the B proper decay-length resolution, S_{ct}. We fix this scale factor to 1.07, which is the average of the scale factors found for the two J/ψ modes (see Table 5.3). This assumption will be propagated as a systematic error in the final measurements of this analysis, B_d^0 oscillation frequency Δm_d and Opposite Side Taggers dilution scale factors. Table 5.11 shows the results for the lifetime fits, and the fit projections are shown in Figs 5.9 and 5.10.

5.4 Summary

The signal yields and lifetimes are summarized in Table 5.12. We note that the fitted lifetimes are in good agreement with PDG values.

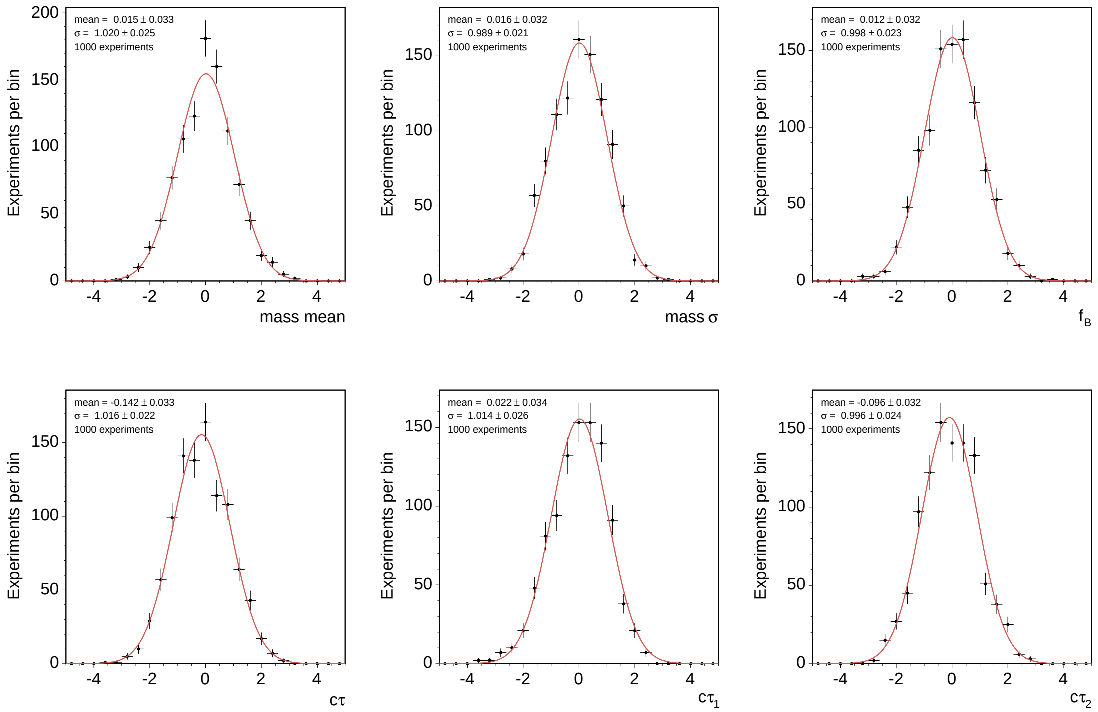

Figure 5.8: Pull distributions for $B_d^0 \to D^-\pi^+$ lifetime fits.

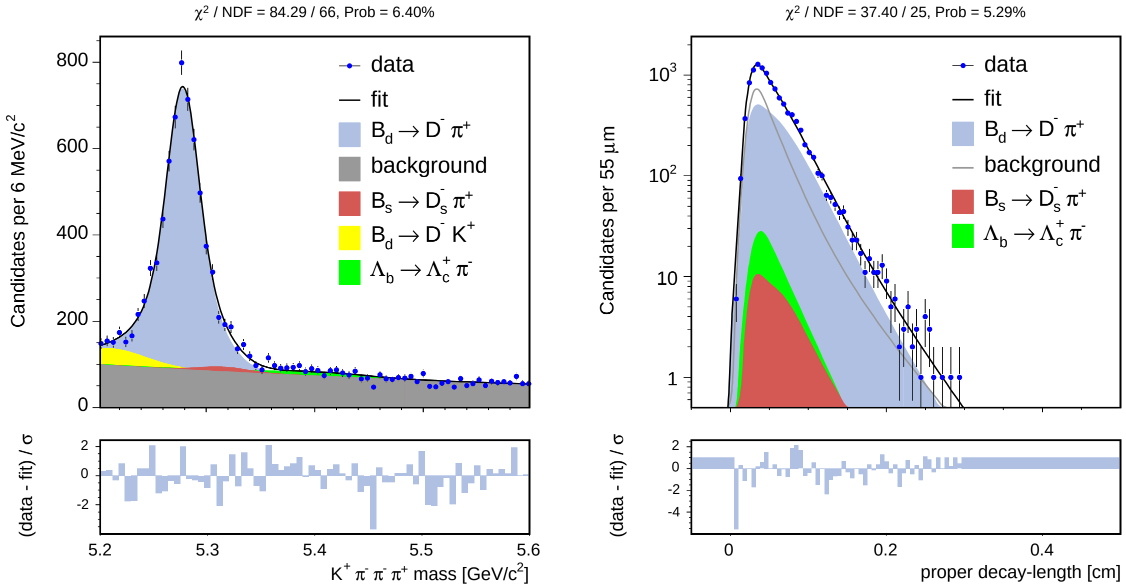

Figure 5.9: Mass and lifetime fit projections for $B_d^0 \to D^-\pi^+$ decay.

parameter		value
$\delta_{\Lambda_b^0}$	[μm]	0.028
$\sigma_{ct_{\Lambda_b^0}}$	[μm]	0.009
$\lambda_{\Lambda_b^0}$	[μm]	0.025
$\delta^{+}_{B_s^0}$	[μm]	0.024
$\sigma^{+}_{ct_{B_s^0}}$	[μm]	0.007
$\lambda^{+}_{B_s^0}$	[μm]	0.036
$f^{++}_{B_s^0}$		0.176
$\delta^{++}_{B_s^0}$	[μm]	0.053
$\sigma^{++}_{ct_{B_s^0}}$	[μm]	0.015
$\lambda^{++}_{B_s^0}$	[μm]	0.019

Table 5.9: B_s^0 and Λ_b^0 backgrounds ct parameter values from MC.

parameter		input	μ_{pull}	σ_{pull}	fit probability (%)
$\langle m \rangle$	[MeV/c^2]	5.279	0.015 ± 0.033	1.020 ± 0.025	53.7
$\sigma_{\langle m \rangle}$	[MeV/c^2]	0.015	0.016 ± 0.032	0.989 ± 0.021	26.0
f_B		0.36	0.012 ± 0.032	0.998 ± 0.023	69.0
$c\tau$	[μm]	454	-0.142 ± 0.033	1.016 ± 0.022	65.4
λ_1	[μm]	160	0.022 ± 0.034	1.014 ± 0.026	13.1
λ_2	[μm]	289	-0.096 ± 0.032	0.996 ± 0.024	4.9

Table 5.10: Gaussian fit results on $B_d^0 \to D^-\pi^+$ lifetime pull distributions.

parameter		$B_d^0 \to D^-\pi^+$	$B^+ \to \bar{D}^0\pi^+$
$\langle m \rangle$	[MeV/c^2]	5278.5 ± 0.4	5277.9 ± 0.3
$\sigma_{\langle m \rangle}$	[MeV/c^2]	13.4 ± 0.3	17.7 ± 0.3
f_B		0.464 ± 0.008	0.600 ± 0.006
$c\tau$	[μm]	457.4 ± 9.8	494.1 ± 10.9
f_2		0.171 ± 0.079	0.102 ± 0.045
λ_1	[μm]	204.6 ± 15.0	236.8 ± 10.9
λ_2	[μm]	462.4 ± 63.7	582.5 ± 80.8
μ	[μm]	250.7 ± 4.1	220.8 ± 2.8
σ_B	[μm]	69.7 ± 2.9	64.6 ± 2.0

Table 5.11: Mass and lifetime fit results for $D\pi$ modes.

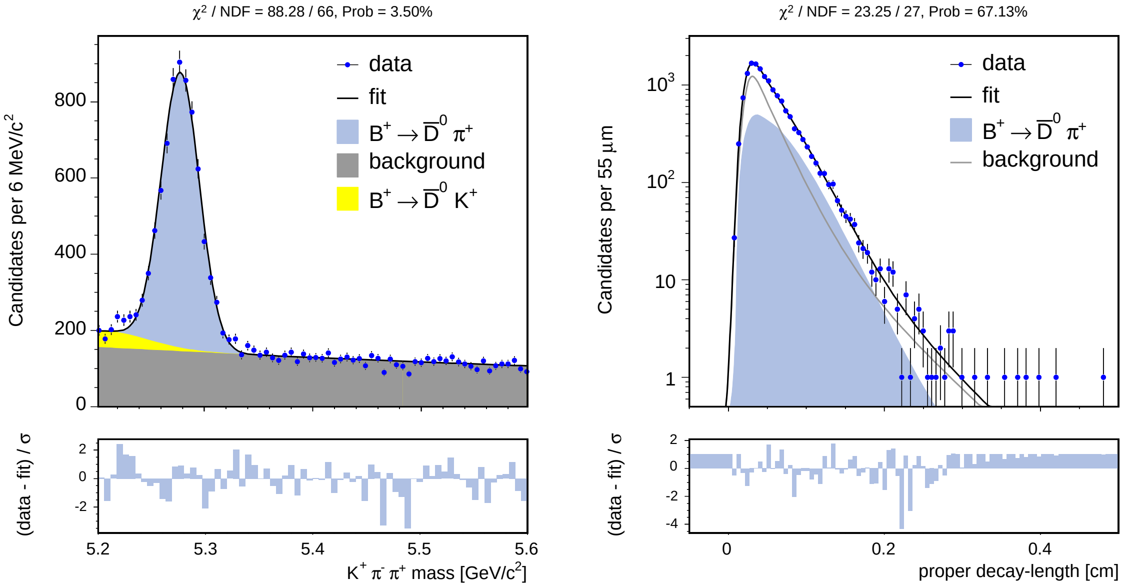

Figure 5.10: Mass and lifetime fit projections for $B^+ \to \bar{D}^0\pi^+$ decay.

mode	yield	$c\tau$ [μm]
$B^+ \to J/\psi K^+$	5323 ± 84	489.2 ± 7.6
$B^+ \to \bar{D}^0\pi^+$	5625 ± 105	494.1 ± 10.9
B^+ PDG	—	501 ± 5
$B_d^0 \to J/\psi K^{*0}$	2231 ± 53	458.5 ± 10.9
$B_d^0 \to D^-\pi^+$	6157 ± 123	457.4 ± 9.8
B^0 PDG	—	460.5 ± 4.2

Table 5.12: Summary of signal event yields and measured lifetimes.

Chapter 6

Flavor Taggers

At the Tevatron b quarks are mostly produced in pairs, i.e., a $b\bar{b}$ quark pair is produced in the hard interaction. The b quarks hadronize, producing b-hadrons, that will travel a finite distance before decaying on more stable particles. It can happen that one of the produced b-hadrons is a neutral B meson, B_d^0 or B_s^0. A neutral B meson will be produced as any other b-hadron in a definite b-flavor state, i.e, with the quantum numbers of a b or a $\bar{b}$ quark. The neutral B mesons will have a probability of mixing during the time it takes from the hadronization to the decay, therefore the b-flavor at decay time can be the same or a different one from the b-flavor they had when they were produced. Fortunately, there are decay signatures that allow us to identify the b-flavor at decay time, e.g., if we reconstruct a $B_d^0(\bar{b}d) \rightarrow D^-(\bar{c}d)\pi^+$ decay, based on the decay sequence $\bar{b} \rightarrow \bar{c}$, we know it is a B_d^0 and not a $\bar{B}_d^0$. In this case the charm meson (D^-), or equivalently the pion charge, has told us the flavor of the neutral B meson candidate when it decayed. In general, the decay b-flavor is obtained from the charge of the daughter particles, as summarized in Table 6.1 for the four analyzed modes:

reconstructed decay	decay b-flavor		reconstructed decay
$J/\psi K^+$	$K^+ \Rightarrow \bar{b}$	$b \Leftarrow K^-$	$J/\psi K^-$
$\bar{D}^0\pi^+$	$\pi^+ \Rightarrow \bar{b}$	$b \Leftarrow \pi^-$	$D^0\pi^-$
$J/\psi K^{*0},\ K^{*0} \rightarrow K^+\pi^-$	$K^+ \Rightarrow \bar{b}$	$b \Leftarrow K^-$	$J/\psi \bar{K}^{*0},\ \bar{K}^{*0} \rightarrow K^-\pi^+$
$D^-\pi^+$	$\pi^+ \Rightarrow \bar{b}$	$b \Leftarrow \pi^-$	$D^+\pi^-$

Table 6.1: Decay b-flavor.

To know if a neutral B meson has mixed we should compare the decay b-flavor with the production b-flavor. The problem arises when aiming for the determination of the production b-flavor. For that purpose we use *flavor taggers*. If a flavor tagger relies on the characteristics of the B meson of interest, or the neighboring particles, it is a *same side tagger*. On the contrary, any flavor tagger that bases its decision on the properties of the other b-hadron of the event, is referred to as *opposite side tagger*. In general, we say that the B meson of interest is located in the *trigger side*, because it is expected that some of its daughter tracks fired the trigger; for completeness, the other b-hadron is located in the *opposite side*. A cartoon of an event accepted by the *lepton+displaced track* trigger is shown in Fig. 6.1. In that figure we can distinguish the trigger side, the opposite side, and the opposite side taggers described later on in this chapter.

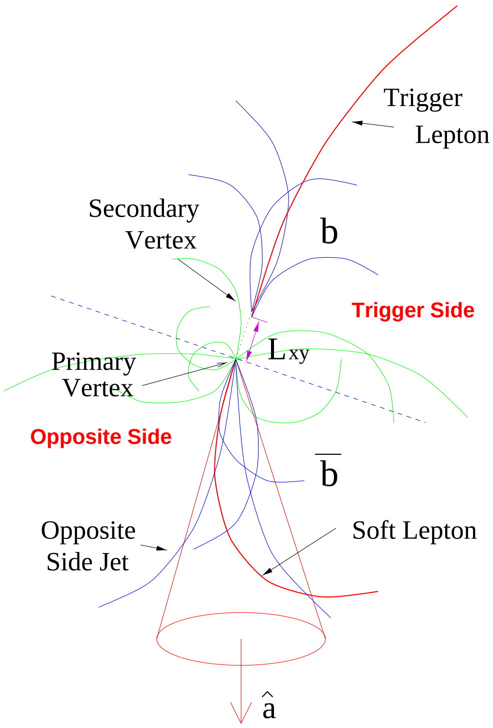

Figure 6.1: Illustration of a $b\bar{b}$ event accepted by the lepton+displaced track trigger. The *trigger lepton* defines the trigger side, and therefore the opposite side.

Tagging Definitions

A flavor tagger is a tool used to determine if the production and the decay b-flavors of a B meson candidate agree or differ. It can be applied on charged B mesons, were a perfect tagger would always say that both production and decay b-flavors are the same. A (flavor) tagger provides one of the following decisions:

Right-Sign	(RS)	production b-flavor $=$ decay b-flavor
Wrong-Sign	(WS)	production b-flavor $\neq$ decay b-flavor
Non-Tagged	(NT)	failed providing a decision

The efficiency ϵ of a tagger is a measurement of the number of B meson candidates we have tagged over the total number of events,

$$\begin{aligned} \epsilon &= \frac{N_{RS} + N_{WS}}{N}\,, \\ N &= N_{RS} + N_{WS} + N_{NT}\,, \end{aligned} \tag{6.1}$$

where N_{RS}, N_{WS} and N_{NT} refer to the number of Right-Sign events, Wrong-Sign events and Non-Tagged events, respectively. The total number of events is N. The dilution $\mathcal{D}$ of a tagger is a measurement of its quality. If we call $\mathcal{P}$ the probability of a tagger to provide the correct decision, then the dilution is defined as

$$\mathcal{D} \equiv 2\mathcal{P} - 1 = \frac{N_{RS} - N_{WS}}{N_{RS} + N_{WS}}\,. \tag{6.2}$$

A perfect flavor tagger would have the maximal dilution $\mathcal{D} = 1$ ($\mathcal{P} = 1$), whereas a completely random tagger would provide the worst dilution $\mathcal{D} = 0$ ($\mathcal{P} = 0.5$).

Finally, the quality of a tagger is given by the *tagging effectiveness* $\epsilon\mathcal{D}^2$. This factor fixes the effective size of a sample of N events used in mixing and CP asymmetries, whose statistical error is proportional to $\sqrt{\epsilon\mathcal{D}^2 N}$.

Tagging Strategy

The dilution of the opposite side taggers is calibrated in a rich inclusive B meson sample, collected by the lepton+displaced track trigger, later on described in this chapter. Thanks to the large size of this sample, we can parameterize the dilution as a function of the relevant characteristics of the event, with reasonable accuracy.

The opposite side taggers are intended to be applied on $B_s^0 \to D_s^- \pi^+$ and $B_s^0 \to D_s^- l^+ \nu_l$ decays. Before applying the taggers on these samples, the dilutions need to be normalized in samples of similar characteristics. That is the goal of this thesis: the absolute calibration of the dilution of the opposite side taggers, for their application on the $B_s^0 \to D_s^- \pi^+$ sample.

At the time of this thesis, the same side tagger was not yet used in the B_s^0 mixing analysis. It is currently a work in progress at CDF, and we plan to include it soon in the measurement, expecting to increase by a factor ×2 the effective size of the B_s^0 samples.

6.1 Opposite Side Taggers

The principle of flavor tagging on the opposite side is quite simple. If the trigger side B meson candidate was produced with a b quark, we know that the opposite side b-hadron was produced with a $\bar{b}$ quark. Assuming the opposite side b-hadron did not oscillate, measuring its decay b-flavor would be the same as measuring its production b-flavor, and such should be the contrary of the same side B meson candidate production b-flavor. Three different opposite side taggers have been developed at CDF and used in this thesis: Soft Muon Tagger, Soft Electron Tagger and Jet Charge Tagger.

Lepton+Displaced Track Trigger Sample

High statistics samples of semileptonic B decays collected with the *lepton+displaced track* trigger path have been used to study and optimize the opposite side flavor taggers. The charge of the trigger lepton in the lepton+displaced track sample provides an estimate of the b-flavor at the time of decay on the trigger side. However, the lepton+displaced track data is not a pure sample of B decays. In addition to signal events, it also contains semileptonic charm decays, hadrons that fake the trigger lepton, and other backgrounds. We briefly list here the trigger and selection cuts required on the lepton+displaced track sample,

1. Trigger selection
    - for the lepton, $p_T^{XFT} > 4$ GeV/c;
    - for the displaced track, $p_T^{SVT} > 2$ GeV/c;
    - for the displaced track, 120 μm $< d_0^{SVT} < 1$ mm.
2. Lepton+displaced track selection
    - $2 < M_{\text{lepton,displaced track}} < 4$ GeV/c^2;
    - $|\Delta z_0| < 2.5$ cm;
    - $|\Delta \cot\theta| < 0.05$.

The remaining background events are removed under the assumption that they are symmetric in the signed impact parameter of the displaced track, which is defined as:

$$\delta_0^{SVT} \equiv |d_0|\, sign(\vec{d_0} \cdot \vec{p}_{\text{lepton,displaced track}})\,, \tag{6.3}$$

where $\vec{d_0}$ is the direction from the primary vertex to the point of closest approach of the displaced track, and $\vec{p}_{\text{lepton,displaced track}}$ is the direction of the combined momentum of the trigger lepton and the displaced track. To obtain any pure distribution of signal events, the distribution with negative δ_0^{SVT} has to be subtracted from the corresponding distribution with positive signed impact parameter, as described in [41]. The reconstructed invariant mass spectrum of the muon+displaced track (electron+displaced track) sample, after trigger and selection cuts, is shown in Fig. 6.2 left (right).

Trigger Side Dilution Correction

The B meson on the trigger side may have mixed at the time it decayed, or the trigger lepton could have been produced in a sequential $b \to c\ell_1^- \bar{\nu}_{\ell_1} X$, $c \to \ell_2^+ \nu_{\ell_2} Y$ transition; due to these processes, the true dilution $\mathcal{D}$ of the opposite side tagger will be greater than the measured raw dilution $\mathcal{D}_{raw}$. The probability of a tagger to provide the correct decision has been named $\mathcal{P}$. Let us call $\mathcal{P}_{raw}$ the probability of a tagger to provide the correct

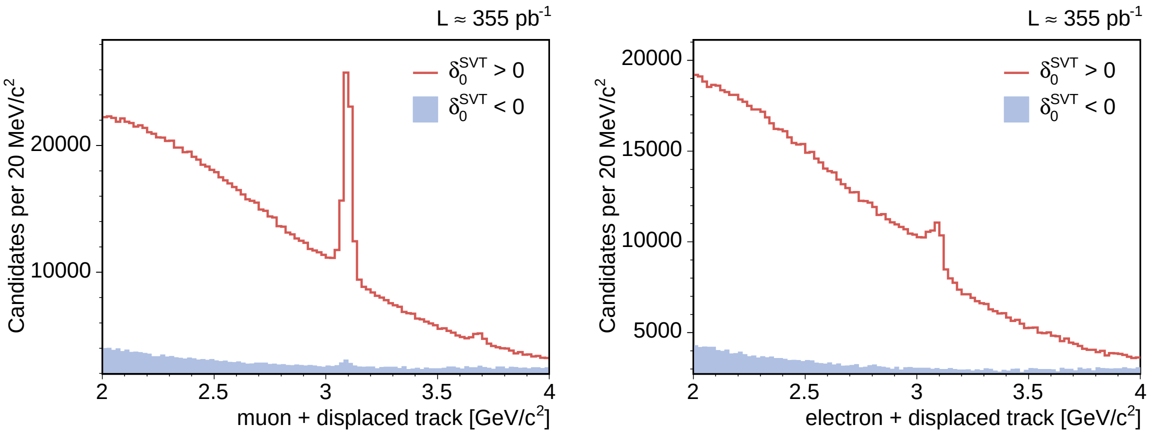

Figure 6.2: Reconstructed invariant mass of the lepton and the displaced track, for the muon (left) and the electron (right) samples. The component relative to $\delta_0^{SVT} < 0$ (blue histogram) has to be subtracted from the $\delta_0^{SVT} > 0$ component (red line). The mass peaks at ~ 3.1 GeV/c^2 correspond to $J/\psi \to \mu^+\mu^-$ (left) and $J/\psi \to e^+e^-$ (right) decays.

b-flavor in the opposite side, and $1 - \mathcal{P}_{trig}$ the probability of the B meson on the trigger side to have mixed, or the trigger lepton produced in a sequential transition. Then

$$\mathcal{P}_{raw} \;=\; \mathcal{P}\,\mathcal{P}_{trig} + (1-\mathcal{P})(1-\mathcal{P}_{trig})\,. \tag{6.4}$$

In (6.4) we can replace the probabilities by their corresponding dilutions,

$$\begin{aligned}\mathcal{D} &\equiv 2\mathcal{P} - 1\,,\\ \mathcal{D}_{raw} &\equiv 2\mathcal{P}_{raw} - 1\,,\\ \mathcal{D}_{trig} &\equiv 2\mathcal{P}_{trig} - 1\,,\end{aligned}$$

obtaining $\mathcal{D} = \mathcal{D}_{raw}/\mathcal{D}_{trig} > \mathcal{D}_{raw}$. The dilution on the trigger side $\mathcal{D}_{trig}$ due to mixing and sequential decays has been estimated using Monte Carlo simulation in [41]. The result is

$$\mathcal{D}_{trig} \;=\; \begin{cases} 0.6412 \pm 0.0015\ (stat.)\ {}^{+0.014}_{-0.023}\ (syst.) & \mu\text{-}track \text{ sample} \\ \\ 0.6412 \pm 0.0015\ (stat.)\ {}^{+0.022}_{-0.037}\ (syst.) & e\text{-}track \text{ sample} \end{cases}$$

6.1.1 Soft Muon Tagger

This method [42] looks for a muon from semileptonic decays of the opposite side b-hadron. The charge of this muon is correlated with the b-flavor at decay time of the b-hadron: a μ^- comes from a $b \to c\,\mu^-\bar{\nu}_\mu X$ transition, while a μ^+ originates from a $\bar{b}$ quark. Track-stub muon matching quantities Δx, $\Delta\phi$ and Δz, along with energy depositions in the electromagnetic (EM) and hadronic (HAD) calorimeters, are the discriminating variables employed in a muon identification likelihood. A brief description of these variables follows:

> **Track-stub matching variables.** Muon candidates are defined as a muon stub matched to a track measured by the COT. The spacial separation between the muon stub and the COT track is characterized by three variables, ΔX, $\Delta\Phi$ and ΔZ. These variables depend on the transverse momentum of the muon, and we use instead the p_T independent scaled variables $\Delta x = \Delta X/\sigma_{\Delta X}$, $\Delta\phi = \Delta\Phi/\sigma_{\Delta\Phi}$ and $\Delta z = \Delta Z/\sigma_{\Delta Z}$.
>
> **Calorimetry variables.** The energy deposited by a muon candidate in the electromagnetic (hadronic) calorimeter is referred to as EM (HAD). The isolation I of a track j is defined as the ratio between the p_T^j of the track, and the sum of the transverse momenta of all tracks in a cone $\Delta R < 0.4$ around the track j,
>
> $$I = \frac{p_T^j}{\sum_i p_T^i}, \qquad \Delta R(i,j) = \sqrt{\Delta\eta^2 + \Delta\phi^2} < 0.4\,. \tag{6.5}$$
>
> It has been found that CMU muons from J/ψ have different EM distributions depending on their isolation. Two different EM templates for isolated muons ($I > 0.5$) and non-isolated muons ($I < 0.5$) are used in the final likelihood. The dependence of the HAD distribution on the isolation is very small and thus it is neglected. On the other hand, the EM barely depends on p_T, whereas HAD is parameterized in three different ranges of p_T.

To study the behavior of the discriminating variables for real and fake muons, the data samples summarized in Table 6.2 were used.

sample	particle
$J/\psi \to \mu^+\mu^-$	real muons
$K_s^0 \to \pi^+\pi^-$	pions faking muons
$\bar{D}^0 \to K^+\pi^-$	kaons faking muons
$\Lambda^0 \to p^+\pi^-$	protons faking muons

Table 6.2: Data samples studied for the muon identification likelihood.

With these samples the discriminating variables distributions of both real and fake muons are parameterized as PDFs. The likelihood that a muon object is a real ($\mathcal{S}^\mu$) or fake ($\mathcal{B}^\mu$) muon can be written as

$$\begin{aligned}\mathcal{S}^\mu &= S_{\Delta x}\, S_{\Delta\phi}\, S_{\Delta z}\, S_{em}\, S_{had}\,,\\ \mathcal{B}^\mu &= B_{\Delta x}\, B_{\Delta\phi}\, B_{\Delta z}\, B_{em}\, B_{had}\,,\\ \\ \mathcal{L}^\mu &= \frac{\mathcal{S}^\mu}{\mathcal{S}^\mu + \mathcal{B}^\mu}\,,\end{aligned}$$

where $\mathcal{L}^\mu$ is the muon identification likelihood. We expect that muon objects with values of $\mathcal{L}^\mu$ close to unity are real muons while likelihood values close to zero indicate most probably fake muons. The total tagging power, averaged over the *electron-track* and *muon-track* samples is

$$\epsilon\mathcal{D}^2_{raw} = (0.698 \pm 0.042\ (stat.)\ {}^{+0.051}_{-0.027}\ (syst.))\ \%\,.$$

The dilution $\mathcal{D}_{raw}$ is parameterized as a function of the muon likelihood $\mathcal{L}^\mu$, as it can be seen in Fig. 6.3.

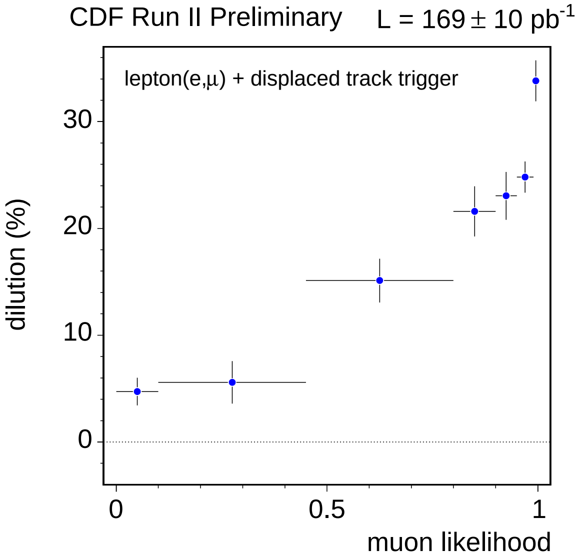

Figure 6.3: Dilution $\mathcal{D}_{raw}$ as a function of the muon likelihood $\mathcal{L}^\mu$, for all muon types (CMU, CMP, CMUP, CMX and BMU).

Let us define p_T^{rel} (different from the SST version in Fig. 6.7) as the transverse momentum of the soft muon with respect to the axis of the jet to which the soft muon belongs. It happens that the dilution depends strongly on this variable, with the following empirical dependence,

$$D(p_T^{rel}) = A_\mu\left(1 - e^{-p_T^{rel}+\delta_\mu}\right), \qquad (6.6)$$

where A_μ and δ_μ are parameters to be fixed in different conditions. For an accurate event-by-event dilution determination, the dilution that is used in the fits of this thesis is parameterized as a function of p_T^{rel}, for different bins of the muon likelihood, and for five different muon types (CMU, CMP, CMUP, CMX and BMU).

6.1.2 Soft Electron Tagger

This method [43] looks for an electron from semileptonic decays of the opposite side b-hadron. The charge of this electron is correlated with the b-flavor at decay time of the b-hadron: an e^- comes from a $b \to c\, e^- \bar{\nu}_e X$ transition, while an e^+ originates from a $\bar{b}$ quark. Electron identification quantities from the calorimeter, Central PReshower (CPR), Central Electromagnetic Strip (CES) and dE/dx are combined into a global likelihood to discriminate real from fake electrons. Here we briefly describe these variables:

HAD/EM. It is the ratio of 2-tower hadronic energy deposited in the hadronic calorimeter (CHA and WHA) to the 2-tower electromagnetic energy deposited in the central electromagnetic calorimeter (CEM). The local isolation I of a track j is defined in a $\Delta R < 0.7$ cone around the track, and all tracks in this cone are extrapolated to the 2-tower cluster formed by the track j. Then, the local isolation I is defined as the ratio between the sum of the transverse momenta of all tracks in the mentioned cone which extrapolate to the 2-tower cluster, to the transverse momentum of the track j,

$$I = \frac{\sum_i p_T^i}{p_T^j}\,, \qquad \Delta R(i,j) = \sqrt{\Delta\eta^2 + \Delta\phi^2} < 0.7\,.$$

Locally isolated candidates ($I = 1$) are required to pass HAD/EM < 0.125, and locally non-isolated candidates ($I > 1$) are required to pass HAD/EM < 0.5.

EM/p. It is the ratio of 2-tower electromagnetic energy deposited in the CEM, to the track momentum. For locally isolated electrons, the EM/p is a very strong discriminator against pions. For locally non-isolated electrons, the EM/p distribution is much broader and therefore much less discriminating.

CES χ^2_x and CES χ^2_z. The Central Electromagnetic Strip (CES) is a shower maximum detector used for $e^\pm/\gamma$ identification. CES χ^2_x (χ^2_z) is a χ^2 comparison of the shower profile in the CES wire (strip) view with the same profile extracted from a test beam of electrons.

CES $q\Delta x$. CES ΔX is the distance in the transverse plane between the track extrapolated to the CES radius, and the actual cluster position measured in the CES; the charge of the track is q. We use $q\Delta x = q\Delta X/\sigma_{\Delta X}$ as discriminating variable in two separate distributions: one for locally isolated candidates, and one for locally non-isolated candidates.

CES Δz . CES ΔZ is the distance in the r-Z plane between the track extrapolated to the CES radius, and the actual cluster position measured in the CES. The discriminating power of $\Delta z = \Delta Z/\sigma_{\Delta Z}$ is very good, and increases with p_T, like $q\Delta x$.

E_{CES}/p^* . It is the wire cluster pulse height measured in the CES, corrected for chamber warps and scaled by $p^* \equiv 10\,(p/10)^{\alpha(p)}$, where p is the track momentum, and $\alpha(p)$ is given by

$$\alpha(p) \equiv 0.85 - \frac{p}{1000} + 0.15\, e^{-\frac{p}{15.0}} \,. \tag{6.7}$$

The variable E_{CES}/p^* provides very good separation between electrons and pions even at low p_T.

Corrected Q_{CPR} . The Central PReshower (CPR) is a set of multiwire proportional chambers in front of the CEM, used as well for $e^{\pm}/\gamma$ identification. Q_{CPR} is the pulse height in the CPR, corrected for its $\sin\theta$ dependence.

dE/dx . It is the energy loss measured in the COT. Its separation power gets larger with decreasing momentum, unlike calorimeters, CES and CPR based variables.

The samples summarized in Table 6.3 have been used to study the distributions of the discriminating variables.

sample	particle
$\gamma \to e^+e^-$	real electrons
$K^0_s \to \pi^+\pi^-$	pions faking electrons

Table 6.3: Data samples studied for the electron identification likelihood.

With these samples of real and fake electrons, the distributions of discriminating variables for real and fake electrons are parameterized as PDFs. The likelihood that an electron object is a real ($\mathcal{S}^e$) or fake ($\mathcal{B}^e$) electron can be written as

$$\begin{aligned}
\mathcal{S}^e &= S_{em/p}\, S_{had/em}\, S_{\chi^2_x}\, S_{\chi^2_z}\, S_{q\Delta x/\sigma_x}\, S_{\Delta z/\sigma_z}\, S_{ces/p^*}\, S_{cpr}\, S_{dE/dx} \,, \\
\mathcal{B}^e &= B_{em/p}\, B_{had/em}\, B_{\chi^2_x}\, B_{\chi^2_z}\, B_{q\Delta x/\sigma_x}\, B_{\Delta z/\sigma_z}\, B_{ces/p^*}\, B_{cpr}\, B_{dE/dx} \,, \\
\mathcal{L}^e &= \frac{\mathcal{S}^e}{\mathcal{S}^e + \mathcal{B}^e} \,,
\end{aligned}$$

where $\mathcal{L}^e$ is the electron identification likelihood. As in the muon likelihood, we expect that electron objects with values of $\mathcal{L}^e$ close to unity are real electrons while likelihood values close to zero indicate most probably fake electrons. The total tagging power, averaged over the *electron-track* and *muon-track* samples is

$$\epsilon\mathcal{D}^2_{raw} = (0.366 \pm 0.031\ (stat.)\ ^{+0.065}_{-0.056}\ (syst.))\ \% \,.$$

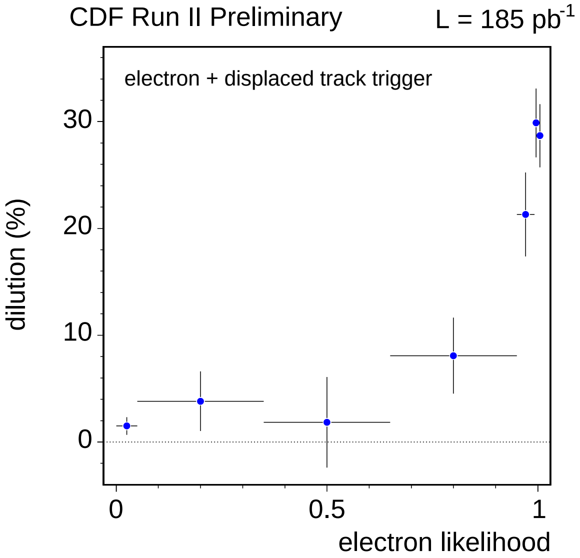

Figure 6.4: Dilution $\mathcal{D}_{raw}$ as a function of the electron likelihood $\mathcal{L}^e$.

The dilution $\mathcal{D}_{raw}$ is parameterized as a function of the electron likelihood $\mathcal{L}^e$, as it can be seen in Fig. 6.4.

The definition of p_T^{rel} given at the end of the soft muon tagger section does not change for the soft electron tagger: it is the transverse momentum of the soft electron with respect to the axis of the jet to which the soft electron belongs. The same can be said about the parameterization of the dilution,

$$D(p_T^{rel}) = A_e \left(1 - e^{-p_T^{rel}+\delta_e}\right), \tag{6.8}$$

where A_e and δ_e will be fitted to different values from the soft muon tagger case. For an accurate event-by-event dilution determination, the dilution that is used in the fits of this thesis is parameterized as a function of p_T^{rel}, for the different bins of the electron likelihood.

6.1.3 Jet Charge Tagger

This method [44] is based on the empirical observation that the sum of all particle charges in a jet containing a B meson is correlated with the b quark charge, and thus with its flavor. An appropriately weighed sum gives a better result. The chosen definition of jet charge Q_{jet} is given by

$$Q_{jet} \equiv \frac{\sum_{i=1}^{N} q^i p_T^i \left(2 - T_P^i\right)}{\sum_{i=1}^{N} p_T^i \left(2 - T_P^i\right)},$$

where the index i refers to the tracks in a jet that contains N tracks. The charge of each track is q^i and p_T^i is the transverse momentum. The variable T_P^i is a Track Probability that indicates how likely a track comes from a secondary vertex. It is based on the measured impact parameter of the track and the expected impact parameter shape for this type of track. The Jet Charge Tagger (JQT) uses a cone clustering algorithm to find track-based jets, with a maximum cone size of $\Delta R = 1.5$. As the first step of the algorithm, all jets in the opposite side are found. Next, the tagging jet is selected out of all available jets. There are three mutually exclusive groups of events:

1. Jets that contain a secondary vertex are looked for. These jets provide the highest dilution, and we refer to them as *SecVtx* jets.

2. If no SecVtx jet is found, the jet with the highest probability to contain displaced tracks is looked for. The Jet Probability J_P, defined in Equation 6.9, is required to satisfy $J_P < 0.12$. These are the J_P jets.

$$J_P = P_N \sum_{j=0}^{N-1} \frac{\left(-\ln P_N\right)^j}{j!}, \tag{6.9}$$
$$P_N = \prod_{i=1}^{N} T_P^i .$$

3. If an event has neither SecVtx jets nor J_P jets, the highest P_T jet among the available jets in the event is chosen. It is called the *high* P_T jet.

The total tagging power is quoted only for the *electron-track* sample because the JQT algorithm was tuned in the *muon-track* sample. Events have been separated into the three subsamples described above, and into 11 bins of Q_{jet},

$$\epsilon\mathcal{D}^2 = (0.715 \pm 0.027\ (stat.))\ \%,$$

where the value of $\epsilon\mathcal{D}^2$ has been corrected for the trigger side mixing and sequential decays. For a more complete picture we summarize in Table 6.4 the tagging power associated with the three different subsamples.

The dilution $\mathcal{D}$ is parameterized as a function of Q_{jet} in the three different JQT subsamples. The generally higher dilution for jets with a secondary vertex can be seen in Fig. 6.5.

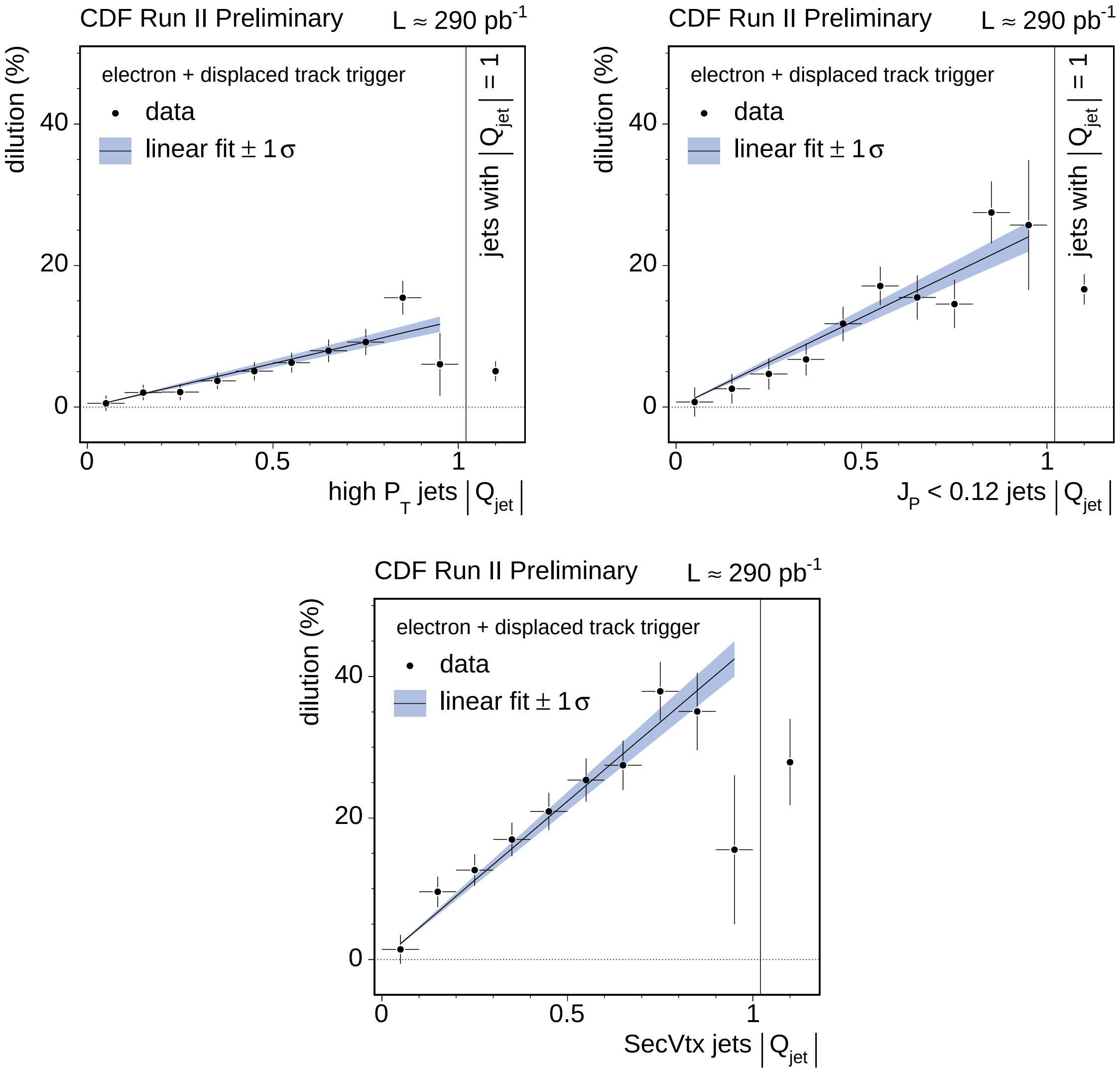

Figure 6.5: Dilution $\mathcal{D}$ as a function of Q_{jet}.

jet type	ϵ (%)	$\mathcal{D}$ (%)	$\epsilon\mathcal{D}^2$ (%)
SecVtx jets	10.9 ± 0.1	18.2 ± 0.5	0.361 ± 0.018
$J_P < 0.12$ jets	15.2 ± 0.1	11.6 ± 0.5	0.206 ± 0.017
high P_T jets	56.3 ± 0.2	5.1 ± 0.2	0.149 ± 0.011
combined	82.3 ± 0.2	9.3[a] ± 0.2	0.715 ± 0.027

---

[a] The effective dilution of the combination of the three JQT types is given by $\mathcal{D}_{eff} = \sqrt{\sum_i \epsilon_i \mathcal{D}_i^2 / \sum_i \epsilon_i}$, with i a jet type.

Table 6.4: Efficiency ϵ, dilution $\mathcal{D}$ and $\epsilon\mathcal{D}^2$, for the three different JQT subsamples.

6.2 Same Side Taggers

Flavor tagging on the same side is different from the previous flavor taggers, in the sense that the tagging performance depends, obviously, on the B meson species reconstructed in the trigger side; therefore, a parameterization of the dilution using the lepton+displaced track sample is meaningless in the sense of same side tagging.

The idea of flavor tagging on the same side can be found in [39]. This method exploits the flavor charge correlations between the B meson and associated particles produced in the hadronization process. The situation is illustrated in Fig. 6.6, which shows that e.g. the *leading* particle in the B^+ fragmentation is often a negatively charged pion.

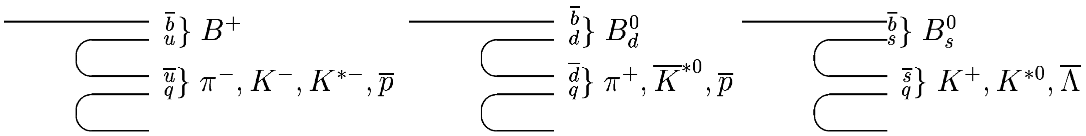

Figure 6.6: Charge correlation of B mesons with fragmentation tracks.

One can think of the hadronization process as pulling light quark pairs from the vacuum and forming hadrons from nearby quarks. In order to form a $B_d^0 = \bar{b}d$ meson, the light quark pair which is nearest in the fragmentation chain to the initial heavy quark $\bar{b}$ must have been a $d\bar{d}$ pair. This leaves a $\bar{d}$ quark at the dangling end of the fragmentation chain. If the second nearest light quark pair is $u\bar{u}$, then the nearest meson in the fragmentation chain will be a π^+, which can be used to tag the flavor of the initial $\bar{b}$. If the second nearest light quark pair is a $d\bar{d}$ pair, then the nearest meson is a π^0, a neutral particle that therefore has no tagging power. However, the dangling end of the fragmentation chain remains a $\bar{d}$. If the third nearest light quark pair is a $u\bar{u}$ pair, then the second nearest meson will be a π^+, which can be used as a flavor tag.

Excited B meson states contribute to flavor tagging in the B_d^0 case, with the emission of charged pions, e.g., $B^{*+} \to B_d^0\pi^+$; in this example, the π^+ from the B^{*+} indicates the $\bar{b}$ content of the B_d^0 when it was produced. A detailed Monte Carlo simulation study is in progress at CDF, to understand the contribution of excited states in the B_d^0 tagging.

The bottom line is that the nearest charged pion tags the birth flavor of the B_d^0 meson.

In Run I, an algorithm to find the nearest charged pion was successfully developed [40], applying it on inclusive B meson decays. We have used such method with fully reconstructed decays, and we briefly describe here the Run II version:

- The track candidate must lie in a cone $\Delta R = \sqrt{\Delta\eta^2 + \Delta\phi^2} < 0.7$ with respect to the momentum vector of the B meson - see Fig. 6.7;
- Transverse momentum $p_T > 450$ MeV;
- The track candidate should originate from the primary vertex, and so the ratio of the impact parameter to its uncertainty is required to be less than 10;
- $|\Delta z_0(track, B)| < 2$ cm;
- In case of multiple tag candidates, the selected track is that with the smallest p_T^{rel} as defined in Fig. 6.7. String fragmentation models indicate that particles produced in the b quark hadronization chain have a small momenta transverse to the direction of the b quark momentum.

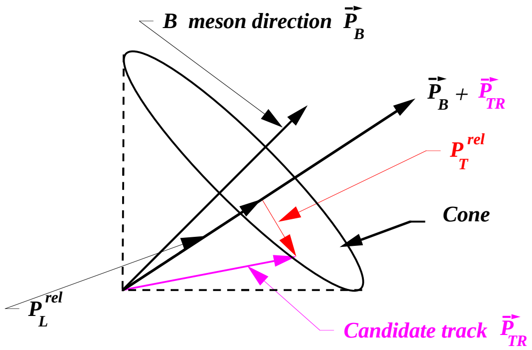

Figure 6.7: Illustration of the construction of the quantity p_T^{rel}.

The SST algorithm has been applied on the four decay modes analyzed in this thesis. We used an unbinned maximum likelihood method to determine the efficiencies and average dilutions of the SST on each sample, for signal and background candidates. With a likelihood expression that closely follows the forthcoming ones in chapter 7, we obtain the results summarized in Table 6.5.

The same fragmentation chain argument is used to show that the nearest charged kaon in the fragmentation chain can be used to tag the flavor of B_s^0 mesons. If the nearest kaon is a K^+ (K^-), then the meson is a B_s^0 ($\bar{B}_s^0$). However, if the nearest kaon is neutral, then there is no kaon tagging power, because the nearest charged neighbor will be a pion. However, excited B meson states that decay to B_s^0 do not emit any charged particle.

Currently, there is an ongoing effort at CDF dedicated to studying the same side kaon tagging: particle identification is necessary to distinguish kaons from pions. At

parameter	$B^+ \to J/\psi K^+$	$B_d^0 \to J/\psi K^{*0}$	$B^+ \to \bar{D}^0\pi^+$	$B_d^0 \to D^-\pi^+$
ϵ (%)	66.2 ± 0.7	63.4 ± 1.1	62.9 ± 0.8	63.4 ± 0.8
ϵ_B (%)	76.1 ± 0.2	86.7 ± 0.3	82.7 ± 0.7	86.0 ± 1.0
$\mathcal{D}$ (%)	19.1 ± 1.8	17.4 ± 4.7	17.0 ± 2.2	16.0 ± 3.8
$\mathcal{D}_B$ (%)	7.5 ± 0.5	-2.0 ± 0.8	10.4 ± 2.0	0.8 ± 2.9

Table 6.5: SST results (errors are statistical only).

CDF, pions, kaons and protons are roughly produced in the ratio 0.8:0.1:0.1; it is thus important to separate kaons from the large background of pions. With this goal, the CDF II Detector has been upgraded for the Run II data taking period with a Time of Flight Detector[1] (TOF). Particle identification at CDF is done with a combination of the TOF information, and the energy loss measured in the COT (dE/dx).

---

[1] Described in Sec. 3.5.

Chapter 7

Absolute Dilution Calibration

When a time dependent mixing measurement is carried out in a *direct* way, i.e., by fitting the mixing asymmetry versus the proper decay-length, the average dilution is also fitted, appearing as a factor dumping the oscillation. A second approach in the determination of the mixing frequency is the so-called *amplitude analysis*; this is a more suitable method for establishing exclusion limits in the oscillation frequency space, whenever the frequency sensitivity is not large enough for a direct measurement, as it has been so far for the case of determining Δm_s. A distinctive feature of the amplitude analysis is that the dilution is no longer an outcome of the fit; on the contrary, the dilution now becomes a measured quantity, i.e., it is part of the input data for the fit, like the mass or the proper decay-length.

In chapter 6 we have seen how the dilutions for the different opposite side taggers were calibrated in a rich inclusive B mesons sample. The calibration of flavor taggers in such a large sample determined a parameterization of the dilution as a function of different properties of the event: topology, energy deposited in the calorimeters, type of jets in the event, etc. Since the taggers calibration sample has, at least, different kinematics with respect to the signal sample $B_s^0 \to D_s^- \pi^+$, it is expected that the absolute scale of the tagger dilution would be different between the previous two samples. To determine the absolute scale for the opposite side taggers we have used the fully reconstructed samples $B^+ \to J/\psi K^+$, $B_d^0 \to J/\psi K^{*0}$, $B^+ \to \bar{D}^0 \pi^+$ and $B_d^0 \to D^- \pi^+$, whose kinematics is more similar to the signal; the absolute scale is quantified with the introduction of a dilution scale factor S_D for each tagger. The goal is therefore clear: the measurement of the dilution scale factors for those taggers that will be used in the B_s^0 sample. To improve the precision in the scale factors measurement, the following actions have been taken:

1. Use event-by-event dilutions. The availability of a dilution D for each B meson candidate, for a given tagger, is necessary to properly determine the dilution PDFs that enter the likelihood. The alternative would be the use of an average dilution $\mathcal{D}$, equal for every event; in this case we would not use the maximal available information.

2. Exclusive combination of the opposite side taggers. If a B meson candidate has

several tags of its b-flavor at the time it was produced, the decision given by the tagger with highest average dilution is chosen.

3. Fit our samples simultaneously. The decay modes studied in this thesis are all of them fully reconstructed B_d^0 and B^+ decays. The kinematic similitudes among the four of them allows us to combine them in a single fit for the determination of the dilution scale factors. Larger number of B meson candidates entering the fit increases the precision and makes the fit more stable.

7.1 Event-by-Event Dilution Likelihood

As we did for the lifetime measurements, we keep using the unbinned maximum likelihood fitting method to determine the dilution scale factors. In this case, in addition of the previous variables that defined a B meson candidate for a lifetime fit, i.e., reconstructed invariant mass m, proper decay-length ct and proper decay-length resolution σ_{ct}, two new variables need to be introduced:

tag – tagger decision. It is a discrete variable that can be

- $tag = +1$ for Right-Sign events, when the tagged b-flavor at the time the B meson was produced coincides with the b-flavor at the time of decay.
- $tag = -1$ for Wrong-Sign events, when the tagged b-flavor at the time the B meson was produced differs from the b-flavor at the time of decay.
- $tag = 0$ for Non-Tagged events, when the tagger failed providing a decision.

D – flavor tagging dilution for each event.

A generic expression for the new likelihood is defined as

$$\begin{aligned} \mathcal{L}(\vec{x}) &= \prod_i P_i(\vec{x})\,, \\ P_i(\vec{x}) &= (1-f_B)\, L_M^S(m_i) L_{ct}^S(ct_i, \sigma_{ct_i}, tag_i, D_i) L_D^S(D_i) \\ &\quad + \; f_B\, L_M^B(m_i) L_{ct}^B(ct_i, \sigma_{ct_i}, tag_i, D_i) L_D^B(D_i)\,, \end{aligned}$$

where $\vec{x} \equiv (m_i, ct_i, \sigma_{ct_i}, tag_i, D_i)$, and the index i runs over the B meson candidates sample. L_D is the PDF component in the new subspace, dilution. The mass PDF components L_M^S and L_M^B remain unchanged from the lifetime version. On the contrary, the proper decay-length PDF components $L_{ct}^S(ct_i, \sigma_{ct_i}, tag_i, D_i)$ and $L_{ct}^B(ct_i, \sigma_{ct_i}, tag_i, D_i)$ now depend upon the new variables tag and D. The analytical expressions of the different PDFs will depend upon the same parameters as before, with the addition of new ones related to flavor tagging:

- ϵ^j – efficiency on signal candidates for the flavor tagger j;

- S_D^j – event-by-event dilution scale factor for the flavor tagger j;
- ϵ_B^j – efficiency on background candidates for the flavor tagger j;
- $\mathcal{D}_B^j$ – background average dilution for the flavor tagger j;
- Δm_d – B_d^0 oscillation frequency,

where j can be Soft Muon Tagger, Soft Electron Tagger, Secondary Vertex Jet Charge Tagger, Jet Probability (J_P) Jet Charge Tagger, and high P_T Jet Charge Tagger.

Combination of Opposite Side Taggers

For a B meson candidate we may have several tags of the production b-flavor, provided by several taggers. To choose a decision among them, the taggers are arranged hierarchically in order of average dilution. Then, we check whether the best tagger has provided a decision. If that is not available we move to the second best and so on, as summarized in Table 7.1. Soft Electron and Soft Muon Taggers are allowed to have lepton identification likelihood $> 5\%$. No cut on Q_{jet} is applied in the Jet Charge Tagger case.

tagger	notation	hierarchy
Soft Muon Tagger	SMT	first of all
Soft Electron Tagger	SET	if SMT failed
SecVtx Jet Charge Tagger	JVX	if SMT and SET failed
J_P Jet Charge Tagger	JJP	if SMT, SET and JVX failed
high P_T Jet Charge Tagger	JPT	if SMT, SET, JVX and JJP failed

Table 7.1: Opposite side taggers notation and hierarchy.

When the opposite side flavor taggers are combined in the exclusive way described in Table 7.1, the efficiency of each tagger has a different meaning with respect to the values determined in chapter 6, where the taggers were calibrated independently. Now the efficiency ϵ^j is defined as the number of events tagged by the opposite side tagger j (and not by the previous taggers) divided by the total number of events that enter the fit; with this definition, the fraction of Non-Tagged candidates is given by

$$\epsilon_{NT} \equiv 1 - \sum_j \epsilon^j \, . \tag{7.1}$$

7.1.1 Proper Decay-Length PDF

Different PDFs are needed for B_d^0 and B^+ decay modes. Whereas the former have the mixing property, the latter have a simpler behavior, given that charge conservation forbids mixing between B^+ and B^-; therefore we describe independently the PDFs for neutral and charged decay modes.

B_d^0 Modes

The probabilities for a B_d^0 meson produced at $ct' = 0$ to decay at a given proper decay-length $ct' > 0$ as B_d^0 or $\bar{B}_d^0$ have been introduced in chapter 2, and given in (2.10). In a good approximation $\Delta\Gamma_d \sim 0$,

$$\begin{aligned} P(ct')_{B_d^0 \to B_d^0} &= \frac{1}{2c\tau}\, e^{-\frac{ct'}{c\tau}} \left[1 + \cos(\Delta m_d t')\right] \theta(ct')\,, \\ P(ct')_{B_d^0 \to \bar{B}_d^0} &= \frac{1}{2c\tau}\, e^{-\frac{ct'}{c\tau}} \left[1 - \cos(\Delta m_d t')\right] \theta(ct')\,. \end{aligned} \tag{7.2}$$

The probability of a tagger j to provide a decision is ϵ^j, and the probability for that decision to be correct is denoted as $\mathcal{P}^j$. Therefore, the probability of a tagger j to provide the correct decision is $\epsilon^j \mathcal{P}^j$, and accordingly, the probability of a tagger j to provide the incorrect decision is $\epsilon^j(1 - \mathcal{P}^j)$. With these probabilities of correct/incorrect tagging, and the probabilities for a B_d^0 meson to mix/unmix in (7.2), we can already describe the probability of a tagger j to tag a B^0 candidate as Right-Sign (RS) or Wrong-Sign (WS),

$$\begin{aligned} \mathcal{P}^j_{RS}(ct') &= \epsilon^j \mathcal{P}^j P(ct')_{B_d^0 \to B_d^0} + \epsilon^j (1 - \mathcal{P}^j) P(ct')_{B_d^0 \to \bar{B}_d^0}\,, \\ \mathcal{P}^j_{WS}(ct') &= \epsilon^j (1 - \mathcal{P}^j) P(ct')_{B_d^0 \to B_d^0} + \epsilon^j \mathcal{P}^j P(ct')_{B_d^0 \to \bar{B}_d^0}\,. \end{aligned} \tag{7.3}$$

The event-by-event dilution D corrected by the scale factor S_D^j is defined as $S_D^j D \equiv 2\mathcal{P}^j - 1$. If we replace $\mathcal{P}^j$ by $(1 + S_D^j D)/2$ in (7.3) and do some trivial algebra,

$$\begin{aligned} \mathcal{P}^j_{RS}(ct') &= \frac{\epsilon^j}{2c\tau}\, e^{-\frac{ct'}{c\tau}} \left[1 + S_D^j D \cos(\Delta m_d t')\right] \theta(ct')\,, \\ \mathcal{P}^j_{WS}(ct') &= \frac{\epsilon^j}{2c\tau}\, e^{-\frac{ct'}{c\tau}} \left[1 - S_D^j D \cos(\Delta m_d t')\right] \theta(ct')\,, \\ \mathcal{P}^j_{NT}(ct') &\equiv 1 - \mathcal{P}^j_{RS}(ct') - \mathcal{P}^j_{WS}(ct') = \frac{1 - \epsilon^j}{2c\tau}\, e^{-\frac{ct'}{c\tau}}\, \theta(ct')\,, \end{aligned} \tag{7.4}$$

where $\mathcal{P}^j_{NT}$ is the probability for a candidate to be Non-Tagged.

Now, if instead of a tagger j we have a combination of n taggers; since we are doing an *exclusive* combination of flavor taggers, $\mathcal{P}^j_{RS}$ and $\mathcal{P}^j_{WS}$ remain unchanged for each tagger j. On the other hand, we define $\mathcal{P}_{NT}$ as the total probability for an event to be non-tagged by any tagger,

$$\mathcal{P}_{NT}(ct') \equiv 1 - \sum_{j=1}^{n} \left(\mathcal{P}^j_{RS}(ct') + \mathcal{P}^j_{WS}(ct')\right) = \left(1 - \sum_{j=1}^{n} \epsilon^j\right) \frac{1}{c\tau}\, e^{-\frac{ct'}{c\tau}}\, \theta(ct')\,. \tag{7.5}$$

After introducing the necessary probabilities when one or several taggers are applied, we can already define the general proper decay-length PDF as

$$L^S_{ct}(\vec{x}, tag^j) \;=\; \begin{cases} L_{NT}(\vec{x}) = \dfrac{\mathcal{P}_{NT}(ct')}{N_{NT}} \otimes G(ct-ct', S_{ct}\sigma_{ct})\,\xi(ct) & \forall\;\; tag^j = 0 \\[2ex] L^j_{WS}(\vec{x}) = \dfrac{\mathcal{P}^j_{WS}(ct')}{N^j_{WS}} \otimes G(ct-ct', S_{ct}\sigma_{ct})\,\xi(ct) & \text{for } tag^j = -1 \\[2ex] L^j_{RS}(\vec{x}) = \dfrac{\mathcal{P}^j_{RS}(ct')}{N^j_{RS}} \otimes G(ct-ct', S_{ct}\sigma_{ct})\,\xi(ct) & \text{for } tag^j = +1 \end{cases} \tag{7.6}$$

where $\vec{x} \equiv (ct, \sigma_{ct}, D)$, and the index i over the B meson candidates sample has been omitted for simplicity. The analytical expressions of the normalization factors N_{NT}, N^j_{WS} and N^j_{RS} can be found in appendix B. Finally, we introduced the decay-length efficiency curve $\xi(ct)$, that was described for the $B \to D\pi$ decay modes in (5.22); a more general definition would be

$$\xi(ct) \;=\; \begin{cases} 1 & \text{for } B \to J/\psi K \text{ decay modes} \\[2ex] \sum_{j=1}^{3} \alpha_j\,(ct-\beta_j)^2\,e^{-\frac{ct}{\gamma_j}}\,\theta(ct-\beta_j) & \text{for } B \to D\pi \text{ decay modes} \end{cases} \tag{7.7}$$

B^+ Modes

Charge conservation forbids the oscillation of B^+ mesons, thus simplifying the probability for a B^+ meson produced at $ct' = 0$ to decay at a given proper decay-length $ct' > 0$ as B^+ or B^-,

$$\begin{aligned} P(ct')_{B^+\to B^+} &= \frac{1}{c\tau} e^{-\frac{ct'}{c\tau}}\,\theta(ct')\,, \\ P(ct')_{B^+\to B^-} &= 0\,. \end{aligned} \tag{7.8}$$

Then, the probability of a tagger j to tag a B^+ candidate as RS (B^+) or WS (B^-) is therefore simpler if compared with the neutral signal,

$$\begin{aligned} \mathcal{P}^j_{RS}(ct') &= \epsilon^j \frac{1+S^j_D D}{2} \frac{1}{c\tau} e^{-\frac{ct'}{c\tau}}\,\theta(ct')\,, \\ \mathcal{P}^j_{WS}(ct') &= \epsilon^j \frac{1-S^j_D D}{2} \frac{1}{c\tau} e^{-\frac{ct'}{c\tau}}\,\theta(ct')\,, \\ \mathcal{P}^j_{NT}(ct') &= (1-\epsilon^j) \frac{1}{c\tau} e^{-\frac{ct'}{c\tau}}\,\theta(ct')\,. \end{aligned} \tag{7.9}$$

With a combination of n taggers, $\mathcal{P}^j_{RS}$ and $\mathcal{P}^j_{WS}$ remain unchanged for each tagger j. We define $\mathcal{P}_{NT}$ as the total probability for an event to be non-tagged by any tagger,

$$\mathcal{P}_{NT}(ct') \equiv 1 - \sum_{j=1}^{n} \left(\mathcal{P}^j_{RS}(ct') + \mathcal{P}^j_{WS}(ct')\right) = \left(1 - \sum_{j=1}^{n} \epsilon^j\right) \frac{1}{c\tau}\, e^{-\frac{ct'}{c\tau}}\, \theta(ct')\,. \tag{7.10}$$

The general proper decay-length PDF for charged decays is formally identical to (7.6). The difference lies in the ct' dependence of $\mathcal{P}^j_{RS}$ and $\mathcal{P}^j_{WS}$. If we write the tag probabilities explicitly,

$$L^S_{ct}(\vec{x}) = \begin{cases} \left(1 - \sum_{j=1}^{n} \epsilon^j\right) L^S_{ct}(ct, \sigma_{ct}) & \forall \;\; tag^j = 0 \\ \epsilon^j \, \frac{1 - S^j_D D}{2} L^S_{ct}(ct, \sigma_{ct}) & \text{for } tag^j = -1 \\ \epsilon^j \, \frac{1 + S^j_D D}{2} L^S_{ct}(ct, \sigma_{ct}) & \text{for } tag^j = +1 \end{cases}, \tag{7.11}$$

where $\vec{x} \equiv (ct, \sigma_{ct}, tag^j, D)$, and the PDF $L^S_{ct}(ct, \sigma_{ct})$ remains unchanged from the lifetime fits, i.e., for the $B \to J/\psi K$ decay modes we use (5.8), whereas the $B \to D\pi$ ones are given by (5.19).

Combinatorial Background

For the combinatorial background proper decay-length PDF, instead of the event-by-event dilution D, we use an average dilution $\mathcal{D}_B$. Only signal events from an inclusive B meson sample were used in the determination of the flavor taggers calibrations; therefore it is meaningless to use event-by-event dilutions and measure any dilution scale factor for combinatorial background candidates. Besides this difference, the analytical expression of $L^B_{ct}(\vec{x})$ is exactly the same as the one used in the case of B_u mesons, assuming that combinatorial background candidates do not mix:

$$L^B_{ct}(\vec{x}) = \begin{cases} \left(1 - \sum_{j=1}^{n} \epsilon^j_B\right) L^B_{ct}(ct, \sigma_{ct}) & \forall \;\; tag^j = 0 \\ \epsilon^j_B \, \frac{1 - \mathcal{D}^j_B}{2} L^B_{ct}(ct, \sigma_{ct}) & \text{for } tag^j = -1 \\ \epsilon^j_B \, \frac{1 + \mathcal{D}^j_B}{2} L^B_{ct}(ct, \sigma_{ct}) & \text{for } tag^j = +1 \end{cases}, \tag{7.12}$$

where $\vec{x} \equiv (ct, \sigma_{ct}, tag^j)$, and $L^B_{ct}(ct, \sigma_{ct})$ is the same as it was in the lifetime fits: (5.10) for the $B \to J/\psi K$ decay modes, and (5.25) for the $B \to D\pi$ ones.

7.1.2 Dilution PDF

The terms $L_D^S(D)$ and $L_D^B(D)$ give the probability density to observe a signal or a background event with the dilution D, and they are obtained from data. We do not attempt to parameterize these PDFs as a function of the event-by-event dilution D, as it has been done for the mass and proper decay-length distributions; this is because the dilution distributions are not smooth enough to be described by a clear shape. The PDFs $L_D^S(D)$ and $L_D^B(D)$ enter the likelihood as normalized histograms, constructed in the following way:

1. There are two histograms for each opposite side tagger: one for signal events and one for background events. Since we are using five taggers, that makes ten histograms for each sample.
2. The histograms are filled based on the parameterizations already presented in chapter 6, for the different opposite side taggers.
3. Combinatorial background histograms are filled with events in the reconstructed invariant mass ranges summarized in Table 7.2. Signal histograms are obtained using the sideband subtraction method. The sideband regions are those ones used for combinatorial background events, and the signal regions are as well quoted in Table 7.2.
4. The binning is chosen such that there are no negative bins. In cases where no reasonable rebinning is possible to remove negative bins, they are set to zero.

The dilution templates are shown in Figs. 7.1-7.4.

decay	left sideband [GeV/c^2]	right sideband [GeV/c^2]	signal region [GeV/c^2]
$B^+ \to J/\psi K^+$	5.170 - 5.229	5.340 - 5.390	5.242 - 5.315
$B_d^0 \to J/\psi K^{*0}$	5.170 - 5.215	5.343 - 5.390	5.247 - 5.311
$B^+ \to \bar{D}^0\pi^+$	—	5.430 - 5.520	5.234 - 5.324
$B_d^0 \to D^-\pi^+$	—	5.430 - 5.520	5.234 - 5.324

Table 7.2: Mass ranges for extracting events used to build the dilution histograms.

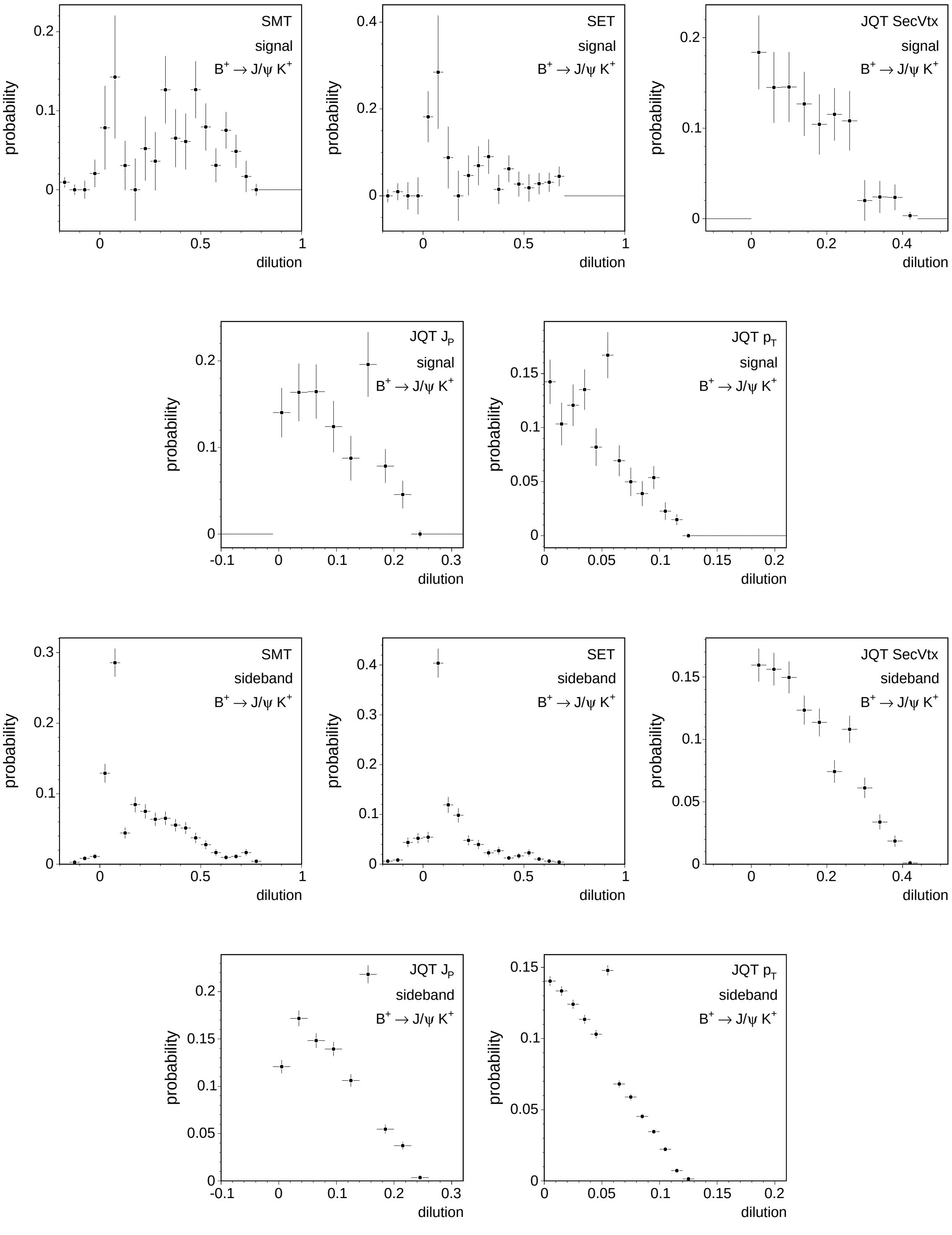

Figure 7.1: Dilution templates for the $B^+ \rightarrow J/\psi K^+$ sample. The five distributions on top correspond to signal events after sideband subtraction. The five distributions on bottom correspond to combinatorial background events from sidebands.

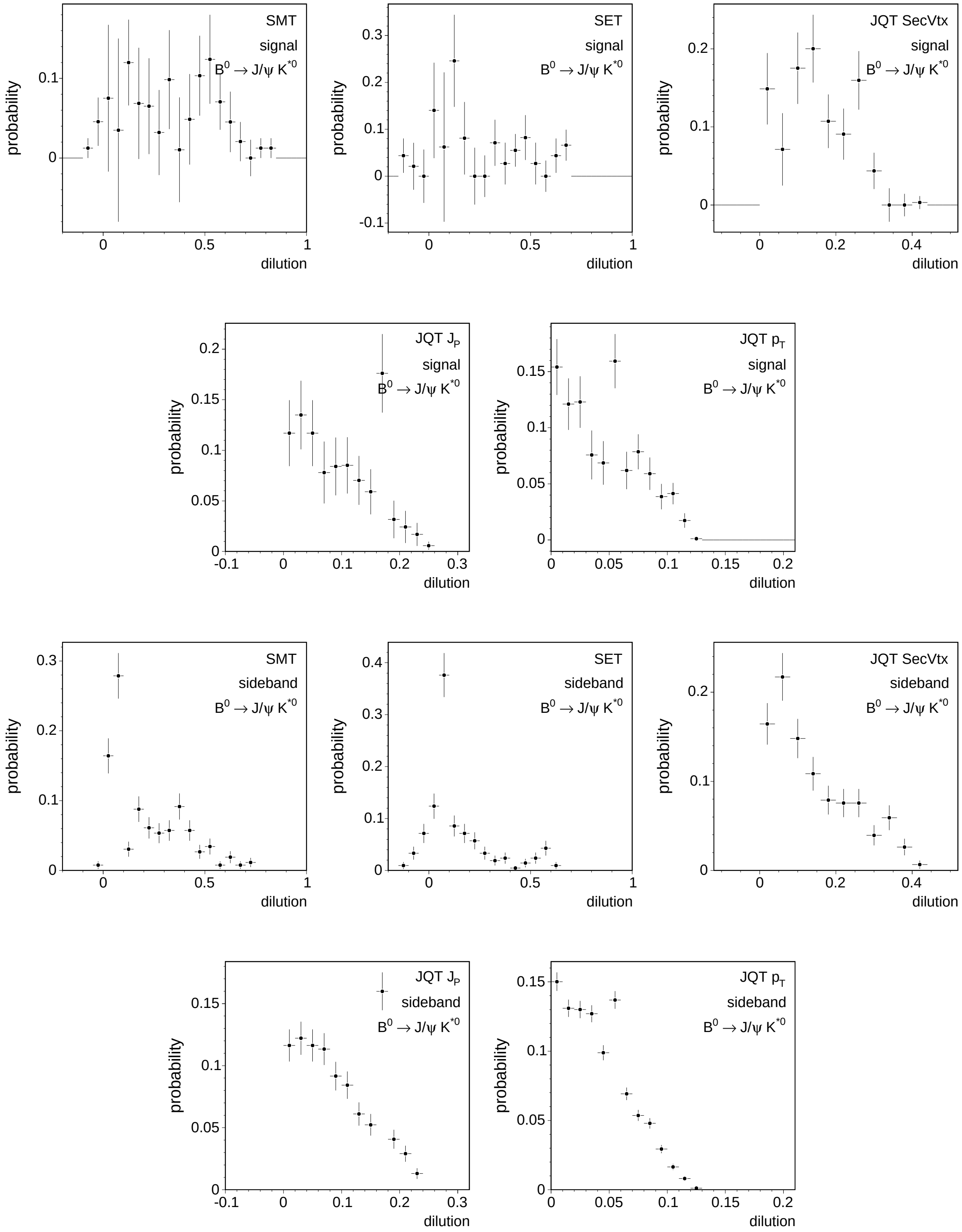

Figure 7.2: Dilution templates for the $B_d^0 \to J/\psi K^{*0}$ sample. The five distributions on top correspond to signal events after sideband subtraction. The five distributions on bottom correspond to combinatorial background events from sidebands.

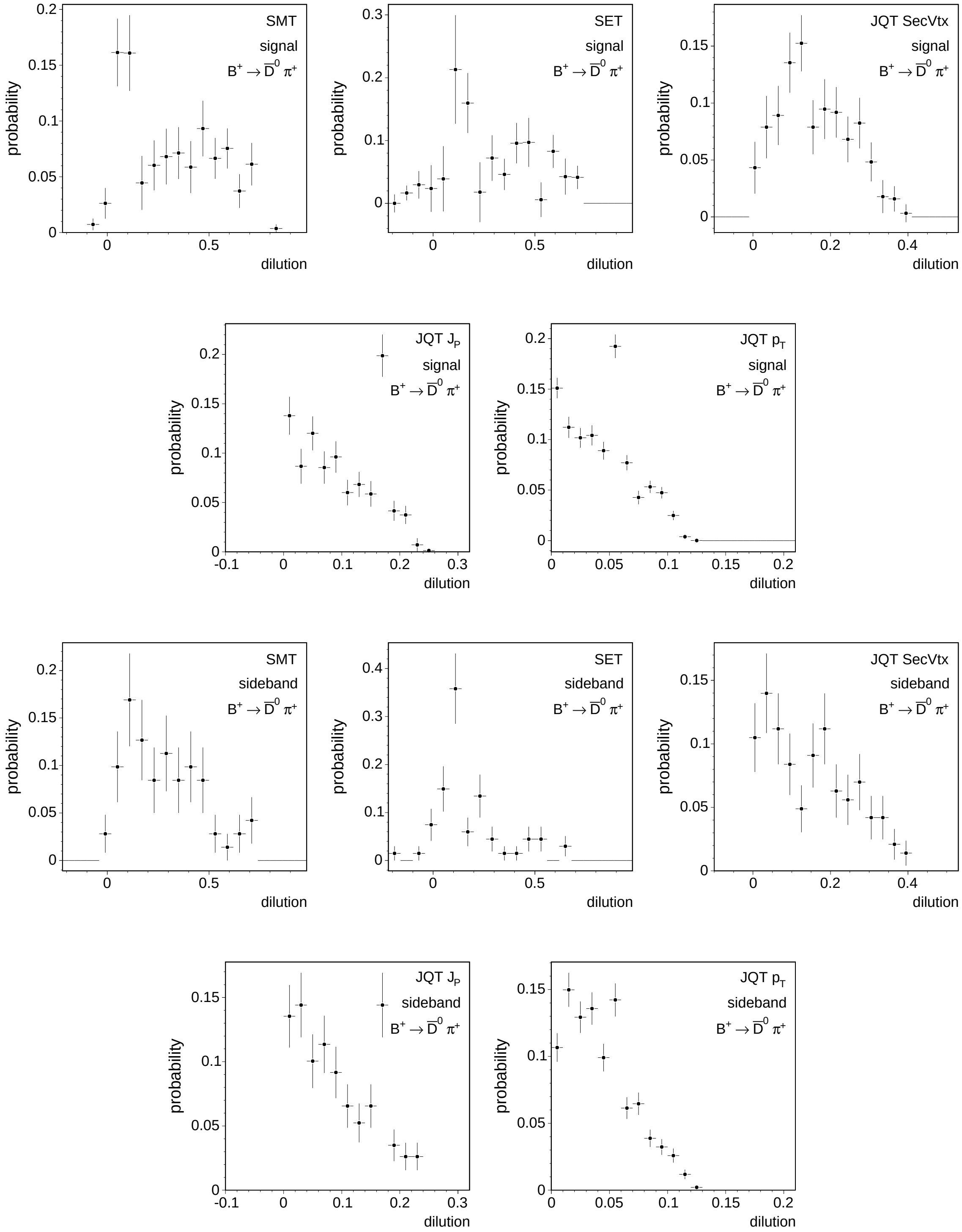

Figure 7.3: Dilution templates for the $B^+ \to \bar{D}^0\pi^+$ sample. The five distributions on top correspond to signal events after sideband subtraction. The five distributions on bottom correspond to combinatorial background events from sidebands.

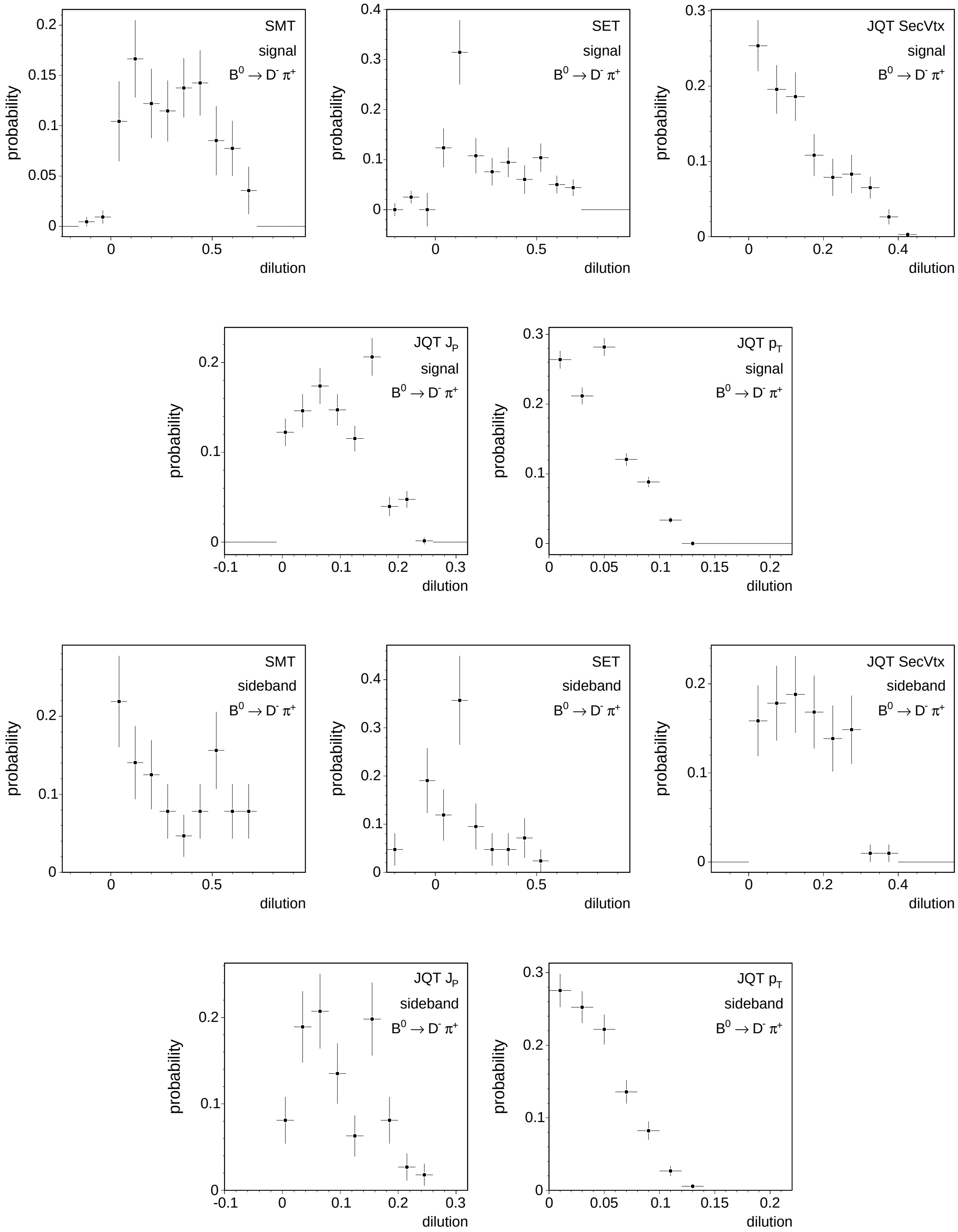

Figure 7.4: Dilution templates for the $B_d^0 \to D^- \pi^+$ sample. The five distributions on top correspond to signal events after sideband subtraction. The five distributions on bottom correspond to combinatorial background events from sidebands.

7.1.3 Likelihood Consistency

Most features of toy Monte Carlo events stay unchanged from the lifetime fits. We have to generate two new variables, the tagging decision and the event-by-event dilution, for signal and background candidates. The tagger decision for neutral signal events is based on whether the event is mixed or not, and also on the dilution generated as above. In contrast, for the background, the event-by-event dilution is not used in generating the tagger decision. Instead, a constant value for background asymmetry which is common for all events is used. We generate ~1,000 $B_d^0 \rightarrow J/\psi K^{*0}$ toy experiments with 5,000 events each, and tagging efficiencies of 80% for signal and 70% for background. Table 7.3 shows the fit parameters pull distributions: efficiencies for signal and background events, the signal scale factor S_D, the background tagging asymmetry $\mathcal{D}_B$ and the mixing frequency Δm_d. The fitted pull distributions are consistent with normal gaussians.

parameter	μ_{pull}	σ_{pull}
ϵ	-0.050 ± 0.032	0.999 ± 0.023
ϵ_B	0.009 ± 0.032	0.988 ± 0.022
S_D	0.033 ± 0.034	1.045 ± 0.024
$\mathcal{D}_B$	0.017 ± 0.033	1.021 ± 0.023
Δm_d	0.003 ± 0.034	1.056 ± 0.024

Table 7.3: Gaussian fit results for toy MC generated with event-by-event dilutions.

7.2 Fit Procedure

The fit at which the dilution scale factors are measured is the final link in a chain of fits growing in complexity. We outline here the necessary steps that precede such grand fit:

1. Any parameter value determined on Monte Carlo is fixed on the fits on data, e.g. the fraction of $K\pi$-swapped candidates ($f_{\text{swap}} = 0.12$) in the $B_d^0 \rightarrow J/\psi K^{*0}$ decay mode, or the shape of the decay-length efficiency curve in the $B \rightarrow D\pi$ decay modes.

2. The $B \rightarrow D\pi$ decay modes require an binned fit of the reconstructed invariant mass distributions to properly determine the exponential shape of the combinatorial background. Furthermore, in the $B_d^0 \rightarrow D^-\pi^+$ decay mode, the same fit provides the shape of the double gaussian that describes the signal peak, i.e., the relative width of the broad gaussian and its fraction. These parameters are fixed in any subsequent fit. The parameters determined at this step can be found in Table 7.13, labelled as M in the "fit" column.

3. For each decay mode separately, we perform a simultaneous fit of the reconstructed invariant mass and proper decay-length distributions. From these fits all parameters but two will be fixed in the final fit: the mass $\langle m \rangle$ and the lifetime $c\tau$. The parameters determined at this step can be found in Table 7.13, labelled as L in the "fit" column.

4. Still treating each decay mode separately, we fix all the parameter values determined previously, $\langle m \rangle$ and $c\tau$ included. The free parameters at this level are the signal and combinatorial background tagging efficiencies for each tagger, as well as the dilution scale factors and the flavor tagging dilution on combinatorial background events. In the neutral modes Δm_d is another free parameter. From these fits we take only the flavor tagging efficiencies on combinatorial background events. The parameters determined at this step can be found in Table 7.13, labelled as B in the "fit" column.

5. Finally we perform the combined fit of all decay modes. Fixed parameter values at this level are the mass and lifetime ones, with the aforementioned exception of $\langle m \rangle$ and $c\tau$. The two neutral decay modes are fitted for $\langle m \rangle_{B_d^0}$ and $c\tau_{B_d^0}$, and the two charged decay modes are fitted for $\langle m \rangle_{B^+}$ and $c\tau_{B^+}$. The flavor tagging efficiencies on combinatorial background events are fixed from the previous fits, while combinatorial background dilution, dilution scale factors and Δm_d are the remaining free parameters in this fit. Parameters determined at this final step can be found in Table 7.13, labelled as S in the "fit" column. The dilution scale factors and Δm_d are in Table 7.12.

A complication arises when one implements the procedure and the described PDFs in the fits that involve dilution scale factors. If a scale factor becomes too large[1], we can have $S_D D > 1$, and negative probabilities are found for some events. By limiting the product $S_D D \leq 1$, we "soften" the physical boundary of all S_D scale factors. Only a small fraction of events runs into this limitation, while most of the events retain their dilution properly scaled by S_D. Nevetheless, this modification is needed to avoid negative probabilities.

The transformation function for the scaled dilution for an event into the scaled dilution actually used in the fit is shown in Fig. 7.5. We have chosen a smooth boundary transition via an arc that preserves continuity of the first derivative. This requirement is necessary for the fit to be stable in the minimization process.

In the following sections, we will detail the partial results of the last two fitting steps, including the specific treatment of the physics backgrounds of each decay mode. Beyond the dilution scale factors, as an immediate result of the absolute tagger calibration, the average performance will be given in terms of the tagging effectiveness, averaged over the four decay modes.

---

[1] The incertitude in the fitted scale factors is still large enough to allow such large scale factors, due to the relative small size of the samples.

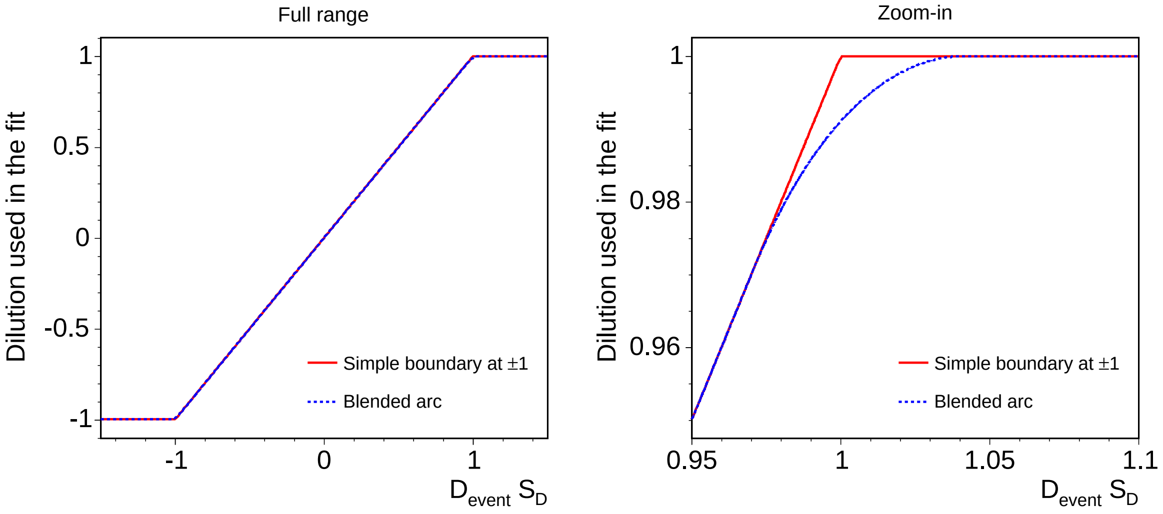

Figure 7.5: Transformation function to map scaled event-by-event dilution $S_D D$ for an event into the value actually used by the fitter. Left plot shows the full range while on the right is the zoomed-in picture. The solid red line is a simple boundary at 1.0 while the dashed blue line shows smooth transition with an arc.

7.2.1 Single Decay Fits

The flavor tagging efficiencies ϵ_B^j on combinatorial background events are specific parameters to every decay mode, i.e., they are independent of the other decay modes. One therefore has the choice to extract these (5 taggers × 4 decay modes) 20 flavor tagging efficiencies from separate fits on each decay mode, or from the single combined fit. Because of the large amount of time required by a fit with many parameters to converge, we chose to extract these parameters from individual fits on each decay mode, later fixed in the combined fit.

For each decay mode, we fix the mass and lifetime parameters to the values quoted in Table 5.3 ($B \to J/\psi K$) and Table 5.11 ($B \to D\pi$). The floating parameters are the flavor tagging efficiencies on signal and combinatorial background events, the dilution scale factors and the flavor tagging dilution on combinatorial background events. In the neutral decay modes an additional free parameter is the oscillation frequency Δm_d.

$B \to J/\psi K$ decay modes

In Sec. 5.2.3 we described the mass and proper decay-length PDFs of the $K\pi$-swapped candidates in the $B_d^0 \to J/\psi K^{*0}$ sample. They are real signal events, were the $K^{*0} \to K^+\pi^-$ candidates are reconstructed with the wrong mass assignments, i.e., a real kaon has been assigned the pion mass, and a real pion has been assigned the kaon mass. The b-flavor at the time of decay of the $B_d^0 \to J/\psi K^{*0}$ candidates is determined by the sign of the kaon ($K^+ \Rightarrow \bar{b}$), and therefore the tagging decision for the swapped candidates should have opposite sign ($K^+ \Rightarrow b$). In our likelihood we consider $-tag$ instead of tag for the swapped candidates.

In the $B^+ \to J/\psi K^+$ decay mode, the tagging decision for the Cabibbo-suppressed $B^+ \to J/\psi\pi^+$ has no difference with respect to the main $B^+ \to J/\psi K^+$ signal, and therefore no tagging adjustment is necessary in this case.

The fitted flavor tagging efficiencies and dilution parameters for both $B \to J/\psi K$ decay modes are listed in Table 7.4. In the $B_d^0 \to J/\psi K^{*0}$ decay mode, the oscillation frequency obtained in the fit is quoted as well.

parameter	$B_d^0 \to J/\psi K^{*0}$	$B^+ \to J/\psi K^+$
ϵ^{SMT}	0.046299 ± 0.004863	0.044220 ± 0.003099
ϵ_B^{SMT} (*)	0.040607 ± 0.001680	0.033103 ± 0.000865
S_D^{SMT}	0.430244 ± 0.373652	0.789928 ± 0.159547
$\mathcal{D}_B^{SMT}$	0.052854 ± 0.040415	0.057537 ± 0.026016
ϵ^{SET}	0.024105 ± 0.003630	0.020312 ± 0.002198
ϵ_B^{SET} (*)	0.034006 ± 0.001537	0.021784 ± 0.000705
S_D^{SET}	0.728334 ± 0.455194	1.064969 ± 0.258173
$\mathcal{D}_B^{SET}$	0.079748 ± 0.045321	0.027169 ± 0.032496
ϵ^{JVX}	0.091463 ± 0.006690	0.082775 ± 0.004153
ϵ_B^{JVX} (*)	0.050609 ± 0.001884	0.040695 ± 0.000962
S_D^{JVX}	1.099703 ± 0.719240	0.358723 ± 0.304107
$\mathcal{D}_B^{JVX}$	0.022207 ± 0.037693	0.048119 ± 0.023982
ϵ^{JJP}	0.150398 ± 0.008445	0.152010 ± 0.005484
ϵ_B^{JJP} (*)	0.115613 ± 0.002739	0.114045 ± 0.001539
S_D^{JJP}	1.176501 ± 0.770964	0.850462 ± 0.331112
$\mathcal{D}_B^{JJP}$	-0.011629 ± 0.025151	0.037143 ± 0.014303
ϵ^{JPT}	0.497595 ± 0.011881	0.497286 ± 0.007689
ϵ_B^{JPT} (*)	0.558407 ± 0.004239	0.543749 ± 0.002404
S_D^{JPT}	1.488608 ± 0.921543	0.798250 ± 0.412365
$\mathcal{D}_B^{JPT}$	0.017648 ± 0.011360	0.023901 ± 0.006528
Δm_d [ps^{-1}]	0.374505 ± 0.147354	—

Table 7.4: Fitted efficiency and dilution parameters for the $B_d^0 \to J/\psi K^{*0}$ and $B^+ \to J/\psi K^+$ decay modes, with previously obtained mass and lifetime parameters fixed. The combinatorial background tagging efficiencies (marked with asterisks) are fixed values in the combined fit of all modes.

$B \to D\pi$ decay modes

With physics backgrounds in the region of the $B_d^0 \to D^-\pi^+$ signal, we must be careful to treat these components correctly in the proper decay-length PDF. For the Cabibbo-suppressed $B_d^0 \to D^- K^+$ contribution, the tagger decision is the same as for the signal, and the proper decay-length PDF does not require adjustment.

The misreconstructed $B_s^0 \to D_s^- \pi^+$ candidates are assumed to have zero flavor tagging asymmetry, i.e., their average dilution is $\mathcal{D}_{B_s^0} \equiv 0$, due to the rapid B_s^0 oscillations. Therefore, the proper decay-length PDF requires minor adjustments,

$$L_{ct}^{B_s^0}(\vec{x}) = \begin{cases} \left(1 - \sum_{j=1}^{n} \epsilon^j\right) L_{ct}^{B_s^0}(ct, \sigma_{ct}) & \forall \ tag^j = 0 \\ \\ \frac{\epsilon^j}{2} L_{ct}^{B_s^0}(ct, \sigma_{ct}) & \text{for } tag^j = \pm 1 \end{cases} , \tag{7.13}$$

where $\vec{x} \equiv (ct, \sigma_{ct}, tag^j)$, and $L_{ct}^{B_s^0}(ct, \sigma_{ct})$ is given in (5.35). The flavor tagging efficiency for this background is assumed to be the same as for the signal, given the similar topologies.

In the misreconstructed $\Lambda_b^0 \to \Lambda_c^+ \pi^-$ candidates, fixed flavor tagging dilutions for each opposite side tagger ($\mathcal{D}_{\Lambda_b^0}^j$) are assumed. They were determined via individual fits for each opposite side tagger in the $B_d^0 \to J/\psi K^{*0}$ sample. In these fits event-by-event dilutions were not used; a single, event-independent dilution, was fitted, appearing in the likelihood as a dumping factor of the oscillation. The results of the fits are summarized in Table 7.5, together with the values taken in the forthcoming systematic studies. The flavor tagging efficiency for $\Lambda_b^0 \to \Lambda_c^+ \pi^-$ candidates is assumed to be the same as for the signal ones.

	fixed $\mathcal{D}_{\Lambda_b^0}^j$		
	low	nominal	high
SMT	0.10	0.36 ± 0.18	0.60
SET	0.10	0.47 ± 0.22	0.65
JVX	0.10	0.33 ± 0.14	0.60
JJP	0.05	0.13 ± 0.09	0.30
JPT	0.01	0.10 ± 0.06	0.20

Table 7.5: Λ_b^0 dilutions and allowed ranges in the evaluation of systematic errors.

The $B^+ \to \bar{D}^0 \pi^+$ decay mode only has to accommodate a Cabibbo-suppressed $B^+ \to \bar{D}^0 K^+$ misreconstructed background, whose flavor tagging decision, event-by-event dilution and efficiency, are the same as for the signal.

The fitted flavor tagging efficiencies and dilution parameters for both $B \to D\pi$ decay modes are listed in Table 7.6. In the $B_d^0 \to D^- \pi^+$ decay mode, the oscillation frequency obtained in the fit is quoted as well.

7.2.2 Simultaneous Fit of All Modes

In order to achieve maximum sensitivity to dilution scale factors, we combine the four decay modes in a single fit. In principle, one can measure all parameters in fits for

parameter	$B_d^0 \to D^-\pi^+$	$B^+ \to \bar{D}^0\pi^+$
ϵ^{SMT}	0.045088 ± 0.003320	0.048389 ± 0.003248
ϵ_B^{SMT} (*)	0.054378 ± 0.003743	0.040854 ± 0.002379
S_D^{SMT}	1.418400 ± 0.341457	0.855162 ± 0.143995
$\mathcal{D}_B^{SMT}$	0.050191 ± 0.067133	0.058491 ± 0.053309
ϵ^{SET}	0.033236 ± 0.002628	0.023004 ± 0.002311
ϵ_B^{SET} (*)	0.034249 ± 0.002809	0.039337 ± 0.002213
S_D^{SET}	2.624421 ± 0.363788	0.328879 ± 0.236534
$\mathcal{D}_B^{SET}$	0.000985 ± 0.073572	0.045432 ± 0.056097
ϵ^{JVX}	0.073486 ± 0.004061	0.066964 ± 0.003920
ϵ_B^{JVX} (*)	0.079972 ± 0.004436	0.077868 ± 0.003192
S_D^{JVX}	0.504877 ± 0.583453	1.213666 ± 0.316486
$\mathcal{D}_B^{JVX}$	0.043692 ± 0.055388	0.061376 ± 0.041310
ϵ^{JJP}	0.135326 ± 0.005291	0.145279 ± 0.005367
ϵ_B^{JJP} (*)	0.117787 ± 0.005398	0.118742 ± 0.003909
S_D^{JJP}	0.555657 ± 0.606502	0.677193 ± 0.324553
$\mathcal{D}_B^{JJP}$	0.008794 ± 0.046901	0.000974 ± 0.034598
ϵ^{JPT}	0.510073 ± 0.007836	0.497271 ± 0.007744
ϵ_B^{JPT} (*)	0.540162 ± 0.008318	0.508377 ± 0.005995
S_D^{JPT}	0.830698 ± 0.735543	1.988365 ± 0.415599
$\mathcal{D}_B^{JPT}$	-0.003829 ± 0.021864	-0.010073 ± 0.016542
Δm_d [ps^{-1}]	0.597949 ± 0.055636	—

Table 7.6: Fitted efficiency and dilution parameters for the $B_d^0 \to D^-\pi^+$ and $B^+ \to \bar{D}^0\pi^+$ decay modes, with previously obtained mass and lifetime parameters fixed. The combinatorial background tagging efficiencies (marked with asterisks) are fixed values in the combined fit of all modes.

individual decays, and then determine a weighted mean from the independent measurements. However, the combination of decay modes gives the highest precision and, as a by-product, makes the fit more stable and its error estimates more accurate, due to the higher sample size that enters in the fit.

Our fitter allows us to combine an arbitrary number of decay modes in a straightforward manner. Each of the decay modes has its own PDF and, for each of its events, the contribution to the likelihood of the total sample is calculated according to the corresponding PDF. Then, the probabilities for all events are multiplied, providing a single product, the negative log of which is minimized by MINUIT [37].

We fix mass and lifetime set of parameters for every decay mode to previously found values, with the exception of $\langle m \rangle$ and $c\tau$. We fix as well the combinatorial background tagging efficiencies, to values found in individual dilution fits. The fit results are summarized in Table 7.7. All errors are standard MINUIT parabolic errors. An alternative error estimate switching on the MINOS option of MINUIT has been performed as well. The

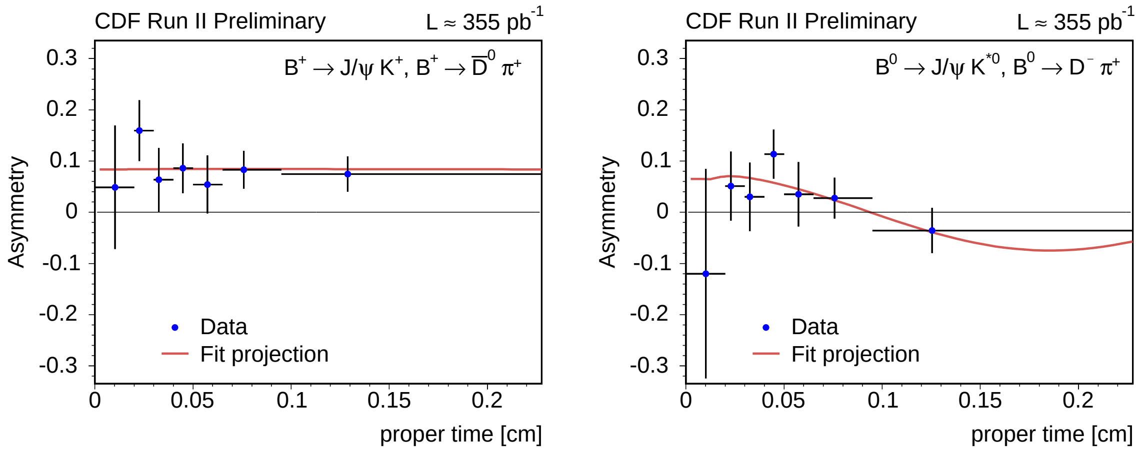

Figure 7.6: Asymmetry projections of the 4-modes combined fit. The left plot corresponds to the charged decays $B^+ \to J/\psi K^+$ and $B^+ \to \bar{D}^0\pi^+$. The neutral decays $B_d^0 \to J/\psi K^{*0}$ and $B_d^0 \to D^-\pi^+$ are presented in the right plot.

positive and negative MINOS errors are close to each other, and to the parabolic value, for all fit parameters. Therefore, the symmetric parabolic errors are quoted in the final results.

As an illustration of the fit results, the asymmetries in data are compared with the fit projection in Fig. 7.6; the red line represents the fit projection, and the background decay-length PDF has been subtracted from the data points. The asymmetries are shown for the exclusive combination of all taggers.

A grand 4-modes combined fit with all the parameters in Tables 7.13 and 7.12 free, except for the mass parameters labelled as M in the "fit" column of Table 7.13, has been performed. For timing comparisons, the fit took 4 hours, whereas the nominal fit takes 30 minutes. In Table 7.8 we see the relative difference in the values of the scale factors and Δm_d, as well as the relative difference in their statistical errors. It is clear from Table 7.8, that the bias introduced by the step-by-step procedure described above is negligible when compared with the statistical errors.

7.3 Systematic Uncertainties

We evaluate systematic uncertainties for six parameters of the 4-modes combined fit: Δm_d and the five scale factors S_D^j. We separate systematic uncertainties into several sources: parameterization in mass subspace, parameterization in ct subspace, event-by-event dilutions and fraction of physics backgrounds.

The systematic uncertainties are estimated in the following way: let us call α a possible source of systematic error. This source α is fixed in the *nominal* 4-modes combined fit to a certain value (set of values in the case of the decay-length efficiency curve). For the

parameter		result
B_u mass	[MeV/c^2]	5278.450 ± 0.000172
B_d mass	[MeV/c^2]	5279.058 ± 0.000227
B_u $c\tau$	[μm]	490.05 ± 5.97
B_d $c\tau$	[μm]	455.07 ± 6.83
Δm_d	[ps^{-1}]	0.502956 ± 0.063315
ϵ^{JVX}		0.076403 ± 0.002141
S_D^{JVX}		0.783788 ± 0.193475
$\mathcal{D}_B^{JVX}$ $(B^+ \to \bar{D}^0\pi^+)$		0.072130 ± 0.041031
$\mathcal{D}_B^{JVX}$ $(B_d^0 \to D^-\pi^+)$		0.033851 ± 0.054356
$\mathcal{D}_B^{JVX}$ $(B^+ \to J/\psi K^+)$		0.045605 ± 0.023891
$\mathcal{D}_B^{JVX}$ $(B_d^0 \to J/\psi K^{*0})$		0.024053 ± 0.037462
ϵ^{JJP}		0.144674 ± 0.002834
S_D^{JJP}		0.755744 ± 0.208899
$\mathcal{D}_B^{JJP}$ $(B^+ \to \bar{D}^0\pi^+)$		-0.000858 ± 0.034141
$\mathcal{D}_B^{JJP}$ $(B_d^0 \to D^-\pi^+)$		0.003081 ± 0.047228
$\mathcal{D}_B^{JJP}$ $(B^+ \to J/\psi K^+)$		0.037492 ± 0.014279
$\mathcal{D}_B^{JJP}$ $(B_d^0 \to J/\psi K^{*0})$		-0.010647 ± 0.025068
ϵ^{JPT}		0.501157 ± 0.004075
S_D^{JPT}		1.353193 ± 0.259837
$\mathcal{D}_B^{JPT}$ $(B^+ \to \bar{D}^0\pi^+)$		-0.004617 ± 0.016299
$\mathcal{D}_B^{JPT}$ $(B_d^0 \to D^-\pi^+)$		-0.009296 ± 0.021444
$\mathcal{D}_B^{JPT}$ $(B^+ \to J/\psi K^+)$		0.023349 ± 0.006521
$\mathcal{D}_B^{JPT}$ $(B_d^0 \to J/\psi K^{*0})$		0.017780 ± 0.011343
ϵ^{SMT}		0.045970 ± 0.001694
S_D^{SMT}		0.832576 ± 0.098531
$\mathcal{D}_B^{SMT}$ $(B^+ \to \bar{D}^0\pi^+)$		0.061405 ± 0.055252
$\mathcal{D}_B^{SMT}$ $(B_d^0 \to D^-\pi^+)$		0.069704 ± 0.066963
$\mathcal{D}_B^{SMT}$ $(B^+ \to J/\psi K^+)$		0.057057 ± 0.026016
$\mathcal{D}_B^{SMT}$ $(B_d^0 \to J/\psi K^{*0})$		0.051214 ± 0.040402
ϵ^{SET}		0.025566 ± 0.001284
S_D^{SET}		0.789661 ± 0.137799
$\mathcal{D}_B^{SET}$ $(B^+ \to \bar{D}^0\pi^+)$		0.033148 ± 0.056294
$\mathcal{D}_B^{SET}$ $(B_d^0 \to D^-\pi^+)$		0.038803 ± 0.080047
$\mathcal{D}_B^{SET}$ $(B^+ \to J/\psi K^+)$		0.028586 ± 0.032714
$\mathcal{D}_B^{SET}$ $(B_d^0 \to J/\psi K^{*0})$		0.079478 ± 0.045715

Table 7.7: Results from the combined fit of all modes.

systematic estimation, the value(s) to which α is fixed is(are) modified, and the 4-modes

parameter	result shift (%)	error shift (%)
Δm_d	0.05	-0.64
S_D^{SMT}	0.01	-0.06
S_D^{SET}	0.27	-0.18
S_D^{JVX}	0.41	0.09
S_D^{JJP}	0.36	-0.28
S_D^{JPT}	0.35	-0.47

Table 7.8: Relative shift in the dilution scale factors and Δm_d, when a fit with all parameters fitted on data are free.

combined fit is repeated. The associated relative systematic error is

$$\frac{\sigma^{\alpha}_{y,syst}}{y} = \left| \frac{y^{\alpha} - y}{y} \right| , \qquad y \equiv \Delta m_d \, , S_D^j \, , \tag{7.14}$$

where y^{α} is the new value of the parameter y, after α has been modified and the 4-modes combined fit has been repeated. The value of the parameter α has been determined either on Monte Carlo or in previous fits on data, with an associated statistical error σ_{α}. In general two new 4-modes combined fits are performed for α, with the values $\alpha \pm \sigma_{\alpha}$. We keep the largest error out of the two iterations.

Finally, any systematic uncertainty with $\sigma^{\alpha}_{y,syst}/y < 0.1\%$ is neglected, and the remaining errors are combined in quadrature to determine the final systematic error. The systematic uncertainties are summarized in Table 7.9.

7.3.1 Mass

Signal shape. For all modes we use a single gaussian to describe signal B meson candidates, except for the $B_d^0 \to D^-\pi^+$ mode. In that mode a double gaussian has to be introduced and provides a much better description, as indicated by the mass fit χ^2/NDF. The mean values for the two gaussians are constrained to be the same. The ratio of the widths of the two components and the fraction of the broad gaussian in the overall signal are found from a stand-alone fit of mass distribution for this decay mode in the mass range $[\mathcal{M}_{\min} - \mathcal{M}_{\max}]$. These two parameters, the ratio and the fraction, are fixed in all subsequent fits while the common mean and the width of the core gaussian are allowed to float. The systematic uncertainty in signal shape is calculated by varying the ratio and the fraction parameters within $\pm 2\sigma$, where σ for each parameter is the error returned in the mass fit; in this case $\sigma^{\alpha}_{y,syst}/y = |(y^{\alpha} - y)/2y|$. The maximum relative variation of the scale factors and Δm_d observed in this procedure are found in Table 7.9, and are fairly small.

Combinatorial background shape. For the $B \to J/\psi K$ decay modes, the parameterization of combinatorial background is linear in the mass space, and raises no questions.

source	relative error, %					
	S_D^{SMT}	S_D^{SET}	S_D^{JVX}	S_D^{JJP}	S_D^{JPT}	Δm_d
mass parameterization for $B \to D\pi$						
signal shape for $B_d^0 \to D^-\pi^+$						
ratio of widths	< 0.1	< 0.1	0.1	0.5	< 0.1	0.3
fraction of wide gaussian	< 0.1	< 0.1	0.3	0.4	< 0.1	0.1
combinatorial background	< 0.1	< 0.1	< 0.1	< 0.1	< 0.1	< 0.1
ct parameterization						
Monte Carlo lifetime	< 0.1	< 0.1	< 0.1	< 0.1	< 0.1	< 0.1
silicon hits	0.1	0.4	< 0.1	0.7	0.9	< 0.1
impact parameter resolution	0.2	0.2	0.2	0.4	0.5	< 0.1
S_{ct}	< 0.1	< 0.1	< 0.1	< 0.1	< 0.1	< 0.1
S_{ct} for background	< 0.1	0.2	0.4	< 0.1	0.1	< 0.1
physics backgrounds						
K^{*0} swap in $B_d^0 \to J/\psi K^{*0}$	0.4	< 0.1	0.2	< 0.1	0.2	0.1
Λ_b^0 in $B_d^0 \to D^-\pi^+$	< 0.1	0.2	< 0.1	0.1	< 0.1	< 0.1
B_s^0 in $B_d^0 \to D^-\pi^+$	< 0.1	< 0.1	< 0.1	< 0.1	< 0.1	< 0.1
Λ_b^0 dilution in $B_d^0 \to D^-\pi^+$	< 0.1	0.4	< 0.1	0.2	< 0.1	0.1
dilution PDF						
binning of templates	3.2	4.3	3.0	0.1	0.1	0.5
statistical smear of templates	2.6	2.9	5.5	3.3	0.7	2.8
ϵ_B	0.3	0.2	0.2	0.8	0.2	< 0.1
total	4.2	5.2	6.3	3.6	1.3	2.9

Table 7.9: Summary of all systematic errors.

For the $B \to D\pi$ decay modes, a decaying exponential shape describes adequately the combinatorial background. The decay constant λ of the exponential from the fits in the mass range $[\mathcal{M}_{\min} - \mathcal{M}_{\max}]$ has an uncertainty, which is translated into the systematic errors by varying it within $\pm 2\sigma$. In all cases the variation in central values of Δm_d and all S_D^j parameters is within 0.1%, and it is thus neglected. Specifically, the variation is in the range 0.01-0.07% relative to the central value for all parameters.

7.3.2 Proper Decay-Length

Monte Carlo lifetime in the decay-length efficiency curve. For the $B \to D\pi$ decay modes, Monte Carlo is used to obtain the decay-length efficiency curves $\xi(ct)$ (5.22). The shape of these curves depends on the $B_{d,u}$ lifetimes assumed in Monte Carlo. To check for systematic effects related to the uncertainty in B lifetimes, we vary Monte Carlo lifetimes within the PDG errors, re-derive the decay-length efficiency curves, and repeat the 4-modes combined fits. Specifically, the following lifetimes and errors are used: $c\tau_{B_d^0} = 460.5 \pm 4.2\ \mu$m, $c\tau_{B^+} = 501 \pm 5\ \mu$m. The variation observed in Δm_d and scale factors S_D^j is rather negligible, below 0.01% in relative value.

Innermost silicon layer in the decay-length efficiency curve. At the time of this thesis, the Monte Carlo decay-length resolution when the hits in the innermost silicon layer[2] are considered in the track refit does not match the decay-length resolution in data. The same problem happens with the efficiency, finding more hits in Monte Carlo than in data. We use Monte Carlo that includes innermost silicon layer hits in the nominal fit, since they are considered in data. To estimate a possible systematic effect, we re-derive the decay-length efficiency curve without using the innermost silicon layer hits in the track refitting in Monte Carlo and repeat the 4-modes combined fit. The value for systematics shifts is shown in Table 7.9; this systematic effect is labelled as "silicon hits" in that table.

Impact parameter resolution in the decay-length efficiency curve. This systematic effect deals with the difference between the SVT impact parameter d_0^{SVT} and the SVX impact parameter d_0^{SVX}, and how this difference changes between data and Monte Carlo. A study has been done in detail using $J/\psi \to \mu\mu$ events. It has been observed a difference in about 2 μm between the $d_0^{SVT} - d_0^{SVX}$ Monte Carlo residuals and the data ones. The residuals are fit with a double gaussian distribution, where the narrower component accounts for about 80%, with widths 26.2 ± 0.2 μm for Monte Carlo and 28.8 ± 0.1 μm for data. Therefore, we introduce an extra smearing in the d_0^{SVX} of $\sqrt{28.8^2 - 26.2^2} \approx 12$ μm before the trigger confirmation in our B candidates and re-derive the decay-length efficiency curve.

Scale factor on $\boldsymbol{\sigma_{ct}}$. One of our model parameters is the scale factor for the error on the decay vertex position. This scale factor is determined in the fits of J/ψ modes where the prompt background component helps to obtain a fairly precise measurement of it. The scale factors in the $D\pi$ modes are fixed to the average value found in $J\psi$ modes. In order to evaluate systematics associated with scale factor in the hadronic modes we vary the value of it within $[1.0 - 1.2]$, range suggested by the difference between scale factors observed in data and Monte Carlo simulation. This is a conservative estimate. However, the range makes little difference as the systematic effects are small. The largest effect is on the Δm_d value at 0.05% while the effect on S_D for all taggers range 0.001-0.008%. This systematic source is negligible.

Scale factor on $\boldsymbol{\sigma_{ct}}$ for background. The scale factor σ_{ct} for combinatorial background events populating positive and negative exponential tails in ct space does not have to be the same as that for the signal events. Our model uses the same scale factor on σ_{ct} for all events. If there is a significant difference in this scale factor between different event types the fit results may be biased. This issue is investigated by setting background scale factor for all modes to 1.0 while keeping the signal scale factor at the old value

---

[2] The innermost silicon layer has not been used in data until very recently.

and comparing the results of the combined fit for dilutions and mixing. The value for systematics shifts is shown in Table 7.9.

7.3.3 Dilution

Dilution PDF. The fitter estimates the probability for an event to have a given dilution as a signal and as a background event from dilution templates. These histograms prepared by applying sideband subtraction technique to each sample are not always highly populated due to relatively low sample sizes and low tagging efficiencies for some taggers. The systematics associated with uncertainty in dilution template is estimated using two methods.

First, the fits are repeated with a different binning of the templates. The binning may be important because the shape of the templates is non-smooth with spikes and discontinuities. The templates shown in Fig. 7.1-7.4 are rebinned and the number of bins is reduced by factor ×3. The procedure is applied to all five tag types for each of the four decay modes, signal and background. The combined fit is then repeated. We take half of the difference in parameter values between the nominal fit and fit with rebinned templates as an estimate of systematic error. The results are shown in Table 7.9. The effect for low efficiency taggers is quite significant.

Another aspect of uncertainty in template histograms is in statistical uncertainty in height of each bin due to limited sample size contributing to that bin. The related systematic error in the quantities of interest can be estimated by re-smearing the bin contents according to their errors. The dilution templates are transformed in a systematic way with each bin i of any histogram with height $Y_i \pm \Delta Y_i$ for dilution D_i and statistical changed to the height Y_i' as follows:

$$Y_i' = Y_i + f_i \Delta Y_i \,, \tag{7.15}$$

where for a histogram with the first significant bin i_1 and the last significant bin i_N

$$f_i = \frac{2i - i_1 - i_N}{i_N - i_i} \,. \tag{7.16}$$

In this way, the first significant bin is shifted one sigma down, the last bin shifted one sigma up while all other bins fall in-between. This procedure is illustrated in Fig. 7.7.

Several fit variations are performed. The first one is as described above, the second with the shift reversed. The observed values are shown in Table 7.10 under “max variation”. But varying the templates in a positively correlated fashion might underestimate the uncertainty. The second column of Table 7.10 shows the results when the signal template is made a constant over the range of bins that are normally non-zero, and leaving the background templates as they are normally—this is presumably a much more violent change than shifting bins by fractions of a sigma. Shifts are generally of the same scale, they bounce around a little, but are in some cases even smaller than the first column. We also determined the results when the original method is done with the signal and background templates shifted in an anti-correlated fashion. The third column

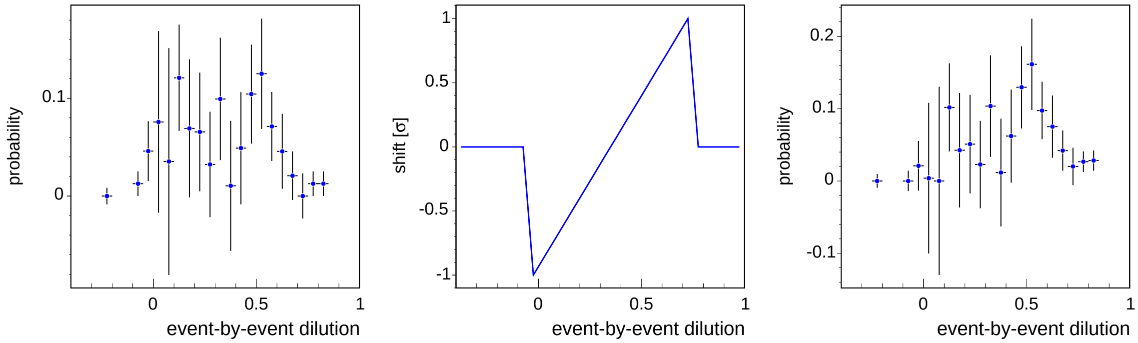

Figure 7.7: Illustration of template transformation for systematic error taking into account statistical uncertainty of bin contents. The left plot is the original template for SMT signal events in $B_d^0 \to J/\psi K^{*0}$ sample. The middle plot is the factor f_i in $Y_i' = Y + f_i \Delta Y_i$ transformation. The right plot is the resulting template.

shows the results when the shift function has a positive slope for signal and negative for background. The fourth column gives the outcome when this is reversed the other way. Values again move around, with somewhat larger outcomes this time. As a further sort of cross-check on these results, we also twisted the templates with signal and background anti-correlated but for only *one mode at a time*. If we add these individual contributions together in quadrature, they roughly track the third and fourth columns where all modes were shifted. We conclude that shifting the templates behaves in a fairly robust way, with stability mostly on the scale of $\sim 1 - 3\%$. In conclusion we take as the systematic uncertainty for the template shapes the *average* of the two uncorrelated versions, column five in Table 7.10.

	dilution templates variations, %				
	max variation same shift	flat signal	shift all $S\uparrow$ $B\downarrow$	shift all $S\downarrow$ $B\uparrow$	average of anti-cor. shift
SMT	1.9	1.29	3.35	1.94	2.64
SET	2.3	0.36	2.56	3.28	2.92
JVX	1.0	3.27	7.57	3.51	5.54
JJP	2.3	0.84	3.03	3.64	3.34
JPT	2.4	1.82	0.94	0.48	0.71

Table 7.10: Several dilution templates variations.

Background tagging efficiencies. The tagging efficiencies for background events are fixed in the combined fit to the values found in individual fits for each of the analyzed decay modes. This may have some effect on Δm_d and dilution scale factors if background tagging efficiencies are correlated in a significant way with these parameters. To evaluate possible systematic effect the combined fit is performed with all of these fixed efficiencies shifted one σ up and then again with all efficiencies shifted one σ down. The maximum deviation from the nominal fit results is taken as a systematic uncertainty for each parameter.

7.3.4 Physics Backgrounds

K^{*0} swap level. In $B_d^0 \to J/\psi K^{*0}$ mode the level of events with incorrect mass assigned in K^{*0} candidates is estimated as 10% and 12% in two independent Monte Carlo studies. The primary fit of this analysis uses the 12% figure. For systematics estimates this measurement is repeated with the 10% level of K^{*0} swaps. The results of this study are shown in Table 7.9.

Λ_b^0 and B_s^0. The decay modes in this study do not suffer from too many physics backgrounds. In addition to combinatorial background, three out of four modes have contribution from Cabibbo-suppressed decays $J/\psi\pi$ and DK. The level of those is well known and the tagging asymmetry along with lifetime are almost identical to those of signal decays. However, in $B_d^0 \to D^-\pi^+$ channel there are two physics backgrounds: B_s^0 and Λ_b^0 decays. The level of these components is not known as well as the level of the Cabibbo contributions and we therefore estimate the related systematic error. The following ratios for events reconstructed as B_d^0 candidates are used in the fitter: $N(B_s^0)/N(B_d^0) = (1.0 \pm 0.3)\%$ and $N(\Lambda_b)/N(B_d^0) = (4.1 \pm 1.3)\%$. Each of these components is varied within $\pm\sigma$ and the combined fit is repeated. The systematics shifts observed are small, only a few are above the level of significance 0.1% chosen for this analyis. The errors are listed in Table 7.9. We expect that Λ_b dilution for opposite side taggers is similar to that of the signal B decays. While in the nominal fit this value for each tagger is fixed to approximately expected average dilution for each tagger, for the systematics studies the value is varied within the limits shown in Table 7.5. The combined fit is repeated with all Λ_b^0 dilutions shifted to the upper limit and then down to the lower limit. The results for this systematic error are found in Table 7.9.

7.4 Results

To conclude this chapter we summarize in Table 7.13 all the parameters that have been obtained from different fits on data. The fit results for the scale factors S_D^j and Δm_d are quoted in Table 7.12.

The *tagging effectiveness* $\epsilon\mathcal{D}^2$ is computed out of the 4-modes combined fit results and the event-by-event dilutions, using (7.17). The results can be found in Table 7.11.

$$\epsilon\mathcal{D}^2 = \epsilon S_D^2 \left\langle D^2 \right\rangle , \tag{7.17}$$

$$\left\langle D^2 \right\rangle = \frac{1}{N_{S+B}} \sum_i^{S+B} D_i^2 - \alpha \frac{1}{N_B} \sum_j^{B} D_j^2 , \tag{7.18}$$

where i and j refer to events in the signal and sideband regions, defined in Table 7.2, respectively; accordingly, N_{S+B} and N_B are the total number of events in each region, and $D_{i,j}$ is the event-by-event dilution of the event i, j. Finally, α is the sideband subtraction correction factor, that accounts for the normalization of background events between the signal and the sideband regions.

tagger	$\epsilon\mathcal{D}^2$ (%)
SMT	0.460 ± 0.111 (*stat.*) ± 0.033 (*syst.*)
SET	0.177 ± 0.063 (*stat.*) ± 0.018 (*syst.*)
JVX	0.135 ± 0.066 (*stat.*) ± 0.007 (*syst.*)
JJP	0.106 ± 0.059 (*stat.*) ± 0.006 (*syst.*)
JPT	0.240 ± 0.092 (*stat.*) ± 0.004 (*syst.*)
total	1.118 ± 0.180 (*stat.*) ± 0.039 (*syst.*)

Table 7.11: Sideband subtracted $\epsilon\mathcal{D}^2$ for all taggers, derived from the combined fit of all modes and the event-by-event dilutions.

parameter	result
Δm_d	(0.503 ± 0.063 (*stat.*) ± 0.015 (*syst.*)) ps^{-1}
S_D^{SMT}	0.83 ± 0.10 (*stat.*) ± 0.03 (*syst.*)
S_D^{SET}	0.79 ± 0.14 (*stat.*) ± 0.04 (*syst.*)
S_D^{JVX}	0.78 ± 0.19 (*stat.*) ± 0.05 (*syst.*)
S_D^{JJP}	0.76 ± 0.21 (*stat.*) ± 0.03 (*syst.*)
S_D^{JPT}	1.35 ± 0.26 (*stat.*) ± 0.02 (*syst.*)

Table 7.12: Main results from the combined fit of all modes.

parameter	fit	$B_d^0 \to J/\psi K^{*0}$	$B_d^0 \to D^- \pi^+$	$B^+ \to J/\psi K^+$	$B^+ \to \bar{D}^0 \pi^+$
λ	M[a]	—	1.52 ± 0.10	—	0.95 ± 0.07
f	M	—	0.547 ± 0.084	—	—
r	M	—	2.082 ± 0.133	—	—
$\sigma_{\langle m \rangle}$ [MeV/c^2]	L[b]	10.5 ± 0.3	13.4 ± 0.3	12.2 ± 0.2	17.7 ± 0.3
f_B	L	0.865 ± 0.003	0.464 ± 0.008	0.893 ± 0.002	0.600 ± 0.006
a	L	-1.79 ± 0.60	—	-1.07 ± 0.34	—
S_{ct}	L	1.084 ± 0.014	1.07	1.062 ± 0.007	1.07
f_-	L	0.047 ± 0.008	—	0.039 ± 0.004	—
f_+	L	0.121 ± 0.012	—	0.097 ± 0.005	—
f_{++}	L	0.043 ± 0.004	—	0.014 ± 0.002	—
λ_- [μm]	L	41.8 ± 3.7	—	45.2 ± 2.5	—
λ_+ [μm]	L	41.9 ± 4.9	—	53.5 ± 3.3	—
λ_{++} [μm]	L	360.9 ± 28.5	—	422.9 ± 38.4	—
f_2	L	—	0.171 ± 0.079	—	0.102 ± 0.045
λ_1 [μm]	L	—	204.6 ± 15.0	—	236.8 ± 10.9
λ_2 [μm]	L	—	462.4 ± 63.7	—	582.5 ± 80.8
μ [μm]	L	—	250.7 ± 4.1	—	220.8 ± 2.8
σ_B [μm]	L	—	69.7 ± 2.9	—	64.6 ± 2.0
ϵ_B^{SMT}	B[c]	0.041 ± 0.002	0.054 ± 0.004	0.033 ± 0.001	0.041 ± 0.002
ϵ_B^{SET}	B	0.034 ± 0.002	0.034 ± 0.003	0.022 ± 0.001	0.039 ± 0.002
ϵ_B^{JVX}	B	0.051 ± 0.002	0.080 ± 0.004	0.041 ± 0.001	0.078 ± 0.003
ϵ_B^{JJP}	B	0.116 ± 0.003	0.118 ± 0.005	0.114 ± 0.002	0.119 ± 0.004
ϵ_B^{JPT}	B	0.558 ± 0.004	0.540 ± 0.008	0.544 ± 0.002	0.508 ± 0.006
$\mathcal{D}_B^{SMT}$	S[d]	0.051 ± 0.040	0.070 ± 0.067	0.057 ± 0.026	0.061 ± 0.055
$\mathcal{D}_B^{SET}$	S	0.079 ± 0.046	0.039 ± 0.080	0.029 ± 0.033	0.033 ± 0.056
$\mathcal{D}_B^{JVX}$	S	0.024 ± 0.037	0.034 ± 0.054	0.046 ± 0.024	0.072 ± 0.041
$\mathcal{D}_B^{JJP}$	S	-0.011 ± 0.025	0.003 ± 0.047	0.037 ± 0.014	-0.001 ± 0.034
$\mathcal{D}_B^{JPT}$	S	0.018 ± 0.011	-0.009 ± 0.021	0.023 ± 0.007	-0.005 ± 0.017
ϵ^{SMT}	S	0.046 ± 0.002			
ϵ^{SET}	S	0.026 ± 0.001			
ϵ^{JVX}	S	0.076 ± 0.002			
ϵ^{JJP}	S	0.145 ± 0.003			
ϵ^{JPT}	S	0.501 ± 0.004			
$\langle m \rangle$ [MeV/c^2]	S	5279.0580 ± 0.0002		5278.4503 ± 0.0002	
$c\tau$ [μm]	S	455.07 ± 6.83		490.05 ± 5.97	

---

[a] Binned mass fit of the $B \to D\pi$ decay modes, in the mass range $[\mathcal{M}_{\min} - \mathcal{M}_{\max}]$.

[b] Unbinned simultaneous fit of mass and proper decay-length distributions.

[c] Unbinned fit for the flavor tagging efficiencies on combinatorial background candidates.

[d] Unbinned fit of the four decay modes simultaneously for the dilution scale factors.

Table 7.13: Fit results summary. The dilution scale factors and Δm_d can be found in Table 7.12.

Chapter 8

Δm_d and Δm_s Amplitude Analysis

The B_s^0 mesons oscillation frequency Δm_s has not yet been measured; the current exclusion limit has been set, $\Delta m_s > 14.5$ ps^{-1} at 95% Confidence Level (CL). Using the expression given in (4.3), we have estimated a Δm_s sensitivity for the current sample size, taggers performance and decay-length resolution. The estimated Δm_s sensitivity is below the current combined Δm_s exclusion limit; therefore, instead of trying a direct fit of the time-dependent mixing asymmetry, an amplitude analysis has been carried out. In this chapter, we use the B_d^0 samples for establishing the method feasibility.

In the amplitude analysis, the dilution is no longer a fit parameter, appearing, on the contrary, as a measured quantity. In the previous chapter we have done the absolute calibration of the dilution of the opposite side flavor taggers; the likelihood expression of the B_d^0 decay modes described in Sec. 7.1 is almost unmodified[1], only the probabilities of a flavor tagger j to tag a signal B^0 candidate as RS or WS, given in (7.4), need to be updated, by including an additional *amplitude* parameter A multiplying the scale factors,

$$\mathcal{P}^j_{\substack{RS\\WS}}(ct') \;=\; \frac{\epsilon^j}{2c\tau}\, e^{-\frac{ct'}{c\tau}} \left[1 \pm A S_D^j D \cos(\Delta m\, t')\right] \theta(ct')\,, \tag{8.1}$$

The amplitude A is the only parameter left free in the fit, while all other parameters are fixed to previously obtained values. The method involves performing one such A-fit for each value of Δm, which is fixed at each step; in the case of infinite statistics, perfect decay-length resolution and perfect tagger calibration, one would expect A to be unit for the true oscillation frequency, and zero for the remaining of the probed spectrum. In practice, the output of the procedure is a list of fitted values (A, σ_A) for each Δm hypothesis. This list of values is used to determine a (measured) sensitivity and an exclusion limit.

The sensitivity is defined as the largest value of the oscillation frequency with a certain significance A/σ_A. Our aim is to estimate the largest Δm which may be excluded at 95% CL, i.e., the oscillation frequency for which the uncertainty σ_A on the measured amplitude is equal to 1/1.645.

---

[1] Since the expressions that follow are valid for both B_d^0 and B_s^0 neutral B mesons, we will refer to them as B^0 candidates, with an associated oscillation frequency Δm.

The expected significance $\mathcal{S}$, given in (4.3), has the following expression,

$$\mathcal{S}(\Delta m) \equiv \frac{A}{\sigma_A} = \frac{S}{\sqrt{S+B}}\sqrt{\frac{\epsilon\mathcal{D}^2}{2}} e^{-\frac{1}{2}\sigma_{ct}^2\Delta m^2} ,$$

At this point we have the necessary information to define an expected sensitivity and a measured sensitivity,

- the oscillation frequency for which $1.645/\mathcal{S} = 1$ is the expected sensitivity;
- the oscillation frequency for which $1.645\,\sigma_A = 1$ is the measured sensitivity.

A Δm hypothesis is excluded to a 95% CL in case the following relation is observed,

$$A + 1.645\,\sigma_A < 1\,. \tag{8.2}$$

In the following section, the amplitude analysis method is validated on our neutral B_d^0 samples. As a validation study, systematic errors were not estimated.

Finally, we report an amplitude analysis performed at CDF [51]. It is an amplitude analysis of Δm_s, using a $B_s^0 \to D_s^- \pi^+$ sample. The absolute calibrations of flavor taggers are taken from this thesis, in particular the scale factors S_D^j summarized in Table 7.12.

8.1 Δm_d Amplitude Analysis

In this section, three different amplitude analyses are presented. The first two are performed individually on each neutral B_d^0 sample, $B_d^0 \to J/\psi K^{*0}$ and $B_d^0 \to D^-\pi^+$. In the final amplitude analysis, both neutral decay modes are combined.

$B_d^0 \to J/\psi K^{*0}$

In the previous chapter we performed a fit on each decay mode independently, aiming for the measurement of the flavor tagging efficiencies on combinatorial background events, that later would be fixed in the fit for all decay modes. The results for these fits on the $B \to J/\psi K$ decay modes were summarized in Table 7.4. For the amplitude analysis of the $B_d^0 \to J/\psi K^{*0}$ decay mode, we fix all the parameters to the values quoted in that table, leaving the amplitude A as the only free parameter. Then we perform N fits for A, fixing Δm_d in each fit, from 0 to 15 ps^{-1}, in regular steps. The result is shown in Fig. 8.1. We observe that the measured amplitude is compatible with unit for values of Δm_d in the vicinity of the true value, and with zero for the remaining frequency values.

$B_d^0 \to D^-\pi^+$

In the same way of the fit performed for the $B_d^0 \to J/\psi K^{*0}$ decay mode, this time all the parameters but the oscillation frequency are fixed to the values in the $B_d^0 \to D^-\pi^+$ column of Table 7.6, leaving the amplitude A as the only free parameter. The amplitude analysis performed for the $B_d^0 \to D^-\pi^+$ decay mode is shown in Fig. 8.2. This sample provides a larger exclusion power for much rapid oscillation frequencies, due to its significantly larger statistics when compared to the $B_d^0 \to J/\psi K^{*0}$ decay mode.

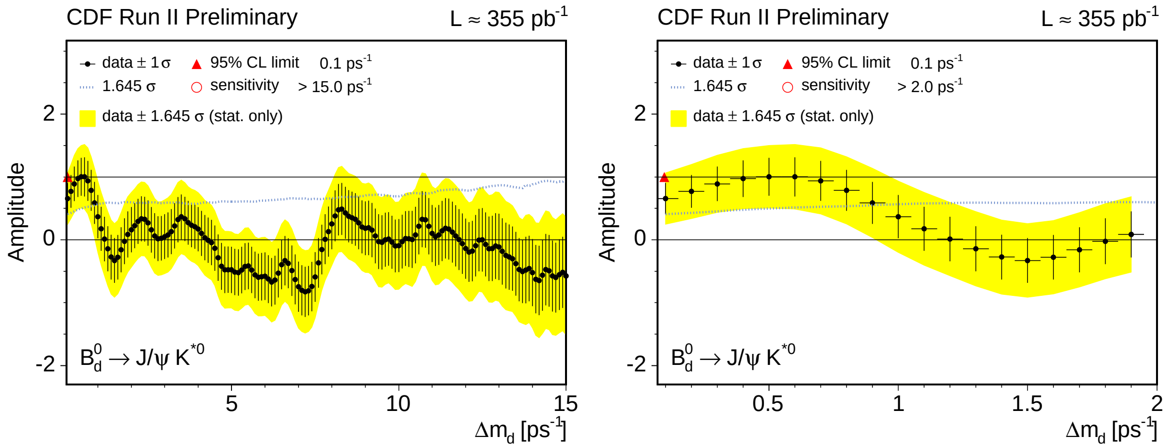

Figure 8.1: Amplitude scan for the $B_d^0 \to J/\psi K^{*0}$ decay mode, with the amplitude A as the only free parameter. The scan has been done from 0 to 15 ps^{-1} (left), and a zoom in the vicinity of the true Δm_d value is shown (right). Systematic effects are not considered.

Combined neutral modes

An amplitude analysis can be as well performed on a combination of decay modes. We first fit for flavor tagging efficiencies and dilution scale factors the two neutral modes simultaneously. For the amplitude scan all fitted values are fixed, and the result is presented in Fig. 8.3. The measured amplitude uncertainty is noticeably reduced when compared to the fits performed on the individual neutral decay modes; this is equivalent to saying that the sensitivity increases significantly for the combined fit.

8.2 Δm_s Amplitude Analysis

To complete this chapter, we will summarize here the Δm_s amplitude analysis [51] done using the absolute dilution calibrations of flavor taggers determined in chapter 7.

8.2.1 Sample Selection

The B_s^0 meson decays are studied in the data sample described in chapter 4. The three channels selected with the two-track trigger are:

- $B_s^0 \to D_s^- \pi^+$, $D_s^- \to \phi\pi^-$, $\phi \to K^+K^-$;
- $B_s^0 \to D_s^- \pi^+$, $D_s^- \to K^{*0}K^-$, $K^{*0} \to K^+\pi^-$;
- $B_s^0 \to D_s^- \pi^+$, $D_s^- \to \pi^-\pi^+\pi^-$.

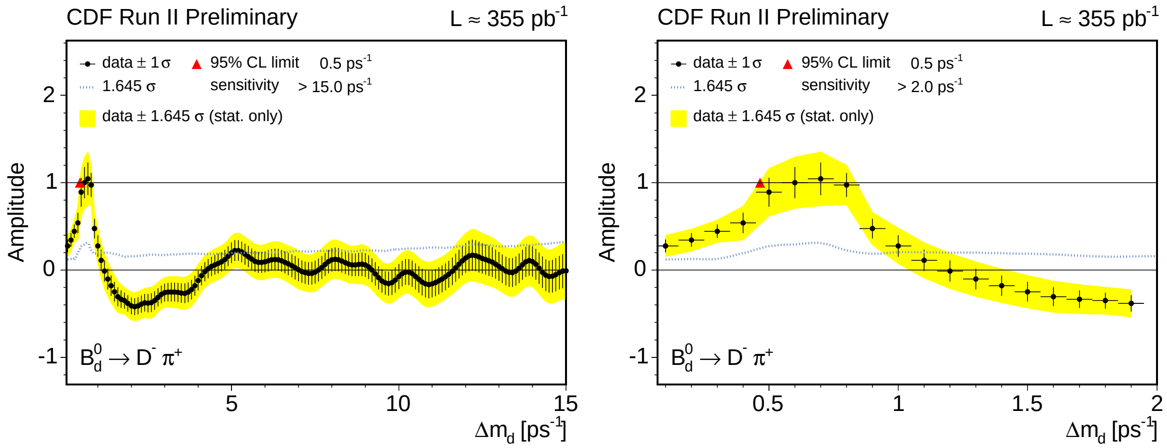

Figure 8.2: Amplitude scan for the $B_d^0 \to D^-\pi^+$ decay mode, with the amplitude A as the only free parameter. The scan has been done from 0 to 15 ps^{-1} (left), and a zoom in the vicinity of the true Δm_d value is shown (right). Systematic effects are not considered.

Kinematic requirements in selection of the three decay modes are listed in Table 8.1.

Similar fits to the ones performed on the $B_d^0 \to D^-\pi^+$ and $B^+ \to \bar{D}^0\pi^+$ decay modes in the wide mass range, are applied to the B_s^0 decay modes to obtain the signal yields. The agreement between the fit templates and the data distributions can be seen in Fig. 8.4, and the signal yields of each sample after trigger and selection cuts are summarized in Table 8.2.

$D_s^- \to \phi\pi^-$	$D_s^- \to K^{*0}K^-$	$D_s^- \to \pi^-\pi^+\pi^-$
$\chi^2_{r-\phi}(B) \leq 15$	$\chi^2_{r-\phi}(B) \leq 8$	$\chi^2_{r-\phi}(B) \leq 6$
$\chi^2_{r-\phi}(D) \leq 14$	$\chi^2_{r-\phi}(D) \leq 15$	$\chi^2_{r-\phi}(D) \leq 15$
$L_{xy}(B \to D) \geq -200\ \mu$m	$L_{xy}(B \to D) \geq -200\ \mu$m	$L_{xy}(B \to D) \geq -100\ \mu$m
$L_{xy}/\sigma_{L_{xy}}(B) \geq 7$	$L_{xy}/\sigma_{L_{xy}}(B) \geq 9$	$L_{xy}/\sigma_{L_{xy}}(B) \geq 13$
–	$\Delta R(D, \pi_B) \leq 1.5$	$\Delta R(D, \pi_B) \leq 1.5$
$p_T(\pi_B) \geq 1.2$ GeV/c	$p_T(\pi_B) \geq 1.3$ GeV/c	$p_T(\pi_B) \geq 1.5$ GeV/c
$\lvert d_0(B)\rvert < 60\ \mu$m	$\lvert d_0(B)\rvert < 60\ \mu$m	$\lvert d_0(B)\rvert < 60\ \mu$m
–	–	$p_T(B) \geq 6.0$ GeV/c

Table 8.1: Selection requirements for $B_s^0 \to D_s^-\pi^+$ decays.

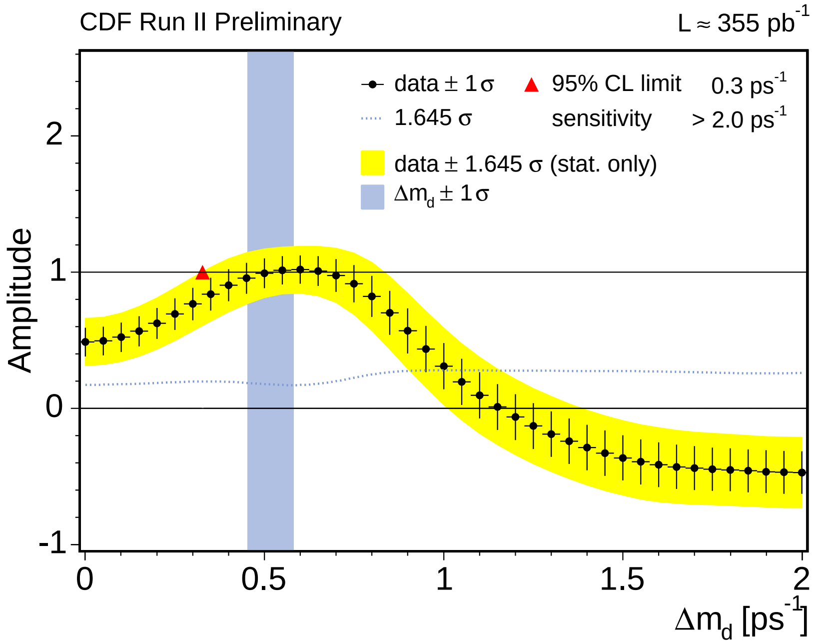

Figure 8.3: Amplitude scan for the simultaneous fit of $B_d^0 \to J/\psi K^{*0}$ and $B_d^0 \to D^-\pi^+$, with the amplitude A as the only free parameter. The vertical band represents the $\Delta m_d \pm 1\sigma$ result from a two neutral decay modes combined fit, with the dilution scale factors and Δm_d as free parameters. The amplitude analysis is performed with the scale factors fixed to the result of this fit.

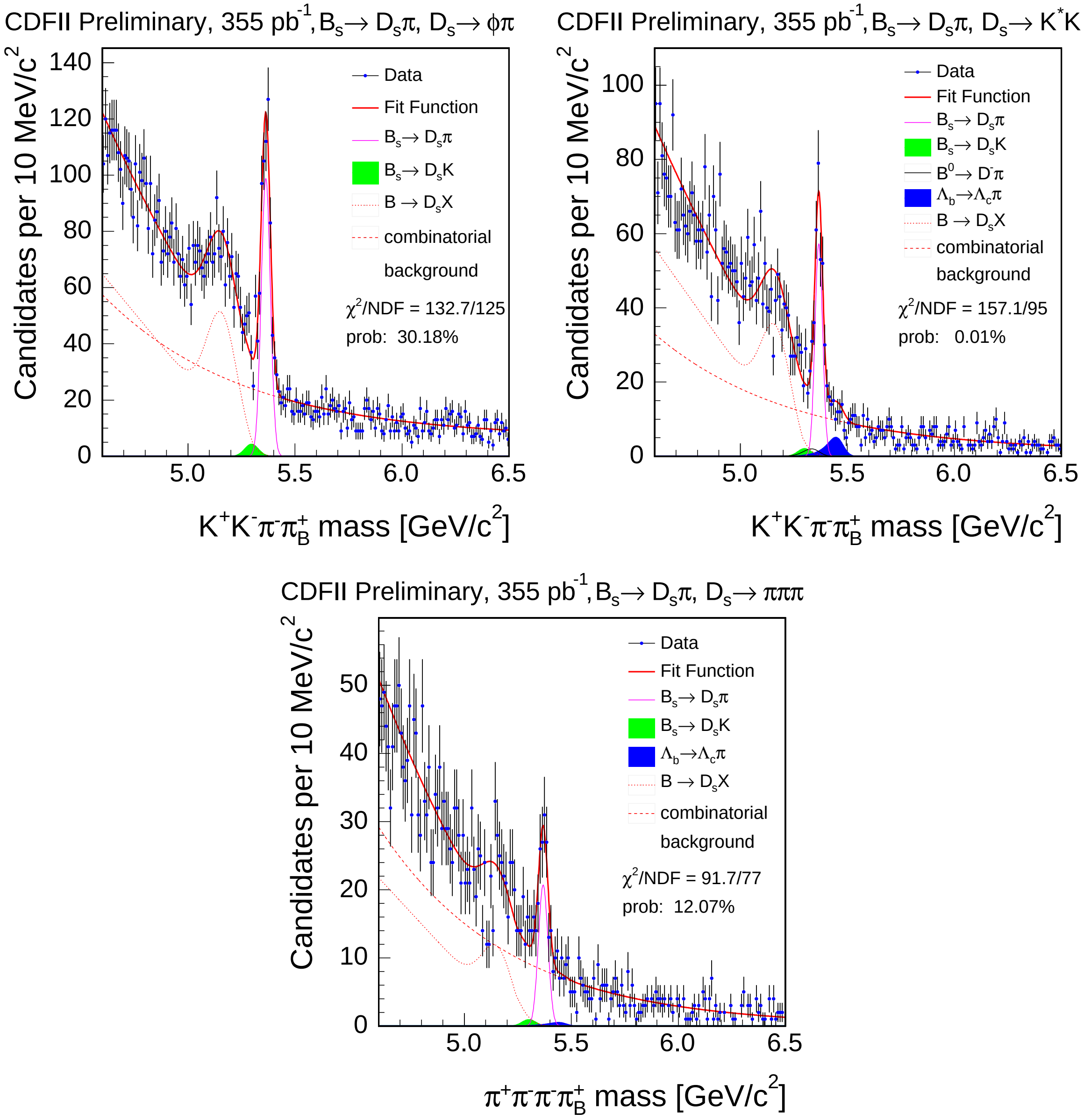

Figure 8.4: Mass distributions of the $B_s^0 \to D_s^- \pi^+$ candidates.

decay	N_B
$B_s^0 \to D_s^- \pi^+$, $D_s^- \to \phi\pi^-$	526 ± 33
$B_s^0 \to D_s^- \pi^+$, $D_s^- \to K^{*0} K^-$	254 ± 21
$B_s^0 \to D_s^- \pi^+$, $D_s^- \to \pi^-\pi^+\pi^-$	116 ± 18

Table 8.2: Signal yields for $B_s^0 \to D_s^- \pi^+$ decays.

8.2.2 Decay-Length Resolution Scale Factors

A decay-length analysis of the samples has to be established before a study of signal oscillations becomes possible. The error σ_{ct} on the proper decay-length comes predominantly from the vertex position measurement. In the $B^{+,0}$ decay modes, a single scale factor S_{ct} has been considered for σ_{ct}. In the B_s^0 samples a more detailed knowledge is needed, due to the rapid B_s^0 oscillations.

An independent sample, consisting of a real D_s^- paired with a fragmentation pion π_f^+ coming from the primary vertex (and charge conjugate $D_s^+ \pi_f^-$), has been used to derive the scale factor as a function of the following variables:

- isolation I of the $D_s^- \pi_f^+$ system,

$$I = \frac{p_T(D_s^- \pi_f^+)}{\sum\limits_j p_T^j}, \qquad \Delta R(D_s^- \pi_f^+, j) = \sqrt{\Delta\eta^2 + \Delta\phi^2} < 0.7\,; \tag{8.3}$$

- pseudorapidity η of the $D_s^- \pi_f^+$ system;
- angular distance ΔR between the real D_s^- and the fragmentation pion;
- transverse momentum $p_T(\pi_f^+)$ of the fragmentation pion.

The scale factor has been determined from the width of a gaussian centered at $ct = 0$ in the decay-length distribution of such calibrating candidates, for different ranges/values of the aforementioned variables. An example illustrating part of the calibration procedure is found in Fig. 8.5. The use of individual measured S_{ct} for each B_s^0 meson candidate provides maximum sensitivity by taking advantage of events with accurately measured decay vertex.

All three B_s^0 samples are fitted at the same time. The common parameters entering the fit models for all channels include B_s^0 mass and lifetime. All other parameters are individual to the channels. The analysis of the proper decay-length allows us to determine the shapes of all components in the ct and mass spaces, and fix them in the amplitude analysis.

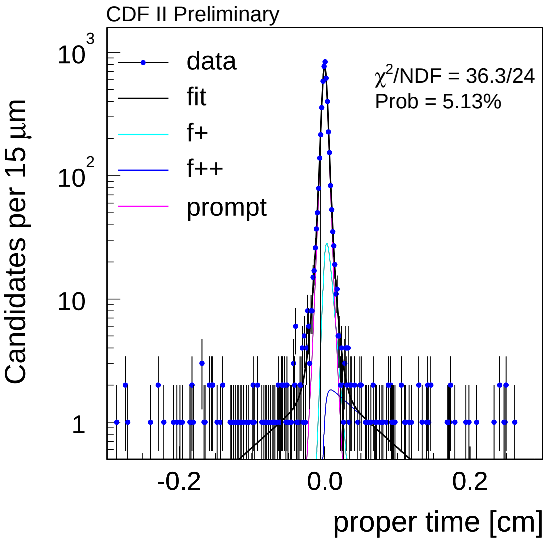

Figure 8.5: Example of a *ct* fit projection for the scale factor calibration. The *prompt* component has a gaussian shape, whereas f_+ is a short-lived positive exponential, and f_{++} is a long-lived positive exponential, both smeared by the decay-length resolution function.

8.2.3 Systematic Uncertainties

Systematic uncertainties have been evaluated using a toy Monte Carlo approach. The toy Monte Carlo simulates data events in all significant aspects including, e.g., individual event vertex errors and dilutions, and detector resolution smearing.

The total systematic error is small when compared to the statistical error on the amplitude. A brief description of individual sources in order of importance follows, with a summary of systematic errors for selected Δm_s points in Table 8.3.

Dilution scale factors. The uncertainty in the magnitude of the predicted dilution for each event is the dominant source of systematic errors. It is taken from the dilution scale factors measured in the previous chapter.

Dilution templates. The probability distributions for signal and background event dilutions used in the fit model are known with limited statistical precision.

Scale factor on σ_{ct}. Any systematic shift between the measured and the true value of the error on the proper decay-length of a B_s^0 meson is accounted for by this systematic contribution.

Detector resolution function. The nominal fit model assumes that the detector resolution function for the proper decay-length is a gaussian. Deviations from the gaussian shape have been studied.

Physics Backgrounds. Several errors have been assigned due to the uncertainty on the knowledge of the sample composition.

Proper Decay-Length resolution PDF. The likelihood does not include $L^{S,B}_{\sigma_{ct}}$. Minor biases are possible, and they are accounted for by this systematic error.

Potentially large $\boldsymbol{\Delta\Gamma/\Gamma}$. The value of $\Delta\Gamma/\Gamma$ for B^0_s mesons affects the proper decay-length fit of the data and can introduce a bias on the amplitude.

Dilution of $\boldsymbol{B \to DX}$ events. Dilution of partially reconstructed $B \to DX$ events is not known. It is assumed to be zero in the nominal fit model, and it is varied in this systematics study.

Efficiency curve systematics. Several systematic sources are considered to describe the uncertainty in the Monte Carlo simulation used to derive the efficiency curve $\xi(ct)$. These sources include B^0_s lifetime uncertainty coming from the PDG error on $c\tau(B^0_s)$, uncertainty of the p_T spectrum of B^0_s mesons in Monte Carlo, and track reconstruction uncertainty that is studied by switching off L00 silicon hits.

8.2.4 Results

For the amplitude scan, the same opposite side taggers that were used in the flavor tagging dilution scale factors determination are applied here. Predicted dilutions for each B^0_s candidate are used, all of them weighed by the flavor tagging dilution scale factors measured in the previoues chapter. The amplitude scan of the data is shown in Fig. 8.6, were all three decay modes are fit at the same time; in that figure, the expectation from the analytical significance $\mathcal{S}$ is overlaid. The input values for the analytical significance curve, summarized in Table 8.4, are: S, S/B and $\langle S_{ct}\sigma_{ct}\rangle$, obtained from the B^0_s data samples; and $\epsilon\mathcal{D}^2$, obtained from the B^0_d, B^+ data samples.

In the fits for amplitude the dilution scale factors are gaussian constrained to their uncertainty via the addition of corresponding χ^2 terms to the likelihood. No limit on Δm_s is set by this analysis alone, and the sensitivity is low when compared to the world combined sensitivity. However, noticeable improvements have been obtained when this amplitude scan is combined with the CDF result from B^0_s oscillations analysis in $B^0_s \to D^-_s l^+ \nu_l X$ decays [52, 53].

Improvements are expected in the short term: there is an ongoing development of new taggers, such as the Same Side Kaon Tagger (SSKT); an optimized version of the

source	selected Δm_s points				
	0.0 ps^{-1}	5.0 ps^{-1}	10.0 ps^{-1}	15.0 ps^{-1}	20.0 ps^{-1}
$B_s^0 \to D_s^- K^+$ level	0.019	0.024	0.030	0.037	0.047
dilution scale factors	0.143	0.168	0.205	0.254	0.314
dilution templates	0.119	0.147	0.178	0.211	0.246
fraction of Λ_b^0	0.014	0.009	0.009	0.011	0.012
probability term for σ_{ct}	0.009	0.008	0.022	0.033	0.030
dilution of $B \to DX$	0.025	0.001	0.000	0.000	0.001
σ_{ct} scale factor	0.000	0.024	0.061	0.090	0.144
silicon hits	0.001	0.001	0.001	0.001	0.001
B_s^0 lifetime uncertainty	0.001	0.001	0.001	0.001	0.001
reweighed p_T spectrum	0.001	0.001	0.001	0.001	0.001
non-gaussian tails in σ_{ct}	0.001	0.027	0.052	0.078	0.104
neglect B_d^0 in fit	0.039	0.036	0.033	0.031	0.028
effect of $\Delta\Gamma/\Gamma = 0.2$	0.028	0.028	0.028	0.028	0.028
total systematic	0.195	0.232	0.289	0.357	0.443
statistical	0.393	1.129	1.010	2.652	5.281

Table 8.3: Systematic errors for selected Δm_s points of the amplitude analysis.

decay	S	S/B	$\langle S_{ct}\sigma_{ct}\rangle$ [fs]
$B_s^0 \to D_s^- \pi^+$, $D_s^- \to \phi\pi^-$	526	1.80	106
$B_s^0 \to D_s^- \pi^+$, $D_s^- \to K^{*0}K^-$	254	1.69	128
$B_s^0 \to D_s^- \pi^+$, $D_s^- \to \pi^-\pi^+\pi^-$	116	1.01	107
combined	896	1.67	113

Table 8.4: Input values for the analytical significance $\mathcal{S}$ that appears in Fig. 8.6. The value of $\epsilon\mathcal{D}^2$ is 1.118%, taken from Table 7.11.

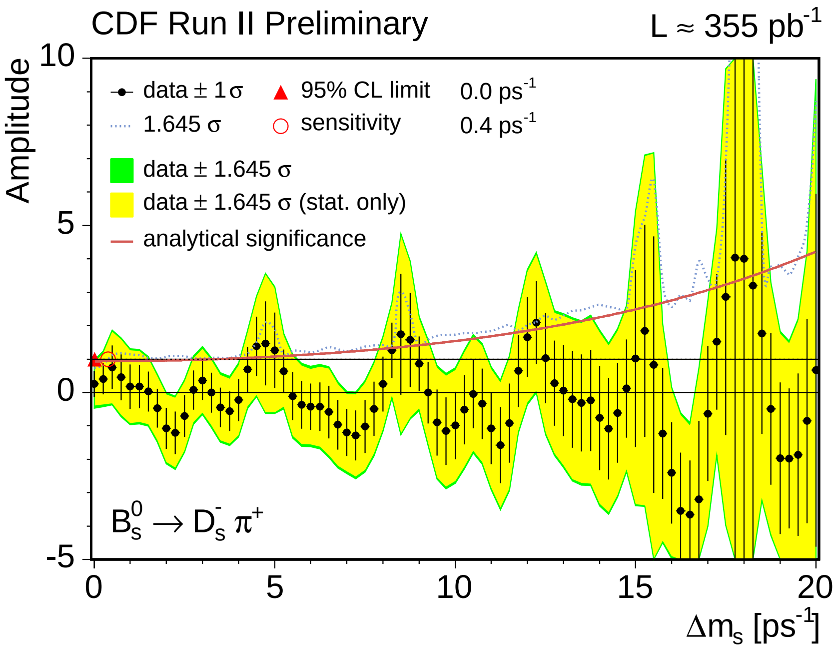

Figure 8.6: Amplitude scan for the $B_s^0 \rightarrow D_s^- \pi^+$ modes, with the analytical significance $\mathcal{S}$ overlaid.

Jet Charge Tagger has been already developed [54], and it will be soon applied; we have already more integrated luminosity, and the L_{xy} resolution is better understood.

Conclusions

The new trigger processor, the Silicon Vertex Tracking (SVT), has dramatically improved the B physics capabilities of the upgraded CDF II Detector; for the first time in a hadron collider, the SVT has enabled the access to non-lepton-triggered B meson decays. Within the new available range of decay modes, the $B_s^0 \to D_s^- \pi^+$ signature is of paramount importance in the measurement of the Δm_s mixing frequency. The analysis reported here is a step towards the measurement of this frequency; two where our goals: carrying out the absolute calibration of the opposite side flavor taggers, used in the Δm_s measurement; and measuring the B_d^0 mixing frequency in a $B \to D\pi$ sample, establishing the feasibility of the mixing measurement in this sample whose decay-length is strongly biased by the selective SVT trigger.

We analyze a total integrated luminosity of 355 pb^{-1} collected with the CDF II Detector. By triggering on muons, using the conventional di-muon trigger; or displaced tracks, using the SVT trigger, we gather a sample rich in bottom and charm mesons. In this sample, two charged and two neutral B meson fully reconstructed decays were studied,

- $B^+ \to J/\psi K^+$, $J/\psi \to \mu^+\mu^-$;
- $B^+ \to \bar{D}^0\pi^+$, $\bar{D}^0 \to K^+\pi^-$;
- $B_d^0 \to J/\psi K^{*0}$, $J/\psi \to \mu^+\mu^-$, $K^{*0} \to K^+\pi^-$;
- $B_d^0 \to D^-\pi^+$, $D^- \to K^+\pi^-\pi^-$.

After sample selection optimization, we obtained the following signal yields:

decay	N_B
$B^+ \to J/\psi K^+$	5323 ± 84
$B^+ \to \bar{D}^0\pi^+$	5625 ± 105
$B_d^0 \to J/\psi K^{*0}$	2231 ± 53
$B_d^0 \to D^-\pi^+$	6157 ± 123

Table 8.5: Signal yields.

The two $B \to J/\psi K$ decay modes are unbiased, in the sense that nor trigger neither selection cuts modify the shape of the proper decay-length distribution. They are used to set the basis of our likelihood model, and more important, they provide a better understanding of the decay-length resolution. The lifetime measurement of the $B \to D\pi$ modes poses a great experimental challenge; we proved here the feasibility of a lifetime analysis on these strongly decay-length biased samples; a required milestone in the road to the B_s^0 mixing in the $B_s^0 \to D_s^- \pi^+$ sample.

Using the previous B_d^0 and B^+ modes, we carried out the absolute dilution calibration of the opposite side flavor taggers currently implemented at CDF: soft lepton and jet charge taggers. The outcome of this calibration has been the determination of the dilution normalization scale factors for each tagger, a requirement for the application of the amplitude analysis to the $B_s^0 \to D_s^- \pi^+$ sample. The Table 8.6 shows the fitted values.

parameter	result
S_D^{SMT}	0.83 ± 0.10 $(stat.)$ $\pm$ 0.03 $(syst.)$
S_D^{SET}	0.79 ± 0.14 $(stat.)$ $\pm$ 0.04 $(syst.)$
S_D^{JVX}	0.78 ± 0.19 $(stat.)$ $\pm$ 0.05 $(syst.)$
S_D^{JJP}	0.76 ± 0.21 $(stat.)$ $\pm$ 0.03 $(syst.)$
S_D^{JPT}	1.35 ± 0.26 $(stat.)$ $\pm$ 0.02 $(syst.)$

Table 8.6: Dilution scale factors for the different opposite side flavor taggers.

As a second outcome of the absolute taggers calibration, we measured by the first time in fully reconstructed decays in a hadron collider, the oscillation frequency Δm_d of B_d^0 mesons, proving the feasibility of the analysis techniques for the Δm_s analysis. We got:

$$\Delta m_d = (0.503 \pm 0.063\ (stat.) \pm 0.015\ (syst.))\ \text{ps}^{-1}.$$

Resumen

El *Modelo Estándar* (ME) de la física de partículas describe las interacciones entre las componentes fundamentales de la materia, fermiones de spin 1/2, mediante el intercambio de bosones de spin 1. De los fermiones elementales, los quarks están ligados por la interacción fuerte, formando hadrones de tres quarks de valencia (bariones), o de quark-antiquark (mesones). En particular los mesones B se componen de un quark ligero q y un antiquark pesado $\bar{b}$, $B_q = \bar{b}q$. Sus antipartículas son los mesones $\bar{B}_q = b\bar{q}$. El quark $b\,(\bar{b})$ se acopla por la fuerza electromagnética a un bosón W y un quark más ligero. El estudio de dichos acoplamientos proporciona información sobre los elementos de la matriz de Cabibbo-Kobayashi-Maskawa (CKM), en particular la tercera fila, V_{td}, V_{cb} y V_{ub}, parámetros del citado ME.

Esta Tesis se ocupa de métodos para la determinación experimental de $|V_{td}|$ y $|V_{ts}|$, mediante el estudio de la oscilación de sabor de los mesones B neutros, $B_d^0-\bar{B}_d^0$ y $B_s^0-\bar{B}_s^0$. En efecto, conocemos, hasta la fecha, que dichos mesones oscilan en sus antimesones con frecuencias $\Delta m_d = 0.502 \pm 0.007$ ps^{-1} y $\Delta m_s > 14.4$ ps^{-1} al 95% de nivel de confianza.

Este estudio utiliza los datos recogidos en el detector CDF II del Tevatron de Fermilab, único capaz de producir estadística suficiente de mesones $B_s^0, \bar{B}_s^0$.

La oscilación es debida a que los autoestados formados en la interacción fuerte no son autoestados de la desintegración débil, sino mezclas de ellos. Utilizando la ecuación de Schrödinger podemos analizar su evolución temporal (2.1) y las probabilidades de mezcla (2.10). En el ME, la oscilación $B_d^0 - \bar{B}_d^0$ viene esquematizada por los diagramas de la Fig. 2.1.

Utilizando una teoría efectiva de campos obtenemos las predicciones dadas por la expresión (2.19) donde, aparte de factores derivados del cálculo de los elementos de matriz hadrónica y de efectos de interacción fuerte, aparecen los elementos de la matriz CKM $V_{q_1q_2}$. Como V es unitaria, se cumple (2.21) así como para las otras filas o columnas. Esto se expresa mediante el triángulo de unitariedad mostrado en la Fig. 2.2.

En la parametrización de Wolfenstein [1], reescalando (2.21) para obtener un triángulo de base unidad y usando los resultados existentes para el resto de los parámetros de (2.19) [2], se obtiene $|V_{td}| = (8.5 \pm 1.0) \times 10^{-3}$, y la dependencia del tamaño del lado derecho del triángulo de unitariedad con Δm_d según se muestra en la expresión (2.28) y anteriores. A su vez el cociente $\Delta m_d/\Delta m_s$ limita R_t según se muestra en (2.31).

Los actuales resultados de oscilaciones B_d^0, B_s^0 han sido recogidos por el "Heavy Flavour Averaging Group" [7] y se muestran en las Figuras 2.3, 2.4, 2.5 y 2.6.

El Colisionador Tevatron de Fermilab (Estados Unidos) es la fuente más potente, en la actualidad, de colisiones proton-antiprotón ($p\bar{p}$). Uno de sus detectores es CDF II, y esta Tesis utiliza los datos obtenidos en él. La máquina se ha mejorado sustancialmente respecto de la existente previamente, tanto en luminosidad, que está en torno a 10^{32} cm^{-2}s^{-1}, como en energía en centro de masas, que alcanza el valor de 1.96 TeV.

El detector CDF II [12] es de propósito general y un esquema del mismo se muestra en la Fig. 3.2. Respecto del "run" anterior ha obtenido notables mejoras, particularmente en: sistema de "trigger", detector de reconstrucción de trazas y vértices, identificación de partículas y aceptancia geométrica de las cámaras de muones. Contrariamente a las colisiones e^+e^-, en $p\bar{p}$ colisionan los partones del protón (antiprotón), reduciendo la energía disponible y produciendo un "boost" no medible en la dirección de los haces; las magnitudes en el plano transverso son, sin embargo, conservadas y, en consecuencia, mucho más precisas.

El detector de trazas contiene varios planos de detectores de vértices, basados en la tecnología del silicio, que permiten medir el desplazamiento de las trazas respecto de los vértices de producción con precisiones de pocas decenas de micras. También contiene un detector central de "barrido", con varias capas radiales de hilos sensibles, hasta un radio cercano a 134 cm. Los detectores de trazas se encuentran encerrados en un solenoide de alta potencia, lo que permite determinar el momento transverso de las partículas cargadas con gran precisión. Asimismo puede medirse la ionización, para usarla en la identificación de las mismas.

Externamente al sistema de reconstrucción de trazas se encuentra un detector de tiempo de vuelo (TOF), que permite discriminar piones de kaones hasta momentos de 1.4 GeV/c.

El sistema de calorimetría no se ha modificado sustancialmente, pero se ha mejorado la electrónica para soportar la alta luminosidad.

Los detectores de muones han aumentado, además, en aceptancia.

Se ha realizado una modificación muy importante para el desarrollo del análisis que se expone en esta Tesis, en el sistema de "trigger". Particularmente se ha incluido la posibilidad de seleccionar trazas desplazadas [26], en los primeros niveles, permitiendo incrementar en varios órdenes de magnitud la capacidad del experimento para el análisis de sucesos con contenido de quark-b.

Los datos analizados en esta Tesis corresponden a una luminosidad integrada de aproximadamente 355 pb^{-1}, utilizando los canales

- $B^+ \to J/\psi K^+$, $J/\psi \to \mu^+\mu^-$;
- $B^+ \to \bar{D}^0\pi^+$, $\bar{D}^0 \to K^+\pi^-$;
- $B_d^0 \to J/\psi K^{*0}$, $J/\psi \to \mu^+\mu^-$, $K^{*0} \to K^+\pi^-$;
- $B_d^0 \to D^-\pi^+$, $D^- \to K^+\pi^-\pi^-$,

y sus conjugados de carga. Hemos utilizado dos tipos de "trigger", el "di-muon" y el de dos trazas. Las eficiencias de los mismos se encuentran en la Tabla 4.1. Una selección posterior está basada en cortes cinemáticos. La evaluación de la eficiencia y pureza de la señal se ha realizado mediante ajustes de máxima verosimilitud a la distribución de masas invariantes de los candidatos, utilizando modelizaciones de las posibles fuentes de ruido procedentes de otros canales, obtenidas mediante simulación de Monte Carlo. En algunos casos el ruido es físico, mientras que en otros casos es puramente combinatorial. Los cortes óptimos para la selección de sucesos $B^+ \to J/\psi K^+$ y $B_d^0 \to J/\psi K^{*0}$ ($B^+ \to \bar{D}^0\pi^+$ y $B_d^0 \to D^-\pi^+$) se muestran en la Tabla 4.3 (Tabla 4.4), y los ajustes de masa en la Fig. 4.7 (Fig. 4.8). El número de sucesos obtenidos se muestra en la Tabla 4.5.

Nuestro primer análisis se ha dedicado al estudio de la **vida media** de los mesones B_d^0 y B^+ usando los canales de desintegración citados, con el fin de determinar las funciones de densidad (PDF) correspondientes al término de longitudes propias de desintegración que aparecen en el ajuste final. Los canales $D\pi$ están sesgados en dicha variable, como consecuencia del corte aplicado al nivel de trigger. Necesitamos Monte Carlo para entender la distribución de dicha variable en estos canales. Los canales $J/\psi K$ no tienen dicho sesgo, y los utilizamos para obtener una comprensión correcta de la resolución en dicha longitud de desintegración.

Las muestras que utilizamos contienen señal y ruido. La separación óptima está basada en la distribución de masa invariante, que la incluimos en la definición de la PDF, de acuerdo a la expresión (5.3). En esta expresión el término de señal incluye el ruido debido a canales físicos, mientras que el llamado ruido se limita al combinatorial. Para los canales $J/\psi K$, los términos de masa en la PDF vienen dados por las expresiones (5.6), (5.7) y las indicadas en la sección de canales físicos de ruido 5.2.3. Correspondientemente, para los canales $D\pi$ utilizamos las expresiones de la sección 5.3.1.

En el caso de las distribuciones de longitud de desintegración, hay que incluir, además de la propia resolución temporal, la eficiencia debida a la selección del trigger y de los cortes de optimización. En el caso de canales sesgados se muestra el efecto indicado en la Fig. 5.4. Para estimar dicha eficiencia utilizamos Monte Carlo. El modelo de expresión utilizado se muestra en la ecuación (5.22).

Las expresiones que utilizamos, una vez estimadas todas las fuentes de ruido, son las que se indican en (5.8), (5.10), (5.19), (5.25) y las derivadas en las secciones 5.2.3 y 5.3.3.

El procedimiento de ajuste ha sido probado mediante el método de “toy Monte Carlo”, generando experimentos simulados con las mismas características que los datos, pero con los parámetros a medir introducidos y aplicando el método de ajuste para extraer dichos parámetros. No observamos sesgos debidos al procedimiento de ajuste.

Los resultados finales se muestran en las Tablas 5.3, 5.11 y 5.12.

Uno de los aspectos más importantes en el estudio de las oscilaciones de sabor de mesones neutros es el denominado **etiquetado de sabor**, que consiste en determinar el sabor del quark pesado componente a tiempo de producción del mesón. En nuestro caso, los quarks $b\bar{b}$ se producen casi siempre en pares, de modo que la determinación de uno de ellos sirve para la determinación del otro. En ese caso hablamos de etiquetado en el lado opuesto. La determinación del sabor a tiempo de producción se realiza mediante el estudio de las partículas de desintegración, como se muestra en la Tabla 6.1. La determinación del sabor a tiempo de producción se realiza, o bien analizando los productos que acompañan a la fragmentación del quark b ó $\bar{b}$ producido, o utilizando, como indicamos arriba, los del lado opuesto. En esta Tesis hacemos especial énfasis en el estudio de los etiquetadores de sabor en el lado opuesto (etiquetadores OST).

Las propiedades de un etiquetador de sabor vienen determinadas por su eficiencia ϵ, su pureza $\mathcal{P}$ (definida en términos de la dilución, $\mathcal{D} \equiv 2\mathcal{P} - 1$) y la efectividad estadística $\epsilon\mathcal{D}^2$.

En esta Tesis hemos utilizado tres etiquetadores OST, optimizados con una muestra obtenida del trigger *leptón+traza*, que tiene una gran cantidad de sucesos. La dilución obtenida en los mismos ha sido corregida por el efecto de oscilación en el lado del propio trigger y por el efecto de ruido procedente de desintegraciones secuenciales $b \rightarrow c \rightarrow l$.

Los etiquetadores citados son los siguientes:

- Etiquetador SMT, basado en la búsqueda de muones de la desintegración semileptónica del hadrón-b del lado opuesto y en la medida de su carga, correlacionada con el sabor-b de dicho hadrón a tiempo de desintegración. Su efectividad resulta ser:

  $$\epsilon\mathcal{D}^2_{raw} = (0.698 \pm 0.042\ (stat.)\ ^{+0.051}_{-0.027}\ (syst.))\ \%\,,$$

  y parametrizada en función de la verosimilitud, como se muestra en la Fig. 6.3.

- Etiquetador SET, basado en la búsqueda de electrones de la desintegración semileptónica del hadrón-b del lado opuesto y en la medida de su carga, correlacionada con el sabor-b de dicho hadrón a tiempo de desintegración. Su efectividad resulta ser:

  $$\epsilon\mathcal{D}^2_{raw} = (0.366 \pm 0.031\ (stat.)\ ^{+0.065}_{-0.056}\ (syst.))\ \%\,,$$

  y parametrizada en función de la verosimilitud, como se muestra en la Fig. 6.4.

- Etiquetador JQT, basado en la observación empírica de que la suma de las cargas de las partículas de un chorro que contenga un mesón B está correlacionada con la carga del quark b y, por tanto, con su sabor.

  Desarrollamos tres métodos, basados en

  - búsqueda de vértices secundarios en el chorro (método *SecVtx*);
  - si no existen vértices secundarios, búsqueda del chorro con mayor probabilidad de traza desplazada, utilizando la ecuación (6.9) y requiriendo un valor máximo de $J_P < 0.12$ (método J_P);
  - en caso de no producirse lo anterior, búsqueda del chorro con mayor momento transverso (método P_T).

La efectividad resultante es:

$$\epsilon\mathcal{D}^2 = (0.715 \pm 0.027\ (stat.))\ \%\,,$$

y mayor detalle se muestra en la Tabla 6.4. La dilución parametrizada como función de la variable de carga efectiva del chorro se muestra en la Fig. 6.5.

Las diluciones obtenidas con la muestra de leptón+traza no tienen por qué coincidir con las correspondientes a las que suponen el objetivo de estos análisis, como es el caso de $B_s^0 \to D_s^- \pi^+$. Como queremos preparar un análisis basado en el método de la amplitud, para determinar el límite de Δm_s, la dilución de los etiquetadores de sabor ha de introducirse previamente al ajuste final, por lo que se requiere conocerla. Para ello se utilizan las diluciones calibradas previamente en la muestra inclusiva leptón+traza multiplicadas por un factor de escala que proporcione la dilución realista para la muestra de $B_s^0 \to D_s^- \pi^+$. Estos **factores de escala**, objetivo principal de esta tesis, los obtenemos del análisis de los modos de desintegración reconstruidos completamente de B_d^0 y B^+, cuya cinemática es similar.

Ahora, adicionalmente a las PDF de masa y de longitud de desintegración, debemos estimar las PDF correspondientes a la decisión del etiquetador y a la dilución del suceso, de acuerdo a las expresiones mostradas en la sección 7.1. Además, la propia PDF de longitud de desintegración es dependiente de las nuevas variables, mediante expresiones analíticas que dependen, además de los parámetros utilizados en el estudio de las vidas medias, de los factores de escala de la dilución para la señal, de la dilución media del ruido combinatorial, de las eficiencias de etiquetado para señal y ruido y de la frecuencia de oscilación Δm_d.

Cuando hay varios etiquetadores seleccionando un suceso, escogemos primero el de mayor jerarquía en orden de dilución media en la señal.

La expresión para la PDF de longitud de desintegración se muestra en (7.6), para el caso de B_d^0 así como para B^+, pero en este último caso la dependencia con la longitud de desintegración real es diferente, por la ausencia de oscilaciones. Para el ruido combinatorial hemos utilizado una dilución promedio. Aparte de ello, la expresión analítica es similar a la de B^+.

La PDF para la dilución se obtiene de los datos, mediante la parametrización de los mismos, según se indicó previamente. Sus modelizaciones se muestran en las Figuras 7.1 a 7.4. La consistencia del ajuste se ha verificado, como anteriormente, con “experimentos” de Monte Carlo.

El ajuste lo hemos realizado tanto para cada modo de desintegración individual como para la combinación de los mismos. En este último caso la sensitividad es máxima. La Fig. 7.6 muestra la bondad del ajuste, cuyos resultados se muestran en la Tabla 7.7.

Hemos analizado los errores sistemáticos, basados en los siguientes aspectos:

- forma de la señal en la modelización de la masa;
- evaluación de la imprecisión existente en los parámetros de entrada en el Monte Carlo, en particular las vidas medias de mesones B;

- discrepancias de datos y Monte Carlo cuando se incluye la capa más interna del detector de silicio;
- efectos asociados a las diferencias entre la resolución de parámetro de impacto del detector de vértices y del trigger de traza desplazada;
- errores sistemáticos en la resolución de la longitud de desintegración, al haber determinado la resolución mediante modos de desintegración J/ψ y estar aplicándolo a modos hadrónicos;
- análogamente para la resolución temporal en los sucesos de ruido combinatorial;
- estudio detallado de los efectos asociados a la estadística limitada en la determinación de la dilución, tanto en cuanto a la calibración de los factores de escala de la dilución, como a su modelización;
- tratamiento detallado de las fuentes de ruido físico.

Finalmente, los resultados del ajuste y sus errores sistemáticos se muestran en la Tabla 7.13.

Para completar el trabajo hemos realizado un **análisis de la amplitud** en oscilaciones de mesones B_s. En primer lugar hemos validado el procedimiento con nuestras muestras de B_d^0. La amplitud obtenida es compatible con el valor esperado de 1 en la vecindad del valor verdadero de Δm_d, y con el valor esperado de cero para los restantes valores de Δm_d, según se muestra en la Fig. 8.3.

Finalmente, ajustes similares a los realizados en los modos de desintegración $B_d^0 \rightarrow J/\psi K^{*0}$ y $B_d^0 \rightarrow D^-\pi^+$ se aplicaron a los modos de desintegración de $B_s^0 \rightarrow D_s^-\pi^+$ usando el método de la amplitud, obteniendo los resultados que se muestran en la Fig. 8.6.

Conclusiones

El nuevo procesador de trigger, el SVT, ha mejorado dramáticamente las capacidades para realizar física de B del nuevo detector CDF II. Por primera vez, en un colisionador hadrónico, el nuevo SVT ha posibilitado el acceso al nivel de trigger, de desintegraciones de B no leptónicas. En este contexto, la desintegración $B_s^0 \rightarrow D_s^-\pi^+$ es de extraordinaria importancia para la medida de la frecuencia de oscilación Δm_s. El análisis que se muestra aquí es una etapa importante hacia dicha medida; dos objetivos teníamos: llevar a cabo la calibración absoluta de los etiquetadores de sabor del lado opuesto a la señal, utilizada en la medida de Δm_s, y medir la frecuencia de oscilación de B_d^0 en una muestra $B \rightarrow D\pi$, estableciendo la capacidad de medir las oscilaciones en esta muestra, cuya longitud de desintegración está fuertemente sesgada por los cortes de selección del SVT.

Hemos analizado ~ 355 pb^{-1} de datos recogidos con el detector CDF II. Utilizando triggers de muones o trazas desplazadas, obtuvimos una muestra enriquecida en mesones con contenido de quarks b y c. En dicha muestra se estudiaron dos modos de desintegración de mesones B cargados y dos de mesones B neutros, reconstruidos completamente:

- $B^+ \to J/\psi K^+$, $J/\psi \to \mu^+\mu^-$;
- $B^+ \to \bar{D}^0\pi^+$, $\bar{D}^0 \to K^+\pi^-$;
- $B_d^0 \to J/\psi K^{*0}$, $J/\psi \to \mu^+\mu^-$, $K^{*0} \to K^+\pi^-$;
- $B_d^0 \to D^-\pi^+$, $D^- \to K^+\pi^-\pi^-$.

Con una selección optimizada y el uso de Monte Carlo para describir los canales de ruido de fondo que pasan el trigger, y los cortes de selección, reconstruimos los sucesos de señal, de acuerdo a la Tabla 1.

desintegración	N_B
$B^+ \to J/\psi K^+$	5323 ± 84
$B^+ \to \bar{D}^0\pi^+$	5625 ± 105
$B_d^0 \to J/\psi K^{*0}$	2231 ± 53
$B_d^0 \to D^-\pi^+$	6157 ± 123

Tabla 1: Número de sucesos de señal.

Los dos modos de desintegración $B \to J/\psi K$ no están sesgados, en el sentido de que ni el trigger ni los cortes de selección modifican la forma de la distribución de la longitud de desintegración propia. Éstos se utilizan como base del método de verosimilitud y, sobre todo, para proveer de un entendimiento más claro de la resolución de la longitud de desintegración.

La medida de la vida media de los modos $B \to D\pi$ impone un reto importante; aquí hemos probado la capacidad de medida de la vida media en muestras de desintegraciones fuertemente sesgadas por el SVT y los cortes posteriores, una etapa esencial para el estudio de la oscilación de B_s^0 en la muestra $B_s^0 \to D_s^-\pi^+$.

Utilizando los modos previos B_d^0 y B^+ llevamos a cabo la calibración absoluta de los etiquetadores de sabor del lado opuesto implementados en CDF: "soft lepton" y "jet charge". El resultado de esta calibración ha sido la determinación de los factores de escala para la normalización de la dilución en cada etiquetador, requerido en la aplicación del método de análisis de la amplitud a $B_s^0 \to D_s^-\pi^+$. En la Tabla 2 mostramos los resultados de nuestro ajuste.

parámetro	resultado
S_D^{SMT}	0.83 ± 0.10 ($stat.$) $\pm$ 0.03 ($syst.$)
S_D^{SET}	0.79 ± 0.14 ($stat.$) $\pm$ 0.04 ($syst.$)
S_D^{JVX}	0.78 ± 0.19 ($stat.$) $\pm$ 0.05 ($syst.$)
S_D^{JJP}	0.76 ± 0.21 ($stat.$) $\pm$ 0.03 ($syst.$)
S_D^{JPT}	1.35 ± 0.26 ($stat.$) $\pm$ 0.02 ($syst.$)

Tabla 2: Factores de escala de la dilución para los diferentes etiquetadores.

Un segundo resultado de la calibración absoluta de los etiquetadores de sabor ha sido la medida, por primera vez en canales de desintegración reconstruidos completamente en un colisionador hadrónico, de la frecuencia de oscilación Δm_d de mesones B_d^0, probando la capacidad de las técnicas de análisis para el análsis de Δm_s. Obtenemos:

$$\Delta m_d = (0.503 \pm 0.063\ (stat.) \pm 0.015\ (syst.))\ \mathrm{ps}^{-1}.$$

Acknowledgements

It was in May 2000 when I first visited Fermilab. A few years have passed since then, full of experiences that by no means can be collected in this thesis. At least I would like to use these lines to thank all the people that made this thesis possible, or a nicer path.

First of all I thank Alberto Ruiz for being so patient with me. He has been a source of theoretical knowledge, helpful at any time I asked him, always with the warmest smile. He always complained about my telegraphic writing, and I hope his efforts had some success. On top of that he is a great person.

What can I say about Iván Vila? We shared an apartment for a while. Seriously, you should have seen this thesis before his corrections. He is a quiet person, and an example of patience against any kind of problem. I can not remember how many times he asked me to note things down.

Guillelmo Gómez-Ceballos helped me whenever I had any doubt about PAW or Fortran, when both of us were at DELPHI. He is an incredibly hard worker, and a friend that has had to overcome really hard moments in the last years. He has been like a supervisor to me, when Alberto and Iván were in Santander while I was at Fermilab.

Christoph Paus made it possible for me to work with the MIT people at Fermilab. The analysis in this thesis has been successfully done thanks to his coordination of the different people involved in it, himself included. Maybe my programming is not better thanks to him, but definitely it is more organized. He is also a great challenge in racquetball.

Nuno Leonardo and I started working together two summers ago, with charged B mesons. Since then we have always worked elbow to elbow. Guillelmo, Nuno and I had unforgettable nights without sleep together, and it is always a pleasure discussing physics with him.

Ivan Furić has been a wonderful help. It seemed like he always had the right answer whenever I asked him. He has been helpful since the time the two of us were working in the TOF detector, until now in the B_s^0 mixing analysis.

During my first days (months) at Fermilab, it was for me quite difficult to understand what Gerry Bauer said. That was how bad my English was. He has been my other source of theoretical knowledge, and even more: everytime I asked him a way to solve a problem, he gave me three or four possible solutions.

Thank you Stephie for staying with me until the problem at hand was solved, at a time when you were extremely busy, and for the nice conversations we had. The opposite side flavor taggers used in this thesis are the result of the enormous work done by Vivek, Gavril, Ilya and Claudia, and I am in debt to them. Thank you, not only for the taggers,

but also for those small but fruitful dialogues between us.

Alberto Belloni, thank you for the Japanese animation nights, the Monte Carlo samples and the C++ help. Boris, your cookies have been very important for the success of this thesis, as well as the signal optimization and the conversations we had. Thank you Konstantin, Sasha, Arkadiy, Andreas, Mike and Jeff.

I am very grateful to Rocío and Gervasio. You really helped me with life in Fermilab during the first and difficult years. Living with you two was really nice. Thank you Kike and Gervasio for standing my music in the office.

Living with Juan Pablo was a very healthy period of my life. With him I learnt how apples can be used in any dish, and how they must be in any salad. He is one of the nicest and healthiest people I have ever met. Thank you Eli for your help in the last period of my thesis. I know the difficulties you had to overcome, and you have been an example for me while I was writing.

Thank you Jesús Marco. You were my first supervisor, and you gave me the chance of my first (and so far last) talk at CERN, energy correction on Z mass measurements. We still have to play a tennis match.

I can't avoid smiling everytime I see Francisco Matorras. Whenever we pass each other he has a joke at hand. Thanks Javier Fernández, another great roommate at Fermilab, and the person who told me about Calvin & Hobbes.

Thank you Teresa, Javier Cuevas, Amparo, Alicia, Rafa, David, Celso, Chiqui, Irma and Dani. With you the atmosphere in Santander is always excellent.

During the last two years of my thesis I have been living with Eiko. My English is now as good as it is thanks to her, otherwise how could I converse with her... or tell her that she is one of my best friends. We had a wonderful time together, with ups and downs, and we have also finished our thesis together.

Most of all, I want to thank my parents. Any time, whatever I wanted, if they could provide it, there it was. Every week I called them from US, everytime they were happy if I was doing well. The same applies when I think of my sister and brother-in-law.

I don't want to forget to mention my friends in Santander, Castro, Barakaldo, Illinois and Australia (Shoshe, that's you). This looks like the Oscar ceremony, saying thanks to every single person I know.

Appendix A

Good Runs

A run is marked as a *good run* if the shift operators, offline production operators and subdetector experts sign off that the data taking conditions for all relevant subdetectors are good enough that the data can be analyzed in a reliable fashion. In practice, the shift takers and subdetector experts mark runs as good or bad by setting appropriate bits to true or false. The B Physics Group at CDF Good Runs Selection requires the following bits to be true:

online bits: trigger good run
`RUNCONTROL_STATUS`
`SHIFTCREW_STATUS`
`CLC_STATUS`
`L1T_STATUS`
`L2T_STATUS`
`L3T_STATUS`
`COT_OFFLINE`

silicon
`SVX_OFFLINE OR (!SVX_OFFLINE AND SVX_STATUS)`

muons
`CMU_OFFLINE OR (!CMU_OFFLINE AND CMU_STATUS)`
`CMP_OFFLINE OR (!CMP_OFFLINE AND CMP_STATUS)`
`SVT_STATUS`
`CAL_OFFLINE`

The first bit to check is `RUNCONTROL_STATUS`, which is set to true if there are at least 10^8 live Tevatron clock cycles, 10^4 Level 1 accepts, 10^3 Level 2 accepts and at least 1 nb^{-1} of luminosity in the run. The `SHIFTCREW_STATUS` bit is set by the data acquisition shift person, who confirms that no undocumented trigger tables were used in the gathering of the data, and the offline shift crew, which confirm that the data collected during the run has been sent through offline production without any problem. The `CLC_STATUS` bit will be set if the high voltage was on for the Čerenkov Luminosity Counters during the run, and luminosity and beam monitor plots are reasonable. This guarantees good quality of the offline luminosity measurement done with the CLC subdetector.

`L1T_STATUS` and `L2T_STATUS` bits are set if Level 1 and Level 2 trigger monitoring plots agree with templates provided to the shift crew. The `L3T_STATUS` bit is set if the rate of SVX data corruption errors is $< 1\%$ and the run number is correctly set. If the SVT online beam position subtraction is done correctly and the SVT occupancy is within limits set by experts, the `SVT_STATUS` will be set. The `SVX_STATUS` bit will be set on if the SVX high voltage is on. For the `COT_OFFLINE` bit to be set, the integrated luminosity of the run has to be larger than 10 nb^{-1} and the number of bad COT channels has to be less than 1%.

Appendix B

Analytical Expressions

One of the major efforts taken in this analysis has been the development of all the PDF expressions in a way they could be analytically integrated. This aim stems in the computation speed. To minimize likelihood expressions for all the events, a precise numerical integration would take long periods of time. On the contrary, the speed is greatly enhanced by the use of analytically integrable expressions.

In the unbiased modes every PDF is analytically integrable. The incorporation of a decay-length efficiency curve in the $B \rightarrow D\pi$ decay modes increased the complexity of every decay-length PDF associated with signal events. This led to the following empirical parameterization of the decay-length efficiency curve, described in (5.22),

$$\xi(ct) \;=\; \begin{cases} 1 & \text{for } B \rightarrow J/\psi K \text{ decay modes} \\ \\ \sum_{j=1}^{3} \alpha_j \, (ct-\beta_j)^2 \, e^{-\frac{ct}{\gamma_j}} \, \theta(ct-\beta_j) & \text{for } B \rightarrow D\pi \text{ decay modes} \end{cases} \tag{B.1}$$

Lifetime Functions

We saw $L^S_{ct}(ct, \sigma_{ct})$ for $B \rightarrow D\pi$ decay modes in (5.19). Here we describe the analytical expression of the normalization factor for each event, $N(\sigma_{ct})$.

$$
\begin{aligned}
L_t^S(t,\sigma_t) &= \frac{1}{N(\sigma_t)}\left[\frac{1}{\tau}e^{-\frac{t'}{\tau}}\theta(t')\otimes G(t-t',\sigma)\right]\xi(t)\,, \\
N(\sigma_t) &\equiv \int_{-\infty}^{+\infty}\frac{1}{\tau}e^{-\frac{t'}{\tau}}\theta(t')\otimes G(t-t',\sigma)\,\xi(t)\,dt \qquad \text{(B.2)} \\
&= \int_{-\infty}^{+\infty}\frac{1}{2\tau}\,e^{-\frac{1}{\tau}\left(t-\frac{\sigma^2}{2\tau}\right)}Erfc\left(\frac{\sigma^2-t\tau}{\sqrt{2}\sigma\tau}\right)\sum_{j=1}^{3}\alpha_j\,(t-\beta_j)^2\,e^{-\frac{t}{\gamma_j}}\,\theta(t-\beta_j)\,dt \\
&= \sum_{j=1}^{3}N_j(\sigma_t)\,, \\
N_j(\sigma_t) &\equiv \frac{\alpha_j}{2\tau}\,e^{\frac{\sigma^2}{2\tau^2}}\int_{\beta_j}^{+\infty}e^{-\left(1+\frac{\tau}{\gamma_j}\right)\frac{t}{\tau}}Erfc\left(\frac{\sigma^2-t\tau}{\sqrt{2}\sigma\tau}\right)(t-\beta_j)^2\,dt \\
&= \frac{\alpha_j}{2b}\,A_j\,, \\
A_j &\equiv \left\{\beta_j^2-2\beta_j\frac{\tau}{b}\left(1-b\frac{\sigma^2}{\tau\gamma_j}\right)+\frac{\tau^2}{b^2}\left[2+\frac{\sigma^2}{\tau^2}\left(1-\frac{\tau}{\gamma_j}\right)b+\frac{\sigma^4}{\tau^2\gamma_j^2}b^2\right]\right\} \\
&\quad\cdot\left[2-Erfc\left(-\frac{\beta_j\gamma_j+\sigma^2}{\sqrt{2}\sigma\gamma_j}\right)\right]e^{\frac{\sigma^2}{2\gamma_j^2}} \\
&\quad+2\frac{\tau^2}{b^2}Erfc\left(-\frac{\beta_j\tau-\sigma^2}{\sigma\tau}\right)e^{-b\frac{\beta_j}{\tau}+\frac{\sigma^2}{2\tau^2}}+\tau\sigma\left(\frac{2}{b}-\frac{\beta_j}{\tau}-\frac{\sigma^2}{\tau\gamma_j}\right)\sqrt{\frac{2}{\pi}}e^{-\frac{\beta_j}{\gamma_j}-\frac{\beta_j^2}{2\sigma^2}}\,,
\end{aligned}
$$

where we use natural units ($c = 1$), and

$$\sigma \equiv S_t\sigma_t\,, \qquad b \equiv 1+\frac{\tau}{\gamma_j}\,.$$

Mixing Functions

In chapter 7 we obtained a general proper decay-length PDF that included tagging decision and event-by-event dilution (7.6). We repeat it here for a single tagger,

$$L^S_{ct}(\vec{x}, tag^j) \;=\; \begin{cases} L_{NT}(\vec{x}) = \dfrac{\mathcal{P}_{NT}(ct')}{N_{NT}} \otimes G(ct-ct', S_{ct}\sigma_{ct})\,\xi(ct) & \forall\;\; tag^j = 0 \\[2ex] L^j_{WS}(\vec{x}) = \dfrac{\mathcal{P}^j_{WS}(ct')}{N^j_{WS}} \otimes G(ct-ct', S_{ct}\sigma_{ct})\,\xi(ct) & \text{for } tag^j = -1 \\[2ex] L^j_{RS}(\vec{x}) = \dfrac{\mathcal{P}^j_{RS}(ct')}{N^j_{RS}} \otimes G(ct-ct', S_{ct}\sigma_{ct})\,\xi(ct) & \text{for } tag^j = +1 \end{cases} \tag{B.3}$$

where $\vec{x} \equiv (ct, \sigma_{ct}, D)$. Let us write L_{NT}, L_{WS} and L_{RS} explicitly,

$$\begin{aligned} L_{NT} &= (1-\epsilon)\frac{1}{N_{NT}}\,\frac{1}{c\tau}\,e^{-\frac{ct'}{c\tau}}\,\theta(ct') \otimes G(ct-ct', S_{ct}\sigma_{ct})\,\xi(ct) \\ L_{RS} &= \epsilon\,\frac{1+S_D D}{2N_{WS}}\,\cos(\Delta m_d t')\frac{1}{c\tau}\,e^{-\frac{ct'}{c\tau}}\,\theta(ct') \otimes G(ct-ct', S_{ct}\sigma_{ct})\,\xi(ct) \\ L_{WS} &= \epsilon\,\frac{1-S_D D}{2N_{RS}}\,\cos(\Delta m_d t')\frac{1}{c\tau}\,e^{-\frac{ct'}{c\tau}}\,\theta(ct') \otimes G(ct-ct', S_{ct}\sigma_{ct})\,\xi(ct) \end{aligned}$$

The normalization N_{NT} reduces to the ones used in the lifetime measurements. In the $B \to J/\psi K$ decay modes it is just $N_{NT} = 1-\epsilon$, whereas in the $B \to D\pi$ decay modes it is $N_{NT} = (1-\epsilon)N(\sigma_{ct})$, with $N(\sigma_{ct})$ described in (B.2). On the contrary, both N_{WS} and N_{RS} are complicated by the cosine term. In the following we will use natural units $(c = 1)$, and

$$\sigma \equiv S_t\sigma_t\,, \qquad \mathcal{D} \equiv S_D D\,.$$

Now we can write N_{WS} and N_{RS} as

$$\begin{aligned} N_{\substack{RS\\WS}} &= \int_{-\infty}^{+\infty} \epsilon\,\frac{1\pm\mathcal{D}}{2}\,\cos(\Delta m_d t')\frac{1}{\tau}\,e^{-\frac{t'}{\tau}}\,\theta(t') \otimes G(t-t', \sigma)\,\xi(t)\,dt \\ &= \epsilon\,\frac{1\pm\mathcal{D}}{4\tau}\sum_{k=\pm1} Re\left[\int_{-\infty}^{+\infty} e^{-\frac{t'}{w}}\,\theta(t') \otimes G(t-t', \sigma)\,\xi(t)\,dt\right], \qquad\qquad (\text{B.4}) \\ w &\equiv \frac{1}{1+ik\Delta m_d\tau}\,, \end{aligned}$$

where $i = \sqrt{-1}$. The expression (B.4) reminds us of the lifetime one, by replacing a real lifetime τ with a complex (non-physical) one, w. For the $B \to J/\psi K$ decay modes the tagged events normalizations are

$$N_{\substack{RS \\ WS}} = \frac{1}{2}\left[1 \pm \frac{\mathcal{D}}{1+\Delta m_d^2 \tau^2}\right].$$

In the more complicated case of the $B \to D\pi$ decay modes, the tagged events normalizations have a similar expression to (B.2). The main difference is the replacement of τ by w. Such modification implies that only the real part has a physical meaning. Furthermore, the complex complementary error function $Erfc(z)$ substitutes the real complementary error function $Erfc(x)$,

$$\begin{aligned} Erfc(x) &= \frac{2}{\sqrt{\pi}} \int_x^\infty e^{-u^2}\, du\,, \\ Erfc(z) &= e^{-z^2} W(iz)\,, \\ W(iz) &= e^{-z^2}\left[1 + \frac{2i}{\sqrt{\pi}} \int_0^z e^{t^2}\, dt\right]\,, \end{aligned}$$

with z a complex number and $W(z)$ the Fadeeva function. A previous study with complex numbers treatment can be found in [55].

Generic Functions

$$\theta(ct' - a) = \begin{cases} 1 & ct' \geq a \\ 0 & ct' < a \end{cases} \tag{B.5}$$

$$\delta(ct' - b) = \begin{cases} \infty & ct' = b \\ 0 & ct' \neq b \end{cases} \tag{B.6}$$

$$f(ct') \otimes g(ct - ct') \equiv \int_{-\infty}^{+\infty} f(ct') \cdot g(ct - ct')\, dt'\,. \tag{B.7}$$

List of Figures

List of Tables

Bibliography

[1] L. Wolfenstein,
Final state interactions and CP violation in weak decays,
Phys. Rev. **D43** (1991) 151

[2] A. Ali,
CKM Phenomenology and B meson Physics present status and current issues,
Proceed. of the XXXI Int. Meet. on Fund. Physics, Spain, 2003

[3] A. J. Buras et al.,
Leading and next-to-leading QCD corrections to ϵ parameter
and $B^0 - \bar{B}^0$ mixing in the presence of a heavy top quark,
Nucl. Phys. **B347** (1990) 491

[4] Proceed. of the Int. Conf. on High Energy Physics, Beijing, 2004

[5] D. Becirevic et al.,
Phys. Lett. **B563** (2003) 150

[6] Proceed. of the CKM Workshop, San Diego, 2005

[7] `http://www.slac.stanford.edu/xorg/hfag/osc/index.html`

[8] G. Aubrecht et al.,
A Teachers Guide to the Nuclear Science Wall Chart,
Contemporary Physics Education Project, 2003,
`http://www.lbl.gov/abc/wallchart/teachersguide/pdf/Chap11.pdf`

[9] C. W. Schmidt,
The Fermilab 400-MeV Linac upgrade,
FERMILAB-CONF-93-111 (1993)

[10] Fermilab Beams Division,
Run II Handbook,
`http://www-bd.fnal.gov/runII/index.html`

[11] J. Marriner,
Stochastic Cooling Overview,
FERMILAB-CONF-03-158 (2003)

[12] R. Blair et al.,
The CDF-II detector: Technical Design Report,
FERMILAB-PUB-96/390-E (1996)

[13] F. Abe et al.,
Nucl. Inst. and Meth. Phys. Res, **271A**, 387 (1988),
FERMILAB-PUB-94/024-E (1994)

[14] T. K. Nelson et al.,
FERMILAB-CONF-01/357-E

[15] A. Sill et al.,
Nucl. Instrum. Methods, **A447**, 1–8 (2000)

[16] T. Affolder et al.,
Nucl. Instrum. Methods, **A485**, 6–9 (2002)

[17] K. T. Pitts et al.,
FERMILAB-CONF-96-443-E

[18] `http://penn01.fnal.gov/∼cot/`

[19] Particle Data Group, S. Eidelman et al.,
Phys. Lett. B **592**, 1 (2004)

[20] R. Brun, K. Hakelberg, M. Hansroul, and J.C. Lasalle,
CERN-DD-78-2;
CERN-DD-78-2-REV

[21] A. Korn,
Measurement of the B Hadron Masses in exclusive J/ψ *Decay Channels*,
CDF Public Note 6963

[22] D. Acosta et al. [CDF Collaboration],
A Time-of-Flight detector in CDF-II,
Nucl. Instrum. Methods A **518**, 605 (2004)

[23] `http://huhepl.harvard.edu/∼cmx/cdfnotes/`

[24] E. J. Thomson et al.,
IEEE Trans. Nucl. Sci. **49**, 1063 (2002)

[25] `http://web.hep.uiuc.edu/Engin/CDF/XTRP/`

[26] W. Ashmanskas et al.,
FERMILAB-CONF-02/035-E;
A. Bardi et al.,
Nucl. Instrum. Methods Phys. Res. A **485**, 6 (2002)

[27] D. Acosta et al.,
Nucl. Instrum. Methods A **494**, 57 (2002)

[28] A. Korn, R. Snyder, J. Boudreau,
`http://cdfcodebrowser.fnal.gov/CdfCode/source/TrackingUserHL/`

[29] M. Feindt, S. Menzemer, K. Rinnert,
TrackingKal -
A Tracking and Alignment Software Package for the CDF-II Silicon Detector,
CDF Public Note 5968

[30] P. Sphicas,
A $b\bar{b}$ *Monte Carlo Generator*,
CDF Public Note 2655;
K. Anikeev, P. Murat, Ch. Paus,
Description of Bgenerator II,
CDF Public Note 5092

[31] P. Nason, S. Dawson and R.K. Ellis,
Nucl. Phys. **B303** (1988) 607;
Nucl. Phys. **B327** (1989) 49

[32] C. Peterson et al.,
Phys. Rev. **D27** (1983) 105

[33] `http://www.slac.stanford.edu/~lange/EvtGen/`

[34] K. Anikeev,
Measurement of the Lifetimes of B Meson Mass Eigenstates,
CDF Public Note 7269

[35] I.K. Furić,
Measurement of the Ratio of Branching Fractions
$\mathrm{BR}\left(B_s^0 \to D_s^- \pi^+\right) / \mathrm{BR}\left(B_d^0 \to D^- \pi^+\right)$,
CDF Public Note 7352

[36] K. Hagiwara et al.,
Phys. Rev. **D66** (2002) 010001

[37] F. James,
MINUIT. Function minimization and error analysis, CERN Program Library Long Write-up D506, `http://consult.cern.ch/writeup/minuit/`

[38] J. Guimarães da Costa,
Beamline constraint in CTVMFT,
CDF Public Note 6439;
J. Marriner,

Secondary Vertex Fit with Mass and Pointing Constraints (CTVMFT),
CDF Public Note 1996

[39] M. Gronau, A. Nippe, J. Rosner,
Phys. Rev. D **47**, 1988 (1993);
M. Gronau, J. Rosner,
Phys. Rev. D **49**, 254 (1994)

[40] F. Abe et al.,
Measurement of the $B_d^0 - \bar{B}^0$ *Flavor Oscillation Frequency and Study of Same Side Flavor Tagging*,
Phys. Rev. **D59** (1999) 032001;
P. Maksimović,
Observation of $\pi - B$ *meson charge-flavor Correlations and Measurement of Time Dependent* $B_d^0 - \bar{B}^0$ *Mixing in* $p\bar{p}$ *Collisions*,
CDF Public Note 4614

[41] M. Jones et al.,
Sample Composition of the l+SVT Triggers,
CDF Public Note 6480

[42] G. Giurgiu et al.,
Muon B Flavor Tagging - A Likelihood Approach,
CDF Public Note 7043,
`www-cdf.fnal.gov/physics/new/bottom/072204.blessed-like-mu-tag/`

[43] V. Tiwari et al.,
Likelihood Based Electron Tagging,
CDF Public Note 7121,
`www-cdf.fnal.gov/physics/new/bottom/081204.blessed-like-el-tag/`

[44] I. Kravchenko et al.,
Improved Jet Charge Tagger for Summer Conferences 2004,
CDF Public Note 7131,
www-cdf.fnal.gov/physics/new/bottom/040812.blessed-jqt-lsvt/

[45] G. Punzi,
Comments on likelihood fits with variable resolution,
e-print `physics/0401045` (2003)

[46] The CDF Collaboration,
Measurement of the Ratios of Branching Fractions $\mathrm{BR}\left(B^+ \to \bar{D}^0\pi^+\right)/\mathrm{BR}\left(B_d^0 \to D^-\pi^+\right)$ *and* $\mathrm{BR}\left(B_s^0 \to D_s^-\pi^+\right)/\mathrm{BR}\left(B_d^0 \to D^-\pi^+\right)$ *with the CDF-II Detector*,
CDF Public Note 7415

[47] Y. Le et al.,
Measurement of the Ratio of Branching Ratios of $\Lambda_b^0 \rightarrow \Lambda_c^+\pi^-$ *to* $B_d^0 \rightarrow D^-\pi^+$ *in* $p\bar{p}$ *Collisions at* $\sqrt{s} = 1.96$ TeV,
CDF Public Note 7427

[48] M. Bishai et al.,
Measurement of the J/ψ *Meson and b-Hadron Production Cross Sections in* $p\bar{p}$ *Collisions at* $\sqrt{s} = 1.96$ TeV,
FERMILAB-PUB-04-440-E

[49] H.G. Moser, A. Roussarie,
Mathematical methods for $B_d^0\overline{B_d^0}$ *oscillation analyses*,
NIM A384 (1997), 491-505

[50] The CDF Collaboration,
Measurement of B_d^0 *Oscillations and Calibration of Flavor Tagging in Semileptonic Decays*,
CDF Public Note 7549,
`http://www-cdf.fnal.gov/physics/new/bottom/050224.blessed-mix-bld/`

[51] The CDF Collaboration,
Study of B_s^0 *Oscillations in* $B_s^0 \rightarrow D_s^-\pi^+$,
CDF Public Note 7538,
`http://www-cdf.fnal.gov/physics/new/bottom/050310-bsmix-hadronic/`

[52] The CDF Collaboration,
Study of B_s^0 *Oscillations in* $B_s^0 \rightarrow D_s^- l^+ X$,
CDF Public Note 7542,
`http://www-cdf.fnal.gov/physics/new/bottom/050310.bsmix-semi/`

[53] The CDF Collaboration,
Combined results from B_s^0 *mixing analyses*,
CDF Public Note 7555,
`http://www-cdf.fnal.gov/physics/new/bottom/050310.bsmix-combined/`

[54] C. Lecci et al.,
Neural Network based Jet Charge Tagger,
CDFNOTE7482,
`http://www-cdf.fnal.gov/physics/new/bottom/050303.blessed-jqtnn/`

[55] F. Bedeschi et al.,
Formulas to describe resolution effects in mixing analysis,
CDF Public Note 2859